

INVESTIGATIONS ON SOLID STATE CONTROL OF DOUBLY FED INDUCTION GENERATOR

*A Thesis submitted
in fulfillment of the requirements
for the Award of the Degree of
Doctor of Philosophy*

in
Electrical Engineering

By

Sandeep Banerjee
2K13/PHD/EE/04

Under the Supervision of

Prof Dheeraj Joshi

&

Prof Madhusudan Singh



**Department of Electrical Engineering,
Delhi Technological University,
Shahbad Daulatpur,
Main Bawana Road
Delhi-110042**

UNDERTAKING

I declare that the work presented in this thesis titled **“INVESTIGATIONS ON SOLID STATE CONTROL OF DOUBLY FED INDUCTION GENERATOR,”** submitted to the Department of Electrical Engineering, Delhi Technological University, Delhi, for the award of the **Doctor of Philosophy** degree is my original work. I have not plagiarized or submitted the same work for the award of any other degree. In case this undertaking is found incorrect, I accept that my degree may be unconditionally withdrawn.

30 July, 2020
Delhi

Sandeep 30.7.2020
Sandeep Banerjee
2K13/PHD/EE/04



DELHI TECHNOLOGICAL UNIVERSITY

(Govt. of National Capital Territory of Delhi)

BAWANA ROAD, DELHI – 110042

CERTIFICATE

Date: 30.7.2020

This is to certify that the work embodied in the thesis titled, “**INVESTIGATIONS ON SOLID STATE CONTROL OF DOUBLY FED INDUCTION GENERATOR,**” submitted by **Sandeep Banerjee** (Roll No. **2K13/PHD/EE/04**) as a research scholar in the Department of Electrical Engineering, Delhi Technological University, is an authentic work carried out by him under our guidance.

The matter embodied in this thesis has not been submitted earlier for the award of any degree or diploma to the best of our knowledge and belief.

Supervisor


Dr Dheeraj Joshi

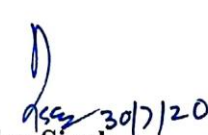
Professor

Dept. of Electrical Engineering

Delhi Technological University

Delhi

Supervisor


Dr Madhusudan Singh

Professor

Dept. of Electrical Engineering

Delhi Technological University

Delhi

DRC Chairman


(Dr Madhusudan Singh)

ACKNOWLEDGEMENT

I take this opportunity to express my sincere gratitude to my supervisors Dr Dheeraj Joshi, Professor, EED, DTU and Dr Madhusudan Singh, Professor, EED, DTU, for their invaluable guidance. It would have been impossible for me to take this project to completion without their innovative ideas, relentless support and constant encouragement. I consider myself extremely fortunate to have had a chance to work under their supervision. In spite of their hectic schedule, they were always approachable and took time off to discuss my problems and render advice and encouragement. It has been a very learning and enjoyable experience to carry out research under their supervision.

I venture to thank Prof. Uma Nangia, HoD, EE, and all the other faculty members of EED, DTU for the invaluable knowledge they imparted in an exciting and enjoyable way during course work. I would like to extend sincere thanks to the staff of EED, DTU for their co-operation and support in all proceedings.

I express my gratitude to Late Prof M. S. Bhattacharya, whose guidance helped me choose the correct over the pleasant. Heartfelt thanks are also due to Prof Dharmender Saini (Principal, BVCoE), Dr Kusum Tharani (HoD, EEE, BVCoE) and Dr Rajasekar S (my ex-senior) whose immense assistance has made me perpetually indebted. It would be sheer egotism on my part not to acknowledge the support provided by my friends Dr Rahul Sharma, Dr Sandeep Sharma and Mrs Gargi Mishra, and my students Nitin, Aashish, Nishtha and Sidharth. Their continuous contributions helped me resolve a number of complex issues.

I express my deep sense of reverence to Ma and Baba without whose love, affection, blessings and sacrifices I wouldn't have reached this stage. Thanks-a-ton to Shraboni, who made immense adjustments to cope up with my watertight schedule.

Lastly and importantly, I wish to invoke the memory of my deceased grandparents, aunt and uncle. I hope they bless me from their heavenly abode.

(Sandeep Banerjee)

2K13/PHD/EE/04

Research Scholar

Department of Electrical Engineering, DTU.

E-mail: sandeepbanerjee25@gmail.com

ABSTRACT

The exponential increase in energy demand and the limited amount of fossil fuels has made the focus of research on ways and means of harnessing renewable energy sources such as solar, wind, biomass etc. Out of all the available renewable sources, wind energy forms a large chunk of the total generation. As on March 2020, the world leaders in wind energy production are China, USA, Germany and India.

The progress of wind power in recent years has exceeded all expectations, with Europe leading the global market. Recent progress in wind technology has led to cost reduction to levels comparable, in many cases, with conventional methods of electricity generation. The present scenario of energy coupled with the extensive growth of wind energy installations in the recent past has led to the motivation for extending research work in the field of wind energy conversion systems (WECS).

For efficiently harnessing wind energy, doubly-fed induction generators (DFIGs) have become extremely popular owing to their large range of operation. DFIGs can be operated both in the grid connected mode as well as the stand-alone mode. The speed of a DFIG can be varied from the sub-synchronous to the super-synchronous. A partially rated power converter can be easily used with a DFIG. This in turn, reduces the cost of the overall system.

DFIGs can be put to use for capturing wind energy from a fixed speed prime mover as well as a variable speed prime mover. This facility leads to immense operational flexibility in terms of the operating speed of the machine. The major drawbacks associated with the DFIG based WECS are their complex control, harmonic distortions and sensitivity to unbalanced grid voltages.

Power electronics is used to efficiently interface renewable energy systems to the grid. It is playing a very important role in modern WECS, especially for control purposes. Control by means of power electronics allows the fulfilment of grid requirements, a better use of the

turbine capacity and the alleviation of aerodynamic and mechanical loads that reduce the lifetime of installation.

This thesis identified the scope of research in the following directions:

- The control strategies associated with DFIGs.
- The performance of solid state converters used in DFIG.
- The power quality issues related to DFIGs.
- The methods of controlling the active power and the reactive power of DFIG based WECS.
- The nature inspired artificial intelligence (AI) techniques for designing DFIG controller parameters.

The major contributions contained in this thesis are as follows:

- Developed two novel rational methods to compute the optimal values of DFIG rotor current commands for enhancing efficiency and power factor of grid connected systems.
- Developed three GA based methods to compute the optimal values of DFIG rotor current commands for enhancing efficiency and power factor of grid connected systems.
- Proposed and validated two novel DFIG topologies for application in WECS based autonomous systems.
- Applied a modified perturb and observe (P&O) algorithm for obtaining faster response with reduced oscillations in the proposed novel DFIG topologies.
- Proposed and validated a simple control for three-lead based autonomous DFIG DC system whose output voltage is held constant under varying wind speeds.
- Presented the analysis of the parallel operation of two DFIGs of different ratings connected in combination of two-lead and three-lead topology.

TABLE OF CONTENTS

UNDERTAKING	i
CERTIFICATE	ii
ACKNOWLEDGEMENT	iii
ABSTRACT	iv
TABLE OF CONTENTS	vi
LIST OF NOTATIONS AND ACRONYMS	viii
LIST OF FIGURES	xiii
LIST OF TABLES	xviii
Chapter 01 Introduction	1-9
1.1 Introduction	2
1.2 Research Motivation	3
1.3 DFIG based Energy Conversion System	3
1.3.1 Wind Generator Systems	3
1.3.2 Power Electronic Converters used in WECS	4
1.4 Control Strategies in WECS	6
1.5 Organization of Thesis	8
1.6 Conclusion	9
Chapter 02 Literature Survey of DFIG based Energy Conversion System	10- 24
2.1 Introduction	10
2.2 Literature Survey	10
2.3 Research Gaps Identified	23
2.4 Research Objective	23
2.5 Research Methodology	24
2.6 Conclusion	24
Chapter 03 Mathematical Modelling of System Components	25-38
3.1 Introduction	25
3.2 Dynamic Modelling of DFIG	26
3.2.1 $\alpha\beta$ Model of DFIG	27
3.2.2 dq Model of DFIG	30
3.2.3 State-Space Representation of $\alpha\beta$ Model	31
3.3 Modelling of Practical DC-DC Converters	32
3.3.1 Modelling of a Step-Down DC-DC Converter	32
3.3.2 Modelling of a Step-Up DC-DC Converter	35
3.4 Conclusion	38
Chapter 04 Simulation and Hardware Implementation of Power Electronic Converters	39-58
4.1 Introduction	39
4.2 VSI Prototypes	40
4.2.1 Single-phase VSI	40
4.2.2 Three-phase VSI	41
4.3 Control Signal Generation Using XSG	41
4.3.1 Sinusoidal Modulating Signal Generation	42
4.3.2 Carrier Signal Generation	43

4.3.3 Automatic Code Dumping in FPGA	46
4.4 Description of Hardware	46
4.5 Application of XSG based PEC in Standalone DFIG System	48
4.6 Results and Analysis	48
4.6.1 Analysis of Single-phase Three-level VSI	49
4.6.2 Analysis of Single-phase Five-level VSI	51
4.6.3 Analysis of Three-phase VSI	53
4.6.4 DFIG system with rotor excited by three-phase inverter	56
4.7 Conclusion	57
Chapter 05 Analysis of Grid-Connected DFIG System using Rational Methods and Genetic Algorithm	59- 88
5.1 Introduction	59
5.2 Steady State DFIG Model	59
5.3 Procedure to determine Optimal Rotor Current Commands	61
5.4 Results and Analysis	70
5.4.1 Results corresponding to the DFIG of low power rating	70
5.4.2 Results corresponding to the DFIG of high power rating	80
5.5 Conclusion	88
Chapter 06 Analysis of Two-lead and Three-lead Configuration of DC Excited DFIG	89-123
6.1 Introduction	89
6.2 System Description	89
6.2.1 DC Two-Lead DFIG Configuration	89
6.2.2 DC Three-Lead DFIG Configuration	90
6.3 Isolated DFIG with Rotor fed by DC-DC Converter	90
6.3.1 Two-Lead and Three-Lead DFIG Systems fed by Boost Converter	91
6.3.2 Control of Three-Lead DFIG System excited by Buck Converter	91
6.4 DFIG DC system with MPPT	92
6.5 Two-lead and Three-lead topologies in parallel	95
6.6 Results and Analysis	97
6.6.1 Comparative of DC Two-Lead System with Three-Lead System	97
6.6.2 Two-Lead and Three-Lead Systems excited by Boost Converter	102
6.6.3 Three-Lead DFIG System excited by Buck Converter	104
6.6.4 MPPT implementation on DFIG DC System	106
6.6.5 Parallel connection of DFIG topologies	108
6.6.5 Hardware Results of Two-lead and Three-lead DFIG topologies	112
6.7 Conclusion	122
Chapter 07 Conclusion and Scope of Future Work	124-126
7.1 Introduction	124
7.2 Scope of Future Work	126
7.3 Conclusion	126
References	127
Appendix	148
Publications	154

I. LIST OF NOTATIONS & ACRONYMS

The list of symbols used in the thesis have been mentioned in Table I.1.

Table I.1 List of symbols

S.No.	Symbol	Meaning	Unit
1	R_s	Stator resistance	Ω
2	$i_{a1s}, i_{b1s}, i_{c1s}$	Stator currents of phases a, b, and c respectively	A
3	$v_{a1s}, v_{b1s}, v_{c1s}$	Applied stator voltages respectively	V
4	$\psi_{a1s}, \psi_{b1s}, \psi_{c1s}$	Stator fluxes of phases a, b, and c respectively	wb
5	ω_s	Angular frequency imposed by the grid	rad/s
6	R_r	Rotor resistance referred to the stator	Ω
7	$i_{a2r}, i_{b2r}, i_{c2r}$	Stator referred rotor currents of phases a, b, and c respectively	A
8	$v_{a2r}, v_{b2r}, v_{c2r}$	Stator referred rotor voltages respectively	V
9	$\psi_{a2r}, \psi_{b2r}, \psi_{c2r}$	Rotor fluxes	wb
10	ω_r	Angular frequency of rotor magnitudes	rad/s
11	ω_m	Electrical angular frequency of the machine	rad/s
12	Ω_m	Mechanical angular speed of the machine	rad/s
13	p	Pair of poles of the machine	
14	\vec{v}_{1s}^s	Stator voltage space vector in stator reference frame	V
15	\vec{i}_{1s}^s	Stator current space vector in stator reference frame	A
16	$\vec{\psi}_{1s}^s$	Stator flux space vector in stator reference frame	wb
17	\vec{v}_{2r}^r	Rotor voltage space vector in rotor reference frame	V
18	\vec{i}_{2r}^r	Rotor current space vector in rotor reference frame	A
19	$\vec{\psi}_{2r}^r$	Rotor flux space vector in rotor reference frame	wb

20	L_s	Stator inductance	H
21	L_r	Rotor inductance referred to the stator	H
22	L_m	Magnetizing inductance	H
23	$L_{\sigma s}$	Stator leakage inductance	H
24	$L_{\sigma r}$	Rotor leakage inductance referred to the stator	H
25	$\vec{\psi}_{2r}^s$	Rotor flux space vector in stator reference frame	wb
26	\vec{i}_{2r}^s	Rotor current space vector in stator reference frame	A
27	\vec{i}_{1s}^r	Stator current space vector in rotor reference frame	A
28	θ_m	Electrical angular position of the shaft	rad
29	\vec{v}_{2r}^s	Rotor voltage space vector in stator reference frame	V
30	$\psi_{\alpha 1s}, \psi_{\alpha 2r}$	α component of stator flux and rotor flux respectively	wb
31	$\psi_{\beta 1s}, \psi_{\beta 2r}$	β component of stator flux and rotor flux respectively	wb
32	$v_{\alpha 1s}, v_{\alpha 2r}$	α component of stator voltage and rotor voltage respectively	V
33	$v_{\beta 1s}, v_{\beta 2r}$	β component of stator voltage and rotor voltage respectively	V
34	$i_{\alpha 1s}, i_{\alpha 2r}$	α component of stator current and rotor current respectively	A
35	$i_{\beta 1s}, i_{\beta 2r}$	β component of stator current and rotor current respectively	A
36	$\vec{\psi}_{2r}^a$	Rotor flux space vector in synchronous reference frame	wb
37	\vec{i}_{2r}^a	Rotor current space vector in synchronous reference frame	A
38	\vec{i}_{1s}^a	Stator current space vector in synchronous reference frame	A
39	\vec{v}_{2r}^a	Rotor voltage space vector in synchronous reference frame	V

40	\vec{v}_{1s}^a	Stator voltage space vector in synchronous reference frame	V
41	$\vec{\psi}_{1s}^a$	Stator flux space vector in synchronous reference frame	wb
42	ψ_{d1s}, ψ_{d2r}	d component of stator flux and rotor flux respectively	wb
43	ψ_{q1s}, ψ_{q2r}	q component of stator flux and rotor flux respectively	wb
44	v_{d1s}, v_{d2r}	d component of stator voltage and rotor voltage respectively	V
45	v_{q1s}, v_{q2r}	q component of stator voltage and rotor voltage respectively	V
46	i_{d1s}, i_{d2r}	d component of stator current and rotor current respectively	A
47	i_{q1s}, i_{q2r}	q component of stator current and rotor current respectively	A
48	T_{em}	Electromagnetic torque	Nm
49	$V, VI, V2$	DC input voltages to power electronic converters	V
50	I	Current through the inductor of DC-DC converter	A
51	i	Instantaneous current through the inductor of DC-DC converter	A
52	r	Coil resistance of DC-DC converter	Ω
53	L	Coil inductance of DC-DC converter	H
54	C	Capacitance of DC-DC converter	F
55	R	Load resistance of DC-DC converter	Ω
56	V_o	DC-DC converter output voltage	V
57	D	Duty ratio of DC-DC converter	
58	P	Power input of DC-DC converter	W
59	k	Instant of time at which measurement has been made	
60	\bar{I}_c	Loss component of no load current	A
61	I_{rd}	Direct axis rotor current	A
62	\bar{I}_e	No load current	A
63	\bar{I}_m	Magnetizing component of no load current	A

64	I_{rq}	Quadrature axis rotor current	A
65	$\bar{I}_r = I_r \angle \theta_r$	Rotor current expressed as magnitude and phase	A
66	$\bar{I}_s = I_s \angle \theta_s$	Stator current expressed as magnitude and phase	A
67	P_m	Maximum mechanical power	W
68	P_r	Rotor active power	W
69	P_s	Stator active power	W
70	Q_r	Rotor reactive power	VAR
71	Q_s	Stator reactive power	VAR
72	R_c	Resistance of core	Ω
73	X_{lr}	Leakage reactance of rotor	Ω
74	X_{ls}	Leakage reactance of stator	Ω
75	X_m	Magnetizing reactance	Ω
76	$s = \omega_s - \omega_r / \omega_s$	Slip	
77	$\bar{V}_r = V_r \angle \phi$	Rotor voltage expressed as magnitude and phase	V
78	$\bar{V}_s = V_s \angle 0^\circ$	Stator voltage expressed as magnitude and phase	V
79	$\bar{\lambda}_s = \lambda_s \angle \theta_{fs}$	Stator flux linkage expressed as magnitude and phase	AT
80	f_s, f_r	Electrical frequency of output voltage for DFIG stator and rotor respectively	Hz
81	N_m	Mechanical speed of DFIG shaft	rpm

The list of acronyms used in the thesis have been mentioned in Table I.2.

Table I.2 List of acronyms

S. No.	Acronym	Full form
1	AI	artificial intelligence
2	ANN	artificial neural network
3	DFIG	doubly-fed induction generator
4	DSP	digital signal processors
5	FL	fuzzy logic

6	FOC	field oriented control
7	FPGA	field programmable gate array
8	GA	genetic algorithm
9	GSC	grid side converter
10	HDL	hardware definition language
11	IGBT	insulated gate bipolar transistor
12	MC	matrix converter
13	MF	membership function
14	MP&O	modified perturb and observe
15	MPPT	maximum power point tracking
16	OF	objective function
17	PEC	power electronic converter
18	PI	proportional-integral
19	PLL	phase-locked loop
20	PMSG	permanent magnet synchronous generator
21	PSO	particle swarm optimization
22	PV	photo voltaic
23	PWM	pulse width modulation
24	RSC	rotor side converter
25	SCIG	squirrel cage induction generator
26	SG	synchronous generator
27	SHE	selective harmonic elimination
28	SMC	sliding mode controller
29	SPWM	sine pulse width modulation
30	VSC	voltage source converter
31	VSI	voltage source inverter
32	WECS	wind energy conversion systems
33	XSG	xilinx system generator

II. LIST OF FIGURES

The list of figures used in the thesis have been mentioned in Table II.1.

Table II.1 List of figures

S. No.	Fig. No.	Caption	Pg. No.
1	Fig. 1.1	Bar graph illustrating the electrical energy generation in India	2
2	Fig. 1.2	Block diagram of a WECS	3
3	Fig. 3.1	DFIG electric equivalent circuit	26
4	Fig. 3.2	DFIG $\alpha\beta$ model in stator co-ordinates	29
5	Fig. 3.3	DFIG dq model in synchronous reference frame	31
6	Fig. 3.4	Circuit diagram of a practical buck converter	32
7	Fig. 3.5	Circuit diagram of a practical buck converter when the switch is ON	33
8	Fig. 3.6	Circuit diagram of a practical buck converter when the switch is OFF	34
9	Fig. 3.7	Circuit diagram of a practical boost converter	35
10	Fig. 3.8	Circuit diagram of a practical boost converter when the switch is ON	36
11	Fig. 3.9	Circuit diagram of a practical boost converter when the switch is OFF	37
12	Fig. 4.1	Power circuit of single phase inverters (a) Three-level diode clamped topology (b) Five-level eight-switch H-bridge topology	40
13	Fig. 4.2	Three-phase voltage source inverter	41
14	Fig. 4.3	Sinusoidal signal generation using XSG	42
15	Fig. 4.4	Triangular signal generation using XSG	44
16	Fig. 4.5	Hardware prototype for single-phase VSI (a) Three-level (b) Five-level	47
17	Fig. 4.6	Hardware for three-phase VSI	47
18	Fig. 4.7	Block Diagram of the isolated DFIG system with rotor excited by three-phase inverter	48

19	Fig. 4.8	SPWM for three-level DCMLI	49
20	Fig. 4.9	Output phase voltage of three-level inverter (a) Simulation result (b) Hardware result	50
21	Fig. 4.10	Control scheme for five-level inverter	51
22	Fig. 4.11	Output phase voltage of five-level inverter (a) Simulation result (b) Hardware result	52
23	Fig. 4.12	Control scheme for three-phase VSI	53
24	Fig. 4.13	Output phase voltage of three-phase VSI (a) Simulation result (b) Hardware result	54
25	Fig. 4.14	Output line voltage of three-phase VSI (a) Simulation result (b) Hardware result	55
26	Fig. 4.15	Three-phase VSI fed DFIG (a) Phase A stator voltage (b) Load current	57
27	Fig. 5.1	Block diagram representation of a grid connected DFIG with back-to-back converters	60
28	Fig. 5.2	Per-phase equivalent circuit of a grid connected DFIG operating in steady state	60
29	Fig. 5.3	Flowchart representation of the methods for optimal rotor current command generation	69
30	Fig. 5.4	Graph of optimal direct axis rotor current command versus slip, obtained using RM	70
31	Fig. 5.5	Graph of optimal direct axis rotor current command versus slip, obtained using GA	71
32	Fig. 5.6	Graph of optimal quadrature axis rotor current command versus slip, obtained using RM	71
33	Fig. 5.7	Graph of optimal quadrature axis rotor current command versus slip, obtained using GA	72
34	Fig. 5.8	Graph of power factor versus slip, obtained using RM	73
35	Fig. 5.9	Graph of power factor versus slip, obtained using GA	74
36	Fig. 5.10	Graph of efficiency versus slip, obtained using RM	74
37	Fig. 5.11	Graph of efficiency versus slip, obtained using GA	75
38	Fig. 5.12	Graph of voltage across the magnetizing branch versus slip, obtained using RM	76

39	Fig. 5.13	Graph of voltage across the magnetizing branch versus slip, obtained using GA	76
40	Fig. 5.14	Graph of angle between the stator axis and direct axis versus slip, obtained using RM	77
41	Fig. 5.15	Graph of angle between the stator axis and direct axis versus slip, obtained using GA	78
42	Fig. 5.16	Graph of DFIG output active power versus slip, obtained using RM	78
43	Fig. 5.17	Graph of DFIG output active power versus slip, obtained using GA	79
44	Fig. 5.18	Graph of DFIG output reactive power versus slip, obtained using RM	80
45	Fig. 5.19	Graph of DFIG output reactive power versus slip, obtained using GA	81
46	Fig. 5.20	Tracking of direct axis rotor current reference	82
47	Fig. 5.21	Tracking of quadrature axis rotor current reference	82
48	Fig. 5.22	Tracking of rotor speed reference	83
49	Fig. 5.23	Tracking of electromagnetic torque reference	84
50	Fig. 5.24	Graph of three-phase stator currents	84
51	Fig. 5.25	Graph of three-phase rotor currents	85
52	Fig. 5.26	Tracking of direct axis grid side converter current reference	86
53	Fig. 5.27	Tracking of quadrature axis grid side converter current reference	86
54	Fig. 5.28	Graph of three-phase grid side converter currents	87
55	Fig. 5.29	Tracking of dc link voltage	88
56	Fig. 5.30	Graph of three-phase stator voltage/ grid voltage	88
57	Fig. 6.1	DC two-lead connection of DFIG	91
58	Fig. 6.2	DC three-lead connection of DFIG	91
59	Fig. 6.3	Block Diagram of an isolated DFIG system with rotor excited by boost converter	92
60	Fig. 6.4	Block Diagram of an isolated DFIG system with rotor excited by buck converter	93

61	Fig. 6.5	Block Diagram of isolated DFIG system for MPPT implementation	93
62	Fig. 6.6	Modified P & O algorithm control flowchart	95
63	Fig. 6.7	Parallel connection of DFIG-1 and DFIG-2 (a) Both DFIGs connected in three-lead (b) Both DFIGs connected in two-lead (c) DFIG-1 is three-lead while DFIG-2 is two-lead (d) DFIG-1 is two-lead while DFIG-2 is three-lead	97
64	Fig. 6.8	Starting transients of two-lead connection of DFIG-2	99
65	Fig. 6.9	Starting transients of three-lead connection of DFIG-2	99
66	Fig. 6.10	Steady state voltages of two-lead connection of DFIG-2	100
67	Fig. 6.11	Steady state voltages of three-lead connection of DFIG-2	100
68	Fig. 6.12	Transient state THD analysis of DFIG-2 two-lead configuration	101
69	Fig. 6.13	Transient state THD analysis of DFIG-2 three-lead configuration	101
70	Fig. 6.14	Steady state THD analysis of DFIG-2 two-lead configuration	102
71	Fig. 6.15	Steady state THD analysis of DFIG-2 three-lead configuration	102
72	Fig. 6.16	DFIG phase A stator voltage under loading conditions	104
73	Fig. 6.17	DFIG phase A load current	104
74	Fig. 6.18	DFIG-DC system output voltage with reference (a) 220 V (b) 110 V	106
75	Fig. 6.19	Output power of three-lead DFIG-DC system with MP&O and P&O MPPT	107
76	Fig. 6.20	Output power of two-lead DFIG-DC system with MP&O and P&O MPPT	108
77	Fig. 6.21	Comparison of two-lead and three-lead power outputs for MP&O Algorithm	108
78	Fig. 6.22	Comparison of two-lead and three-lead power outputs for P&O Algorithm	109
79	Fig. 6.23	Experimental setup	113

80	Fig. 6.24	Stator line voltage for two-lead connection without stator capacitor. $V_{ac}=0.2$ pu, $f=0.4$ pu	115
81	Fig. 6.25	Stator line voltage for two-lead connection with stator capacitor. $V_{ac}=0.38$ pu, $f=0.4$ pu	115
82	Fig. 6.26	Stator line voltage for three-lead connection without stator capacitor. $V_{ac}=0.24$ pu, $f=0.4$ pu	116
83	Fig. 6.27	Stator line voltage for three-lead connection with stator capacitor. $V_{ac}=0.43$ pu, $f=0.4$ pu	116
84	Fig. 6.28	Stator line voltage for two-lead connection without stator capacitor. $V_{ac}=0.22$ pu, $f=0.4$ pu	117
85	Fig. 6.29	Stator line voltage for two-lead connection with stator capacitor. $V_{ac}=0.43$ pu, $f=0.4$ pu	117
86	Fig. 6.30	Stator line voltage for three-lead connection without stator capacitor. $V_{ac}=0.26$ pu, $f=0.4$ pu	118
87	Fig. 6.31	Stator line voltage for three-lead connection with stator capacitor. $V_{ac}=0.46$ pu, $f=0.4$ pu	118
88	Fig. 6.32	Stator line voltage for two-lead connection without stator capacitor. $V_{ac}=0.28$ pu, $f=0.5$ pu	119
89	Fig. 6.33	Stator line voltage for two-lead connection with stator capacitor. $V_{ac}=0.83$ pu, $f=0.5$ pu	119
90	Fig. 6.34	Stator line voltage for three-lead connection without stator capacitor. $V_{ac}=0.32$ pu, $f=0.5$ pu	120
91	Fig. 6.35	Stator line voltage for three-lead connection with stator capacitor. $V_{ac}=0.86$ pu, $f=0.5$ pu	120
92	Fig. 6.36	Stator line voltage for two-lead connection without stator capacitor. $V_{ac}=0.31$ pu, $f=0.5$ pu	121
93	Fig. 6.37	Stator line voltage for two-lead connection with stator capacitor. $V_{ac}=0.86$ pu, $f=0.5$ pu	121
94	Fig. 6.38	Stator line voltage for three-lead connection without stator capacitor. $V_{ac}=0.36$ pu, $f=0.5$ pu	122
95	Fig. 6.39	Stator line voltage for three-lead connection with stator capacitor. $V_{ac}=0.88$ pu, $f=0.5$ pu	122

III. LIST OF TABLES

The list of tables used in the thesis have been mentioned in Table III.1.

Table III.1 List of tables

S. No.	Table. No.	Title	Pg. No.
1	Table I.1	List of symbols	viii
2	Table I.2	List of acronyms	xi
3	Table II.1	List of figures	xiii
4	Table III.1	List of tables	xviii
5	Table 1.1	Contribution of different modes of generation towards the total production in India	1
6	Table 1.2	Comparison of different machines employed in WECS	5
7	Table 1.3	Comparison of PECs employed in WECS	6
8	Table 1.4	Comparison of various wind turbine systems	7
9	Table 6.1	Input and output of two-lead topology and three-lead topology	98
10	Table 6.2	Comparison of the boost fed two-lead and three-lead DFIG-2 configurations	105
11	Table 6.3	Parallel combination of three-lead topologies of DFIG-1 and DFIG-2	110
12	Table 6.4	Parallel combination of two-lead topologies of DFIG-1 and DFIG-2	111
13	Table 6.5	Parallel combination of three-lead DFIG-1 and two-lead DFIG-2 topology	111
14	Table 6.6	Parallel combination of two-lead DFIG-1 and three-lead DFIG-2 topology	112
15	Table 6.7	Comparison of the DFIG parallel topologies under loading conditions	112
16	Table 6.8	Summary of the hardware results	114
17	Table A.1	Parameters of machines 1, 2, 3 and 4	151
18	Table B.1	Design parameters of buck converter	152

19	Table C.1	Electrical characteristics of IGBT switch FGA15N120AND	153
20	Table D.1	Electrical characteristics of IGBT driver IC TLP 250	154
21	Table E.1	Electrical characteristics of voltage regulator IC 7812	155
22	Table F.1	Electrical characteristics of voltage regulator IC 7912	156

CHAPTER 1

INTRODUCTION

1.1 INTRODUCTION

Wind is one of the most copious renewable sources of energy in nature. The economic and environmental benefits offered by wind energy are the reasons why electrical systems based on wind energy are receiving extensive global attention.

As on July, 2020, India has a total installed capacity of 371.054 GW. The renewable energy capacity, excluding generation through large hydropower plants, is 87.669 GW. The contribution of wind power in India is to the tune of 37.7 GW [1]. India is the fourth largest producer of electricity from wind energy after China, United States and Germany respectively [2]. Table 1.1 lists the contribution of different modes of electricity generation towards the total production in India [1].

Table 1.1 Contribution of different modes of generation towards the total production in India

Generation Type	Capacity (MW)	% of Total
Thermal	2,30,906	62.2%
Hydro	45,699	12.3%
Nuclear	6,780	1.8%
Renewable Energy Sources	87,669	23.6%

Figure 1.1 is a bar graph illustrating the electrical energy generation in India from 2009-10 to 2020-21 [1].

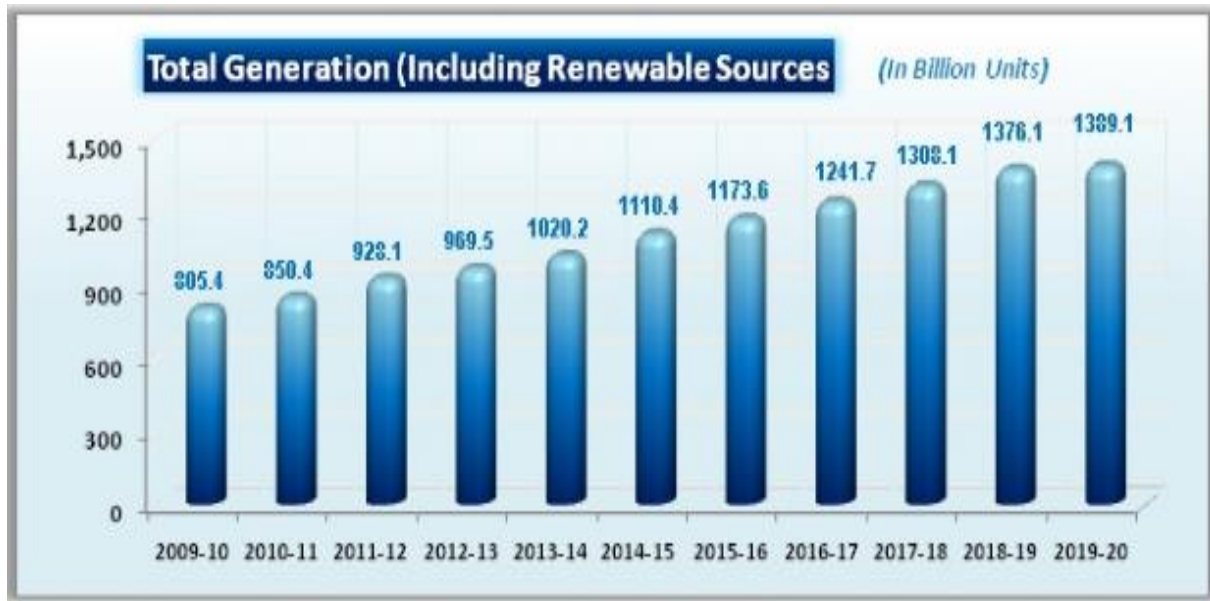


Fig. 1.1 Bar graph illustrating the electrical energy generation in India

Wind energy can be harnessed by a wind energy conversion system (WECS), composed of wind turbine blades, an electric generator, a power electronic converter (PEC) and the corresponding control system. Owing to overall increased flexibility, research on WECS has been steadily focussing on the variable speed approach.

Since the early nineties, many manufacturers have been replacing the traditional asynchronous generator in their wind turbine designs with doubly-fed induction machines. Specifically, using variable-speed approach increases the energy output up to 20% in a typical wind turbine system [3].

For operating the wind turbine in variable speed mode, a number of schemes have been proposed. Some of these schemes are based on estimating the wind speed in order to optimize wind turbine operation [4]. Figure 1.2 shows the block diagram of basic components of a WECS.

Since the last 25 years, several generations of wind turbine systems have been developing [5].

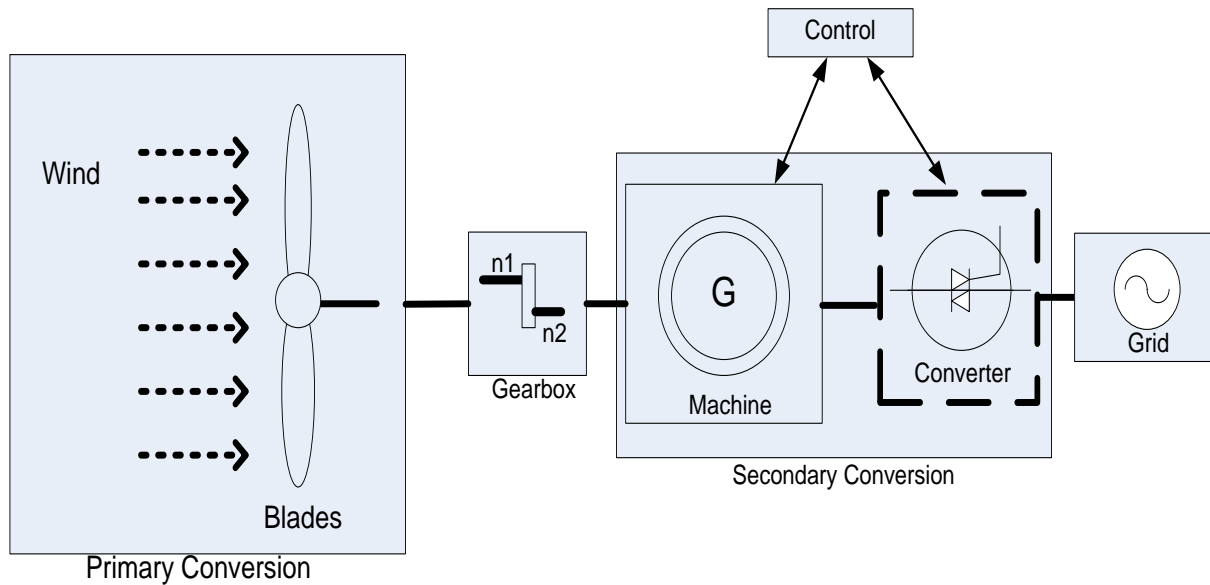


Fig. 1.2 Block diagram of a WECS

1.2 RESEARCH MOTIVATION

The ever growing demand of electrical energy and the inadequate stocks of conventional assets have resulted in improved attention towards the use of renewable resources. Hence, intense research is being undertaken in the domains of solar energy and wind energy. Electricity production using wind energy is eco-friendly, socially beneficial and economically competitive. Wind has become one of the most attractive energy resources as it is nearly pollution-free when used for production of electricity (except for the noise from the rotating turbine). So, in this thesis, research has been focussed on the production of electrical energy using wind energy.

1.3 DFIG BASED ENERGY CONVERSION SYSTEMS

A review of wind generator systems, their control strategies and the power electronic converters used in WECS is contained in this section.

1.3.1 Wind Generator Systems

Wind turbine generator systems have to fulfill certain requirements, some of which are as follows:-

- **Grid Connection:** To allow large-scale application of wind energy without compromising the stability of the power system, operators have to stick to certain grid

codes. These codes define the requirements for the power quality to be delivered to the system [6].

- **Reliability:** Cost of operating a plant forms a substantial part (in the order of 30%) of the generated energy cost. Therefore, requirements related to reliability have been getting increased attention [7]–[13].
- **Variable Speed:** Variable speed of the generator system ensures an optimal match with the aerodynamic of the rotor. Equation (1.1) describes the power that can be captured by a wind turbine [14]:-

$$P=0.5 \rho_{\text{air}} C_p \pi r_b^2 v_w^3 \quad (1.1)$$

where ρ_{air} is the density of air, v_w is the speed of the wind, r_b is the radius of the rotor and C_p is the coefficient of power. C_p depends on the blade design, the pitch angle θ , and the tip speed ratio λ .

The generator systems mostly used in wind turbines have been discussed in [15]–[20]. They are as follows:-

- Squirrel-Cage Induction Generator (SCIG)
- Permanent Magnet Synchronous Generator (PMSG)
- Synchronous Generator (SG)
- Doubly-Fed Induction Generator (DFIG)

1.3.2 Power Electronic Converters used in WECS

The power electronic converters (PECs) are an integral part of control for WECS with variable-speed systems. Constant-speed WECS include PECs mostly for reactive power compensation.

The role of PECs in a variable speed WECS are as follows [21]:-

- Facilitating the attainment of maximum power transfer from the wind by controlling the turbine rotor speed as the wind speed varies with time.
- Conditioning the variable-frequency and variable-magnitude output of the generator into a supply of constant-frequency and constant-magnitude which is suitable for feeding an electrical grid.

Table 1.2 gives a comparison of different generators which are used in WECS while table 1.3 gives the comparison of PECs used in WECS.

Table 1.2 Comparison of different generators employed in WECS

S.No.	Type of the generator	Benefits	Drawbacks
1	Squirrel-Cage Induction Machine	<ul style="list-style-type: none"> • Low cost machine. • Rugged. • Excellent damping of torque pulsation. 	<ul style="list-style-type: none"> • Large inrush current while starting. • Fulfills reactive power requirement from the grid. • High cost of fully rated PEC.
2	Permanent Magnet Synchronous Machine	<ul style="list-style-type: none"> • It is usually gearless. • Good efficiency. • High torque even at low speeds. 	<ul style="list-style-type: none"> • Costly material. • Used in small scale applications. • Expensive converter.
3	Synchronous Machine	<ul style="list-style-type: none"> • Direct drive system. • Reactive power injection is not required. 	<ul style="list-style-type: none"> • Very expensive. • Needs to be excited externally.
4	Doubly-Fed Induction Machine	<ul style="list-style-type: none"> • Flexible speed control owing to variable speed operation. • Four quadrant active and reactive power capabilities. • Partially rated converter usage. • Better execution of power factor correction. • Can operate at high power. 	<ul style="list-style-type: none"> • Control schemes are complex. • Need regular maintenance.

Table 1.3 Comparison of PECs employed in WECS

S. No.	PEC	Benefits	Drawbacks
1	Thyristor grid side converter	<ul style="list-style-type: none"> • Low cost. • High power rating. 	<ul style="list-style-type: none"> • Active compensator is needed.
2	Back-to-back Converters	<ul style="list-style-type: none"> • Low cost. 	<ul style="list-style-type: none"> • Enhanced switching losses. • High frequency harmonics.
3	Matrix converter	<ul style="list-style-type: none"> • Elimination of DC link. • High efficiency. 	<ul style="list-style-type: none"> • No provision of decoupling. • Higher losses during conduction.
4	Multi-level converter	<ul style="list-style-type: none"> • Reduced dv/dt. • Low distortion in input current drawn. • Reduced losses during switching 	<ul style="list-style-type: none"> • Voltage imbalance due to multiple capacitors. • High cost due to large number of switches. • Complex control.
5	Z-source converter	<ul style="list-style-type: none"> • The output voltage can be varied over a large range. • Fewer components are needed. • Good reliability. • Low cost and reduced size. • Very efficient. 	<ul style="list-style-type: none"> • Both voltage surges and current surges occur. • The converter is inherently unidirectional.

1.4 CONTROL STRATEGIES IN WECS

In general, the control schemes for WECS are usually segregated into the following categories:-

- Constant speed techniques
- Variable speed techniques

Table 1.4 is a comparison of various wind turbine systems.

Table 1.4 Comparison of various wind turbine systems

S. No.	Wind Turbine System	Benefits	Drawbacks
1	Fixed Speed System	<ul style="list-style-type: none"> • Simple construct and control. • Robust operation. • Cost effective. 	<ul style="list-style-type: none"> • Low yield of energy. • Active/ reactive power controllability is absent. • High mechanical stress. • High losses on gear.
2	Variable Speed System with partially rated Power Electronics.	<ul style="list-style-type: none"> • High yield of energy. • High active/ reactive power controllability. • Reduced cost, losses and mechanical stress. 	<ul style="list-style-type: none"> • Maintenance requirements. • High losses on gear.
3	Variable Speed System with fully rated Power Electronics.	<ul style="list-style-type: none"> • Enhanced technical performance. • Rapid control of active power and reactive power. 	<ul style="list-style-type: none"> • Additional losses in power conversion. • Increased system complexity.

1.5 ORGANIZATION OF THESIS

The present Ph.D. thesis is organized into seven chapters and the work done is briefly explained below;

Chapter 1 introduces the area of interest mentioned in the thesis. It projects the utility of DFIG based WECS in the present energy scenario. It includes the overview to wind energy systems with brief introduction of the turbines, generators and the power electronic converters used in it.

Chapter 2 comprises the state of the art literature review relevant to research area of PhD work. It offers a methodical scrutiny of latest research publications for the purpose of defining the research objectives.

Chapter 3 contains the mathematical modelling of grid connected DFIG, DC-DC step down converter and DC-DC step-up converter. The DFIG model has been developed in the stator co-ordinates. Modelling of the DC-DC converters has been done by considering a practical inductor with parasitic resistance.

Chapter 4 focuses on the power electronic converters (PECs) used in DFIG based WECS. It contains the simulation results and hardware implementation of the PECs.

Chapter 5 details out the computation methods of DFIG direct axis and quadrature axis rotor current commands I_{rq} and I_{rd} corresponding to three distinct cases which are as follows:

- a) Maximum active power and minimum losses
- b) Minimum reactive power and minimum losses
- c) Maximum active power and minimum reactive power.

The original work carried out in this chapter relates to the computation of rotor currents corresponding to cases (b) and (c). The other novelty of this work is the application of GA for determining the optimal rotor current values corresponding to all the aforementioned three cases. The efficiency and power factor of the system owing to all the three cases using rational methods as well as GA have been compared and analyzed.

Chapter 6 proposes two novel topologies of DFIG for feeding DC grid/ load. These configurations are called two-lead and three-lead connections. A modified Perturb and Observe (MP&O) Algorithm, has been applied to the two configurations for maximum power point tracking. The benefits of the proposed DFIG topology and the benefits of MP&O over the traditional P&O algorithm have been validated. Chapter 6 also contains the analysis of a three-lead based autonomous DFIG DC system whose output voltage is held constant under varying

wind speeds. Hardware results of two-lead and three-lead DFIG system with rotor excited via DC-DC Converter have also been included. The DC-DC converter input is variable but its output is held constant by applying proper control. The parallel operation of two DFIGs of different ratings connected in combination of two-lead and three-lead topology has also been presented.

Chapter 7 gives the major conclusions based upon the research work presented in this thesis. It gives a detailed account of the problems mitigated during the course of the research. The scope of building upon the current work has been presented in a brief manner.

1.6 CONCLUSION

In this chapter, the structure of the thesis has been outlined in detail. The motivation for undertaking the research has been briefly touched upon. A general overview of DFIG based WECS has been discussed with a focus on the wind generator systems, power electronic converters and the associated control strategies used in WECS.

CHAPTER 2

LITERATURE SURVEY OF DFIG BASED ENERGY CONVERSION SYSTEM

2.1 INTRODUCTION

Literature survey is an essential activity for research. It needs to be carried out comprehensively. This chapter comprises the state of the art study of literature relevant to the DFIG based WECS. It offers a systematic exploration of research publications for the purpose of outlining the research objectives.

2.2 LITERATURE SURVEY

The large range of operation of doubly fed induction generators (DFIGs) has made them very popular in the field of renewables related to wind energy. With DFIGs, there is the facility of employing partially rated power electronic converters (PECs). Hence, the overall system budget is effectively reduced. The control of a doubly-fed induction machine using back-to-back PECs was proposed in [22]. Vector-control scheme for the grid-side converter results in decoupled control of active power and reactive power. It also ensures sinusoidal supply currents.

The authors of [23] describe a topology using a thyristor based grid side converter that allows continuous control over the inverter firing angle. The turbine speed is regulated through the DC-link voltage for ensuring optimum energy capture. The benefits of this topology include reduced cost of device and increase in available power rating. The main drawback of this converter is the requirement of a compensator for the reactive power and the harmonic distortion.

The usage of a voltage source converter (VSC) accompanied by a DC-DC converter is investigated in [24]. Incorporating an additional DC- DC converter results in the following advantages:

- Variation of the switching ratio can be used to control the generator side DC voltage.
- Appropriate inverter side DC voltage can be maintained.
- Selective harmonic elimination (SHE) is possible.
- The control is flexible.

A topology proposed in [25] has two DC link capacitors and two B-4 converters. Maximum power point tracking (MPPT) has been employed to yield the generator output power. MPPT is applied by measuring the DC link current and voltage. The operating point is accordingly altered by changing the magnitude of the reference current.

The matrix converter (MC) has the capability to alter in one stage the variable generator output into a constant AC as required by the grid [26]–[32]. Hence the matrix converter does not require any bulky energy storage like DC-link. The application of a matrix converter in a DFIG based WECS has also been widely explored [33]–[40]. In a DFIG system employing matrix converter, the control of the direct axis current allows for the regulation of the stator side reactive power. The quadrature axis current command regulation results in control of the stator side active power [33]. Interaction of matrix converter and power filter usually leads to instability [34]–[39].

The commutation problems in the conventional MC topology ruins its performance in industrial applications. Hence, an improved topology free of commutation problems had been proposed and validated for the system presented in [40].

A multi-level converter is an AC-DC-AC converter which consists of 12 insulated gate bipolar transistors (IGBT's) used as a rectifier and as an inverter [41]. The rectifier is connected between a capacitor bank and the machine. The inverter is connected between a filter and the capacitor bank. The filter is connected to an electric network.

The authors of [42] proposed the usage of a three-phase semi-controlled rectifier for WECS based on generators employing permanent magnets. The proposed topology is simple, robust and efficient. However, the harmonic distortion in generator current is high.

A novel converter with boost capability is proposed for WECS in [43].

The researchers of [44]–[53] deal with the effect of the WECS technologies on the power system stability.

The authors of [54] discuss the stator flux oriented vector control strategy for decoupled control of DFIG active power and reactive power. In [55], authors presents a complete comparative analysis of proportional-integral (PI) controller, sliding mode controller (SMC) and Fuzzy-PI controllers for DFIG based WECS. It concludes that the transient response provided by the Fuzzy-PI is best.

In [56], power factor improvement using vector control has been implemented on a DFIG based WECS. The authors of [57] have investigated the role played by MPPT controller in the power conversion of a DFIG based variable speed WECS. Control laws have been analyzed for optimal power production.

The authors of [58] deal with the operation of a DFIG combined with active filter capability. A Grid Side Converter (GSC) is also integrated into the system. The authors have proposed a novel indirect current control algorithm for the compensation of the harmonics created by non-linear loads. In [59], a micro grid system has modeled and analyzed. It consists of a DFIG based WECS and two diesel generators. To improve the voltage profile, GSC in reactive power compensation mode has been used.

In [60], the authors propose a low cost and efficient integration of the solar photo voltaic (PV) and DFIG based hybrid system. The authors of [61] have proposed Voltage and Frequency Controllers (VFC) for feeding unbalanced loads and dynamic loads in a DFIG based system. In [62], the authors employ active disturbance rejection control based on the extended state observer. It is used to achieve the control of both rotor side converter and grid side converters. In [63]–[68], the use of brushless doubly fed induction generator based WECS has been proposed. The brushless DFIG has two stator windings. One winding is connected to the grid. It is called the “power winding.” The other winding has been termed as the “control winding.” The control winding is supplied by a converter in the same way as a DFIG.

The authors of [69] have provided a novel solution for the “tracking speed versus control efficiency” trade-off problem of hill climb searching. Its strategy ensures that the changing wind conditions do not lead HCS in the incorrect path. The authors of [70] have discussed the effectiveness of various intelligent design approaches like mean-variance optimization algorithms and particle swarm optimization (PSO) algorithms for the control of generators.

In [71], authors present the principles of mechanical sensorless MPPT control for WECS. It compares the artificial neural network (ANN) and hill climb search based MPPT algorithms. The authors of [72] propose an intelligent MPPT algorithm for variable-speed WECS. The proposed algorithm is based on an online Q-learning algorithm. ANNs are used as function

approximators to output the action values. The output is computed by using the rotor speed of the generator and the electrical power as inputs.

The authors of [73] propose a coordinated derived current control strategy of the DFIG system under unbalanced grid voltage conditions. The GSC and the RSC have been synchronized to the grid with a virtual phase angle of nominal frequency. Thus, the proposed control strategy can be implemented in an arbitrary reference frame without phase-locked loop (PLL).

Control on DFIG speed can be easily exercised from the sub-synchronous to the super-synchronous region [74]-[87]. Maximum possible energy from the wind can be captured by exercising control over the generator speed [88]. Simultaneously, provision must be made for ensuring minimum losses and reduced reactive power. As a consequence, output active power would get increased. Operating an induction machine with least copper losses necessitates the presence of a varying rotor flux. For fulfilling the requirement of a varying rotor flux, Hamiltonian structure of a motor/ converter model is used and a novel non-linear controller is proposed in [89]. This safeguards the technical boundaries of the converter while functioning under field oriented control (FOC) to achieve precise speed regulation with changeable rotor flux as per the minimal loss requirements. A method for global loss modelling of an induction machine with the aid of the Design of Experiments is presented in [90]. The applied technique is simple as it requires a limited number of experiments. Using the suggested method it is possible to take into account different factors and their interactions. A vector control (direct Adaptive Neuro-Fuzzy Inference System) of the rotor and grid side converters of DFIG for controlling the generated stator powers, has been discussed in [91]. A neuro-fuzzy algorithm based controller design was introduced and validated using MATLAB/ SIMULINK.

In [92], an improved efficiency control strategy for a DFIG based WECS has been presented. The proposed method minimizes the loss in the DFIG thereby yielding maximum power. The power loss is decreased by applying flux weakening control at the reduced wind speeds. The magnetic flux is regulated through control conditions that also govern the flux reduction to normal flux operation.

The effect of rotor excitation voltage on steady-state stability and output power of a DFIG has been investigated in [93]. Detailed formulae for stator power, rotor power, stator loss, rotor loss, and electrical power have been framed as functions of the generator speed and rotor voltage.

The active-reactive power diagrams for a variable speed DFIG fed by matrix converter (MC) has been presented in [94]. The diagrams are akin to the operational chart of a synchronous generator. The power diagrams are put to use for estimating the available reactive power support to the grid. The authors have developed an algorithm for computing the optimal reactive power share of the DFIG stator as well as the MC for maximization of the grid injected active power. In [95], a sliding mode regulator is discussed. It is put to use for regulating the rotor current of a DFIG. The rotor currents yielded, correspond to the target commands for maximum power and minimum copper loss.

For exercising control over efficiency, the field-weakening operation of a DFIG connected to a dc-link is analyzed in [96]. The authors have presented simplified formulae for influencing the optimal reference magnetization current. In [97], a control method for isolated DFIG-DC is discussed. The suggested method does not require sensing of stator quantities. Instead, the control variables, i.e. rotor circuit currents, and the controlled variable, i.e. output DC link voltage have been sensed. A detailed mathematical analysis of the system has also been done.

In [98], a logical approach to compute rotor reference currents for maximum power tracking and loss minimization has been proposed. The optimal value of d - axis component of rotor current (I_{rd}) and its q - axis component (I_{rq}), was determined as a formula. The detailed model of DFIG was used for the analysis. This resulted in a less time consuming approach as compared to exhaustive search methods [93].

That the extraction of mechanical power from a turbine is significantly determined by I_{rq} while I_{rd} affects the copper losses has been proved in [99]. Corresponding to maximum output power and minimum losses, the optimal values of I_{rq} and I_{rd} can be calculated using the method mentioned in [98]. For analyzing the transient response under various grid conditions, [100] and [101] can be perused. For a comprehensive investigation of some state of the art DFIG control strategies, [102] to [105] may be referred.

Inverters are used widely in applications varying from renewable energy systems to household electronics products [106-108]. The control signal generation for PECs can be implemented by analog methods as well as digital methods. Owing to their increased accuracy and lower complexity, digital controllers are preferred over analog controllers. Typically, microcontrollers and digital signal processors (DSPs) were employed to execute the pulse width modulation (PWM) schemes for converters. But this family of digital controllers are characterized by inadequate throughput as well as reduced speed corresponding to complex

codes. Digital control signal generation using DSP makes flexible alteration possible with ease. But for intricate operations, the processing-power requirement of DSPs is high. This leads to an increase in cost [109, 110]. Field Programmable Gate Arrays (FPGAs) are a better substitute as compared to DSPs, microcontrollers and analog solutions owing to their re-configurability, reliability and versatility [111-116].

FPGAs were developed by the Xilinx Inc. and are basically integrated circuits which are reconfigurable by the end user [117, 118]. They contain programmable logic blocks and interconnects. Some of these blocks are grouped together to enhance the functionality for higher level design issues. Owing to its programmability and re-configurability, an FPGA is deemed as an excellent prototyping option. However, the traditional method of coding the control signals using hardware definition language (HDL) is tedious and necessitates a high degree of specialized training. This is a disadvantage for researchers not adept in programming. As the controller complexity increases, control signal development by HDL becomes exasperating even for the experts [119-122].

Various platforms like Opal-RT, digital signal processing and control engineering etc. can be employed for simulating and fabricating PECs [123, 124]. However, their cost consideration is greater. Moreover, the lower versions of these packages suffer from an inadequate functionality. The increased usage of FPGAs in converter control applications has necessitated the need for a low-cost, easy-to-use digital platform.

The Xilinx System Generator (XSG) method of control signal generation using FPGAs is a flexible and low-cost method for rapidly designing novel hardware prototypes. The biggest advantage of this method is that the designer need not be acquainted with HDL [125, 126]; the control code is automatically generated by XSG. This leads to ease in generation of control signals. As a consequence, the end user can quickly construct various power electronic devices [127–130]. Even though DSP-based rapid prototyping controllers are available, they are unsuitable for high-end applications [131–133]. The XSG-based control signal generation is briskly gaining popularity in the research field. The realization of a high-resolution unipolar pulse width modulator for converters, using XSG, has been discussed in [134]. A hardware-in-loop design of a grid-connected inverter has been discussed in [135].

Artificial intelligence (AI) has developed into a key tool to sort out engineering problems. The number of researchers in AI is briskly increasing with the growing number of its prospective uses in the current technology. This has enthused the researchers for developing many

algorithms based upon AI. In this part of the chapter, the utility of AI in wind energy conversion system (WECS) has been elucidated with a focus on Doubly Fed Induction Generator (DFIG).

From critical literature survey it can be concluded that AI may be put to use for solving numerous complications related to WECS. A DFIG is one of the key components of WECS and consequently needs proper attention. There are several operational uncertainties in DFIG due to its nonlinear magnetization characteristics. For analysing DFIG operation, there is a necessity to map the nonlinearity of its magnetic circuit. AI can also be put to use for determining rotor current control commands corresponding to maximum efficiency or minimum losses or minimum reactive power or a combination of such factors. In this chapter an attempt has been made to explain the possibilities of AI for the analysis and control of DFIG. Artificial Neural Network (ANN), Fuzzy Logic (FL) and Genetic Algorithm (GA) are found to be very effective for solving many problems related to DFIG.

ANN is mainly categorized by its architecture, topology and learning regime. The main benefits of ANN are as follows:

- It is fast.
- It has learning capability.
- It can adapt to the target data.
- It is robust.
- It is suitable for non-linear modelling.

The aforementioned advantages suggest the usage of ANN for developing control models where the output and input of variables is unrelated by an exact mathematical function. ANN training is computationally costly. But it takes negligible time to deliver accurate output once the network has been trained. The major shortcomings of ANN are as follows:

- It has a large dimensionality.
- Issues related to the choice of the optimal configuration.
- The selection of training methodology.
- Lack of explanation capability.
- Generation of results even when the input data are unreasonable.

In spite of these shortcomings, various researchers [136-138] have employed ANN for WECS. For WECS, [136] proposed an adaptive self-tuning control strategy with neural network Morlet wavelet. The proposed approach is built on single-layer feed-forward neural networks. It has

hidden nodes of adaptive Morlet wavelet functions controller as well as an infinite impulse response recurrent structure. The controller is based on a model structure which can approximately detect the system dynamics. The proposed ANN controller has been applied in three distinct situations as follows:

- without noise
- with measurement input noise
- with disturbance output noise

In [137], authors have presented short term forecasting of wind speed using ANN. Seven years' data was compiled using a network of measurement stations situated at the place of interest. Diverse ANN configurations have been generated. These configurations have been compared through error measures, thereby guaranteeing the model accuracy and performance.

The authors of [138] deal with a data-driven approach for the spatial estimation of the wind fields. Commencing with the outcomes of an introductory study, development of a novel technique by integrating neural and geo-statistical methods has been done. The novel technique is capable of obtaining the wind speed maps for the region at particular heights. Weibull distribution function defining the wind profile, has been applied for training a multi-layer perceptron. The aim of the multi-layer perceptron is to compute most of the wind spatial trends. The authors of [139] presented use of ANN based pitch controller for a grid-connected WECS. The turbine blades' pitch angle is controlled by the pitch controller so as to extract maximum power from the wind. This approach demonstrates an overwhelming dominance over the PI controller approach. Cascaded ANN has been put to use by Khela et al [140, 141] for the steady state analysis of separately excited induction generator operating under varying speed with load. ANN has also been put to use by Giraud et al [142] to capture the unknown WECS dynamics. This method is very convenient for accurately envisaging the WECS dynamic performance. It finds especial use in challenging dynamic environments such as high winds. In [143], authors proposed a novel scheme for WECS integration into an electrical network. ANN has been used to model the security and the economy of the dispatching task. This has been done for properly integrating the wind farm. In [144], a neuro-fuzzy gain tuner has been proposed for the vector control of a DFIG. The input for each neuro-fuzzy system is either the error value of generator speed or the active power or the reactive power. The choice of a single input to the system makes the design simple. In [145], authors proposed an ANN model to represent type-3 DFIG. The chief benefits of these models are their simplicity, accuracy and

computational speed. The authors of [146] present a DFIG direct power control strategy. An ANN controller with multilayer perceptron structure has been used for the purpose. The proposed strategy permits the rotor side converter (RSC) to operate with constant switching frequency. In [147], authors deal with an ANN based sensor less wind speed MPPT algorithm for DFIG based turbines. The ANN has been designed to produce the optimum control signal for the DFIG controller. These optimal parameters have been determined by using PSO algorithm. The authors of [148] present an ANN based power controller for improving the efficiency level of DFIG based turbines during shifting wind operating situations. It exploits the ANN's generalization and approximation abilities to design a robust control during wind variation uncertainties. Thereafter, to accelerate the convergence, a time varying learning rate has been proposed. In [149], authors have discussed a real time sliding mode field oriented control (FOC) for a grid connected DFIG. The proposed controller has been used to track the desired DC voltage reference at the output of the DC link capacitor. This has been done to retain a constant grid power factor at the step-up transformer which is controlled by the GSC. The controller is also capable of independently forcing the stator active power and the stator reactive power to track the reference commands via the rotor currents controlled by the RSC. Fuzzy logic (FL) is a category of programming and mathematics that accurately characterizes how the human mind classifies objects, assesses conditions and processes choices. It was developed by Zadeh in 1964. Zadeh intended to address ambiguity and inaccuracy which commonly occur in the engineering problems. FL was first put to use in 1979 for resolving power system problems. Fuzzy set theory can be thought of as a generalization of the conventional set theory. In traditional set theory, any universal element either belongs to or does not belong to a particular set. Hence, for any element, the degree of association is crisp. In fuzzy set theory, any element can have a continuously varying association. Mathematically, a "fuzzy set" is a mapping (called "membership function") from the "universe of discourse" to the closed interval $[0,1]$. The membership function (MF) is generally designed by considering the prerequisites and restrictions on the problem. FL implements human experiences and human preferences via MFs and fuzzy rules. By using fuzzy variables a system can be made comprehensible to any non-expert operator. Hence, FL can be put to use as a mechanism for incorporating heuristics or knowledge or theory into controllers. The benefits of fuzzy theory are as follows:

- Accurate representation of operational constraints
- Fuzzified constraints are less rigid as compared to the traditional constraints

Many researchers have used FL in WECS. The design of an FL supervisor has been proposed in [150] for minimizing active power variation and reactive power variation generated by fixed-speed WECS. Stator voltage regulation has been performed while imposing a reference for reactive power. The turbine blades' pitch angle is set so as to capture maximum power.

Long term performance of isolated electrical generation systems reinforced with hybrid renewable energy systems with a smart control strategy has been presented in [151]. It has been proven that fuzzy based control promises improved performance on long term operations vis-à-vis the conventional approaches. This is because the fuzzy approach takes into account the fuzziness of the intermittent resources and the user load demand.

In [152], authors present the implementation and laboratory testing of a novel FLC for an induction generator-electric utility DC link interface scheme. The purpose of the FLC in the proposed scheme is to maximize the wind power utilization to the electric utility grid. The authors of [153] describe an FL based steady-state analysis of an induction generator. The nodal admittance method has been used to develop matrix equations. FL has been applied to solve the obtained equations. Consequently, the steady-state performance of the machine can be pre-determined.

FL has been applied by Simos et al [154] for a variable wind generation system consisting of a self-excited induction generator. FLC has been put to use for extracting the maximum power while ensuring robust speed control and light load efficiency improvement, under all conditions. In [155], authors offer an enhanced tip speed ratio procedure for grid tied DFIG. A model reference adaptive system based on FLC has been put to use for estimating the rotational mechanical speed of the generator. The authors of [156] have proposed the design and application of a control scheme that uses interval type-2 fuzzy sets for grid tied DFIG based turbines. The existence of a third dimension in the type-2 MF leads to additional flexibility in the controller design. Hence, the controller can contribute in damping the power oscillations and aid in voltage recovery during network parameter uncertainties. Vector control with the proposed control strategy is capable of handling uncertainties like faults and load changes in the operating conditions of the network. The authors of [157] have discussed the design of an FL based intelligent controller for improving the robustness and reference tracking of DFIG based WECS. Fuzzy logic controller has been made to operate as a supervisory controller for tuning the PI controller gains. The method of gain scheduling has been used to track the stator active power reference and stator reactive power reference. In [158], a developed integrated intelligent automatic control system has been proposed. The controller action leads to an

increase in energy extraction and improvement in the power system performance. ANN, FLC and support vector machines (SVM) models have been used for comparison and validation. In [159], authors proposed an FLC based speed controller for DFIG based WECS. The wind speed and the DFIG rotor speed serve as the inputs. The controller parameters have been optimized using PSO algorithm. To accelerate the MPPT, the conventional controller has been augmented with a compensator. The compensator contains a high-pass filter and uses the wind speed as input. In [160], the inertia of a DFIG with a super capacitor based energy storage system has been described. Based on FLC, an inertia response control strategy has been proposed and validated. In [161], authors proposed a variable FLC strategy for a DFIG with battery energy storage operating in islanded mode. The proposed scheme has a range of functionalities such as elimination of harmonics, compensation of asymmetries and maximum power extraction from the wind. Field-oriented approach has been used for the control of the RSC as well as the load side converter. The proposed control exhibits good dynamic response when compared with conventional methods.

The purpose of optimization techniques is to discover a result which will either efficiently minimize the goal or maximize it, as fast as possible. The job of an effective optimization algorithm is to find the correct optimum solution by assessing feasible points. Genetic algorithm (GA) based optimization algorithms involve relatively fewer evaluations as compared with conventional optimization algorithms. This leads to a reduction in the computational complexity.

The advantages of GA based optimization are as follows:

- GAs manipulate control variable representations at the basic string level to utilize likenesses amongst high performance strings. Usually, other approaches directly deal with functions and their control variables. Since GA operates at the basic coding level, they are hard to dupe even for functions that are deemed to be challenging for the traditional schemes.
- GAs operate from a population. Several other methods operate from a single point. Hence, GA finds security in numbers. By retaining a populace of well adapted sample points, the possibility of searching a wrong peak is diminished.
- GAs accomplish much of their breadth by disregarding information, excluding that concerning the objective function (OF). Several other methods comprehensively rely on such extraneous information. In problems where the obligatory information is unobtainable, the other methods fail in totality. GAs remain general by manipulating

information accessible in any search problem. GAs process similarities in the fundamental coding along with information ranking the structures. The ranking is done according to the survival ability in the present environment. By manipulating such broadly accessible information, GAs may be put to use on a wide variety of applications.

- The evolution rubrics of GAs are stochastic. Most other AI methods have deterministic evolution rules. A dissimilarity exists between the randomized operators of GAs as compared to other methods. GAs use arbitrary selection to guide an extremely exploitative search. The procedure of using chance to arrive at the best results seems unusual; yet such precedents are abundantly present in nature.

The major disadvantage of GA is the large amount of computational time needed. However, as compared to ANN and FL, GA has the competence to deliver more exact solutions. Further, no stringent learning algorithm is enforced on GA as in ANN. Further GA operators involve no mathematics as is needed in FL.

During the previous years, numerous researchers have focussed attention on evolutionary algorithms for solving real world problems related to optimization. In [162], GA has been put to use for the generating control command signals of a grid connected DFIG. Three distinct methods have been formulated and described for determining the value of direct axis rotor current and quadrature axis rotor current for maximizing active power while minimizing losses and reactive power of a grid connected DFIG. The optimal values of DFIG rotor current have been obtained using three different rational techniques and corresponding three cases of GA. In a real coded GA, variables are coded using real numbers [163]. After proper coding, GA operators have been directly applied on the numbers. Three key operators responsible for the functioning of the GAs are mutation, reproduction and crossover.

Dynamic performance of grid based WECS has been analysed in [164]. Analysis has been done using the rotor speed stability. For improving the WECS low voltage ride-through during faults and for damping the machine's rotor speed oscillations, unified power flow controller (UPFC) has been employed. The gains of the UPFC controller have been tuned with a simple GA. It has been witnessed that the UPFC regulates the voltage and mitigates the instability of the rotor speed. In [165], authors have presented multiple capacitor connection for a variable speed arrangement of induction generator using GA. Pole changing windings have been substituted by a switching scheme. Performance constraint on flux densities, terminal voltage and current have been accounted. The authors of [166] have proposed GA to minimize the net impedance

of induction generator. In [167], the authors have presented a design procedure based GA combined with the formal pole placement project. The control scheme has been used for obtaining optimal controllers of the DFIG RSC. The procedure improves the dynamic behaviour of the system during faults. It also augments the fault ride through capability. The authors of [168] have proposed a coordinated control strategy of the DFIG converters during a fault of the grid. The co-ordinated control is capable of riding through the fault minus the usage of supplementary hardware. The coordination has been attained via an FLC tuned using GA. In [169], the authors have proposed controllers for DFIG based WECS. The proposed controllers include a main speed controller and two secondary speed controllers. The main speed controller is an FLC. The FLC parameters have been optimized using GA for achieving optimal response. Frequency deviation controller as well as wind speed oscillations controller have also been put forward. In [170], the authors have proposed a technique for mitigating the sub-synchronous oscillations in a wind farm by adding a “virtual impedance controller” to a DFIG RSC. GA has been used to achieve the controller optimal parameters. The authors of [171] have presented a scheme to optimise the network loss and system voltage. The DFIG terminal voltage is the target for control. The immune GA has been used to overcome the reactive power optimisation problem related to offshore wind farms. The authors of [172] have detected the sub-synchronous interactions primarily determined by the DFIG converters’ PI parameters. With the goal of restraining the oscillations, an optimization model has been developed to envision optimal ranges of PI parameters. Such models facilitate the choice of the suitable PI parameters for augmenting the damping.

Ongoing research on DFIG systems is focussed on unconventional applications. These include the following systems:

- Variable frequency adjustable speed generation [173].
- Dual converter topologies used in reversible speed drives [174].
- DC power generation.

They aforementioned systems utilize the advantages of intrinsic DFIG flexibility and controllability. The flexibility and controllability are used for minimizing the sizing, ratings as well as the amount of controlled PECs. The most prominent use deals with the incorporation of a DFIG into a dc power system. Such applications are relevant to usual grid based WECS [175], dc micro-grids [176]-[177], distributed generation as well as standalone power systems for mines [178] and on-board power generation [179]. The natural DFIG ability of functioning

with variable speed and fixed frequency with partially rated PECs has been reclaimed for DC generation. The proposed topologies include single voltage source converter (VSC) with uncontrolled rectifier [180], [181], [182]-[187], [188]-[201], [202]-[203], [204]-[205] and double VSC [206], [207], [208]-[214] layouts. These topologies can provide an inexpensive solution in the domain of dc power generation.

2.3 RESEARCH GAPS IDENTIFIED

Based on the literature review of wind energy conversion systems, following gaps were identified:-

- Complexity in the various control methodologies is high [23]-[25], [40], [41], [55], [104], [159].
- Harmonic distortion which occurs in output voltage and currents is a persisting problem [23], [34]-[39], [44]-[53], [105], [161].
- Power quality issues due to wind speed variations [7]-[13], [21], [59], [103].
- Intermittent nature of wind causes difficulties in the islanding mode of operation [5], [171], [173], [175].
- Sensitivity of DFIG to unbalanced grid voltage [13], [22], [44], [101], [149], [168].
- In a weak network, a change in either active or reactive power can cause a considerable change in the voltage [44], [45], [47], [53], [102].
- Solutions to protect the rotor side converter during abrupt voltage drops, results in adverse impact on the stability of the power networks when penetration of wind power becomes high [18], [47].
- Non linear controllers are harder to implement in practice whereas linear controllers have a limited range of operation [20], [155].
- Absence of a good control methodology for smoothing the grid frequency fluctuation without excessive spillage [55], [57].
- In WECS, where artificial intelligence has been applied, rapidly changing wind conditions may lead to wrong implementation of control strategy [69], [70], [156], [157].

2.4 RESEARCH OBJECTIVES

Based on the research gaps identified, the research objectives were as follows:-

- To analyze a model of a DFIG and investigate the control strategies associated with it.
- To investigate the performance of solid state converters used in DFIG.
- To investigate the power quality issues related to DFIG.
- To investigate the methods of controlling the active power and the reactive power of DFIG.
- To apply genetic algorithm (GA) for designing controller parameters.

2.5 RESEARCH METHODOLOGY

The research methodology followed in this work focused on the simulation of the stated objectives using matrix laboratory (MATLAB 2016a). Controller parameter design has been implemented using analytical methods as well as genetic algorithm. The control signals for the power electronic converters have been generated using Xilinx System Generator (XSG) and Spartan 3e Field Programmable Gate Array (FPGA). The switching signals of the DC-DC converters have been developed using the Arduino integrated development environment and Arduino Mega microcontroller. TLP 250 driver integrated circuit has been used for the amplification of the control signals for the converters. The converters have been fabricated using FGA15N120 Insulated Gate Bipolar Transistors (IGBT). A one HP DFIG hardware prototype has been used for the experimental set up.

2.6 CONCLUSION

The research objectives were framed according to the gaps identified in literature. The problem identification and the roadmap followed for obtaining the solution have been broadly outlined in this chapter.

CHAPTER 3

MATHEMATICAL MODELLING OF SYSTEM COMPONENTS

3.1 INTRODUCTION

This dynamic performance of machines is generally studied by their dynamic models. It is also very essential to know how a steady-state can be attained when the machine is in a different state. The DFIG's dynamic behaviour expresses the performance of the machine's variables in both the steady state and the transition period. The dynamic behaviour of the doubly-fed induction generator (DFIG) must be examined for modelling purposes and for developing the subsequent machine control. By means of the dynamic model it is possible to discern at all times the performance of the machine variables. By using the info delivered by the dynamic model, it is possible to predict how the state transitions may be accomplished. Such information allows the operator to ascertain unsafe behaviours like instabilities and high transients. The dynamic model also offers additional system information during the steady-state operation.

Thus, the dynamic DFIG model, expressed usually in the form of differential equations, is often organized as a compact set of equations. Such representation allows it to be simulated by digital devices like computers. Using these simulations, it is possible to derive valuable information related to the DFIG's variables. This is often called a "simulation model." It permits one to identify the continuous performance of all machine variables.

This chapter develops DFIG dynamic model based on the space vector theory. By applying this potent mathematical tool, the DFIG modelling differential equations have been derived. Then, from the obtained models, numerical instances as well as graphical illustration of performances have been achieved by dynamic simulation, providing practical information and a profound understanding of the machine's behaviour.

3.2 DYNAMIC MODELLING OF DFIG

The simplified and ideal DFIG model consists of three windings each in the stator and the rotor. The DFIG equivalent electric circuit has been illustrated in figure 3.1.

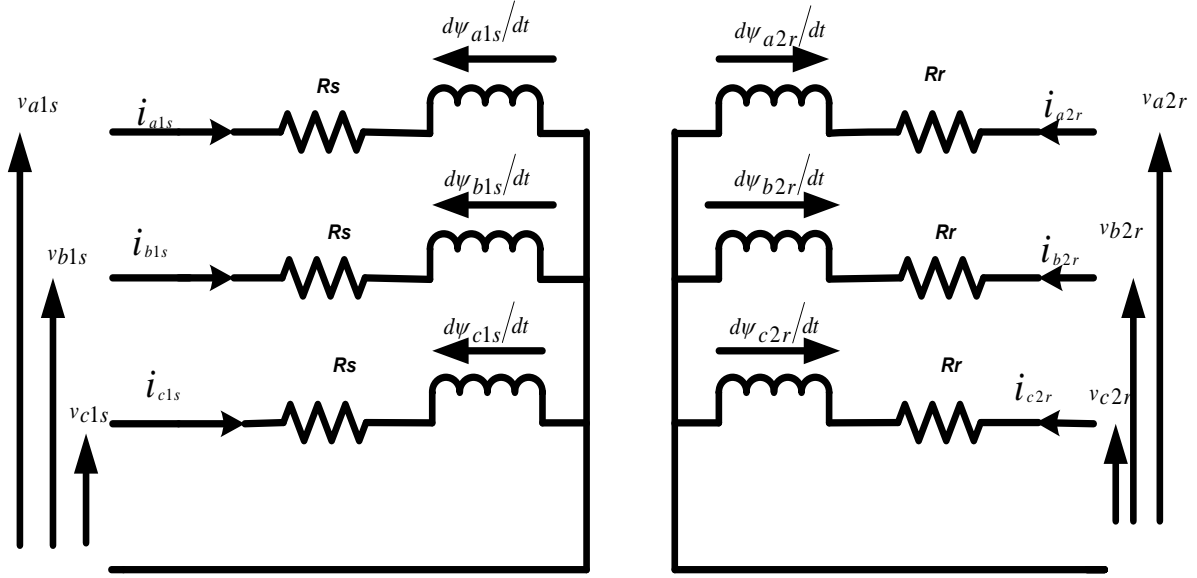


Fig. 3.1 DFIG electric equivalent circuit

For the illustration of figure 3.1, the instantaneous values of stator voltages, stator current and fluxes of the DFIG have been expressed by the equations (3.1) to (3.3).

$$v_{a1s} = R_s i_{a1s} + \frac{d\psi_{a1s}}{dt} \quad (3.1)$$

$$v_{b1s} = R_s i_{b1s} + \frac{d\psi_{b1s}}{dt} \quad (3.2)$$

$$v_{c1s} = R_s i_{c1s} + \frac{d\psi_{c1s}}{dt} \quad (3.3)$$

At steady state, the electric magnitudes at the stator exhibit a fixed angular frequency ω_s . This frequency is forced by the grid.

The rotor related variables have been expressed by the equations (3.4) to (3.6).

$$v_{a2r} = R_r i_{a2r} + \frac{d\psi_{a2r}}{dt} \quad (3.4)$$

$$v_{b2r} = R_r i_{b2r} + \frac{d\psi_{b2r}}{dt} \quad (3.5)$$

$$v_{c2r} = R_r i_{c2r} + \frac{d\psi_{c2r}}{dt} \quad (3.6)$$

At steady-state operating conditions, the magnitudes at the rotor have constant angular frequency ω_r .

For modelling purposes, a general DFIG constructed with dissimilar turns in the stator and rotor has been assumed. All parameters and magnitudes of the rotor have been referred to the stator.

Equation (3.7) relates the stator angular frequency with the rotor angular frequency.

$$\omega_r + \omega_m = \omega_s \quad (3.7)$$

Equation (3.8) gives the relation among the mechanical angular speed (Ω_m), the electrical frequency (ω_m) and the pair of poles.

$$\omega_m = p\Omega_m \quad (3.8)$$

3.2.1 $\alpha\beta$ Model of DFIG

In this section, the DFIG model's differential equations have been derived using the space vector notation. Modelling has been done in the stator reference frame. By performing Clarke's transformation on the DFIG stator as well as rotor voltage equations in the natural reference frame, voltage equations in the space vector form is obtained. Equations (3.9) and (3.10) represent the equation of the DFIG voltages in the space vector form.

$$\vec{v}_{1s}^s = R_s \vec{i}_{1s}^s + \frac{d\vec{\psi}_{1s}^s}{dt} \quad (3.9)$$

$$\vec{v}_{2r}^r = R_r \vec{i}_{2r}^r + \frac{d\vec{\psi}_{2r}^r}{dt} \quad (3.10)$$

Equation (3.9) has been represented in the stator coordinates; hereafter referred to as the “ $\alpha\beta$ reference frame.” Equation (3.10) has been represented in the rotor coordinates. The superscripts ‘s’ and ‘r’ specify that space vectors have been referred to the stator and the rotor reference frames respectively. In space vector notation, equations (3.11) to (3.14) state the correlation between the DFIG currents and the fluxes.

$$\vec{\psi}_{1s}^s = L_s \vec{i}_{1s}^s + L_m \vec{i}_{2r}^s \quad (3.11)$$

$$\vec{\psi}_{2r}^r = L_m \vec{i}_{1s}^r + L_r \vec{i}_{2r}^r \quad (3.12)$$

$$L_s = L_{\sigma s} + L_m \quad (3.13)$$

$$L_r = L_{\sigma r} + L_m \quad (3.14)$$

Equation (3.11) has been represented in the stator reference frame, while equation (3.12) is in the rotor reference frame. Applying coordinate transformation leads to equations (3.15) and (3.16).

$$\vec{\psi}_{1s}^s = L_s \vec{i}_{1s}^s + L_m \vec{i}_{2r}^s = L_s \vec{i}_{1s}^s + L_m e^{j\theta_m} \vec{i}_{2r}^r \quad (3.15)$$

$$\vec{\psi}_{2r}^r = L_m \vec{i}_{1s}^r + L_r \vec{i}_{2r}^r = L_m e^{-j\theta_m} \vec{i}_{1s}^s + L_r \vec{i}_{2r}^r \quad (3.16)$$

For obtaining the $\alpha\beta$ model of the DFIG, the corresponding space vectors are referred to the stator reference frame. Equations (3.17) to (3.20) express the DFIG related actuating entities in the stator reference frame.

$$\vec{v}_{1s}^s = R_s \vec{i}_{1s}^s + \frac{d\vec{\psi}_{1s}^s}{dt} \quad (3.17)$$

$$\vec{v}_{2r}^s = R_r \vec{i}_{2r}^s + \frac{d\vec{\psi}_{2r}^s}{dt} - j\omega_m \vec{\psi}_{2r}^s \quad (3.18)$$

$$\vec{\psi}_{1s}^s = L_s \vec{i}_{1s}^s + L_m \vec{i}_{2r}^s \quad (3.19)$$

$$\vec{\psi}_{2r}^s = L_m \vec{i}_{1s}^s + L_r \vec{i}_{2r}^s \quad (3.20)$$

For the transformation related to equation (3.18), it is essential to consider equation (3.21).

$$\frac{d\vec{\psi}_{2r}^r}{dt} e^{j\theta_m} = \frac{d \overbrace{(\vec{\psi}_{2r}^r e^{j\theta_m})}^{\vec{\psi}_{2r}^s}}{dx} - j\omega_m \overbrace{\vec{\psi}_{2r}^r e^{j\theta_m}}^{\vec{\psi}_{2r}^s} \quad (3.21)$$

Figure 3.2 illustrates the DFIG circuit diagram in the stator co-ordinates.

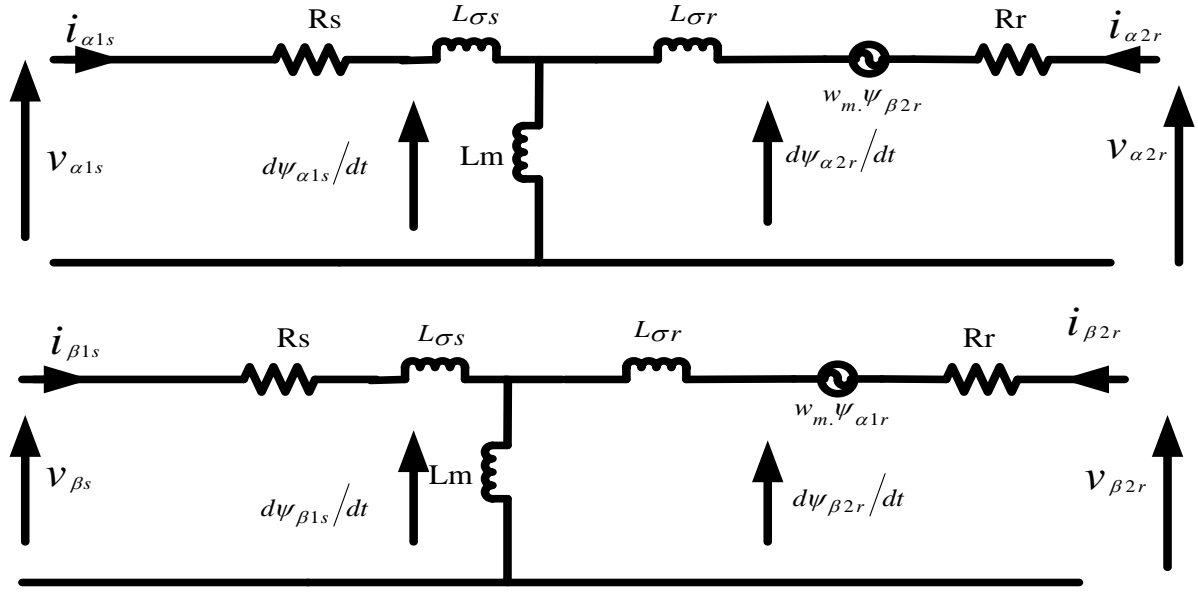


Fig. 3.2 DFIG $\alpha\beta$ model in stator co-ordinates

As per the DFIG $\alpha\beta$ model, the expressions of electric powers on the stator side and on the rotor side have been represented by equations (3.22) to (3.25).

$$P_s = \frac{3}{2} \text{Re}\{\vec{v}_{1s} \cdot \vec{i}_{1s}^*\} = \frac{3}{2} (v_{\alpha 1s} i_{\alpha 1s} + v_{\beta 1s} i_{\beta 1s}) \quad (3.22)$$

$$P_r = \frac{3}{2} \text{Re}\{\vec{v}_{2r} \cdot \vec{i}_{2r}^*\} = \frac{3}{2} (v_{\alpha 2r} i_{\alpha 2r} + v_{\beta 2r} i_{\beta 2r}) \quad (3.23)$$

$$Q_s = \frac{3}{2} \text{Im}\{\vec{v}_{1s} \cdot \vec{i}_{1s}^*\} = \frac{3}{2} (v_{\beta 1s} i_{\alpha 1s} - v_{\alpha 1s} i_{\beta 1s}) \quad (3.24)$$

$$Q_r = \frac{3}{2} \text{Im}\{\vec{v}_{2r} \cdot \vec{i}_{2r}^*\} = \frac{3}{2} (v_{\beta 2r} i_{\alpha 2r} - v_{\alpha 2r} i_{\beta 2r}) \quad (3.25)$$

In the equations (3.22) to (3.25), the superscript ‘*’ represents the complex conjugate of the mentioned space vector.

The electromagnetic torque of the machine has been expressed using equation (3.26).

$$T_{em} = \frac{3}{2} p \text{Im}\{\vec{\psi}_{2r} \cdot \vec{i}_{2r}^*\} = \frac{3}{2} p (\psi_{\beta 2r} i_{\alpha 2r} - \psi_{\alpha 2r} i_{\beta 2r}) \quad (3.26)$$

By substitution of equations (3.19) and (3.20) into equation (3.26), the equivalent representations of electromagnetic torque can be framed. Equation (3.27) expresses the equivalent representations of the torque.

$$\begin{aligned}
T_{em} &= \frac{3}{2} p \frac{L_m}{L_s} \text{Im}\{\vec{\psi}_{1s} \cdot \vec{i}_{2r}^*\} = \frac{3}{2} p \text{Im}\{\vec{\psi}_{1s}^* \cdot \vec{i}_{1s}\} = \frac{3}{2} p \frac{L_m}{L_r} \text{Im}\{\vec{\psi}_{2r}^* \cdot \vec{i}_{1s}\} \\
&= \frac{3}{2} p \frac{L_m}{\sigma L_r L_s} \text{Im}\{\vec{\psi}_{2r}^* \cdot \vec{\psi}_{1s}\} = \frac{3}{2} L_m p \text{Im}\{\vec{i}_{1s} \cdot \vec{i}_{2r}^*\}
\end{aligned} \tag{3.27}$$

where $\sigma = 1 - \frac{L_m^2}{L_s L_r}$

3.2.2 dq Model of DFIG

In this subsection, the differential equations expressing the model of the DFIG have been derived using the space vector notation in the synchronous reference frame. Multiplying the equations (3.9) and (3.10) by $e^{-j\theta_s}$ and $e^{-j\theta_r}$ respectively, the stator voltage and rotor voltage equations in the synchronous reference frame have been obtained.

$$\vec{v}_{1s}^a = R_s \vec{i}_{1s}^a + \frac{d\vec{\psi}_{1s}^a}{dt} + j\omega_s \vec{\psi}_{1s}^a \tag{3.28}$$

$$\vec{v}_{2r}^a = R_r \vec{i}_{2r}^a + \frac{d\vec{\psi}_{2r}^a}{dt} + j(\overbrace{\omega_s - \omega_m}^{\omega_r}) \vec{\psi}_{2r}^a \tag{3.29}$$

In the equations (3.28) and (3.29), the superscript ‘a’ indicates space vectors referred to a synchronously rotating frame. Equations (3.11) and (3.12) can be transformed to equations (3.30) and (3.31).

$$\vec{\psi}_{1s}^a = L_s \vec{i}_{1s}^a + L_m \vec{i}_{2r}^a \tag{3.30}$$

$$\vec{\psi}_{2r}^a = L_m \vec{i}_{1s}^a + L_r \vec{i}_{2r}^a \tag{3.31}$$

In the steady state, the dq components of sinusoidal quantities become constant. Hence, the dq equivalent circuit model of the DFIG is represented as illustrated in figure 3.3.

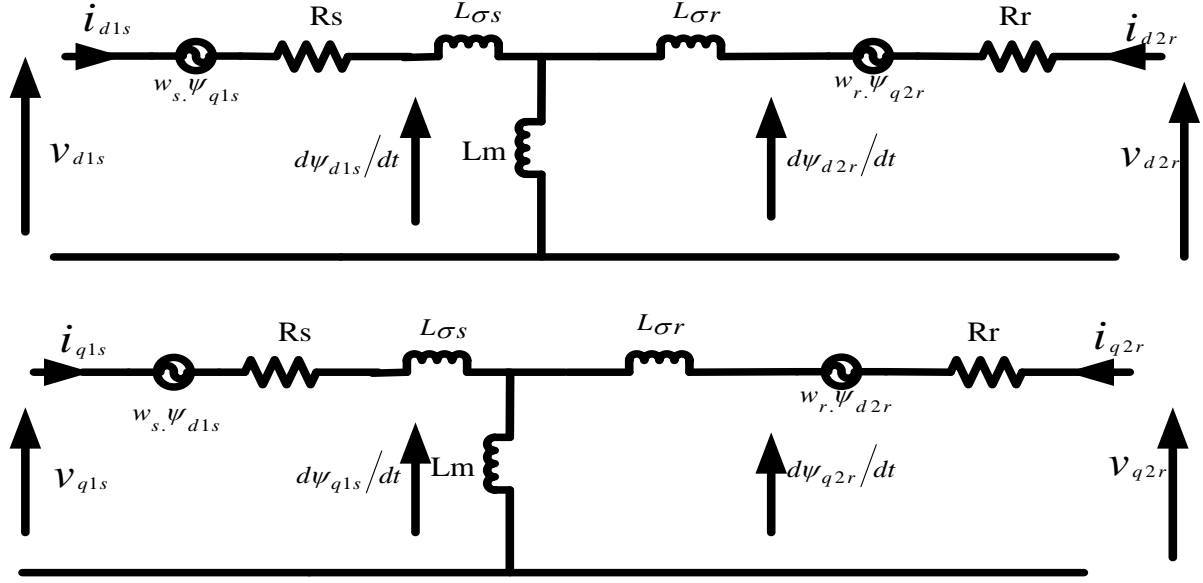


Fig. 3.3 DFIG dq model in synchronous reference frame

The DFIG power expressions and torque in the dq reference frame have been represented by equations (3.32) to (3.36).

$$P_s = \frac{3}{2} \text{Re}\{\vec{v}_{1s} \cdot \vec{i}_{1s}^*\} = \frac{3}{2} (v_{d1s} i_{d1s} + v_{q1s} i_{q1s}) \quad (3.32)$$

$$P_r = \frac{3}{2} \text{Re}\{\vec{v}_{2r} \cdot \vec{i}_{2r}^*\} = \frac{3}{2} (v_{d2r} i_{d2r} + v_{q2r} i_{q2r}) \quad (3.33)$$

$$Q_s = \frac{3}{2} \text{Im}\{\vec{v}_{1s} \cdot \vec{i}_{1s}^*\} = \frac{3}{2} (v_{q1s} i_{d1s} - v_{d1s} i_{q1s}) \quad (3.34)$$

$$Q_r = \frac{3}{2} \text{Im}\{\vec{v}_{2r} \cdot \vec{i}_{2r}^*\} = \frac{3}{2} (v_{q2r} i_{d2r} - v_{d2r} i_{q2r}) \quad (3.35)$$

$$T_{em} = \frac{3}{2} p \frac{L_m}{L_s} \text{Im}\{\vec{\psi}_{1s} \cdot \vec{i}_{2r}^*\} = \frac{3}{2} p \frac{L_m}{L_s} (\psi_{q1s} i_{d2r} - \psi_{d1s} i_{q2r}) \quad (3.36)$$

3.2.3 State-Space Representation of $\alpha\beta$ Model

State space representation of equations is very convenient for simulating components on computers using any utility software. For obtaining a dynamic model of the DFIG in the stator reference frame, equations (3.17)–(3.20) have been used. The state space expression so obtained has been expressed by equation (3.37).

$$\frac{d}{dt} \begin{bmatrix} \psi_{\alpha 1s} \\ \psi_{\beta 1s} \\ \psi_{\alpha 2r} \\ \psi_{\beta 2r} \end{bmatrix} = \begin{bmatrix} \frac{-R_s}{\sigma L_s} & 0 & \frac{R_s L_m}{\sigma L_s L_r} & 0 \\ 0 & \frac{-R_s}{\sigma L_s} & 0 & \frac{R_s L_m}{\sigma L_s L_r} \\ \frac{R_r L_m}{\sigma L_s L_r} & 0 & \frac{-R_r}{\sigma L_r} & -\omega_m \\ 0 & \frac{R_r L_m}{\sigma L_s L_r} & \omega_m & \frac{-R_r}{\sigma L_r} \end{bmatrix} \cdot \begin{bmatrix} \psi_{\alpha 1s} \\ \psi_{\beta 1s} \\ \psi_{\alpha 2r} \\ \psi_{\beta 2r} \end{bmatrix} + \begin{bmatrix} v_{\alpha 1s} \\ v_{\beta 1s} \\ v_{\alpha 2r} \\ v_{\beta 2r} \end{bmatrix} \quad (3.37)$$

Equation (3.37) and equation (3.27) have been used in this work to develop the model of DFIG.

3.3 MODELLING OF PRACTICAL DC-DC CONVERTERS

For modelling a practical DC-DC converters, the parasitic resistance of the inductive coil has to be considered.

3.3.1 Modelling of a Step-Down DC-DC Converter

Figure 3.4 is an illustration of a practical buck converter.

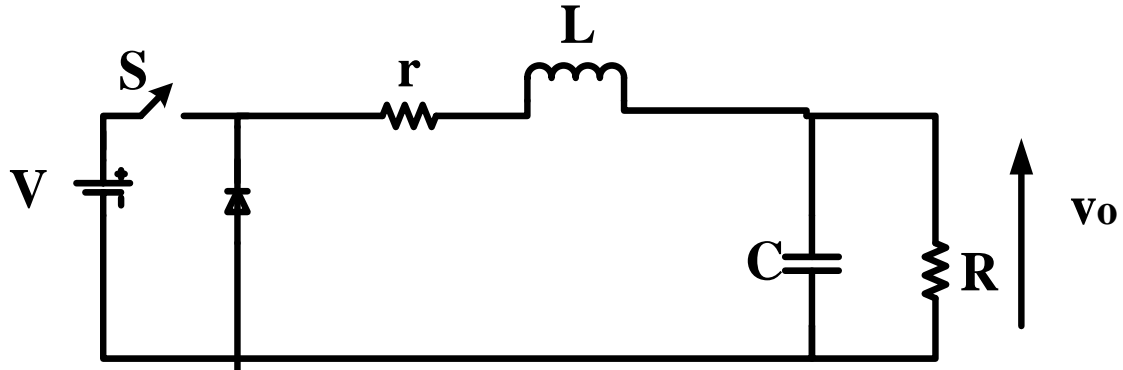


Fig. 3.4 Circuit diagram of a practical buck converter

When the switch \$S\$ is ON, the circuit diagram of figure 3.4 is transformed as shown in figure 3.5.

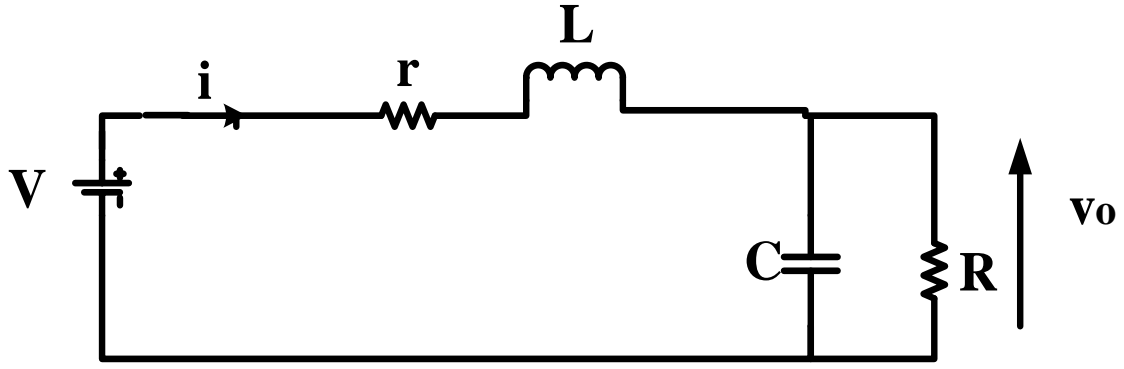


Fig. 3.5 Circuit diagram of a practical buck converter when the switch is ON

Equations (3.38) and (3.39) correspond to the circuit illustrated in figure 3.5.

$$V = ri + L\left(\frac{di}{dt}\right) + v_o \quad (3.38)$$

$$i = C\left(\frac{dv_o}{dt}\right) + \left(\frac{v_o}{R}\right) \quad (3.39)$$

Re-arranging equations (3.38) and (3.39), the equations (3.40) and (3.41) are obtained.

$$\left(\frac{di}{dt}\right) = \left(-r/L\right)i + \left(-1/L\right)v_o + \left(1/L\right)V \quad (3.40)$$

$$\left(\frac{dv_o}{dt}\right) = \left(1/C\right)i + \left(-1/RC\right)v_o \quad (3.41)$$

Arranging equations (3.40) and (3.41) in the state space form yields equation (3.42).

$$\begin{bmatrix} \dot{i} \\ \dot{v}_o \end{bmatrix} = \begin{bmatrix} -r/L & -1/L \\ 1/C & -1/RC \end{bmatrix} \begin{bmatrix} i \\ v_o \end{bmatrix} + \begin{bmatrix} 1/L \\ 0 \end{bmatrix} V \quad (3.42)$$

Comparing with the standard state space form yields equations (3.43) and (3.44)

$$A_{on} = \begin{bmatrix} -r/L & -1/L \\ 1/C & -1/RC \end{bmatrix} \quad (3.43)$$

$$B_{on} = \begin{bmatrix} 1/L \\ 0 \end{bmatrix} \quad (3.44)$$

When the switch is OFF, the circuit diagram of figure 3.4 is transformed as shown in figure 3.6.

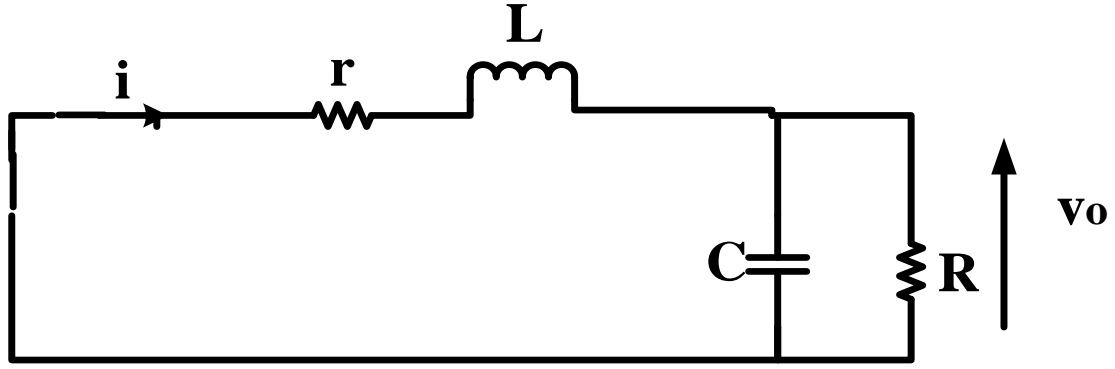


Fig. 3.6 Circuit diagram of a practical buck converter when the switch is OFF

Equations (3.45) and (3.46) correspond to the circuit illustrated in figure 3.6.

$$0 = ri + L \left(\frac{di}{dt} \right) + v_o \quad (3.45)$$

$$i = C \left(\frac{dv_o}{dt} \right) + \left(\frac{v_o}{R} \right) \quad (3.46)$$

Re-arranging equations (3.45) and (3.46), the equations (3.47) and (3.48) have been obtained.

$$\left(\frac{di}{dt} \right) = \left(-r/L \right) i + \left(-1/L \right) v_o \quad (3.47)$$

$$\left(\frac{dv_o}{dt} \right) = \left(1/C \right) i + \left(-1/RC \right) v_o \quad (3.48)$$

Arranging equations (3.47) and (3.48) in the state space form yields equation (3.49).

$$\begin{bmatrix} \dot{i} \\ \dot{v}_o \end{bmatrix} = \begin{bmatrix} -r/L & -1/L \\ 1/C & -1/RC \end{bmatrix} \begin{bmatrix} i \\ v_o \end{bmatrix} + \begin{bmatrix} 0 \\ 0 \end{bmatrix} V \quad (3.49)$$

Comparing with the standard state space form yields equations (3.50) and (3.51).

$$A_{off} = \begin{bmatrix} -r/L & -1/L \\ 1/C & -1/RC \end{bmatrix} \quad (3.50)$$

$$B_{off} = \begin{bmatrix} 0 \\ 0 \end{bmatrix} \quad (3.51)$$

For both ON and OFF, matrix A is the same. However, B_{on} is different from B_{off} . The time averaged value of B can be computed as follows:

$$B = B_{on}D + B_{off}(1-D)$$

$$= \begin{bmatrix} 1/L \\ 0 \end{bmatrix} D + \begin{bmatrix} 0 \\ 0 \end{bmatrix} (1-D)$$

This implies that $B = \begin{bmatrix} 1/L \\ 0 \end{bmatrix} D$

Hence for a practical buck converter, the dynamic state space representation is denoted by equations (3.52) and (3.53).

$$\begin{bmatrix} \dot{i} \\ \dot{v}_0 \end{bmatrix} = \begin{bmatrix} -r/L & -1/L \\ 1/C & -1/RC \end{bmatrix} \begin{bmatrix} i \\ v_0 \end{bmatrix} + \begin{bmatrix} 1/L \\ 0 \end{bmatrix} DV \quad (3.52)$$

$$v_0 = \begin{bmatrix} 0 & 1 \end{bmatrix} \begin{bmatrix} i \\ v_0 \end{bmatrix} \quad (3.53)$$

3.3.2 Modelling of a Step-Up DC-DC Converter

Figure 3.7 is an illustration of a practical boost converter.

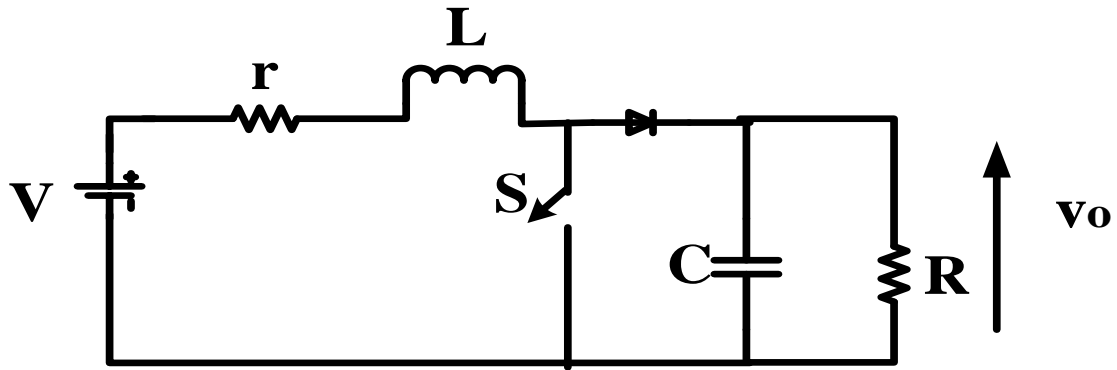


Fig. 3.7 Circuit diagram of a practical boost converter

When the switch S is ON, the circuit diagram of figure 3.7 is transformed as illustrated in figure 3.8.

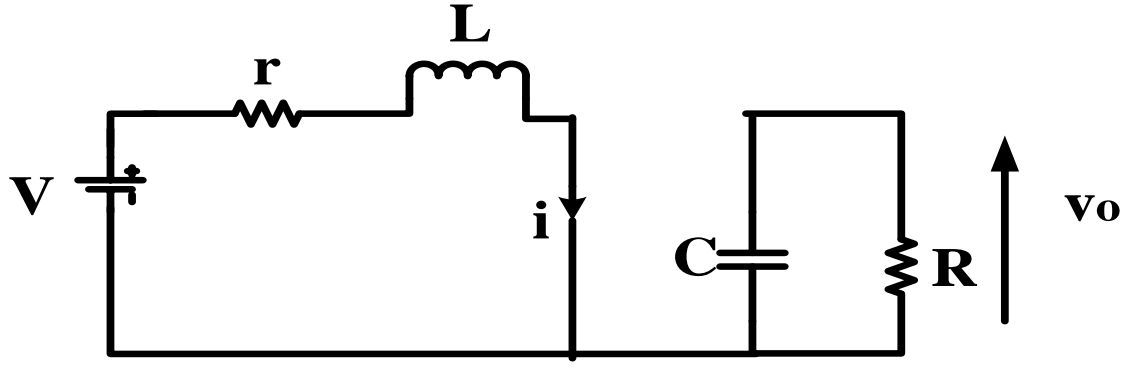


Fig. 3.8 Circuit diagram of a practical boost converter when the switch is ON

Equations (3.54) and (3.55) correspond to the circuit illustrated in figure 3.8.

$$V = ri + L\left(\frac{di}{dt}\right) \quad (3.54)$$

$$0 = C\left(\frac{dv_o}{dt}\right) + \left(\frac{v_o}{R}\right) \quad (3.55)$$

Re-arranging equations (3.54) and (3.55), the equations (3.56) and (3.57) are obtained.

$$\left(\frac{di}{dt}\right) = \left(-r/L\right)i + \left(1/L\right)V \quad (3.56)$$

$$\left(\frac{dv_o}{dt}\right) = \left(-1/RC\right)v_o \quad (3.57)$$

Arranging equations (3.56) and (3.57) in the state space form yields equation (3.58).

$$\begin{bmatrix} \dot{i} \\ \dot{v_o} \end{bmatrix} = \begin{bmatrix} -r/L & 0 \\ 0 & -1/RC \end{bmatrix} \begin{bmatrix} i \\ v_o \end{bmatrix} + \begin{bmatrix} 1/L \\ 0 \end{bmatrix} V \quad (3.58)$$

Comparing with standard state space form yields equations (3.59) and (3.60)

$$A_{on} = \begin{bmatrix} -r/L & 0 \\ 0 & -1/RC \end{bmatrix} \quad (3.59)$$

$$B_{on} = \begin{bmatrix} 1/L \\ 0 \end{bmatrix} \quad (3.60)$$

When the switch is OFF, the circuit diagram of figure 3.7 is transformed as shown in figure 3.9.

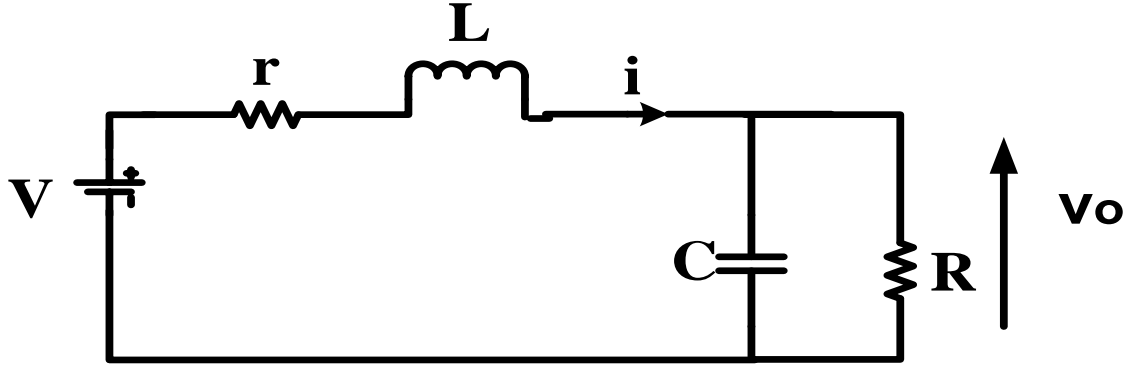


Fig. 3.9 Circuit diagram of a practical boost converter when the switch is OFF

Equations (3.61) and (3.62) correspond to the circuit illustrated in figure 3.9.

$$V = ri + L \left(\frac{di}{dt} \right) + v_o \quad (3.61)$$

$$i = C \left(\frac{dv_o}{dt} \right) + \left(\frac{v_o}{R} \right) \quad (3.62)$$

Re-arranging equations (3.61) and (3.62), the equations (3.63) and (3.64) are obtained.

$$\left(\frac{di}{dt} \right) = \left(-r/L \right) i + \left(-1/L \right) v_o + \left(1/L \right) V \quad (3.63)$$

$$\left(\frac{dv_o}{dt} \right) = \left(1/C \right) i + \left(-1/RC \right) v_o \quad (3.64)$$

Arranging equations (3.63) and (3.64) in the state space form yields equation (3.65).

$$\begin{bmatrix} \dot{i} \\ \dot{v}_o \end{bmatrix} = \begin{bmatrix} -r/L & -1/L \\ 1/C & -1/RC \end{bmatrix} \begin{bmatrix} i \\ v_o \end{bmatrix} + \begin{bmatrix} 1/L \\ 0 \end{bmatrix} V \quad (3.65)$$

Comparing with standard state space form yields equations (3.66) and (3.67)

$$A_{off} = \begin{bmatrix} -r/L & -1/L \\ 1/C & -1/RC \end{bmatrix} \quad (3.66)$$

$$B_{off} = \begin{bmatrix} 1/L \\ 0 \end{bmatrix} \quad (3.67)$$

For both ON and OFF, matrix B is the same. However, A_{on} is different from A_{off} . The time averaged value of A can be computed as follows:

$$A = A_{on}D + A_{off}(1-D)$$

$$= \begin{bmatrix} -r/L & 0 \\ 0 & -1/RC \end{bmatrix} D + \begin{bmatrix} -r/L & -1/L \\ 1/C & -1/RC \end{bmatrix} (1-D)$$

This implies that $A = \begin{bmatrix} -r/L & -(1-D)/L \\ (1-D)/C & -1/RC \end{bmatrix}$

Hence for a practical boost converter, the dynamic state space representation is denoted by equations (3.68) and (3.69).

$$\begin{bmatrix} \dot{i} \\ \dot{v}_0 \end{bmatrix} = \begin{bmatrix} -r/L & -(1-D)/L \\ (1-D)/C & -1/RC \end{bmatrix} \begin{bmatrix} i \\ v_0 \end{bmatrix} + \begin{bmatrix} 1/L \\ 0 \end{bmatrix} V \quad (3.68)$$

$$v_0 = \begin{bmatrix} 0 & 1 \end{bmatrix} \begin{bmatrix} i \\ v_0 \end{bmatrix} \quad (3.69)$$

3.4 CONCLUSION

This chapter focused on the development of a DFIG mathematical model and practical DC-DC converter models using differential equations. Such modelling can be used to design proper controller parameters for the efficient control of any DFIG based wind energy conversion system. Mathematical modelling of any machine/ converter yields a great insight into its dynamics. Such clarity can be put to use for efficient conditioning of the dynamic responses.

CHAPTER 4

SIMULATION AND HARDWARE IMPLEMENTATION OF POWER ELECTRONIC CONVERTERS

4.1 INTRODUCTION

The power electronic converters (PECs) have an important role in modern wind energy conversion systems (WECS) with variable-speed control method. The PEC and its control strategy in a variable speed WECS is usually used for converting the variable-frequency and variable-magnitude AC output from the electrical generator into a constant-frequency and constant-magnitude supply which can be utilized for grid connected mode or isolated mode.

Distributed generation (DG) using locally existing renewable sources can facilitate the achievement of energy self-reliance for remote locations. Doubly-fed Induction Generator (DFIG) is widely used for commercial WECS. DFIG based variable speed energy conversion systems require PECs for signal conditioning. This chapter encompasses a method for easy fabrication of DC-AC converters. It elaborates on the Xilinx System Generator (XSG) based control signal generation for voltage source converters (VSC). The signals are created via a field programmable gate array (FPGA). The converters have been simulated in MATLAB 2010a environment and fabricated thereafter to authenticate the real time processing capability of the FPGA controller. XSG 12.4 creates the hardware description language (HDL) code automatically for the FPGA. Hence, an end user who is unfamiliar with coding can easily build a converter.

The foremost benefit of the FPGA-based XSG technique is that it yields a functional assessment of the FPGA as controller, prior to linking it to the actual system. FPGA is an excellent converter prototyping option due to its programmability and re-configurability. However, the traditional method of coding control signals of FPGA using HDL is very complex. Hence, there is a need of a coding independent control signal generation platform for power electronics engineers/ researchers. The XSG method of control signal generation using FPGAs is a low cost and flexible option. The XSG method also leads to ease in generation of converter control signals owing to automatic code generation by XSG. Previous research works invoked the usage of XSG but

do not explicitly explain the method of implementation. In this work, a detailed explanation of the XSG-based technique used for the construction of the triangular and the sinusoidal signal has been presented.

A three-phase VSI and two single-phase VSIs have been implemented. The XSG simulation platform has been utilized to automatically create the HDL code corresponding to different switching strategies. These codes have been used to analyse various control algorithms in hardware via FPGAs. A DFIG rotor has been excited by a three-phase inverter. The control of the PECs has been done via XSG. The application and utility of XSG based PECs in renewable energy has been brought out by the isolated mode DFIG system.

4.2 VSI PROTOTYPES

In this section, the construction of two single-phase VSIs and a three-phase VSI have been presented.

4.2.1 Single-phase VSI

Figure 4.1(a) illustrates a single-phase three-level diode clamped inverter while figure 4.1 (b) shows a five-level eight-switch H-bridge topology.

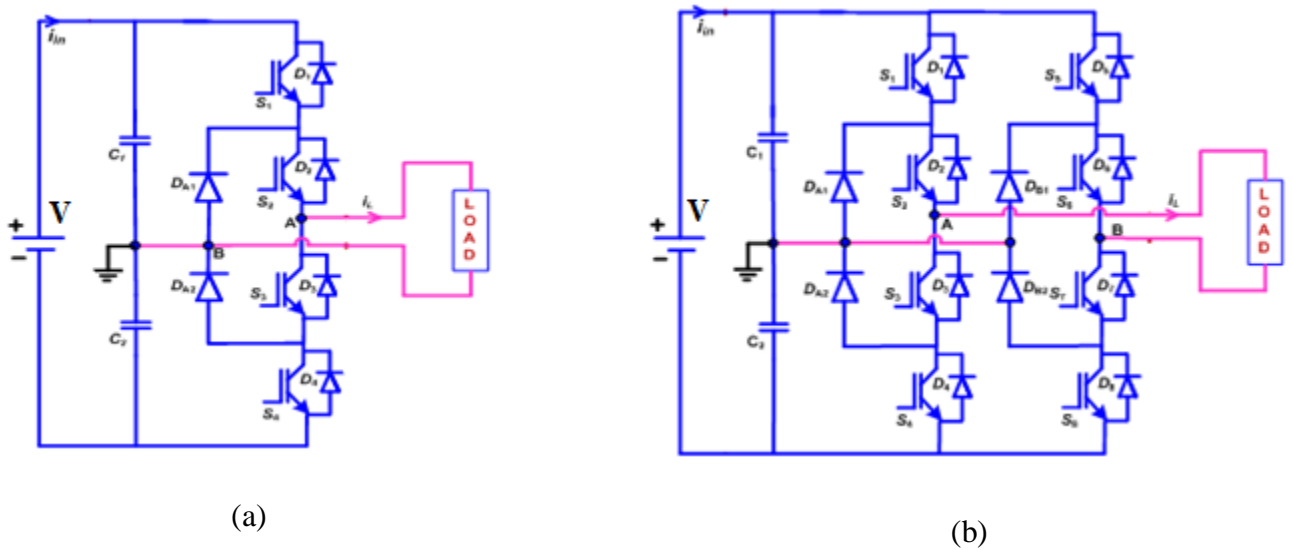


Fig. 4.1 Power circuit of single phase inverters (a) Three-level diode clamped topology (b) Five-level eight-switch H-bridge topology

4.2.2 Three-phase VSI

The topology of a three-phase inverter comprises of three legs. Each leg consists of two switches, as illustrated in figure 4.2.

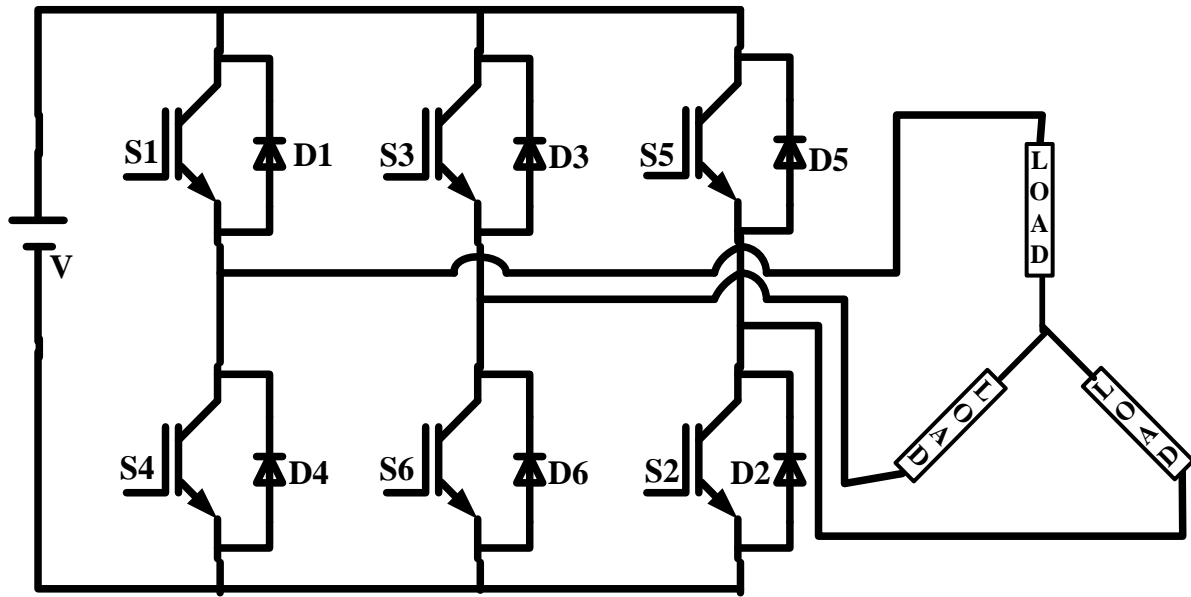


Fig. 4.2 Three-phase voltage source inverter

The power electronic converters shown in figures 4.1 and 4.2 have been modelled using the MATLAB/SIMULINK environment. The real-time switching signals for the inverters have been developed via XSG-coded FPGA. The details of the control signal generation have been elucidated in the following section.

4.3 CONTROL SIGNAL GENERATION USING XSG

The SPWM control scheme for inverters requires sinusoidal signals and triangular signals. In this section, the XSG methods of developing the sinusoids as well as the triangular signals have been described in detail.

In order to obtain the inverter output, different sinusoidal PWM methods have been implemented via FPGA by the application of XSG simulation toolset. The high-frequency carrier signal as well as the fundamental frequency modulating signal has been simulated in SIMULINK by applying the XSG interface. The initial testing is done in the simulation environment. After the output functionality is established through the simulations, the code generation for the FPGA is carried out by XSG token compilation.

In this work, the a Spartan 3E FPGA has been used. The code dumped by XSG in the FPGA is actually synthesized by an integrated software environment (ISE) simulator. The switching signals output by the

FPGA are amplified and isolated prior to feeding the respective switches. Insulated gate bipolar transistors (IGBTs) have been used to construct the power circuit of the inverters.

4.3.1 Sinusoidal Modulating Signal Generation

Figure 4.3 is a snapshot of the XSG block arrangement for the generation of a sinusoidal reference signal at 50 Hz.

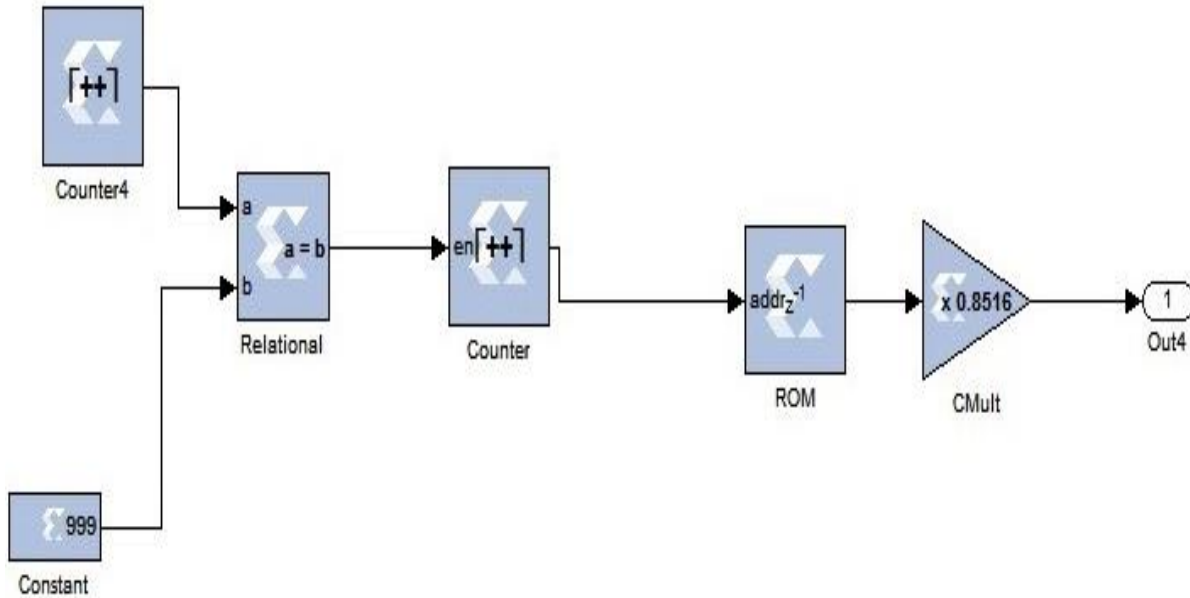


Fig. 4.3 Sinusoidal signal generation using XSG

For constructing the reference wave using XSG, the step by step approach is as follows:

1. The clock frequency of the FPGA used is 50 MHz, which corresponds to a time period of 20 ns. The required frequency of the sinusoidal signal is 50 Hz. The consequent time period is 20 ms. Hence, a counter needs to be employed which will generate a reference pulse after counting $\frac{(20 \times 10^{-3})}{(20 \times 10^{-9})}$ times relative to each pulse of the FPGA. This value equals 10^6 . The Xilinx “Up Counter” block can be employed specifically for this role.

$$2. \text{ Counter value} = \frac{\text{Time period of modulating signal}}{\text{Time period of FPGA clock}}.$$

The time period of the FPGA clock is mentioned as the “explicit period” in the “System Generator” icon of Simulink. The count limit of a counter in XSG is $2^{16} = 65536$. Since 10^6 is greater than 65536, two back to back counters are used to count to 10^6 .

3. As illustrated in figure 4.3, the first counter ‘Counter4’ counts from 0 to 999, i.e. effectively 1000. Its limit is set to $2^{10} = 1024$, which is within its count range. A relational operator is placed next to the first counter and gets enabled as soon as ‘Counter4’ count reaches 999. Thereafter, it enables the second counter ‘Counter’ which is also set to count from 0 to 999. The cascaded effect of the two counters yields a net count of $10^3 \times 10^3 = 10^6$.
4. The “ROM” block of XSG is used for generating the sine wave. The output of ‘Counter’ shown in figure 4.3 serves as the input to the ‘ROM’. The “ROM” block “depth” equals the highest count of its input counter. The “initial value vector” is assigned a value $\sin \left[2 * \pi * \{0:(d-1)\} / d \right]$; where ‘d’ is the “ROM” block “depth”. The output of this block will yield a sine wave of amplitude 1. A phase-displaced sine wave can be obtained by using the expression $\sin \left[2 * \pi * \{0:(d-1)\} / d - \theta \right]$; where ‘ θ ’ is the required phase angle.
5. To obtain a level-shifted sinusoid, an arbitrary number can be added to the signal obtained in step 4. The “Constant” block and “AddSub” block of XSG is used for this purpose.
6. As illustrated in figure 4.3, the “gain” block ‘CMult’ of XSG is used to change the sine wave amplitude according to the modulation index.
7. As illustrated in figure 4.3, the “Gateway Out” block ‘Out4’ of the XSG is used to route the signal to the corresponding pin of FPGA. The pin number has to be entered using single quotes.

By following the above seven steps, a modulating signal of the required magnitude, frequency and phase can be easily generated.

4.3.2 Carrier Signal Generation

The triangular carrier signal illustrated in figure 4.4 has been developed in the XSG domain, at a frequency of 2 kHz.

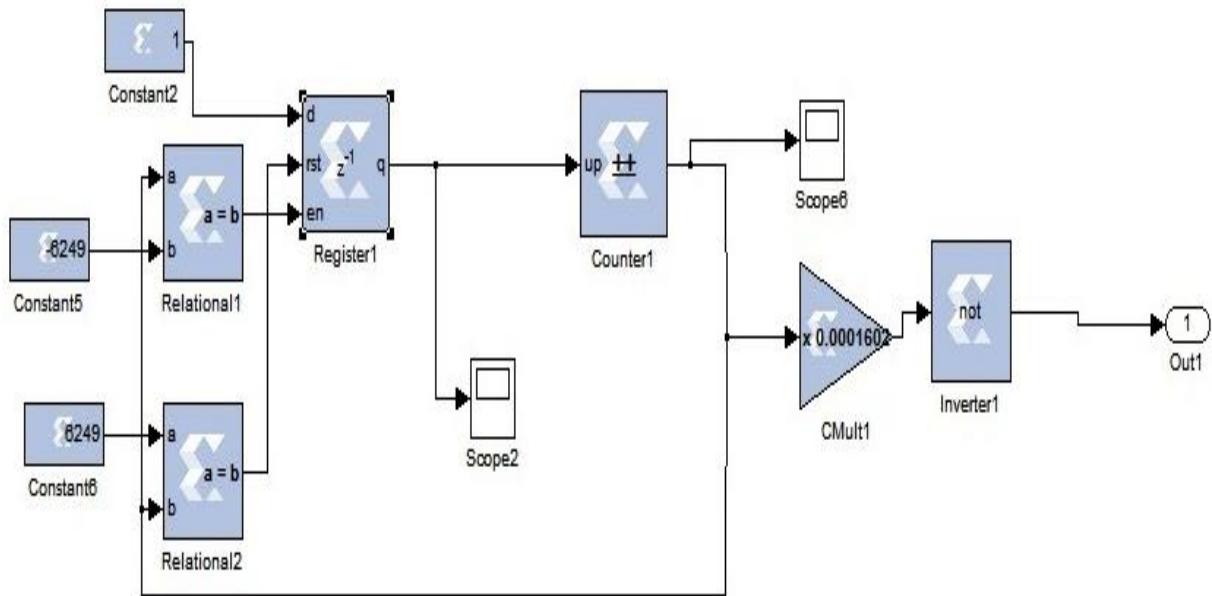


Fig. 4.4 Triangular signal generation using XSG

For constructing the carrier wave using XSG, the step by step approach is as follows:

1. The clock frequency of the FPGA is 50 MHz, which corresponds to a time period of 20 ns. The required frequency of the triangular carrier is 2 kHz, with the corresponding time period of 0.5 ms. Hence, there is a need for a counter which will generate a carrier pulse after counting $\frac{(0.5 \times 10^{-3})}{(20 \times 10^{-9})}$ times relative to each pulse of the FPGA; this value equals 25000.

2. The carrier wave will have a negative peak and a positive peak. The first peak of the triangle occurs at a value equal to one quarter of the time period; where one time period of the carrier corresponds to a count of 25000. This means that the quarter time period will occur at a value $\frac{25000}{4} = 6250$.

The Xilinx “Up/down Counter” block is used for designing the triangular signal, since it can generate the negative peak as well as the positive peak. If the counter input is zero, it acts as a down counter. However, if the counter input is one, it acts as an up counter.

$$3. \text{ Counter value} = \left\lceil \left(\frac{\text{Time period of carrier signal}}{\text{Time period of FPGA clock}} \right) / 4 \right\rceil.$$

The time period of the FPGA clock is mentioned as the “explicit period” in the “System Generator” icon of Simulink as well as the counter. Since the counter needs to count till 6250 which is well within the maximum possible range of 65536, a single counter will suffice.

4. As illustrated in figure 4.4, the input of the “up/down counter” block ‘Counter1’ is actuated by the output of the “Register” block ‘Register1’ from XSG. The three inputs of ‘Register1’ are individually fed. A “constant” block ‘Constant2’ and two “relational operator” blocks ‘Relational1’ and ‘Relational2’ of XSG are used for this purpose. The connections are done as follows:

- i) The input port “d” of ‘Register1’ is connected to the “Constant” block of XSG having value 1.
- ii) The input port “rst” of ‘Register1’ is connected to ‘Relational2’. The ‘a’ input of ‘Relational2’ is connected to a constant value of 6249 and the “b” input is connected to the output of ‘Counter1’. ‘Counter1’ performs 6250 counts, i.e. it starts from zero—and counts till 6249. Whenever the counter count equals 6249, ‘Relational2’ actuates the “rst” input of the ‘Register1’. This in turn puts ‘Counter1’ input to zero. Thereafter ‘Counter1’ operates like a down counter and counts down till its value reaches -6249.
- iii) The input port “en” of ‘Register1’ is connected to ‘Relational1’. The “b” input of ‘Relational1’ is connected to a constant value of -6249, while the “a” input is connected to the output of ‘Counter1’. As soon as the count of ‘Counter1’ reaches -6249, ‘Relational1’ activates the “en” input of ‘Register1’ and ‘Register1’ output “q” becomes high. This means that ‘Counter1’ input becomes one. Thus, ‘Counter1’ starts operating as an up counter from -6249 to 6249.

5. After ‘Counter1’ count reaches 6249, ‘Relational2’ actuates the “rst” input of the ‘Register1’. The output of the register changes from 1 to 0. ‘Counter1’ becomes a down counter again and the process gets repeated. Consequently, a triangular wave with a maximum value of 6249 and a phase shift of 180° is obtained.

6. As illustrated in figure 4.4, to make the peak magnitude of the triangular signal equal to 1, the output of ‘Counter1’ is passed through the “gain” block ‘CMult1’ of XSG. The gain of ‘CMult1’ is set to (1/6250).

7. As illustrated in figure 4.4, to obtain a carrier signal with 0° phase shift, the output of ‘CMult1’ is passed through a “NOT” Gate of XSG.

8. If a phase-shifted carrier is required, the initial value of ‘Counter1’ has to be altered depending upon the configuration. For example, the initial value of the counter is put to 6249 if a 90° phase shift is needed.

9. To obtain a level-shifted carrier, an arbitrary number can be added to the signal obtained in step 7. The “Constant” block and “AddSub” block of XSG is used for this purpose.

10. As illustrated in figure 4.4, the “Gateway Out” block ‘Out1’ is used to route the signal to the corresponding pin of the FPGA. The pin number has to be entered in single quotes.

By following the above ten steps, a carrier signal of the required magnitude, frequency level shift and phase can be easily generated.

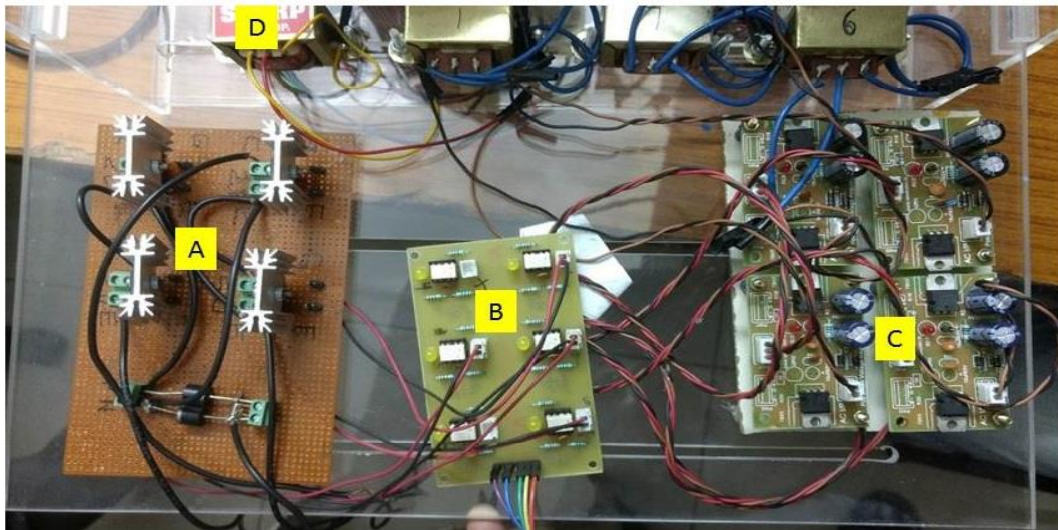
4.3.3 Automatic Code Dumping in FPGA

While the simulation runs in the Simulink environment consisting of the XSG blockset, HDL code is automatically generated by the ISE Foundation software. The result is an automatically generated bit stream, also known as the HDL co-simulation. The FPGA design flow is explained hereafter. To begin with, XSG is used to fabricate a circuit. Thereafter, the VHDL code generation occurs. It is followed by synthesis, during which the code gets converted to a proper permutation of logic gates, multiplexers and interconnects. During design implementation, the blocks of logic get appropriately re-arranged. Subsequently, pin mapping on the FPGA is carried out. The next step relates to the verification of the design. Once the aforementioned processes actuate successfully, a bit stream is generated which is then downloaded on the FPGA and run.

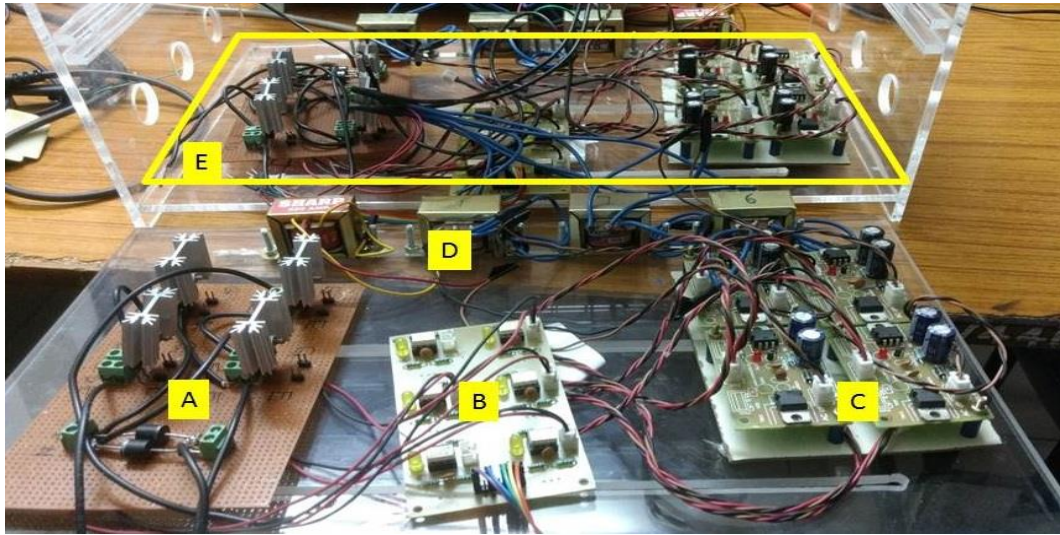
4.4 DESCRIPTION OF HARDWARE

In this section, the hardware used to construct the DC-AC converters has been discussed. Control signals have been generated using the Spartan 3E FPGA Basys 2 board.

Figure 4.5 and figure 4.6 present the hardware for the single-phase inverter and the three-phase VSI, respectively.



(a)



(b)

Fig. 4.5 Hardware prototype for single-phase VSI (a) Three-level (b) Five-level

A- Power circuit containing IGBT switches FGA15N120. B- Driver circuit using TLP 250. C- Power supply for driver circuits. IC 7812 and 7912 are used. D- (12-0-12) transformers for feeding the power supply. E- A complete leg consisting of A, B, C and D.

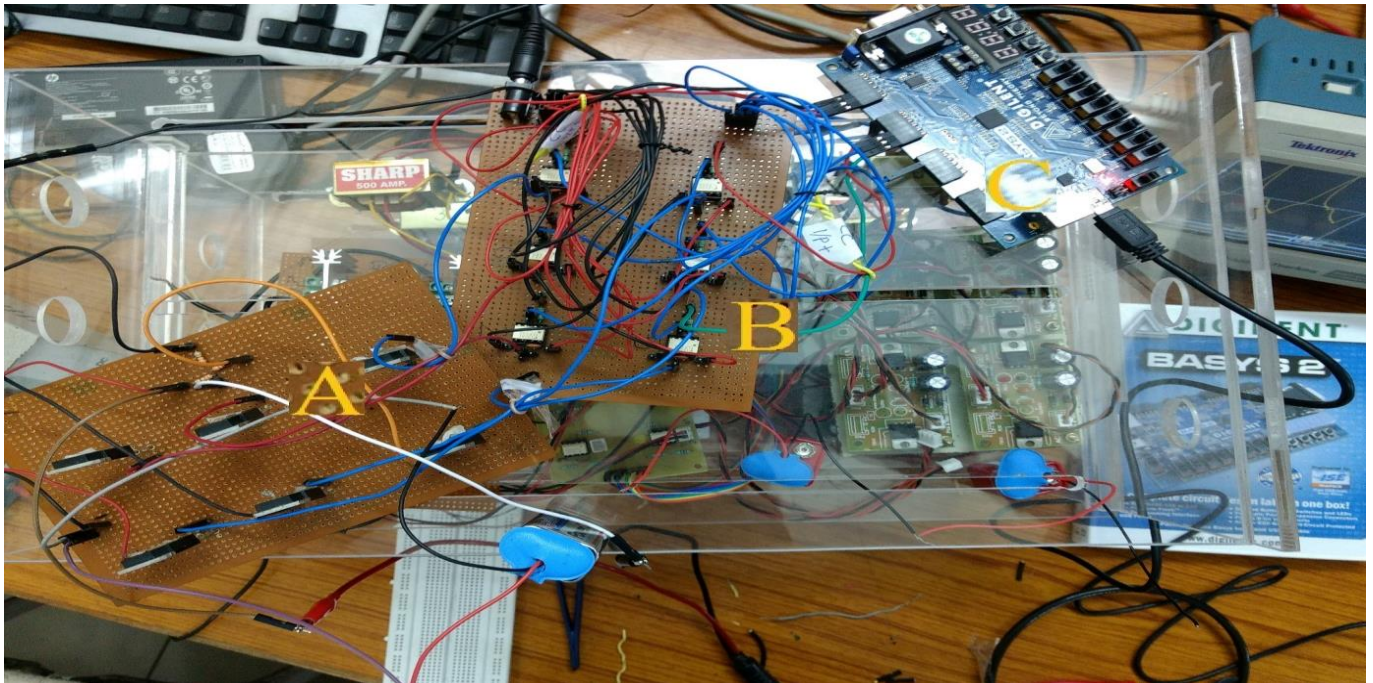


Fig. 4.6 Hardware for three-phase VSI

A- Power circuit containing IGBT switches FGA15N120. B- Driver circuit using TLP 250 powered by 12 V adapter. C- Spartan 3E FPGA for generation of control signal.

The driver circuits have been developed using IC TLP 250. The power supply of the driver is produced by employing IC 7812 and 7912. The input to the voltage regulator ICs are provided by 12-0-12 transformers. The power circuits of the inverters have been constructed using FGA15N120ANTDTU IGBT switches. These switches are rated at 1200 V, 15 A. The electrical characteristics of the ICs have been provided in the appendix.

4.5 APPLICATION OF XSG BASED PEC IN STANDALONE DFIG SYSTEM

The PECs developed by XSG can be used in renewable energy systems. In this section, the application of XSG in renewable has been explored. An isolated DFIG with rotor excited by three phase inverter has been demonstrated. The switching signals of the inverter have been generated using XSG. XSG is versatile and can be put to use for easily generating control signals as simple as that of choppers and as complex as that of poly-phase multilevel inverters. Figure 4.7 is an illustration of the proposed XSG controlled system.

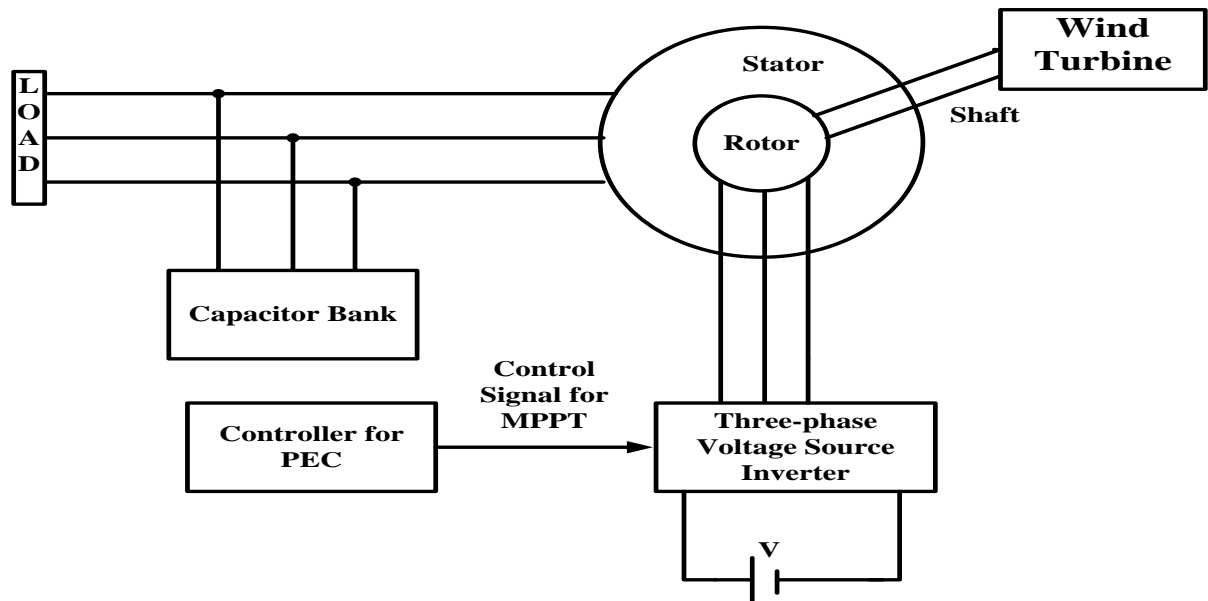


Fig. 4.7 Block diagram of the isolated DFIG system with rotor excited by three-phase inverter

4.6 RESULTS AND ANALYSIS

In this section, all the results corresponding to the different switching strategies for the output voltage control of the inverters has been presented.

The SIMULINK platform containing the XSG block set has been used for constructing:

- a single-phase three-level inverter

- a single-phase five-level inverter, and
- a three-phase voltage source inverter.

In all the succeeding discussions, the triangular signal frequency is 2 kHz and that of the sinusoid is 50 Hz. The modulation index is 0.8. The frequency of switching equals the frequency of the carrier. The output voltage is generated at the frequency of the modulating waveform.

4.6.1 Analysis of Single-phase Three-level VSI

For the inverter shown in figure 4.1(a), the first and third switch pair (S1, S3) as well as the second and fourth switch pair (S2, S4) are complementary. The diodes clamp the switch voltage to half the level of the DC bus voltage V_{dc} . When S1 and S2 turn on, the voltage across the load becomes $V_{dc}/2$. When S1 and S3 are ON, the load voltage is 0 V. However, when S3 and S4 are ON, the load voltage is $-V_{dc}/2$. The control signal generation scheme is illustrated in figure 4.8.

Two level-shifted triangular carriers are compared with a sinusoidal modulating signal. The comparison of the sine with the upper triangle yields the signals for S1 and S3. The switching signals for the other two switches are obtained by comparing the lower triangle with the sinusoid. The output voltage obtained in simulation is a three-level waveform as shown in figure 4.9(a). The hardware output voltage of the three level inverter with control signal generated through XSG is shown in figure 4.9(b).

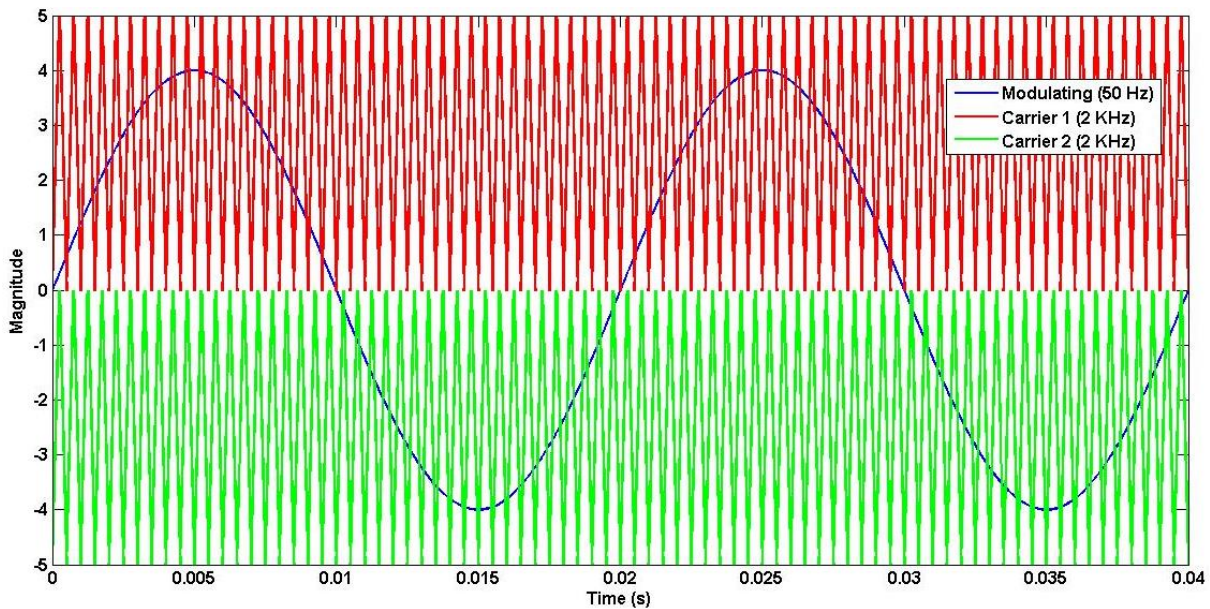
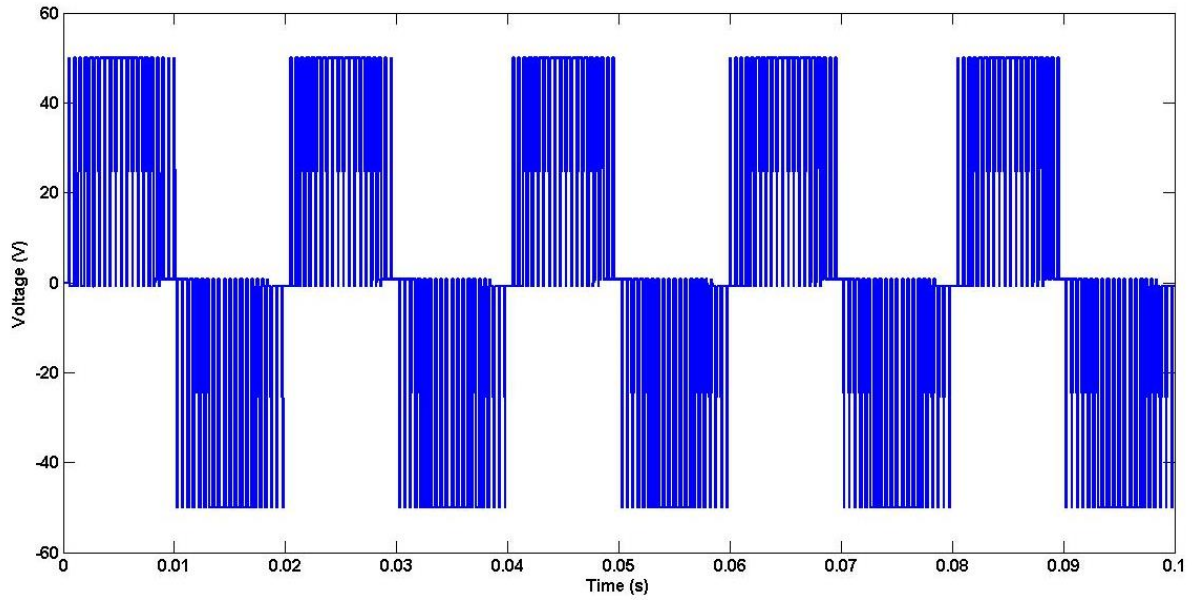
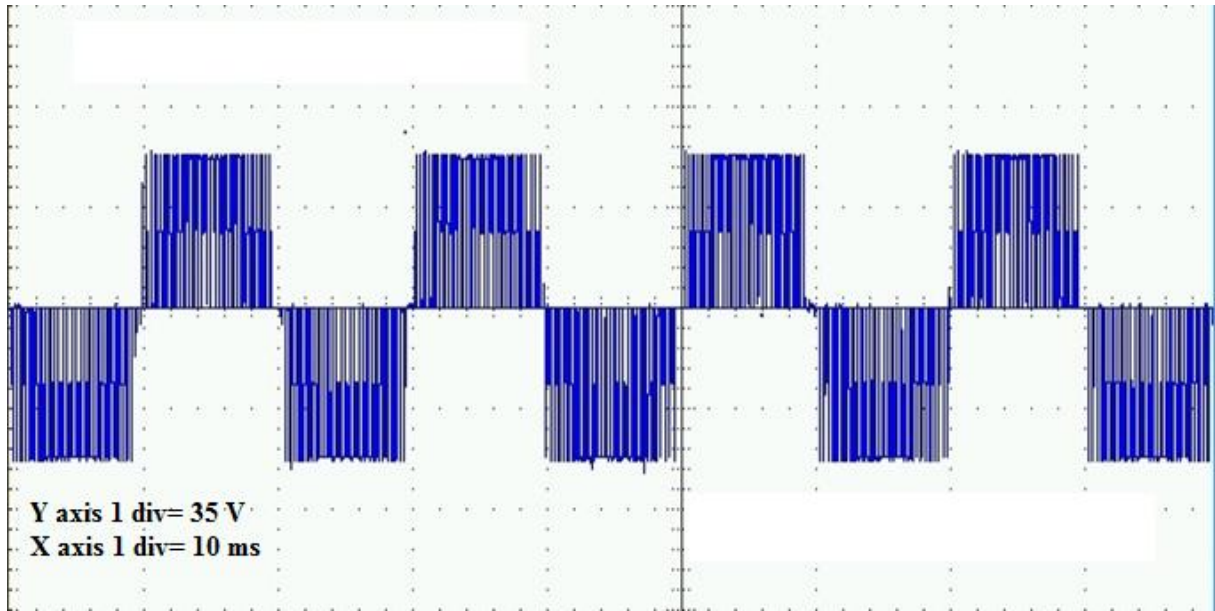


Fig. 4.8 Control scheme for single-phase three-level inverter



(a)



(b)

Fig. 4.9 Output phase voltage of three-level inverter (a) Simulation result (b) Hardware result

Comparison of figure 4.9(a) and 4.9(b) prove that the hardware result obtained is a replica of the simulation result. This validates the control signal generation using XSG.

4.6.2 Analysis of Single-phase Five-level VSI

The inverter of figure 4.1(b) can be considered as a cascade connection of two three-level inverters. Hence, the switching scheme is similar. The control signal generation scheme for the five-level inverter is illustrated in figure 4.10. The modulating signal having a 0° phase shift and the two carriers are used to generate the signals for the switches of the left leg of the inverter. The 180° phase-shifted sinusoid is compared with the triangles to provide the firing signals for the right leg. The maximum output voltage is equal to the input dc.

The output voltage obtained is a five level waveform as shown in figure 4.11 (a). The hardware output voltage of the five-level inverter with control signal generated through XSG is shown in figure 4.11(b).

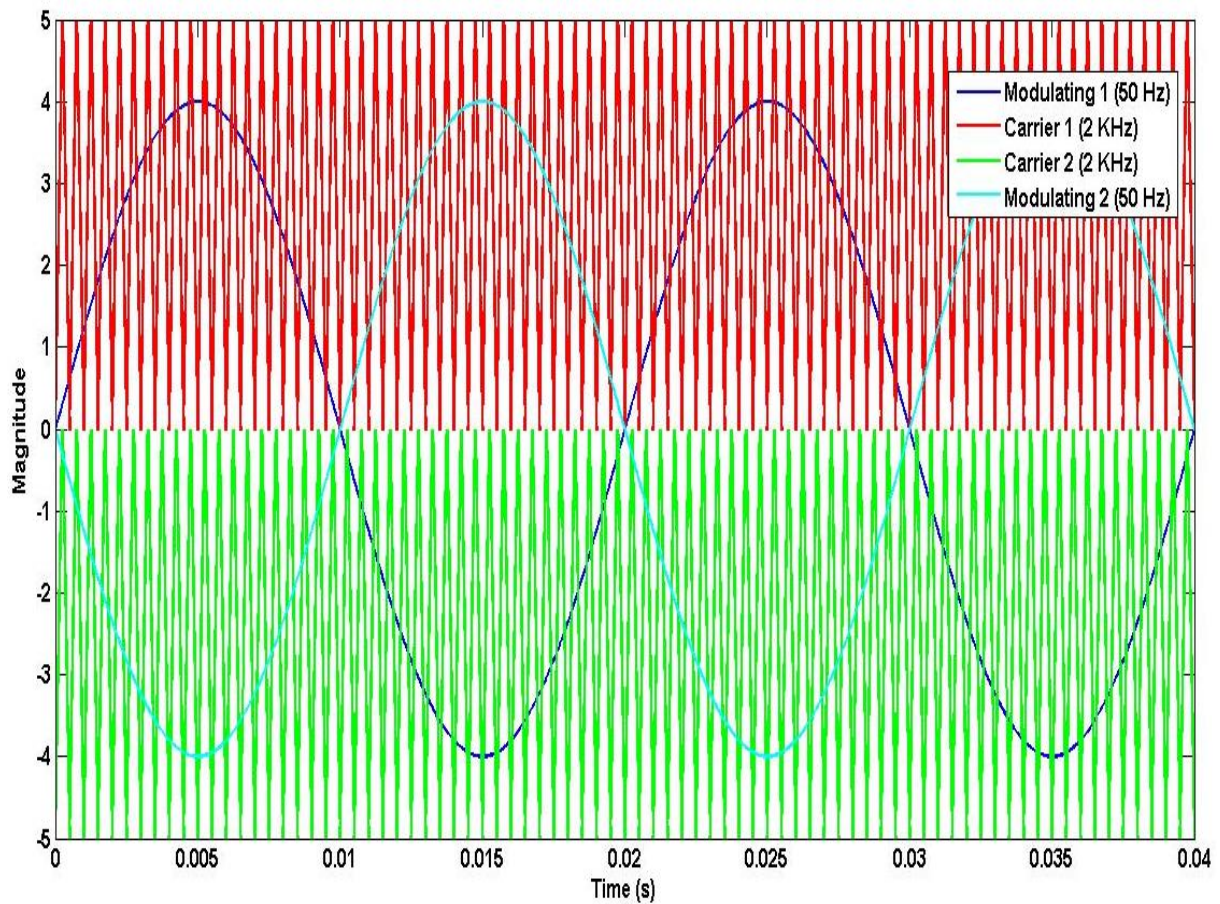
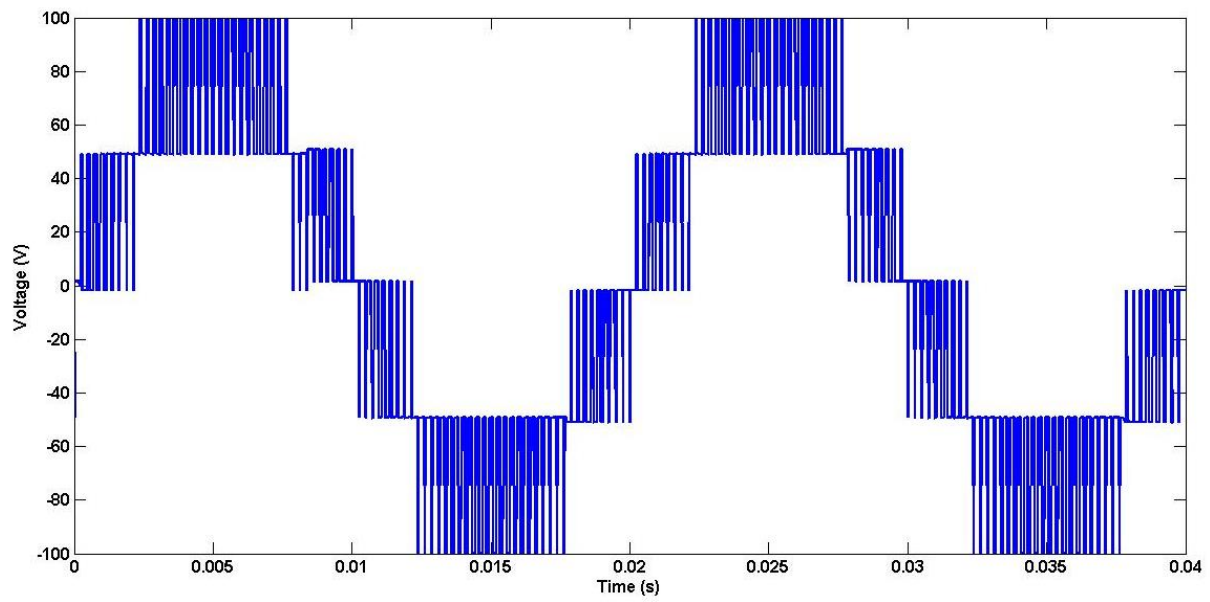
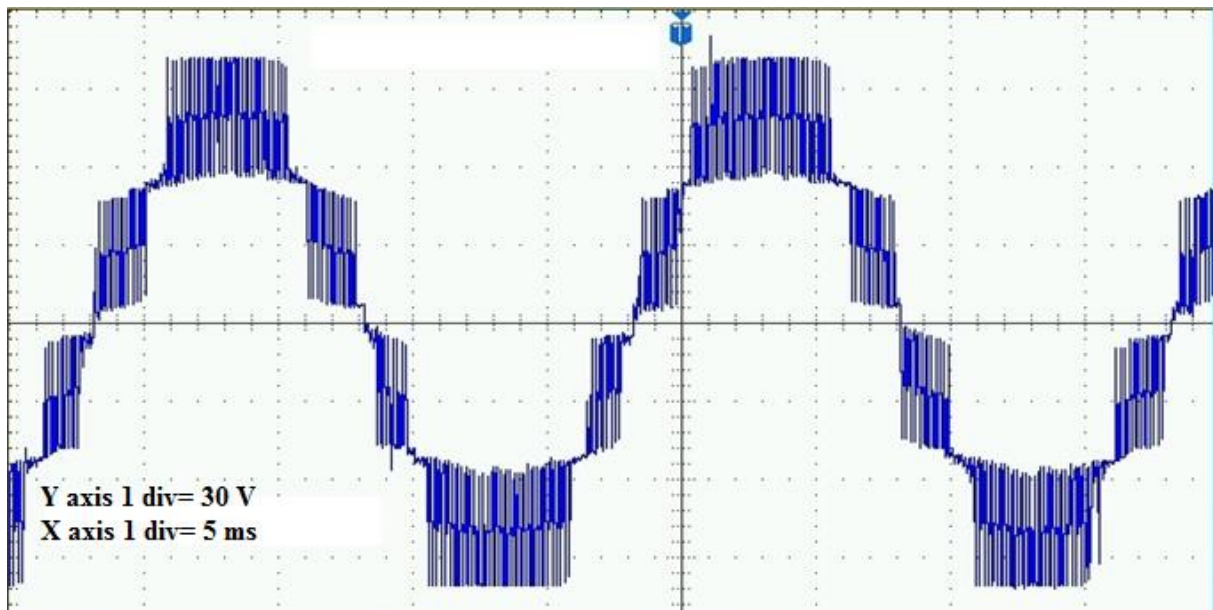


Fig. 4.10 Control scheme for five-level inverter



(a)



(b)

Fig. 4.11 Output phase voltage of five-level inverter (a) Simulation result (b) Hardware result

From the figures 4.11(a) and 4.11(b) it can be observed that the hardware result obtained is a replica of the simulation result. This in turn validates the control signal generation using XSG.

4.6.3 Analysis of Three-phase VSI

For the inverter illustrated in figure 4.2, the switching signals are developed by comparing three 120° shifted sinusoids with a triangular carrier. Comparison of the first sinusoid with the triangle generates the signals for the first leg. If the magnitude of the in phase sine is greater than that of the triangle, the upper switch of the first leg is turned ON. When the condition reverses, the lower switch is actuated. The two switches in a leg act complementary to each other. The second and the third legs are switched using the other two modulating signals, respectively.

The control signal generation scheme for the three-phase inverter is shown in figure 4.12. The output phase voltage and the output line voltage in simulation are obtained as illustrated in figures 4.13(a) and 4.14(a) respectively. The hardware results for the phase output voltage and the line output voltage of the three-phase VSI with control signal generated through XSG are depicted in figures 4.13(b) and 4.14(b), respectively.

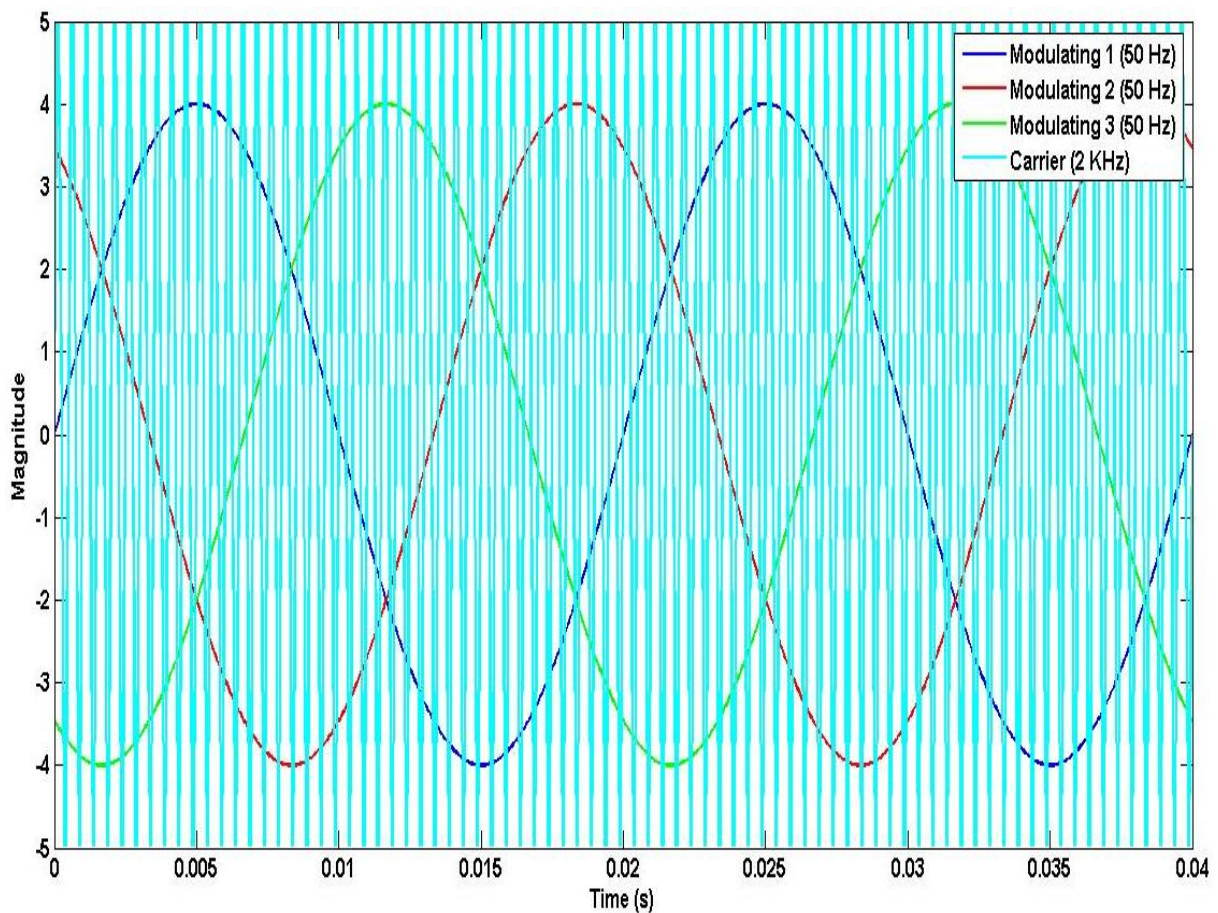
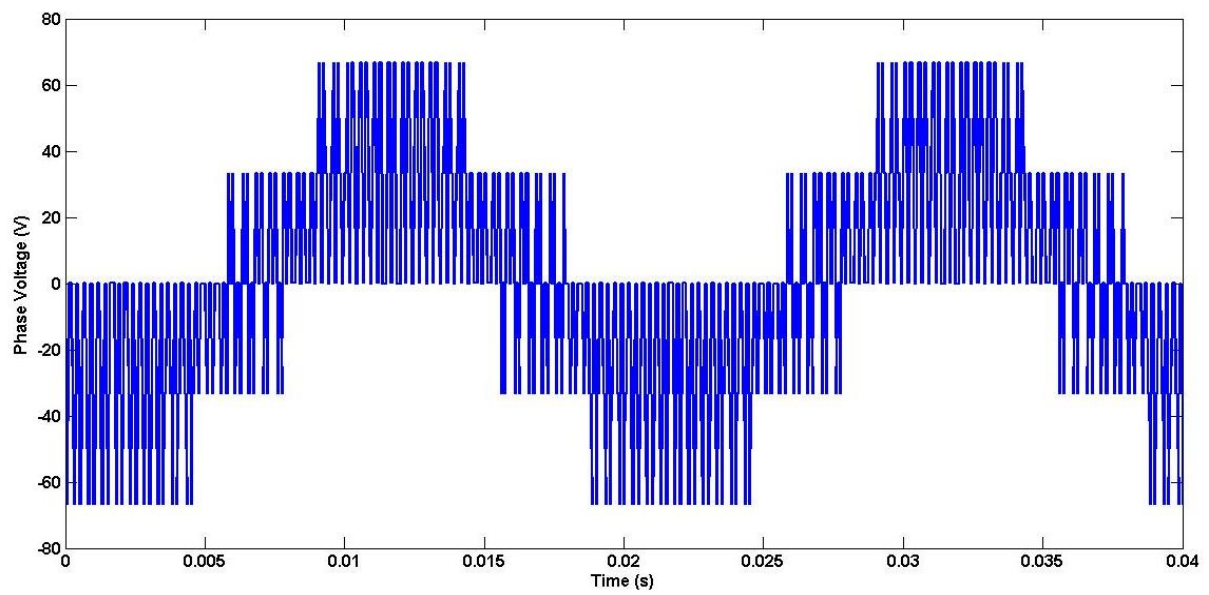
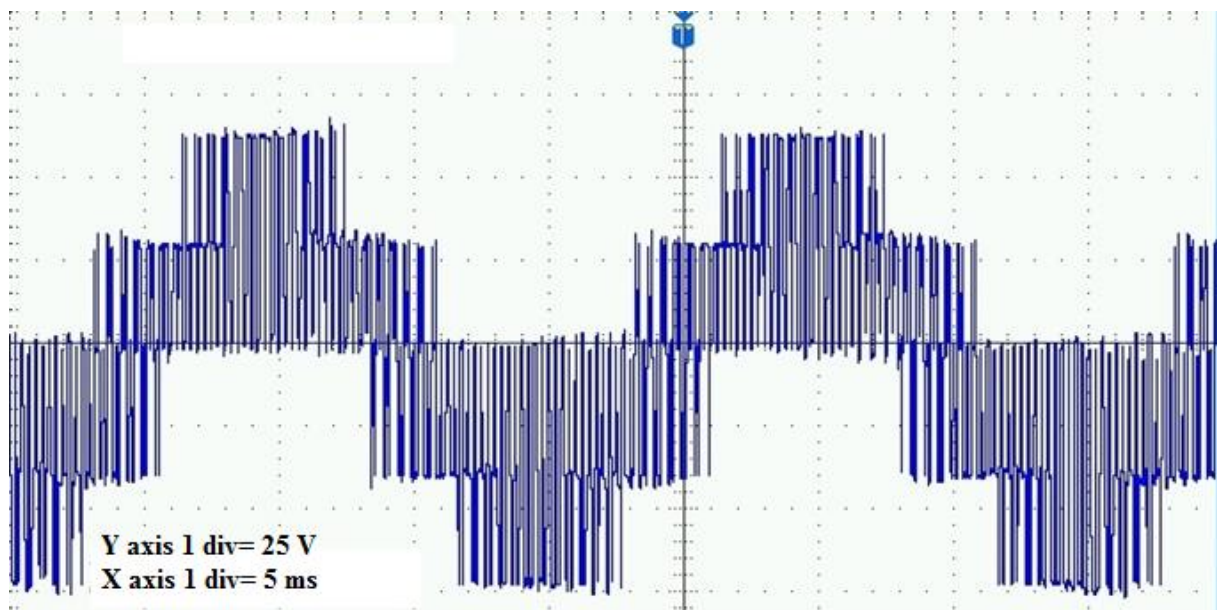


Fig. 4.12 Control scheme for three-phase VSI

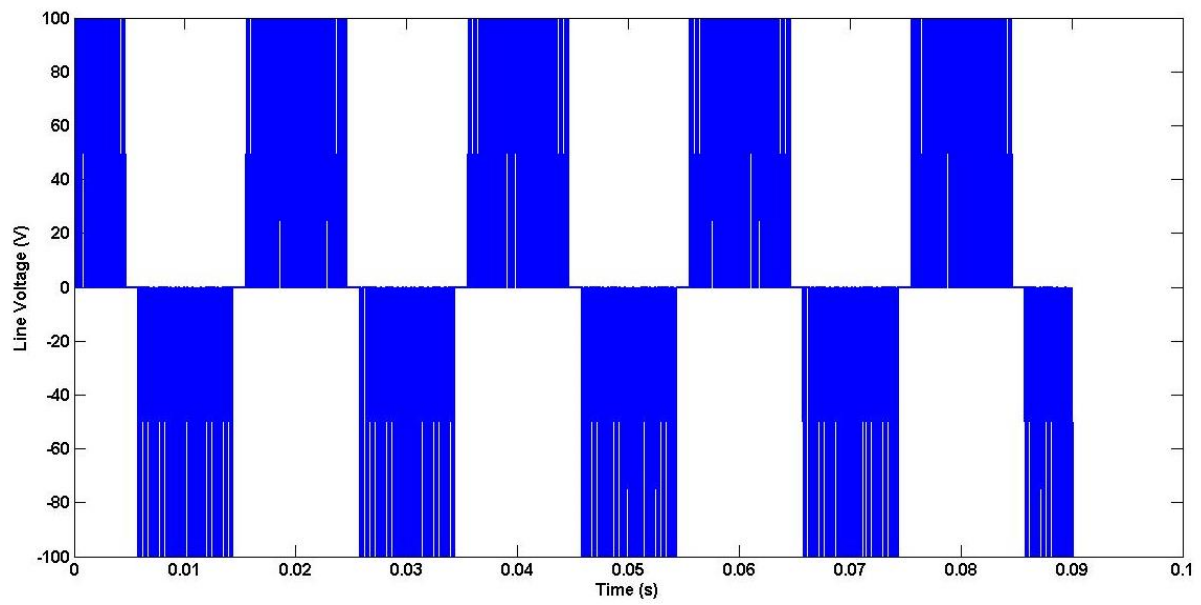


(a)

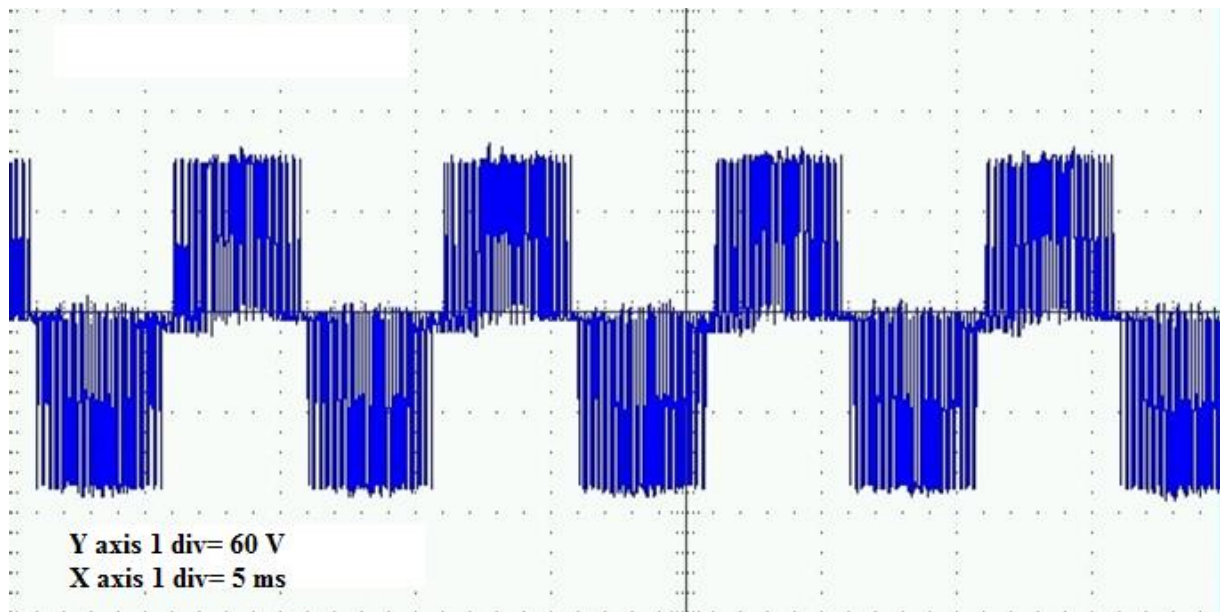


(b)

Fig. 4.13 Output phase voltage of three-phase VSI (a) Simulation result (b) Hardware result



(a)



(b)

Fig. 4.14 Output line voltage of three-phase VSI (a) Simulation result (b) Hardware result

It can be observed that the hardware results obtained are a replica of the simulation results. This validates the control signal generation using XSG.

4.6.4 DFIG system with rotor excited by three-phase inverter

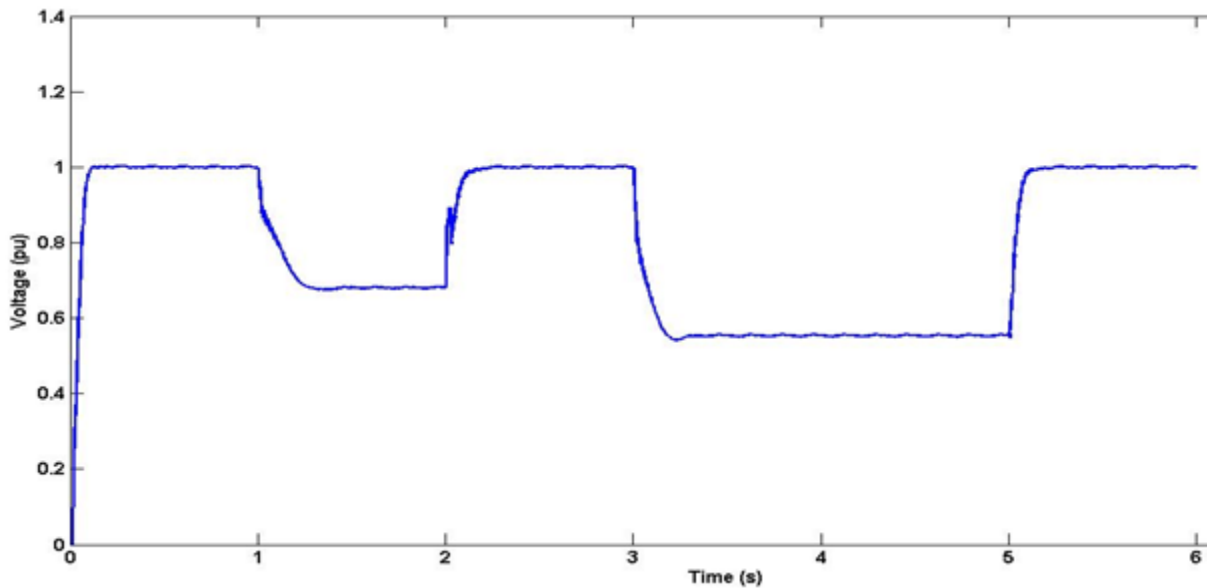
The three-phase VSI illustrated in figure 4.7(a) has been used to excite the rotor of a DFIG referred to in this work as ‘DFIG-2.’ Parameters of DFIG-2 have been mentioned in Appendix A. The three-phase VSI can be operated at a frequency that ensures the stator voltage frequency is 50 Hz irrespective of the generator shaft speed. Such control is achievable because in a four pole DFIG, the frequency of stator voltage (f_s), the frequency of rotor voltage (f_r) and the mechanical rotor speed (N_m) are related as follows:

$$f_s = f_r + \frac{N_m}{30} \quad (4.1)$$

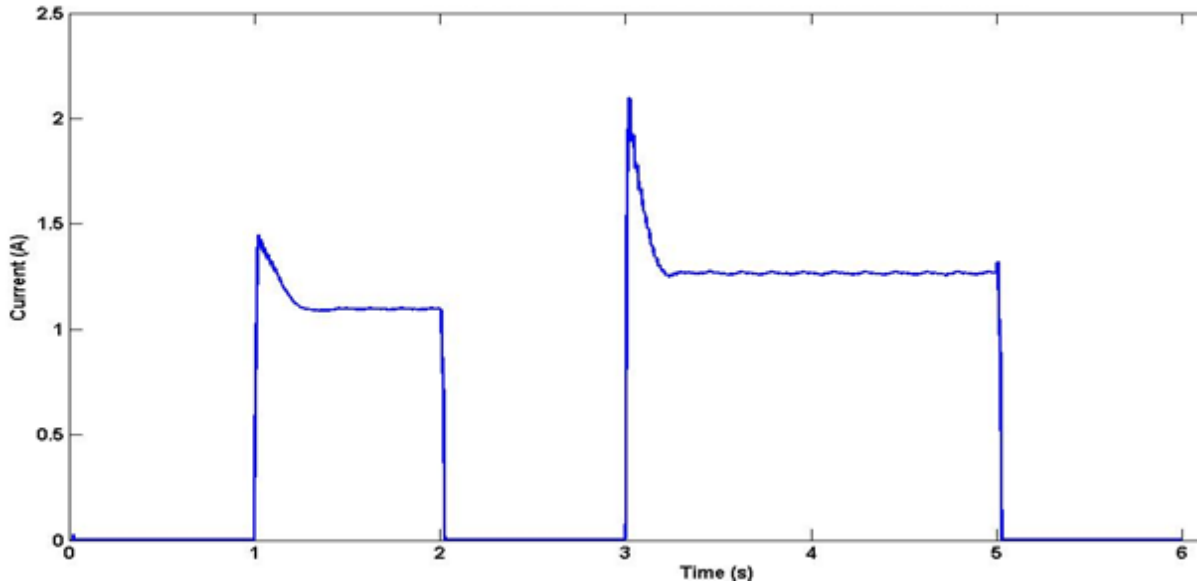
Since the rotor is fed by a three-phase inverter, the rotor voltage frequency can be easily varied by exercising suitable control on the inverter. Hence rotor voltage frequency is changed according to the changing mechanical rotor speed such that the stator voltage frequency remains constant.

The parameters of DFIG used in this work are mentioned in the Appendix A. For the duration of the experimentation, the DFIG stator had been connected to a purely resistive load between one second and two second. An R-L load of power factor 0.9 had been connected to the stator between three second and five second. Other than the mentioned durations, the DFIG is made to run on no load.

Figure 4.15 is an illustration of the stator phase A output voltage in pu and load current of the DFIG with rotor excited via three-phase inverter.



(a)



(b)

Fig. 4.15 Three-phase VSI fed DFIG (a) Phase A stator voltage (b) Load current

The output of the stator is a balanced three phase voltage with a frequency of 50 Hz. For a rotor phase voltage of 17 V, the DFIG no-load phase voltage is 219 V at steady state. The voltage falls to about 149 V when the resistive load is connected. The resistive load draws a current of 1.10 A at steady state. The stator voltage attains a value of 120 V with the application of RL load. The RL load draws a current equal to 1.26 A at steady state.

4.7 CONCLUSION

This chapter elucidates a simple method for the quick development of PECs. A DFIG standalone system has been presented as a practical application of XSG based converters in the domain of renewables. It has been conclusively demonstrated via hardware that the Simulink-based XSG platform is a diligent tool for the generation of control schemes. The work is facilitated by an automatic HDL code generation made possible by XSG.

Two topologies of single-phase inverters and a three-phase inverter have been realised in simulation as well as hardware. A detailed explanation of the XSG-based technique used for the construction of the triangular and the sinusoidal signal has been presented. This chapter is especially useful for researchers working to develop PECs of various topologies at different frequencies of operation. Moreover, this work can also serve as a tutorial for researchers who are new to the field of converter fabrication. Such detailed description is usually absent in the literature invoking XSG platform for converter fabrication. The usage of XSG nullifies the

need of learning programming techniques, thereby speeding up hardware prototyping of converters. This is a huge advantage in terms of saving time as well as increased flexibility.

The absolute correspondence between the simulation results and the hardware results completely justify the ease of usage by invoking XSG.

The contribution presented in this chapter is as follows:

- It has been established that for a standalone four pole DFIG system with rotor fed by a three-phase inverter, the frequency of stator voltage (f_s), the frequency of rotor voltage (f_r) and the mechanical rotor speed (N_m) are related as follows:

$$f_s = f_r + \frac{N_m}{30}$$

Hence, by varying the frequency of output voltage of the three-phase inverter according to the changing DFIG shaft speed, the stator voltage frequency can be held constant.

- An easy to construct, less-expensive and rapid prototyping method for power electronic converter fabrication using XSG has been described.
- The novelty of this work lies in the detailed description of the methods for generating the modulating signal as well as the level-shifted or phase-shifted carrier signals at different frequencies.
- This work facilitates the readers and researchers who are not experts in programming to familiarize themselves with XSG and henceforth develop various converter topologies.

CHAPTER 5

ANALYSIS OF GRID-CONNECTED DFIG SYSTEM USING RATIONAL METHODS AND GENETIC ALGORITHM

5.1 INTRODUCTION

This chapter details out the computation of direct axis and quadrature axis reference rotor currents I_{rq} and I_{rd} of a doubly fed induction generator (DFIG), corresponding to three distinct cases which are as follows:

- a) Maximum active power and minimum losses
- b) Minimum reactive power and minimum losses
- c) Maximum active power and minimum reactive power.

The original work carried out in this chapter relates to the computation of rotor currents corresponding to cases (b) and (c). The other novelty of this work is the application of genetic algorithm (GA) for determining the optimal rotor current values corresponding to all the aforementioned three cases. Application of MATLAB GA toolbox nullifies the need of manual computations and is an extremely flexible and easy method of determining the optimal values. The efficiency and power factor of the system owing to all the three cases using rational methods as well as GA have been compared and analyzed.

A MATLAB script file of the equations derived from the aforementioned conditions has been constructed. Results are obtained and validated for all the above-mentioned cases.

5.2 STEADY STATE DFIG MODEL

Figure 5.1 illustrates the block diagram of the system. The circuit diagram of the DFIG is shown in figure 5.2 [98]. It is the per phase equivalent of a grid connected DFIG under steady state conditions. This model is valid for both sub-synchronous operation and super-synchronous operation.

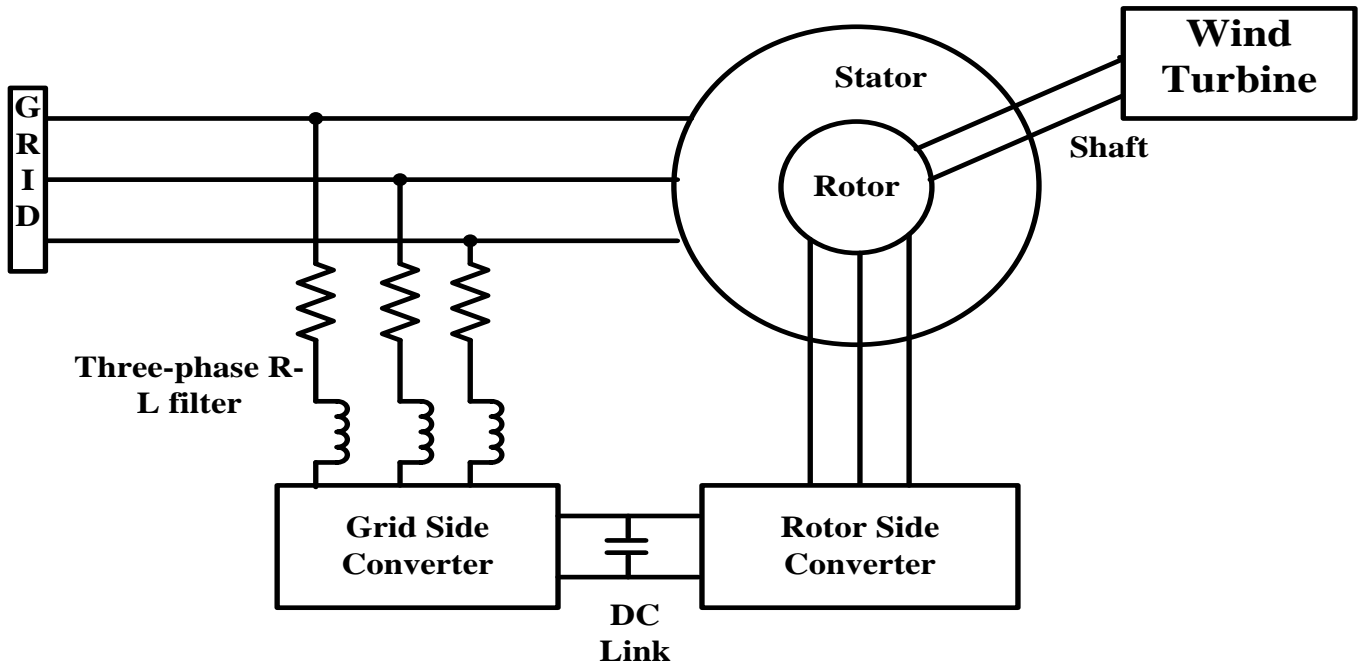


Fig 5.1 Block diagram representation of a grid connected DFIG with back-to-back converters

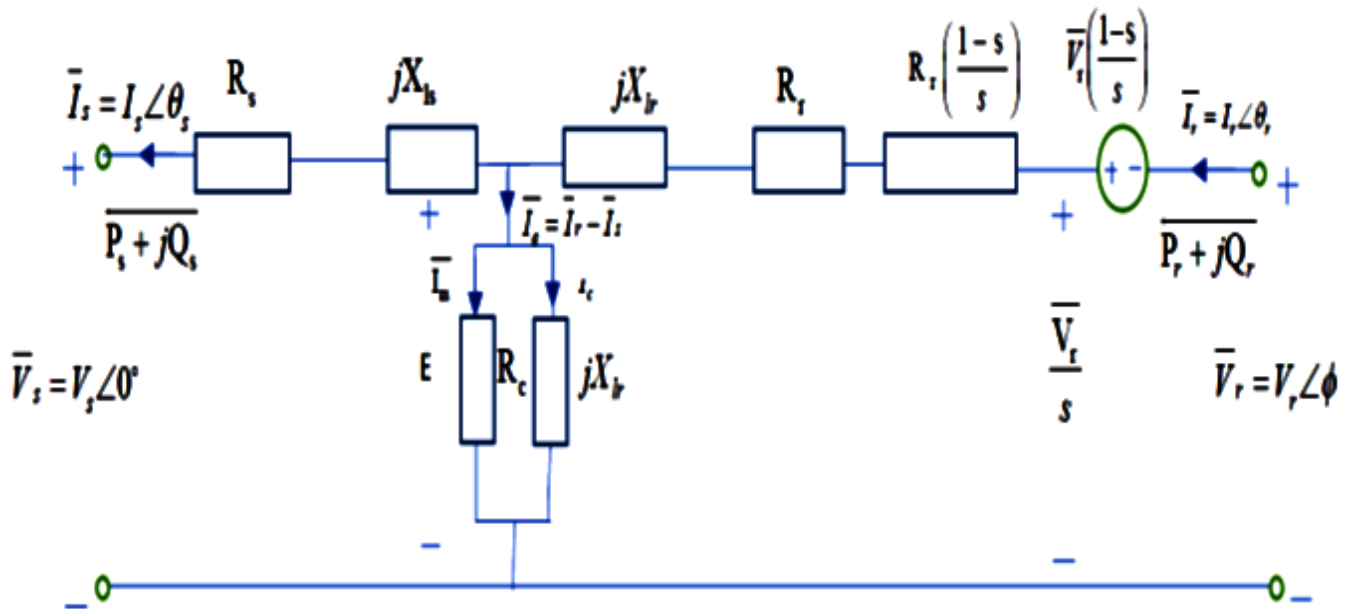


Fig. 5.2 Per-phase equivalent circuit of a grid based DFIG operating in steady state

By applying KVL, equations for stator voltages and currents and rotor voltages and currents are written.

From figure 5.2, the basic equations are as follows:

$$V_s = Z_m I_e - (R_s + jX_s) I_s \quad (5.1)$$

$$Z_m = \frac{R_c X_m}{R_c^2 + X_m^2} (X_m + jR_c) \quad (5.2)$$

$$I_e = I_r - I_s \quad (5.3)$$

Equation (5.1) gives the expression of the stator voltage. This equation, along with equations (5.2) and (5.3), form the crux of the further derivations.

5.3 PROCEDURE TO DETERMINE OPTIMAL ROTOR CURRENT COMMANDS

In the equation (5.1), the real parts and the imaginary parts are segregated. For further calculations, the different parts are assigned new variables. The process is executed as shown by equations (5.4) and (5.5).

$$\begin{aligned} &-(B_6 R_s + A_6 X_m) I_s^R + (B_6 X_{ls} + A_6 R_c) I_s^I = \\ &-A_6 X_m I_r^R + A_6 R_c I_r^I + B_6 V_s \end{aligned} \quad (5.4)$$

$$\begin{aligned} &(B_6 X_{ls} + A_6 R_c) I_s^R + (B_6 R_s + A_6 X_m) I_s^I = \\ &A_6 R_c I_r^R + A_6 X_m I_r^I \end{aligned} \quad (5.5)$$

In all the steps mentioned subsequently, aforementioned procedure is adopted.

A. The stator current as well as the rotor current are split into their individual real component and imaginary component. Equations are framed with the rotor current as the independent variable.

$$I_s = I_s^R + jI_s^I \quad (5.6)$$

$$I_r = I_r^R + jI_r^I \quad (5.7)$$

$$I_s^R = \frac{1}{C_6} (D_6 I_r^R - E_6 I_r^I + F_6) \quad (5.8)$$

$$I_s^I = \frac{1}{C_6} (E_6 I_r^R + D_6 I_r^I + G_6) \quad (5.9)$$

Where

$$A_6 = (R_c X_m), \quad B_6 = (R_c)^2 + (X_m)^2, \quad C_6 = (B_6 R_s + A_6 X_m)^2 + (B_6 X_{ls} + A_6 R_c)^2,$$

$$D_6 = A_6 B_6 (A_6 + R_c X_{ls} + R_s X_m), \quad E_6 = A_6 B_6 (R_c R_s - X_m X_{ls}), \quad F_6 = -B_6 V_s (B_6 R_s + A_6 X_m),$$

$$G_6 = B_6 V_s (B_6 X_{ls} + A_6 R_c)$$

The stator currents are expressed in terms of rotor currents, as expressed by equations (5.6), (5.7), (5.8) and (5.9).

B. The total output active power (P_m) is expressed as a function of the rotor current. The expression for P_m is obtained by computing stator active power (P_s), rotor active power (P_r), core loss (P_{core}) and copper loss (P_{Cu}). This operation will provide an equation with the real part and imaginary part of rotor current as the independent variables.

$$\begin{aligned} P_s &= 3 \operatorname{Re}(\bar{V}_s \bar{I}_s^*) \\ &= 3 V_s I_s^R \\ &= 3 \frac{V_s}{C_6} (D_6 I_r^R - E_6 I_r^I + F_6) \end{aligned} \quad (5.10)$$

Rotor voltage equation is needed for computation of rotor active power. It is shown by equation (5.11).

$$\frac{\bar{V}_r}{s} = \bar{V}_s + (R_s + jX_{ls}) \bar{I}_s + \left(\frac{R_r}{s} + jX_{lr} \right) \bar{I}_r \quad (5.11)$$

Substituting the values from (5.6), (5.7), (5.8) and (5.9) into (5.11), following expression is obtained:

$$\begin{aligned} \bar{V}_r &= V_r^R + j V_r^I \\ &= \left[\left(\frac{s}{C_6} H_6 + R_r \right) I_r^R - \left(\frac{s}{C_6} I_6 + sX_{lr} \right) I_r^I + \frac{D_6}{C_6} s V_s \right] \\ &\quad + j \left[\left(\frac{s}{C_6} I_6 + sX_{lr} \right) I_r^R + \left(\frac{s}{C_6} H_6 + R_r \right) I_r^I + \frac{s}{C_6} K_6 \right] \end{aligned} \quad (5.12)$$

Where

$$H_6 = A_6 B_6 [A_6 R_s + X_m (R_s^2 + X_{ls}^2)], \quad I_6 = A_6 B_6 [A_6 X_{ls} + R_c (R_s^2 + X_{ls}^2)], \quad K_6 = A_6 B_6 V_s (R_c R_s - X_m X_{ls})$$

Equation (5.12) gives rotor voltage purely in terms of real and imaginary rotor current commands. Rotor active power is computed as follows:-

$$\begin{aligned} P_r &= 3 \operatorname{Re}(\bar{V}_r \bar{I}_r^*) \\ &= 3 (V_r^R I_r^R + V_r^I I_r^I) \\ &= 3 \{ L_6 [(I_r^R)^2 + (I_r^I)^2] + \frac{D_6}{C_6} s V_s I_r^R + \frac{s}{C_6} K_6 I_r^I \} \end{aligned} \quad (5.13)$$

Where

$$L_6 = \frac{s}{C_6} H_6 + R_r$$

Equations (5.10) and (5.13) are expressions for stator active power and rotor active power respectively. The machine losses are calculated as mentioned below:

$$\begin{aligned}
P_{cu} &= 3[(I_s^R)^2 + (I_s^I)^2]R_s + 3[(I_r^R)^2 + (I_r^I)^2]R_r \\
&= \frac{3}{C_6^2} \{M_6[(I_r^R)^2 + (I_r^I)^2] + N_6 I_r^R + P_6 I_r^I + Q_6\}
\end{aligned} \tag{5.14}$$

Where

$$\begin{aligned}
M_6 &= (D_6^2 + E_6^2)R_s + C_6^2 R_r, \quad N_6 = 2(E_6 G_6 + D_6 F_6)R_s, \quad P_6 = 2(D_6 G_6 - E_6 F_6)R_s, \quad Q_6 = (F_6^2 + G_6^2)R_s \\
\bar{I}_c &= I_c^R + jI_c^I \\
&= \frac{\bar{E}}{R_c} \\
&= \frac{1}{R_c} [\bar{V}_s + (R_s + jX_{ls})\bar{I}_s].
\end{aligned} \tag{5.15}$$

The formula for core loss current is yielded by equation (5.15).

$$\begin{aligned}
P_{core} &= 3[(I_c^R)^2 + (I_c^I)^2]R_c \\
&= \frac{3}{R_c C_6^2} [R_6(D_6^2 + E_6^2)\{(I_r^R)^2 + (I_r^I)^2\} \\
&\quad + T_6 I_r^R + U_6 I_r^I + V_6]
\end{aligned} \tag{5.16}$$

Where

$$\begin{aligned}
R_6 &= R_s^2 + X_{ls}^2, \quad T_6 = \frac{N_6}{R_s} R_6 + 2C_6 V_s (D_6 R_s - E_6 X_{ls}), \quad U_6 = \frac{P_6}{R_s} R_6 - 2C_6 V_s (E_6 R_s + D_6 X_{ls}), \\
V_6 &= \frac{Q_6}{R_s} R_6 + 2C_6 V_s (F_6 R_s - G_6 X_{ls}) + C_6^2 V_s^2
\end{aligned}$$

Equations (5.14) and (5.16) are expressions for copper loss and core loss respectively. The total output active power (P_m) can be related to rotor speed using a cubic relation.

$$\begin{aligned}
P_m &= K_{opt} \omega_m^3 \\
&= P_s - P_r + P_{Cu} + P_{core} \\
&= W_6 (I_r^R)^2 + W_6 (I_r^I)^2 + X_6 I_r^R + Y_6 I_r^I + Z_6
\end{aligned} \tag{5.17}$$

Where

$$\begin{aligned}
W_6 &= \frac{3}{C_6^2} \left[-C_6^2 L_6 + M_6 + \frac{R_6 (D_6^2 + E_6^2)}{R_c} \right], \quad X_6 = \frac{3}{C_6^2} \left[C_6 D_6 V_s (1-s) + N_6 + \frac{T_6}{R_c} \right] \\
Y_6 &= \frac{3}{C_6^2} \left(-C_6 E_6 V_s - C_6 K_6 s + P_6 + \frac{U_6}{R_c} \right), \quad Z_6 = \frac{3}{C_6^2} \left(C_6 F_6 V_s + Q_6 + \frac{V_6}{R_c} \right)
\end{aligned}$$

Equation (5.17) yields the condition of maximum active power.

C. Core loss and copper loss are added. The sum is differentiated with respect to the real part of rotor current and subsequently equated to zero. This operation is impemented to obtain another equation in terms of the real part and imaginary part of rotor current.

$$\frac{\partial(P_{cu} + P_{core})}{\partial I_r^R} = 0. \quad (5.18)$$

The partial derivative of equation (5.17) with respect to the real component of rotor current yields the following equation:-

$$\frac{\partial I_r^I}{\partial I_r^R} = -\frac{2W_6 I_r^R + X_6}{2W_6 I_r^I + Y_6}. \quad (5.19)$$

The derivative value obtained from (5.19) is substituted in the expression of (5.18). Re-arranging the resultant expression leads to the subsequent equation:

$$A' I_r^R + B' I_r^I + C' = 0 \quad (5.20)$$

Where

$$A' = 2Y_6 \left[M_6 R_c + R_6 (D_6^2 + E_6^2) \right] - 2W_6 (P_6 R_c + U_6), \quad B' = -2X_6 \left[M_6 R_c + R_6 (D_6^2 + E_6^2) \right] + 2W_6 (N_6 R_c + T_6),$$

$$C' = Y_6 (N_6 R_c + T_6) - X_6 (P_6 R_c + U_6)$$

Equation (5.20) can be used to re-arranged as follows:

$$I_r^I = -\frac{A' I_r^R + C'}{B'} \quad (5.21)$$

Equation (5.21) yields the condition of minimum losses.

D. Stator reactive power and rotor reactive power are added. The sum is differentiated with respect to the imaginary part of rotor current. The resultant equation is put to zero. This operation is the mathematical equivalent of reactive power minimization. It yields the third equation in terms of the real part and imaginary part of rotor current.

$$Q_s = 3 \text{Im}(V_s I_s^*)$$

$$= 3V_s I_s^I \quad (5.22)$$

$$= 3V_s \frac{1}{C_6} (E_6 I_r^R + D_6 I_r^I + G_6)$$

$$\frac{\partial Q_s}{\partial I_r^I} = 3 \frac{V_s}{C_6} (E_6 \frac{\partial I_r^R}{\partial I_r^I} + D_6) \quad (5.23)$$

$$\begin{aligned} Q_r &= 3 \text{Im}(\bar{V}_r \bar{I}_r^*) \\ &= 3(-V_r^R I_r^I + V_r^I I_r^R) \\ &= 3 \left[- \left(\frac{s}{C_6} H_6 + R_r \right) I_r^R \right. \\ &\quad \left. + \left(\frac{s}{C_6} I_6 + sX_{lr} \right) I_r^I - \frac{D_6}{C_6} sV_s \right] I_r^I \\ &\quad + 3 \left[\left(\frac{s}{C_6} I_6 + sX_{lr} \right) I_r^R \right. \\ &\quad \left. + \left(\frac{s}{C_6} H_6 + R_r \right) I_r^I + \frac{s}{C_6} K_6 \right] I_r^R. \end{aligned} \quad (5.24)$$

Equations (5.22) and (5.24) are the expressions of stator reactive power and rotor reactive power respectively.

The equation of rotor reactive power transforms to:

$$\begin{aligned} Q_r &= 3(l_6 I_r^I - m_6) I_r^I \\ &\quad + 3(l_6 I_r^R + n_6) I_r^R \end{aligned} \quad (5.25)$$

Where

$$l_6 = \frac{s}{C_6} I_6 + sX_{lr}, \quad m_6 = \frac{D_6}{C_6} sV_s, \quad n_6 = \frac{sK_6}{C_6}$$

Equation (5.25) is obtained by altering equation (5.24).

$$\begin{aligned} \frac{\partial Q_r}{\partial I_r^I} &= 3[2l_6 I_r^I - m_6] \\ &\quad + 3[2l_6 I_r^R \frac{\partial I_r^R}{\partial I_r^I} + n_6 \frac{\partial I_r^R}{\partial I_r^I}] \end{aligned} \quad (5.26)$$

The partial derivative of equation (5.17) with respect to the imaginary component of rotor current yields the following equation on re-arrangement:

$$\frac{\partial I_r^R}{\partial I_r^I} = \frac{-(2W_6 I_r^I + Y_6)}{2W_6 I_r^R + X_6} \quad (5.27)$$

Equations (5.23) and (5.26) are summed up and put to zero for achieving the condition of minimum reactive power. Equation (5.27) is substituted in the same. The resultant equation is as follows:

$$b_6 I_r^R + c_6 I_r^I + d_6 = 0 \quad (5.28)$$

Where

$$b_6 = -2\left(\frac{V_s}{C_6} D_6 + m_6\right)W_6 - 2l_6 Y_6, \quad c_6 = -2\left(-\frac{V_s}{C_6} E_6 + n_6\right)W_6 + 2l_6 X_6,$$

$$d_6 = -\left(\frac{V_s}{C_6} D_6 + m_6\right)X_6 - \left(-\frac{V_s}{C_6} E_6 + n_6\right)Y_6$$

Equation (5.28) corresponds to the condition of minimum reactive power.

E. One set of optimal rotor current value is obtained by using the equations (5.17) and (5.21) from steps (B) and (C). The values will correspond to the case of maximum active power and minimum losses [98].

$$I_r^R = \frac{-E' \pm \sqrt{(E')^2 - 4D'F'}}{2D'} \quad (5.29)$$

Where

$$D' = W_6 + W_6 \frac{(A')^2}{(B')^2}, \quad E' = W_6 \frac{2A'C'}{(B')^2} + X_6 - Y_6 \frac{A'}{B'}, \quad F' = W_6 \frac{(C')^2}{(B')^2} - Y_6 \frac{C'}{B'} + Z_6 - P_m^*$$

In this case, equations (5.21) and (5.29) form the pair of solutions.

F. Another set of optimal rotor current value is obtained by using the equations (5.21) and (5.28) from steps (C) and (D). This value will correspond to the case of minimum losses and minimum reactive power.

$$I_r^R = -\frac{c_6 C' + d_6 B'}{b_6 B' + c_6 A'} \quad (5.30)$$

In this case, equations (5.21) and (5.30) form the pair of solutions.

G. The third set of optimal rotor current value is obtained by using the equations (5.17) and (5.28) from steps (B) and (D). This value will correspond to the case of maximum active power and minimum reactive power.

$$I_r^R = \frac{-u_6 \pm \sqrt{(u_6)^2 - 4t_6 v_6}}{2t_6} \quad (5.31)$$

Where

$$t_6 = W_6(c_6^2 + b_6^2), \quad u_6 = 2b_6 d_6 W_6 + c_6^2 X_6 - b_6 c_6 Y_6, \quad v_6 = W_6 d_6^2 - c_6 d_6 Y_6 + c_6^2 (Z_6 - P_m^*)$$

In this case, equations (5.28) and (5.31) form the pair of solutions.

H. The efficiency (n) and power factor (pf) are computed as expressed by equations (5.32) and (5.33) respectively.

$$n = \frac{(P_s - P_r)}{P_m^*} \quad (5.32)$$

$$pf = \frac{P_s - P_r}{\sqrt{(P_s - P_r)^2 + (Q_s + Q_r)^2}} \quad (5.33)$$

I. The direct axis rotor command and quadrature axis rotor command for the DFIG are expressed in terms of the optimal values obtained either from step (E) or from step (F) or from step (G). The expressions are given by equations (5.34) and (5.35).

$$I_{rd} = I_r^R \cos \theta_{fs} + I_r^I \sin \theta_{fs} \quad (5.34)$$

$$I_{rq} = -I_r^R \sin \theta_{fs} + I_r^I \cos \theta_{fs} \quad (5.35)$$

$$\theta_{fs} = -a \tan \frac{V_s + I_s^R R_s}{I_s^I R_s} \quad (5.36)$$

θ_{fs} is the angle between the direct axis and the stator axis. Its expression is given in equation (5.36).

J. Three objective functions are formed corresponding to the three distinct cases for GA implementation. Equations (5.37) to (5.39) represent the three functions which are then processed using the GA toolbox of MATLAB.

The objective function $y1$ for the case of maximum active power and minimum losses is represented by equation (5.37).

$$y1 = \frac{0.5}{1 + (P_s - P_r)} + 0.5(P_{core} + P_{Cu}) \quad (5.37)$$

The first component of the aforementioned objective function corresponds to active power maximization while the second component relates to loss minimization. The objective function yields the optimal values of I_r^R and I_r^I , which are subsequently put to use for computing the quantities of concern. The toolbox of GA in MATLAB can only minimize an objective function. Hence to maximize any component of a function, its

reciprocal is added to one and the resultant expression is minimized. The value of 0.5 is the weight assigned to the two components of the objective function. It implies that equal weight is allotted to active power maximization as well as loss minimization.

The objective function y_2 for the case of minimum reactive power and minimum losses is represented by equation (5.38).

$$y_2 = 0.5(P_{core} + P_{Cu}) + 0.5(Q_s + Q_r) \quad (5.38)$$

The first component of the aforementioned objective function corresponds to loss minimization while the second component relates to reactive power minimization. The objective function yields the optimal values of I_r^R and I_r^I , which are subsequently put to use for computing the quantities of concern.

The objective function y_3 for the case of maximum active power and minimum reactive power is represented by equation (5.39).

$$y_3 = \frac{0.5}{1 + (P_s - P_r)} + 0.5(Q_s + Q_r) \quad (5.39)$$

The first component of the aforementioned objective function corresponds to active power maximization while the second component relates to reactive power minimization. The objective function yields the optimal values of I_r^R and I_r^I , which are subsequently put to use for computing the quantities of concern.

The flowchart for the procedure mentioned in Section 5.3 has been illustrated using figure 5.3.

5.4 RESULTS AND ANALYSIS

This section has been segregated under two heads. Sub-section 5.4.1 contains results obtained for a DFIG of low power rating; referred to as ‘DFIG-3’ in this work. DFIG-3 is a machine of 2.2 KW rating. The methods of optimal rotor current command generation discussed in section 5.3 have been validated using simulations carried out on DFIG-3.

Sub-section 5.4.2 contains results obtained by implementing vector control on a DFIG of high power rating; referred to as ‘DFIG-4’ in this work. DFIG-4 is a machine of 2 MW rating. The parameters of DFIG-3 and DFIG-4 have been mentioned in Appendix A.

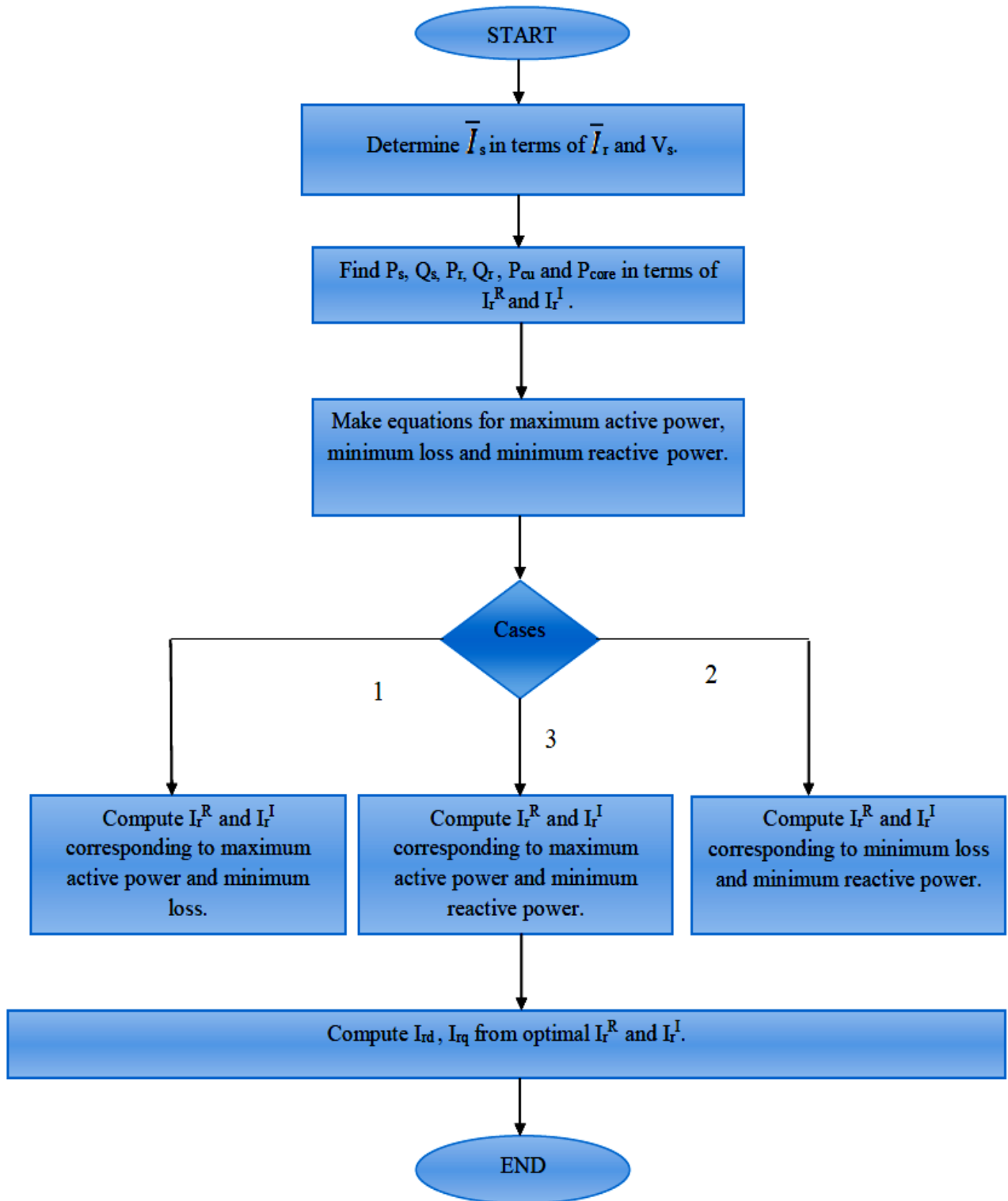


Fig 5.3 Flowchart representation of the methods for optimal rotor current command generation

5.4.1 Results corresponding to the DFIG of low power rating

For validating the methods of optimal rotor current command generation mentioned in section 5.3, simulations have been done on DFIG-3.

For all the succeeding diagrams, the legend is as stated below:

- 1) ----- corresponds to the situation of maximum active power and minimum losses.
- 2) ----- corresponds to the situation of minimum reactive power and minimum losses.
- 3) ----- corresponds to the situation of maximum active power and minimum reactive power.

A. Optimal direct axis rotor current with slip variation

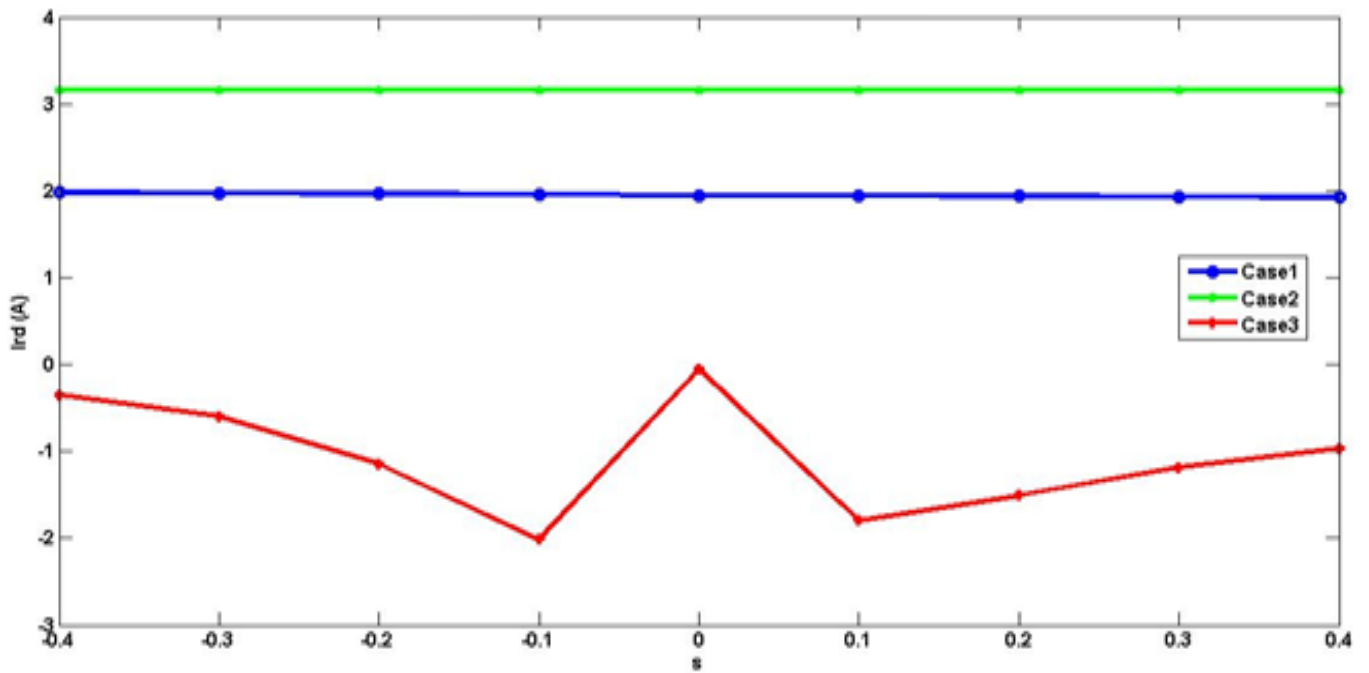


Fig. 5.4 Graph of optimal direct axis rotor current command versus slip, obtained using RM

From figure 5.4, it is evident that the range of optimal I_{rd} values is throughout positive for both case 1 and case 2 in RM. However, the values are negative for case 3. In case 1, there is little variation of I_{rd} with respect to the slip. For case 2, I_{rd} remains almost constant throughout the range of slip. There is a significant variation of I_{rd} in case 3. The I_{rd} values of the three cases are quite different from each other.

For the graph obtained by the application of GA (figure 5.5), the range of optimal I_{rd} values are throughout positive for case 1. There is little variation of I_{rd} . However, the values for case 2 and case 3 are negative in the super-synchronous region (negative slip) and positive in the sub-synchronous region (positive slip).

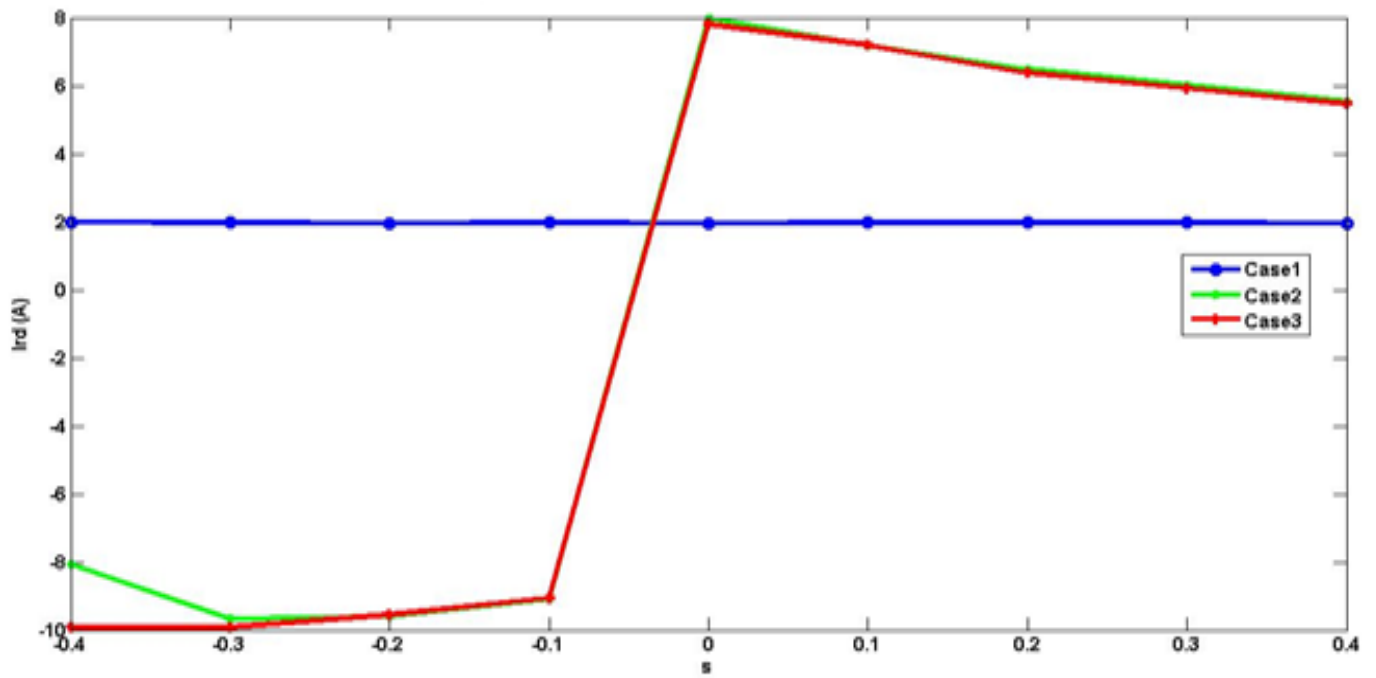


Fig. 5.5 Graph of optimal direct axis rotor current command versus slip, obtained using GA

For case 1, the I_{rd} values corresponding to RM as well as GA are nearly same. However, for case 2 and case 3 the I_{rd} values corresponding to RM are lower as compared to the ones yielded by GA.

B. Optimal quadrature axis rotor current with slip variation

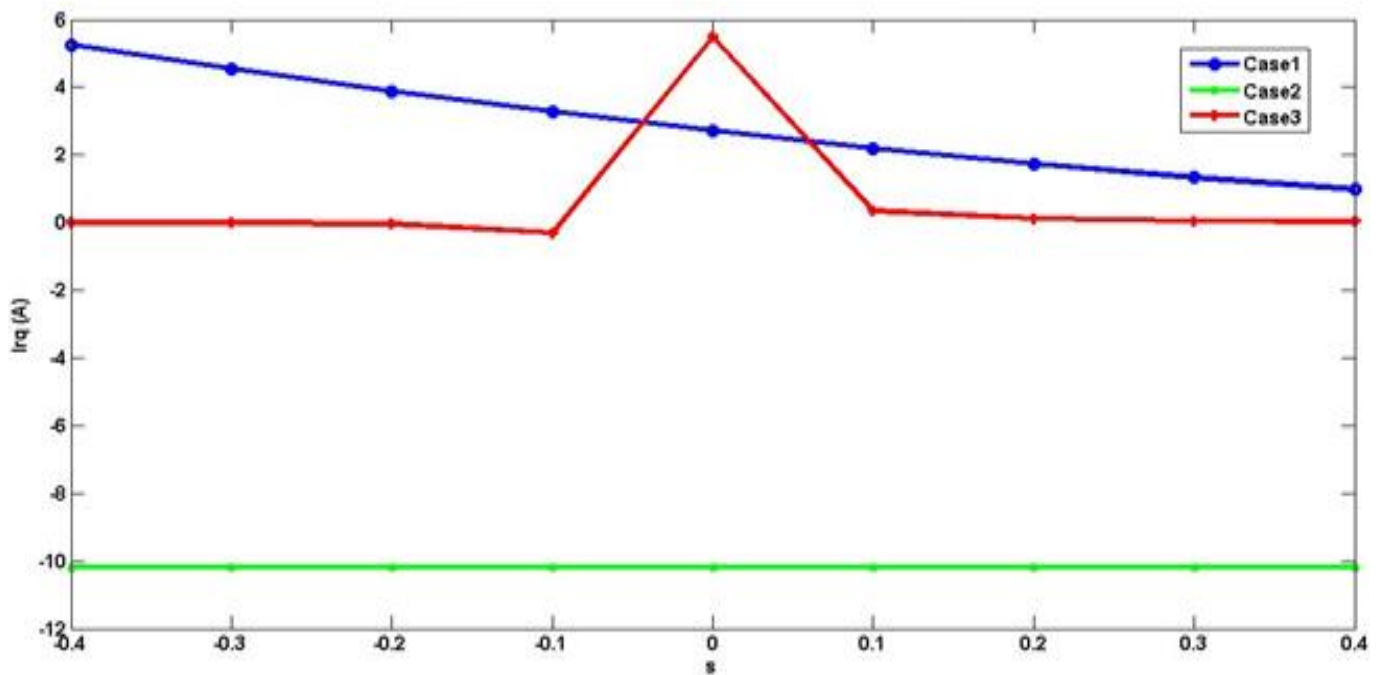


Fig. 5.6 Graph of optimal quadrature axis rotor current command versus slip, obtained using RM

From figure 5.6, it is evident that the range of optimal I_{rq} values is throughout positive for case 1 and throughout negative for case 2 for the RM illustration. The I_{rq} values are positive in the sub-synchronous region and negative in the super-synchronous region for case 3. In case 1, I_{rq} decreases from negative slip to positive slip. For case 2, I_{rq} remains almost constant throughout the range of slip. I_{rq} varies widely in case 3 with a sudden change spike at the synchronous point. The I_{rq} values of the three cases are quite different from each other.

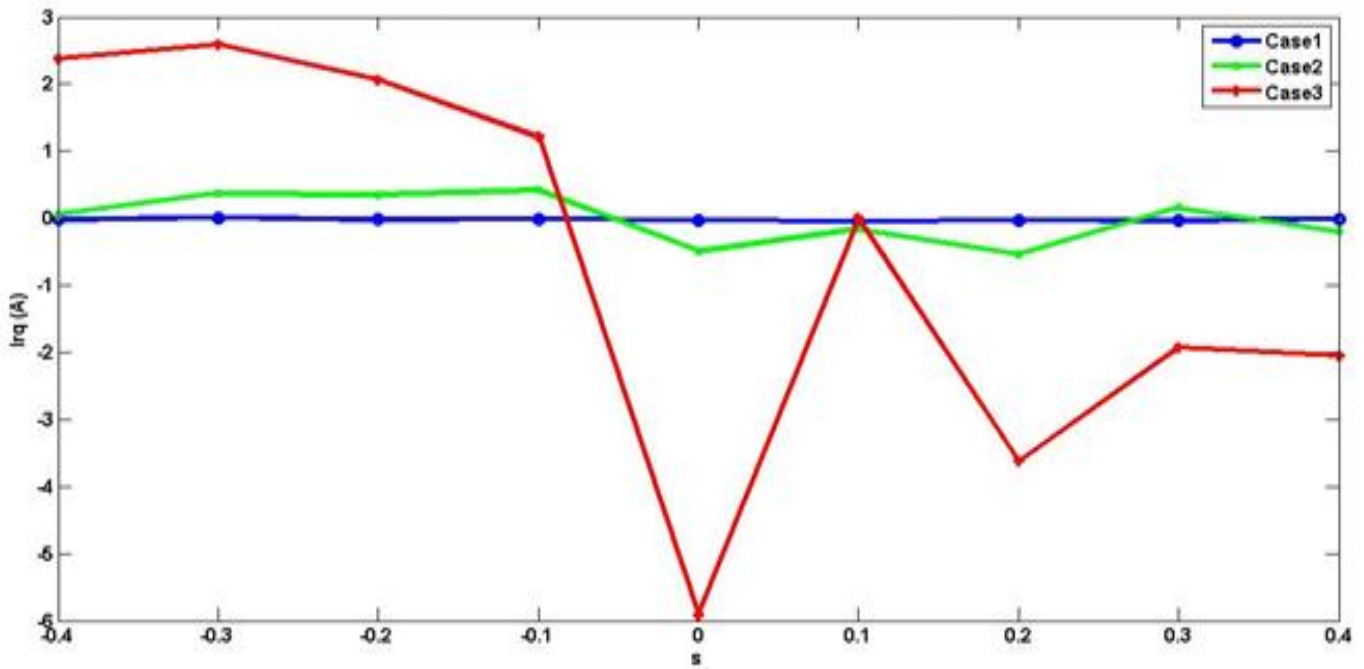


Fig. 5.7 Graph of optimal quadrature axis rotor current command versus slip, obtained using GA

For the graph obtained by the application of GA (figure 5.7), the range of optimal I_{rq} values have a small negative magnitude for case 1. There is very little variation. The I_{rq} values for case 2 and case 3 are positive in most of the super-synchronous region and negative in the sub-synchronous region.

For all the three cases, the I_{rq} values corresponding to RM as well as GA are vastly different. The I_{rq} values corresponding to RM have a larger magnitude as compared to those obtained via GA.

C. DFIG power factor with slip variation

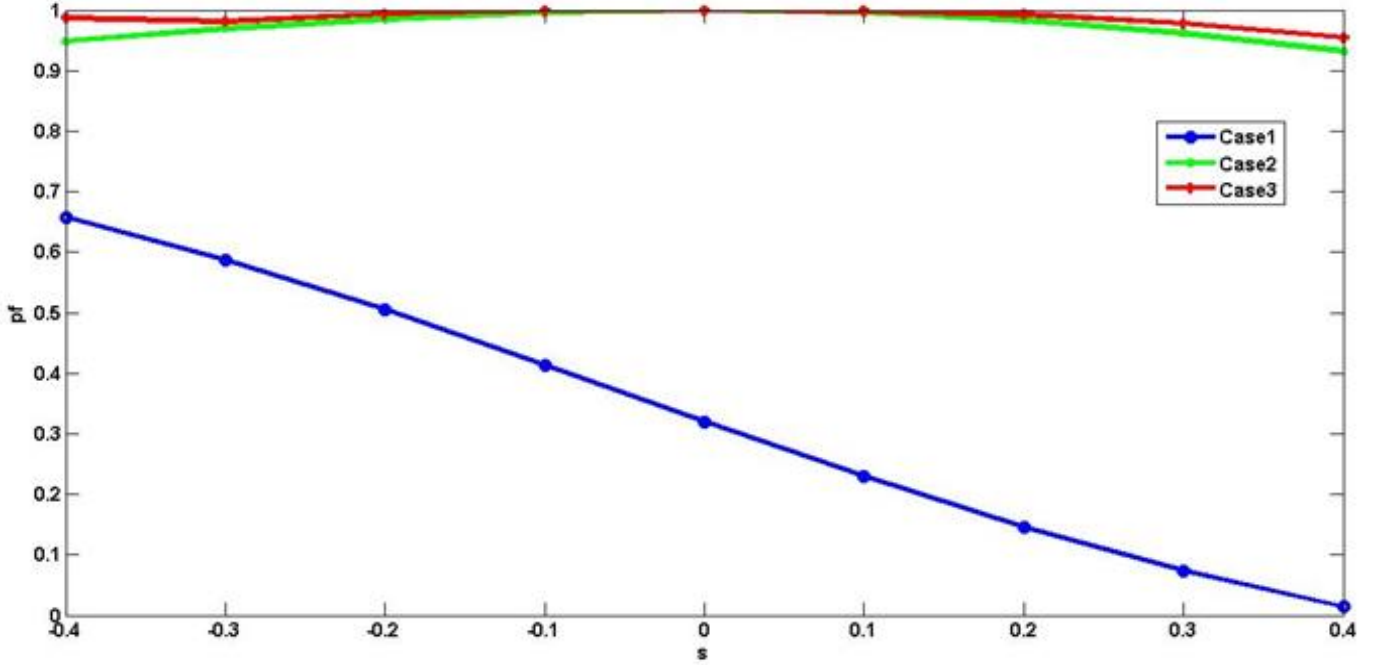


Fig. 5.8 Graph of power factor versus slip, obtained using RM

From figure 5.8, it is interesting to see that the best range of power factor is obtained in case 3 for RM. The power factor values obtained in case 2 are less than 1 in most of the super-synchronous region. In the sub-synchronous region, the power factor achieves its highest value of 1. However, in case 1, the power factor falls progressively from the super-synchronous to the sub-synchronous region. The results clearly validate that reactive power minimization takes place in case 2 and case 3 as expected. Reactive powers are mainly affected by direct axis currents. Since the currents are significantly different in the three cases, therefore the power factor also differs. Better range of power factors are obtained in case 2 and case 3 owing to minimization of reactive power.

For the graph obtained by the application of GA (figure 5.9), the power factor is throughout 1 in case 3. The power factor values obtained in case 2 are low in most of the super-synchronous region. In the sub-synchronous region, the power factor achieves its highest value. In case 1, the power factor has a poor value and remains nearly constant from the super-synchronous to the sub-synchronous region. The results clearly validate that reactive power minimization takes place in case 2 and case 3 as expected.

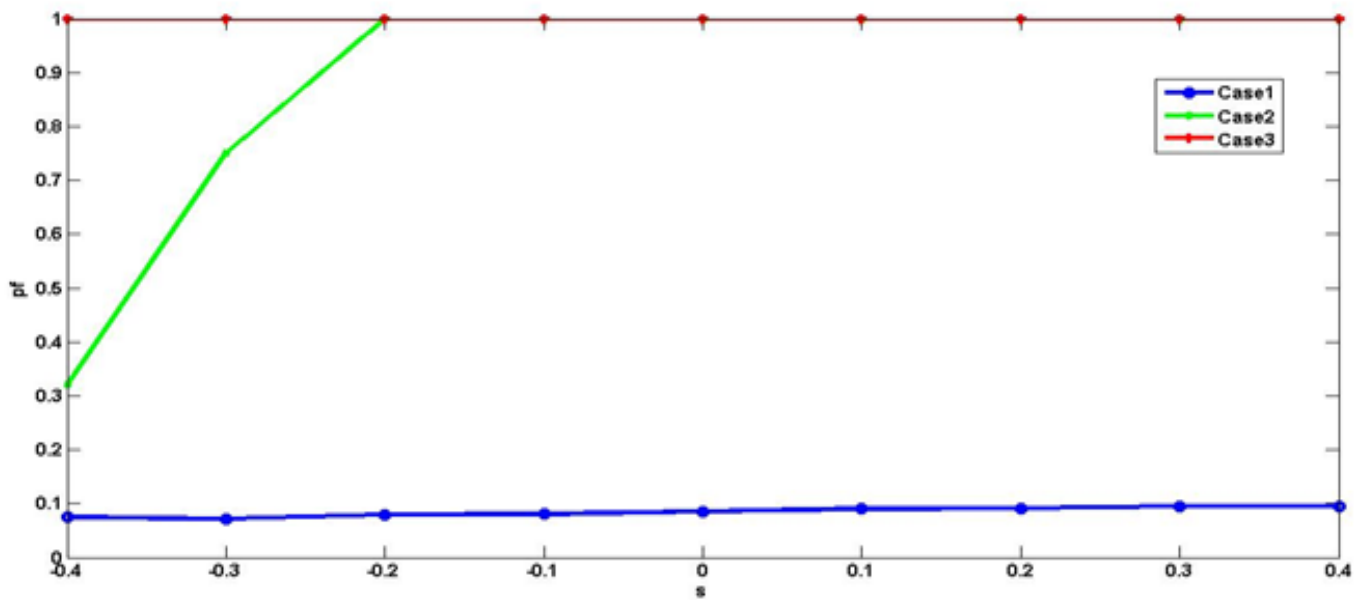


Fig. 5.9 Graph of power factor versus slip, obtained using GA

For case 3, the power factor values corresponding to RM as well as GA are nearly same. For case 1 and case 2, RM yields a better range of power factor as compared to GA. Both RM and GA validate that the best range of power factors is obtained when case 3 is invoked.

D. DFIG Efficiency with slip variation

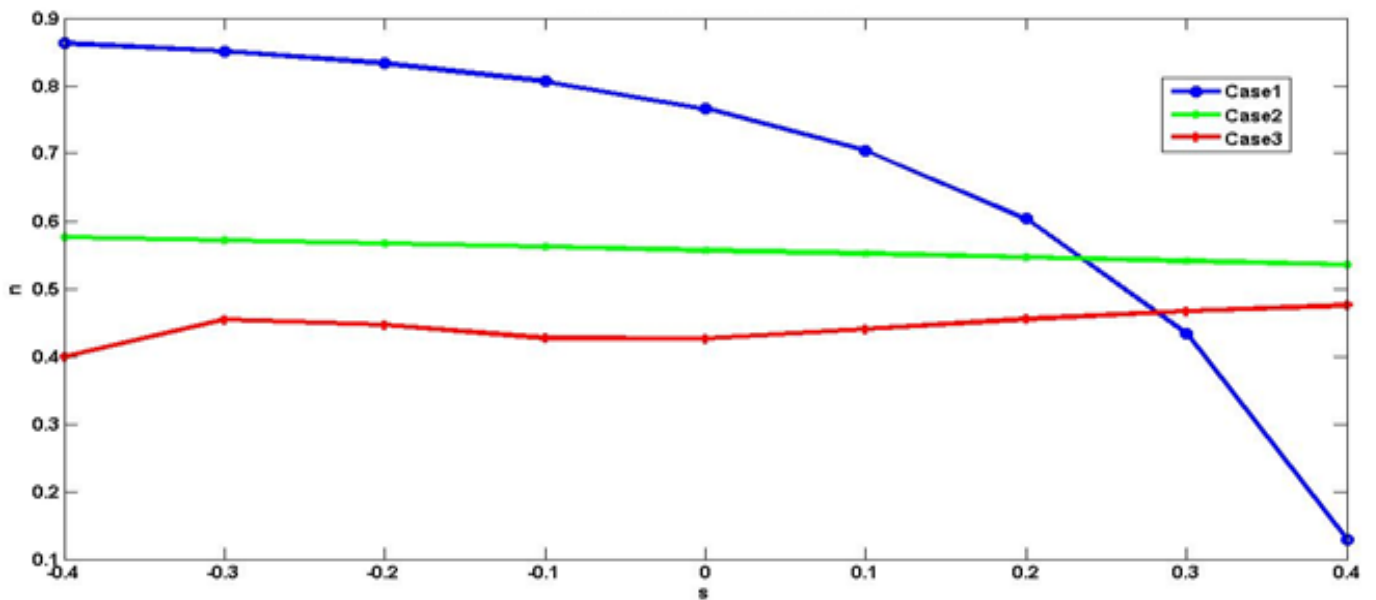


Fig. 5.10 Graph of efficiency versus slip, obtained using RM

From figure 5.10, it is evident that the best efficiency corresponds to case 1 for RM. For case 3, the efficiency is the lowest. In case 2 the efficiency is greater than case 3 but lesser than case 1 and remains nearly constant from the super-synchronous to the sub-synchronous region. Real powers are mainly affected by quadrature axis currents. Since the currents are significantly different in the three cases, therefore the efficiency also differs. Since case 2 and case 3 mainly concern with the reactive power minimization, hence their efficiency range is inferior to that of case 1.

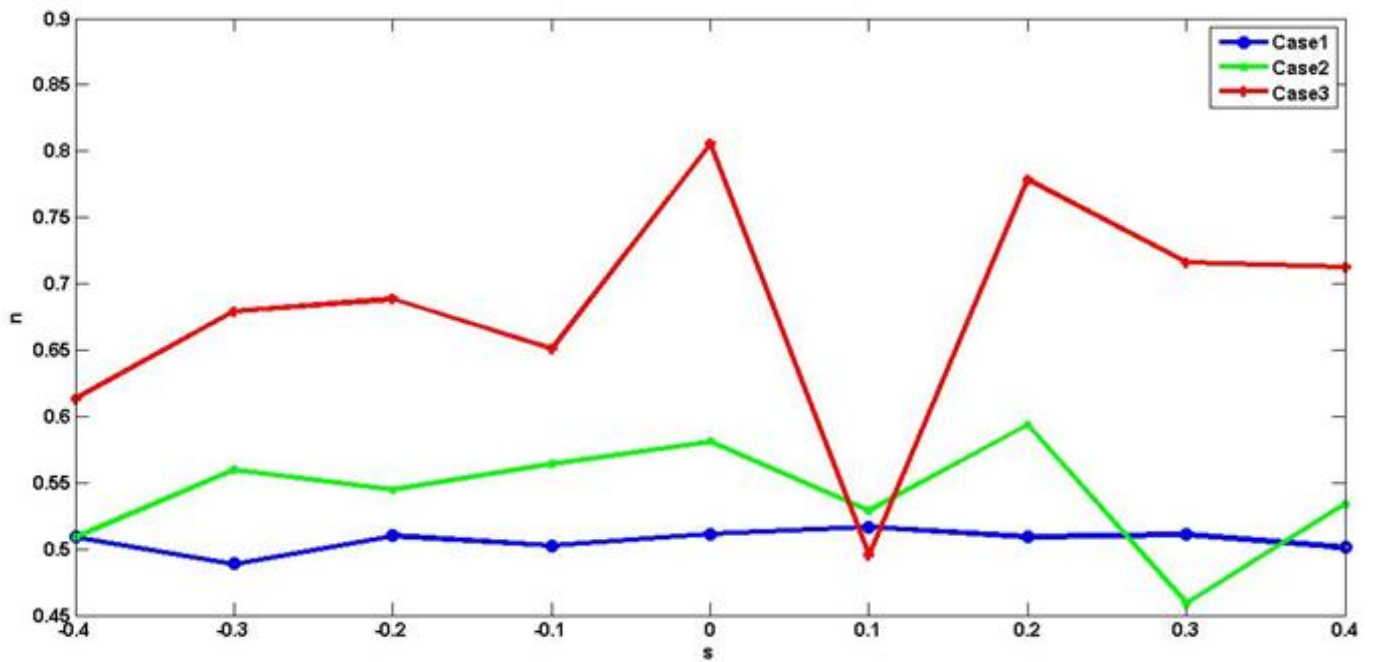


Fig. 5.11 Graph of efficiency versus slip, obtained using GA

For the graph obtained by the application of GA (figure 5.11), it is evident that the best efficiency range corresponds to case 3. Conversely, for case 1, the efficiency is the lowest and remains nearly constant from the super-synchronous to the sub-synchronous region. In case 2 the efficiency is greater than case 1 but lesser than case 3.

For case 3, the efficiency values corresponding to RM are less than those obtained via GA. For case 2, the efficiency values corresponding to RM as well as GA are nearly same. Case 1 of RM yields the best efficiency range in the super-synchronous region. However for the entire operating region, efficiency range is best for case 3 of GA.

E. Voltage across the magnetizing branch of DFIG with slip variation

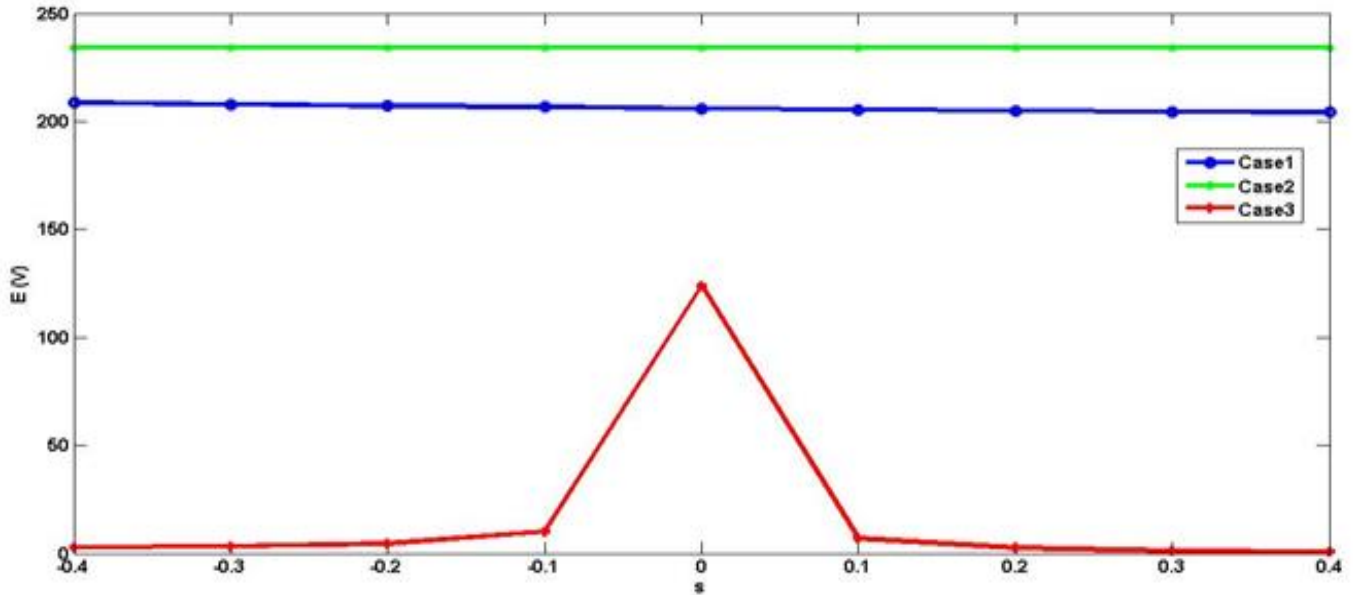


Fig. 5.12 Graph of voltage across the magnetizing branch versus slip, obtained using RM

Figure 5.12 illustrates the DFIG magnetizing branch voltage versus slip. In RM case 1, there is little variation of E with respect to slip. For case 2, E remains almost constant throughout the range of slip. There is a significant variation of E in case 3 during the transition from the super-synchronous to the sub-synchronous region. The values of the magnetizing branch voltage are in the same range for cases 1 and 2. For case 3, the values are significantly lesser as compared to the other two cases.

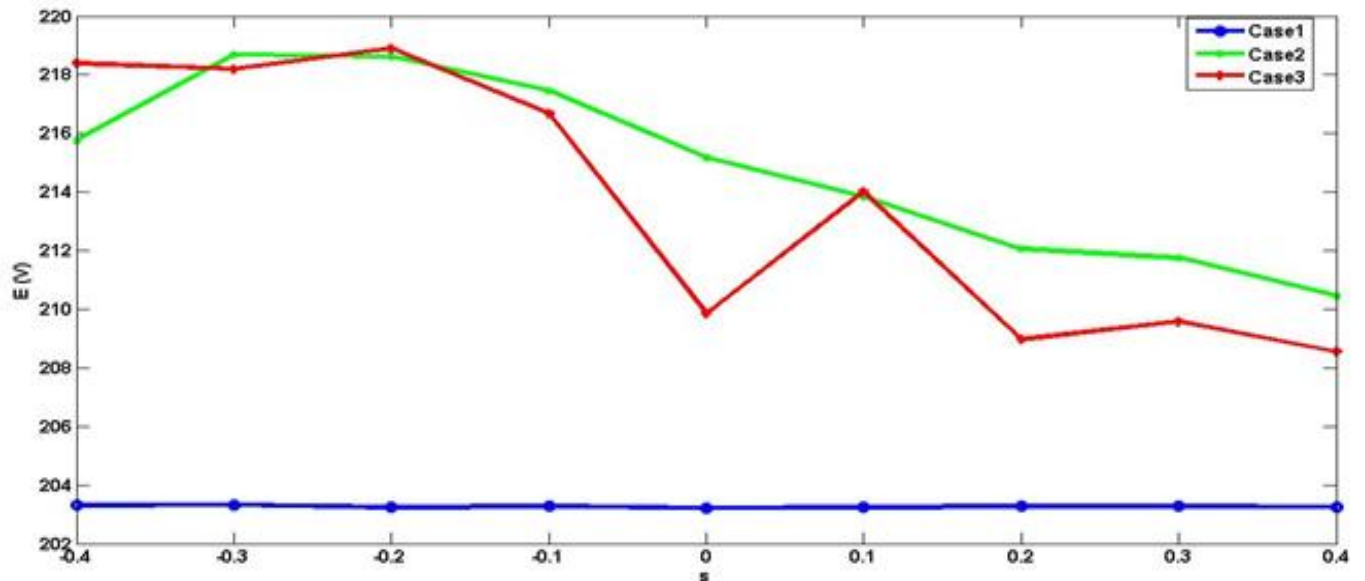


Fig. 5.13 Graph of voltage across the magnetizing branch versus slip, obtained using GA

For the graph obtained by the application of GA (figure 5.13), in case 1, there is little variation of E with respect to slip. For case 2 and case 3, E decreases from the super-synchronous to the sub-synchronous region. The values of the magnetizing branch voltage are in the same range for cases 2 and 3. For case 1, the values are slightly lower as compared to the other two cases.

For case 3, the range of values of E , corresponding to RM is less than those obtained via GA. For case 2, the values corresponding to RM are greater than those obtained via GA. For case 1, the values of E corresponding to RM as well as GA are nearly same. Case 2 of RM yields the highest value of E throughout the entire operating region.

F. Angle between the stator axis and direct axis with slip variation

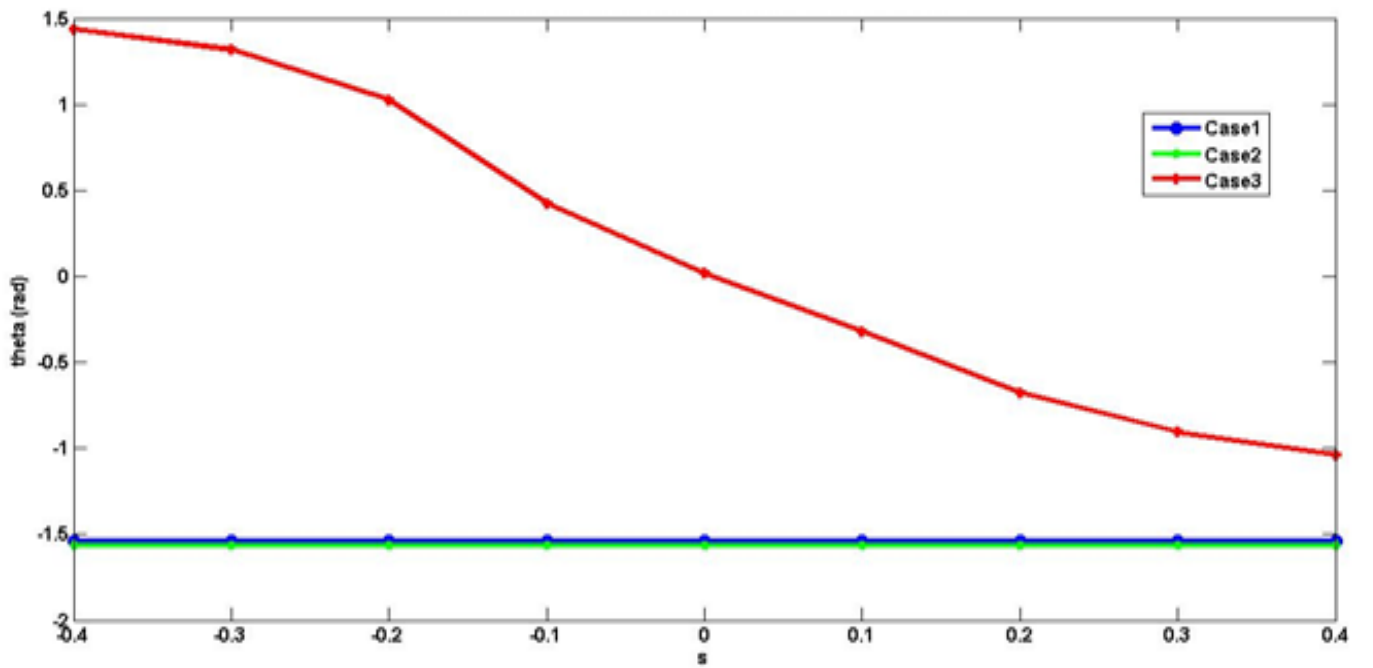


Fig. 5.14 Graph of angle between the stator axis and direct axis versus slip, obtained using RM

Figure 5.14 illustrates that the value of θ_{fs} is negative and almost similar for cases 1 and 2 of RM. For case 3, sub-synchronous region yields negative θ_{fs} while super-synchronous region gives positive angle. The values of the angle are similar for cases 1 and 2. For case 3, the values are greater as compared to the other two cases. For the graph obtained by the application of GA (figure 5.15), for case 1, the value of θ_{fs} is negative and almost constant throughout the range of operation. For cases 2 and 3, sub-synchronous region yields negative θ_{fs} while super-synchronous region gives positive angle. The values of the angle are similar for cases 2 and 3.

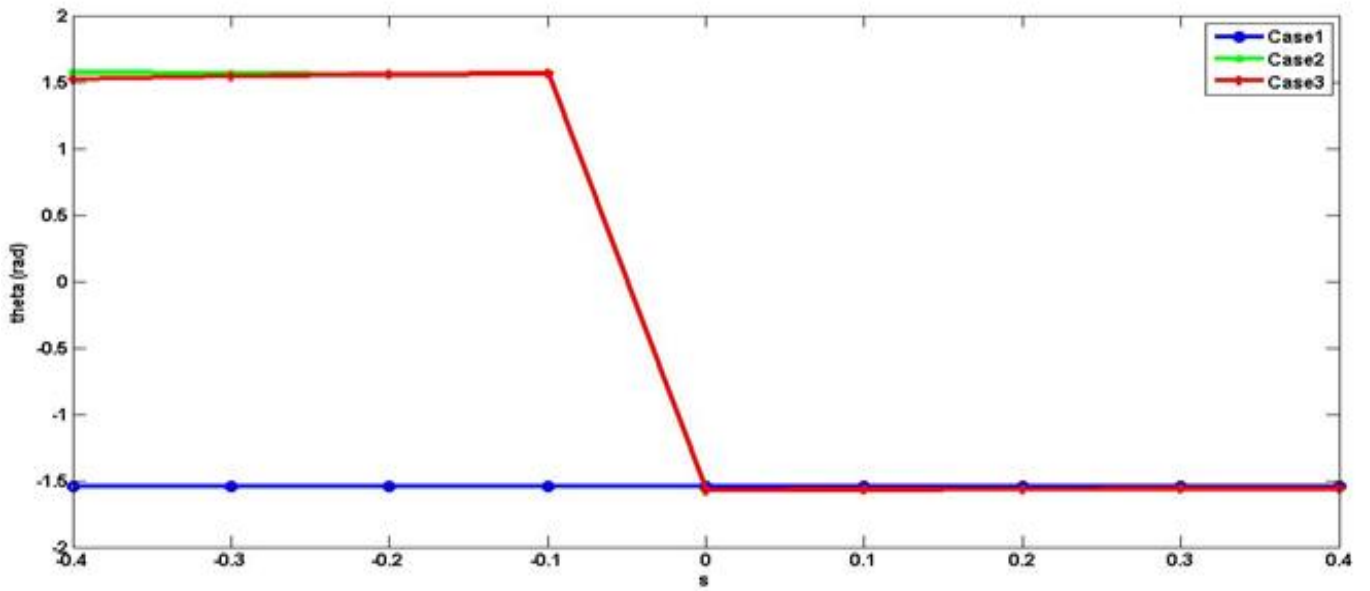


Fig. 5.15 Graph of angle between the stator axis and direct axis versus slip, obtained using GA

For cases 1 and 3, the values of angle corresponding to RM as well as GA are nearly same. Case 2 of GA and RM yield different results in the super-synchronous range.

G. DFIG output active power with slip variation

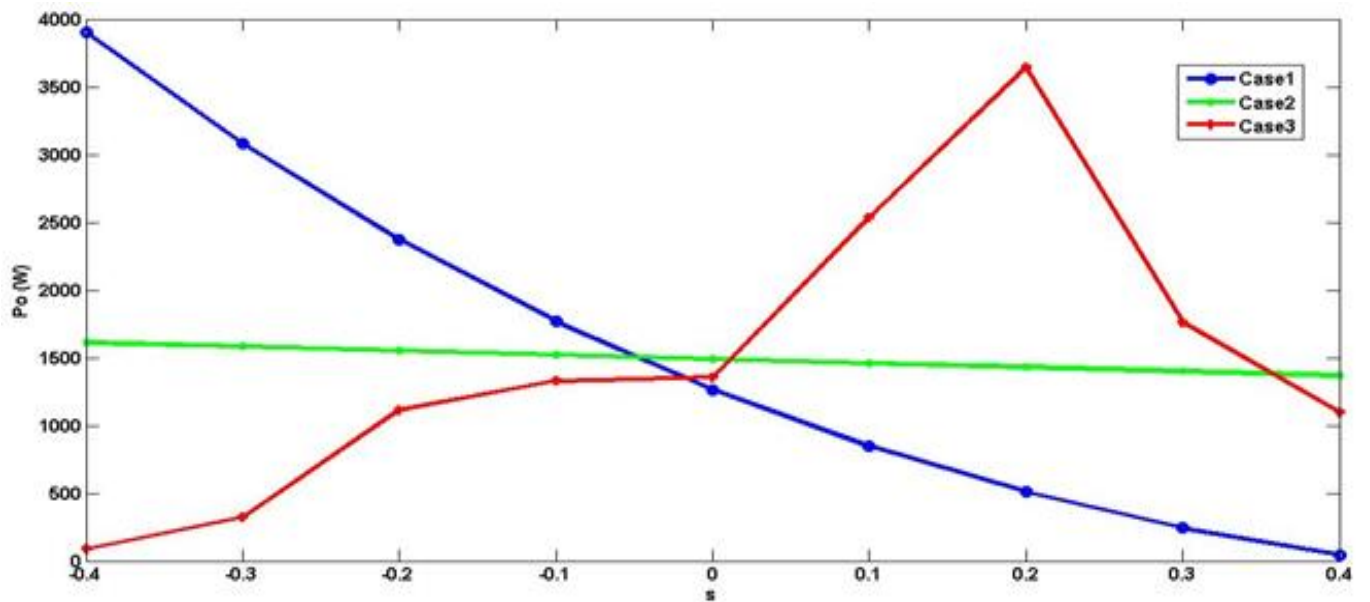


Fig. 5.16 Graph of DFIG output active power versus slip, obtained using RM

From figure 5.16, it is deduced that a high magnitude of active power is obtained in the super-synchronous region of case 1 for RM. However, the active power output diminishes steadily from the super-synchronous to the sub-synchronous region. For case 2, the power output remains nearly constant from the super-synchronous to the sub-synchronous region. For case 3, the active power output increases steadily from the super-synchronous to the sub-synchronous region.

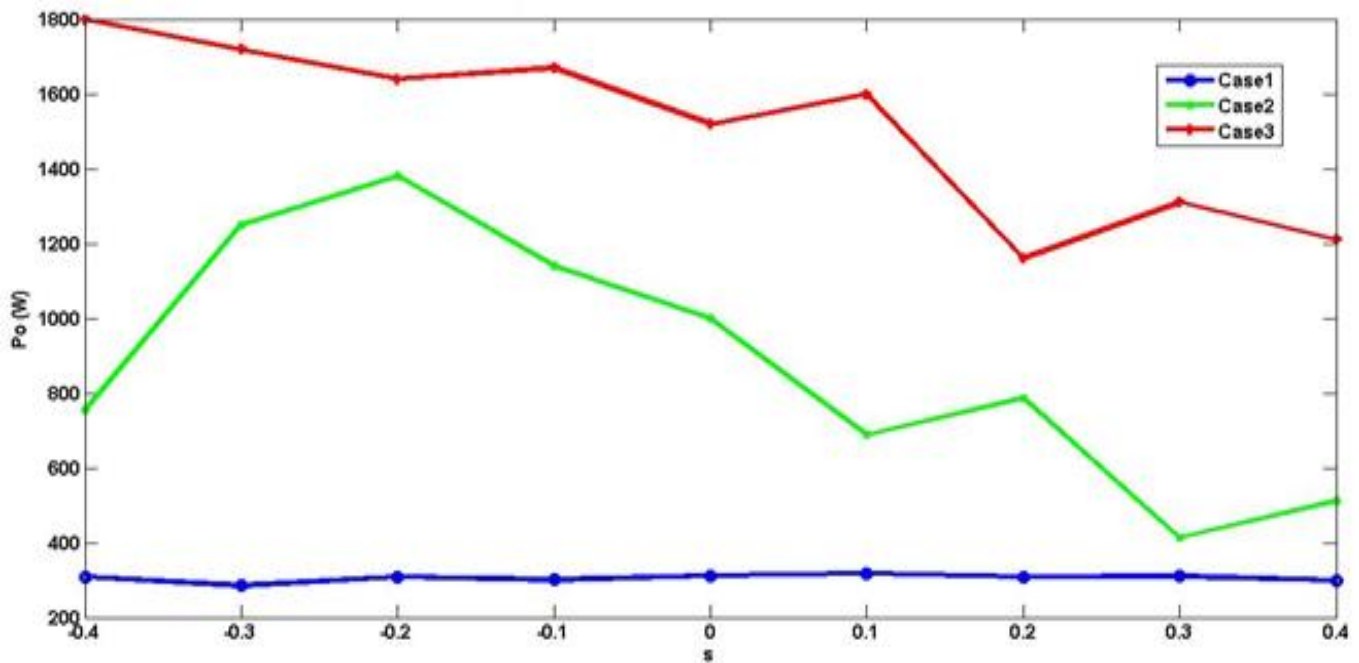


Fig. 5.17 Graph of DFIG output active power versus slip, obtained using GA

For the graph obtained by the application of GA (figure 5.17), it is evident that the best active power range corresponds to case 3. Conversely, for case 1, the output active power is the lowest and remains nearly constant from the super-synchronous to the sub-synchronous region. In case 2 the output is greater than case 1 but lesser than case 3.

The active power output varies widely for the three cases corresponding to both RM and GA. Comparative analysis of the graphs reveal that the most suitable range of values are obtained corresponding to case 2 of RM.

H. DFIG reactive power with slip variation

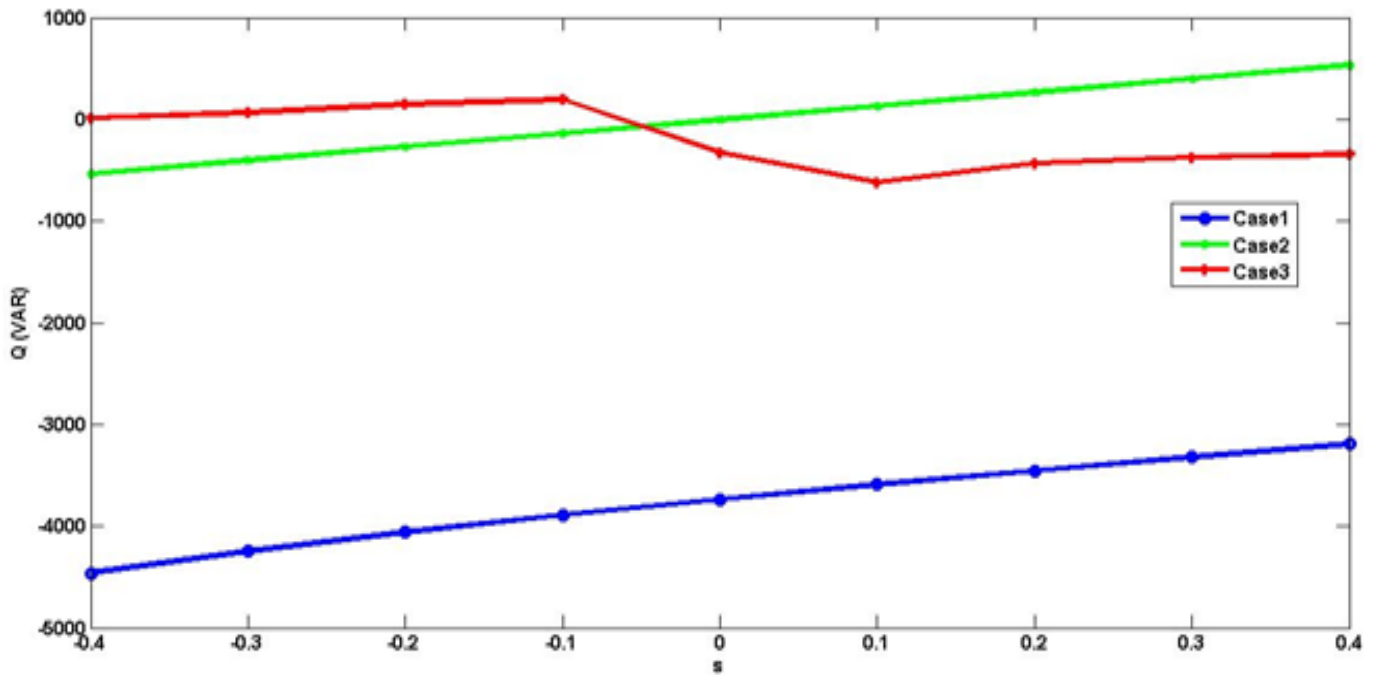


Fig. 5.18 Graph of DFIG output reactive power versus slip, obtained using RM

From figure 5.18, it is deduced that a high magnitude of reactive power is obtained for case 1 of RM. However, the magnitude of the reactive power slightly diminishes from the super-synchronous to the sub-synchronous region. For case 2, the reactive power has a lower magnitude as compared to case 1. The reactive power value is negative in the super-synchronous region while it becomes positive in the sub-synchronous region. For case 3, the reactive power is nearly zero in the super-synchronous region while it attains a small negative value beyond $s=-0.1$.

For the graph obtained by the application of GA (figure 5.19), it is evident that the reactive power is nearly zero corresponding to case 3. Conversely, for case 1, the reactive power has a significant magnitude which diminishes slightly from the super-synchronous to the sub-synchronous region. In case 2 the reactive power is finite for the initial portion of the super-synchronous region while it attains a value close to zero beyond a slip of -0.2.

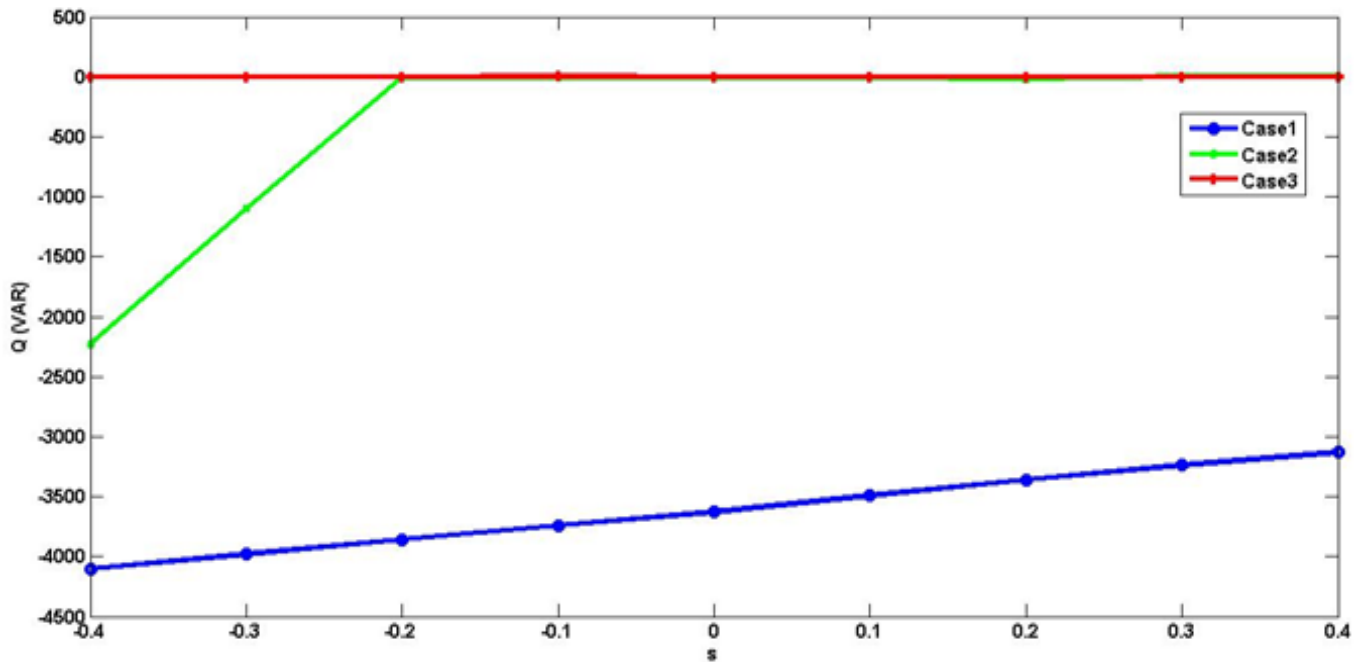


Fig. 5.19 Graph of DFIG output reactive power versus slip, obtained using GA

Comparative analysis of the reactive power graphs for RM and GA reveal that the reactive power is best mitigated corresponding to case 3 of GA. Case 3 of RM also yields low values of reactive power over the entire operating range.

The results clearly validate that reactive power minimization takes place in case 2 and case 3 as expected. Both RM and GA validate that the reactive power is best mitigated when case 3 is invoked.

5.4.2 Results corresponding to the DFIG of high rating

Vector control has been implemented on a standard multi megawatt DFIG referred to as 'DFIG-4' in this work. The DFIG used has a rating of 2 MW and is usually employed with Vestas V-80, Gamesa G-87 or Ecotecnia Eco-80 wind turbine.

For carrying out the simulations on DFIG-4, it has been assumed that the wind speed is 12 m/s at the time the input is initiated into the wind turbine. After five seconds, wind speed changes to 10 m/s. Seven seconds from the initiation, wind speed falls to 7 m/s.

A. Tracking of direct axis rotor current reference

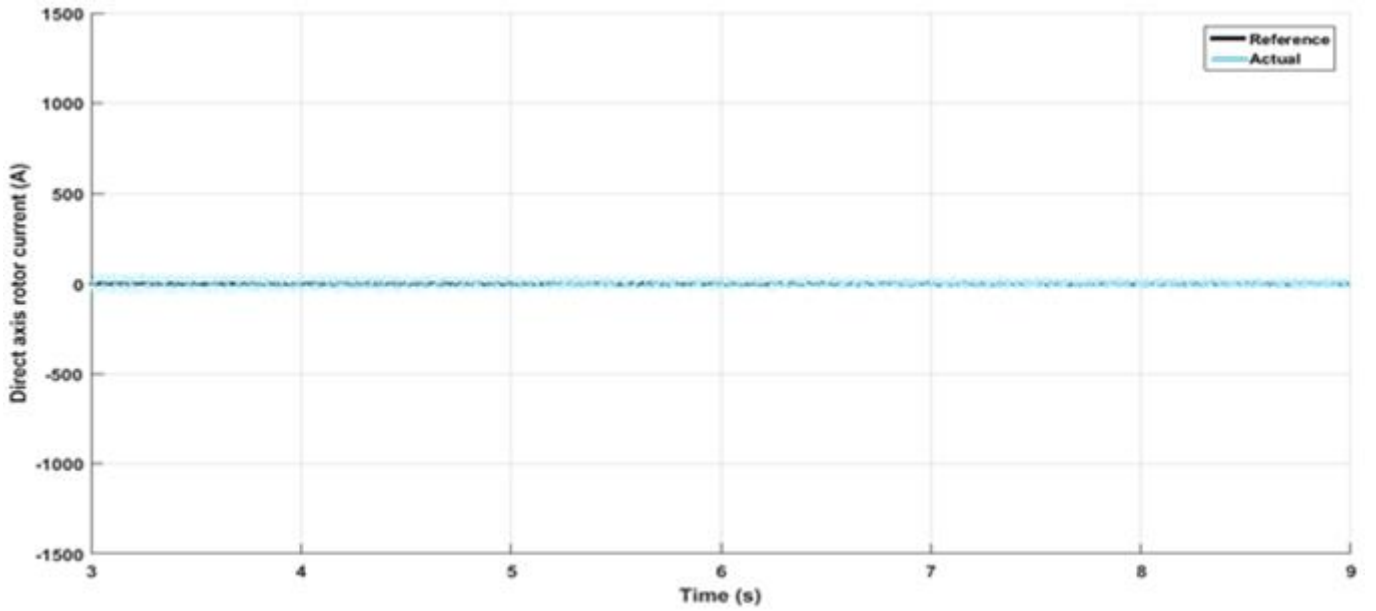


Fig. 5.20 Tracking of direct axis rotor current reference

Figure 5.20 illustrates that the direct axis rotor current reference has been properly tracked. For the rotor side converter in vector control, the reactive power is directly proportional to the direct axis rotor current. Hence, maintaining a zero value of I_{rd} ensures minimization of reactive power.

B. Tracking of quadrature axis rotor current reference

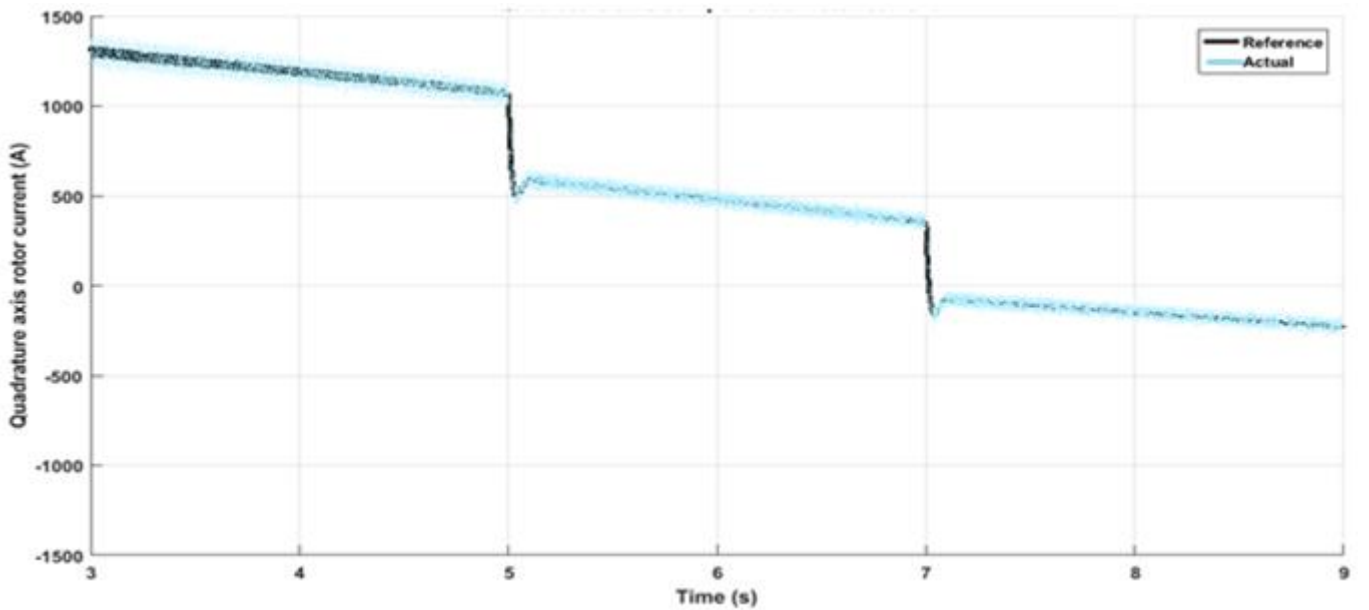


Fig. 5.21 Tracking of quadrature axis rotor current reference

Figure 5.21 illustrates that the quadrature axis rotor current reference has been properly tracked. For the rotor side converter in vector control, the active power is directly proportional to the quadrature axis rotor current. Hence, maintaining the optimum value of I_{rq} ensures maximization of active power. From figure 5.21 it is evident that I_{rq} changes with a change in wind speed at five second and seven second.

C. Tracking of rotor speed reference

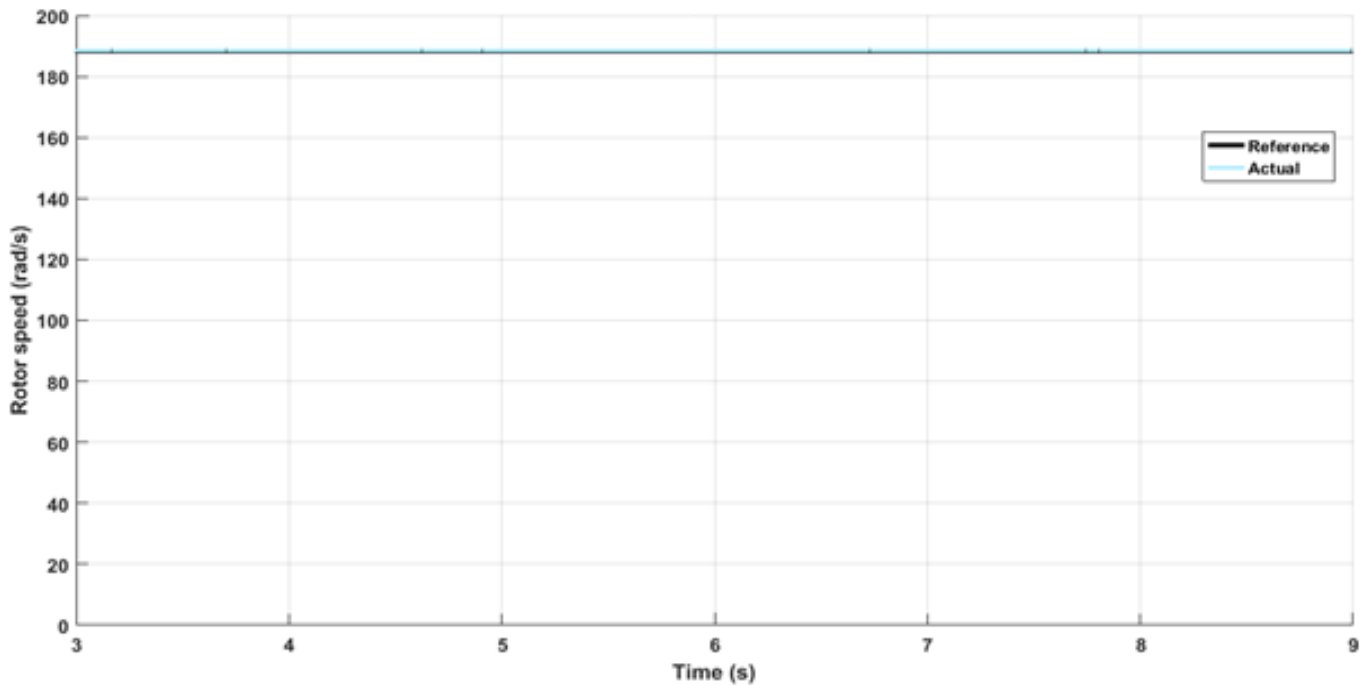


Fig. 5.22 Tracking of rotor speed reference

Figure 5.22 illustrates that the rotor speed reference has been properly tracked. It is evident that the changes in wind speed at five second and seven second are properly smoothed out by the control strategy. Hence, the rotor continues to rotate at the reference speed.

D. Tracking of Electromagnetic Torque reference

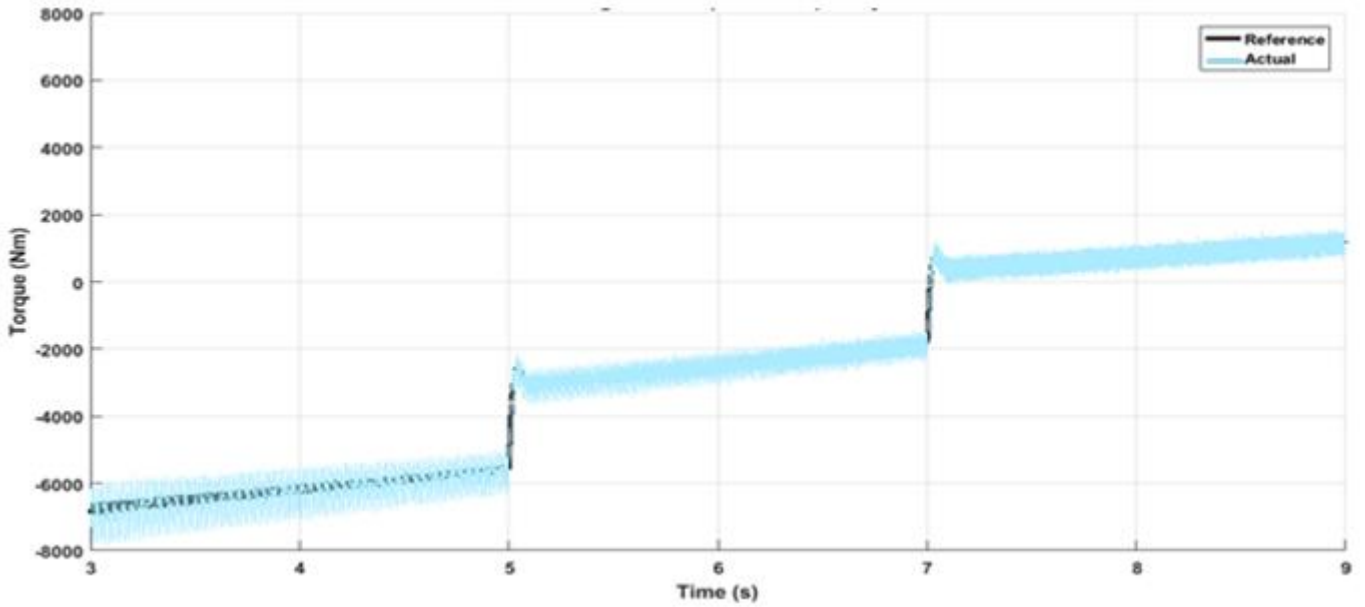


Fig. 5.23 Tracking of electromagnetic torque reference

Figure 5.23 illustrates that the torque reference has been tracked properly. It is evident that the changes in wind speed at five second and seven second has been factored in by the control strategy to optimize the active power generation.

E. Three-phase Stator Currents

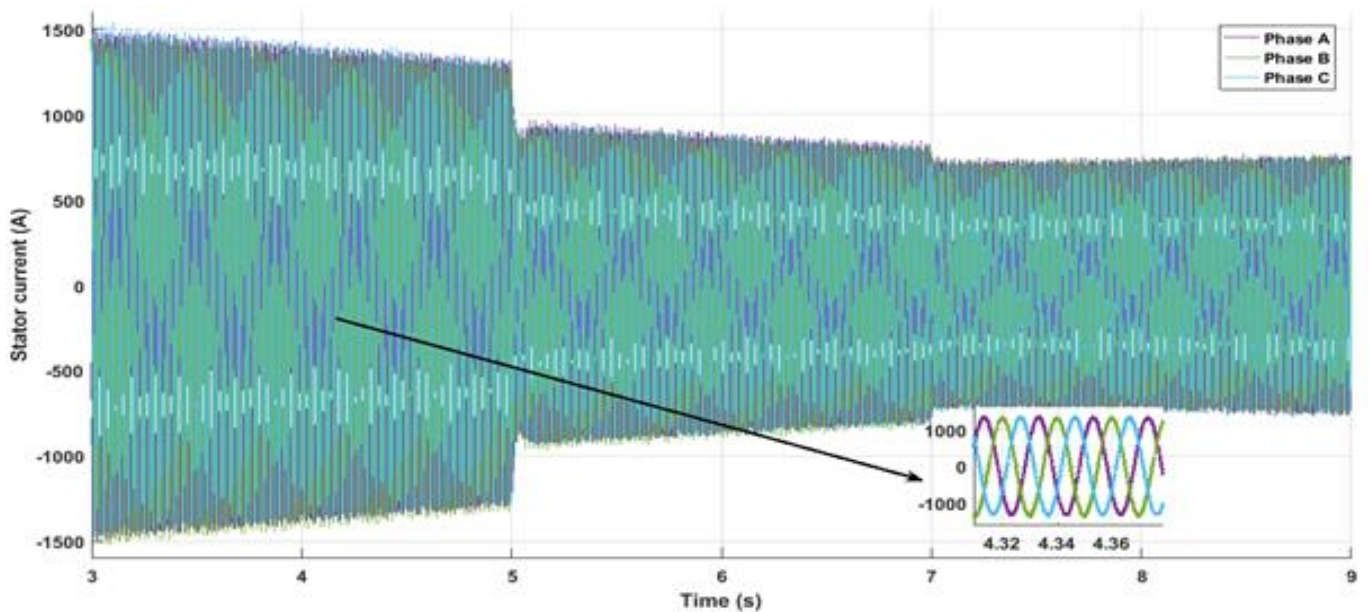


Fig. 5.24 Graph of three-phase stator currents

Figure 5.24 is a graph of the three-phase balanced stator currents. Since the system is grid connected, the DFIG stator voltage and frequency is constant. Hence the changes in wind speed are reflected in the magnitude of the stator current. From the figure it can be observed that the decrease in wind speed at five second and seven second results in a decreased magnitude of the stator currents.

F. Three-phase Rotor Currents

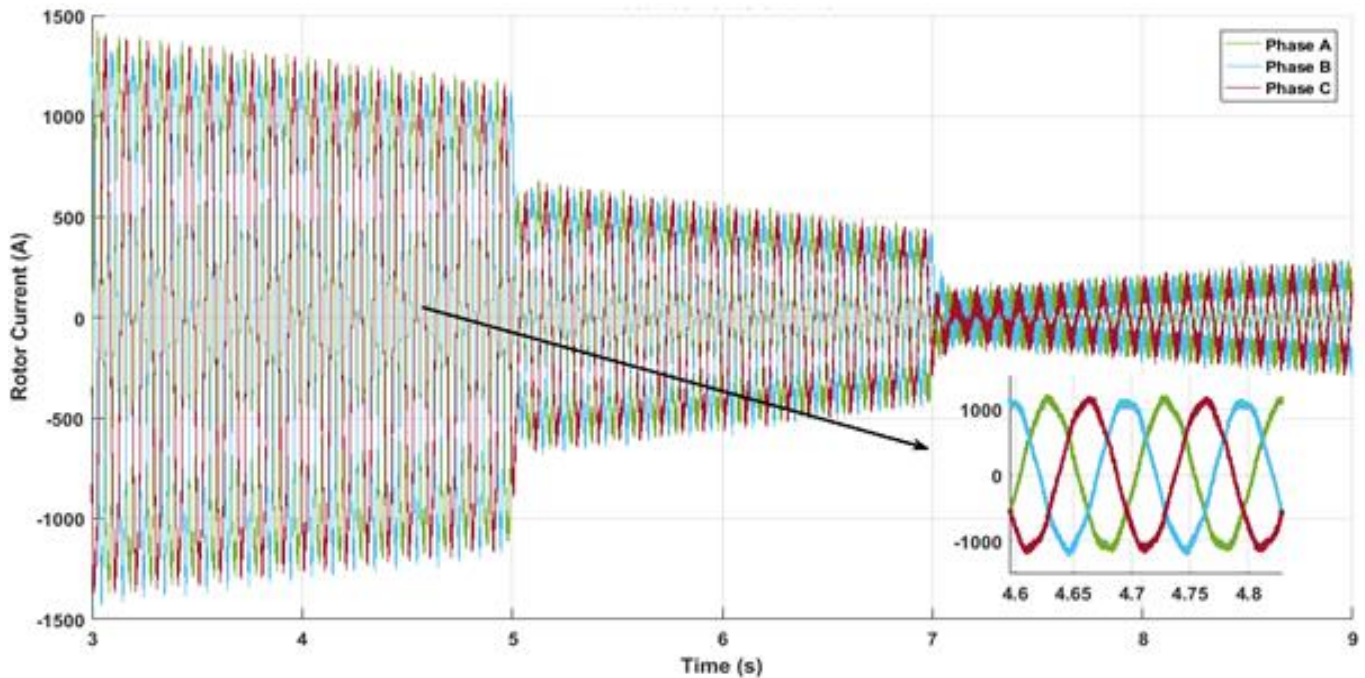


Fig. 5.25 Graph of three-phase rotor currents

Figure 5.25 is a graph of the three-phase balanced rotor currents. Since the system is grid connected, the DFIG stator voltage and its frequency is constant. The stator currents also have a constant frequency but their magnitude varies in direct co-relation to wind speed. However, the rotor current magnitude as well as frequency changes according to change in wind speed so as to maintain the grid code and ensure optimum power capture.

G. Tracking of direct axis grid side converter current

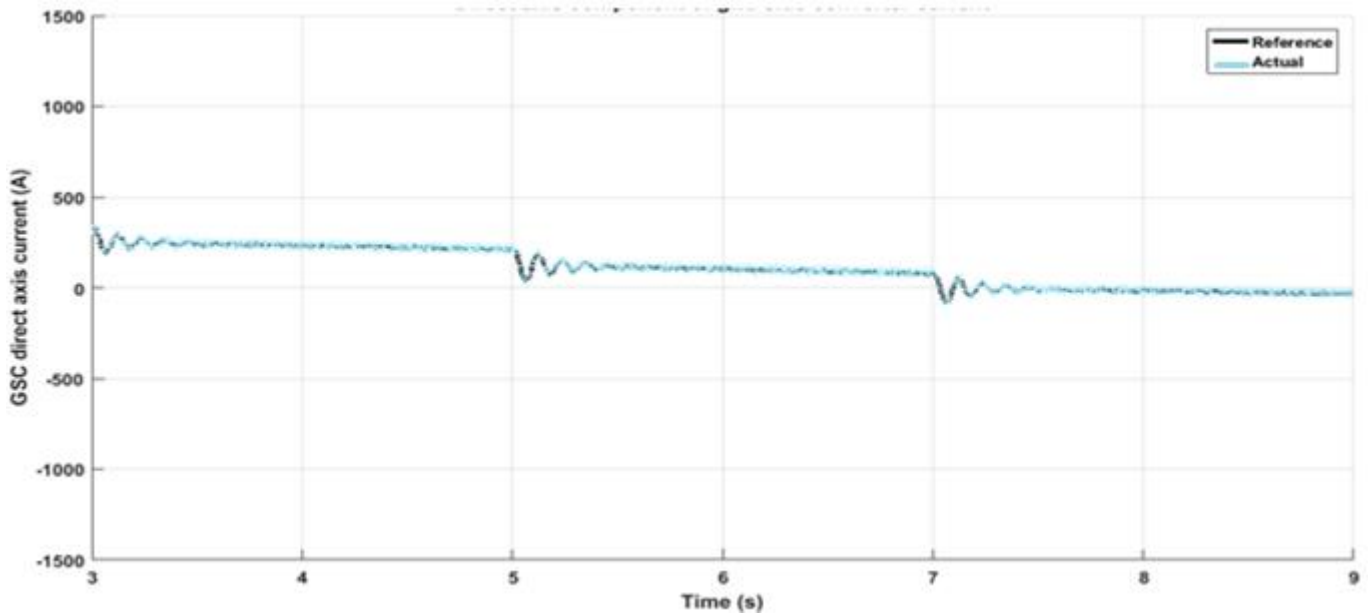


Fig. 5.26 Tracking of direct axis grid side converter current reference

Figure 5.26 illustrates that the direct axis grid side converter current reference has been properly tracked. For the grid side converter in vector control, the active power is directly proportional to the direct axis converter current. Hence, maintaining the optimum value of I_{gd} ensures maximization of active power. From figure 5.26 it is evident that I_{gd} changes with a change in wind speed at five second and seven second.

H. Tracking of quadrature axis grid side converter current

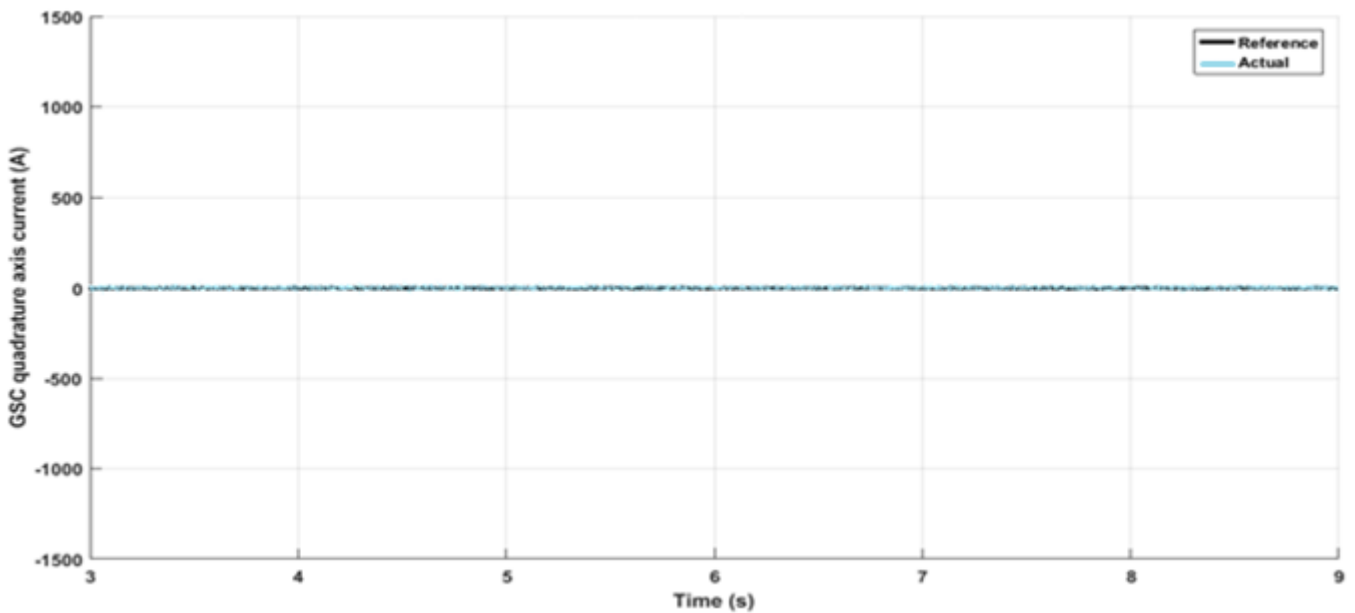


Fig. 5.27 Tracking of quadrature axis grid side converter current reference

Figure 5.27 illustrates that the quadrature axis grid side converter current reference has been properly tracked. For the grid side converter in vector control, the reactive power is directly proportional to the quadrature axis converter current. Hence, maintaining a zero value of I_{gq} ensures minimization of reactive power.

I. Three-phase Grid Side Converter Currents

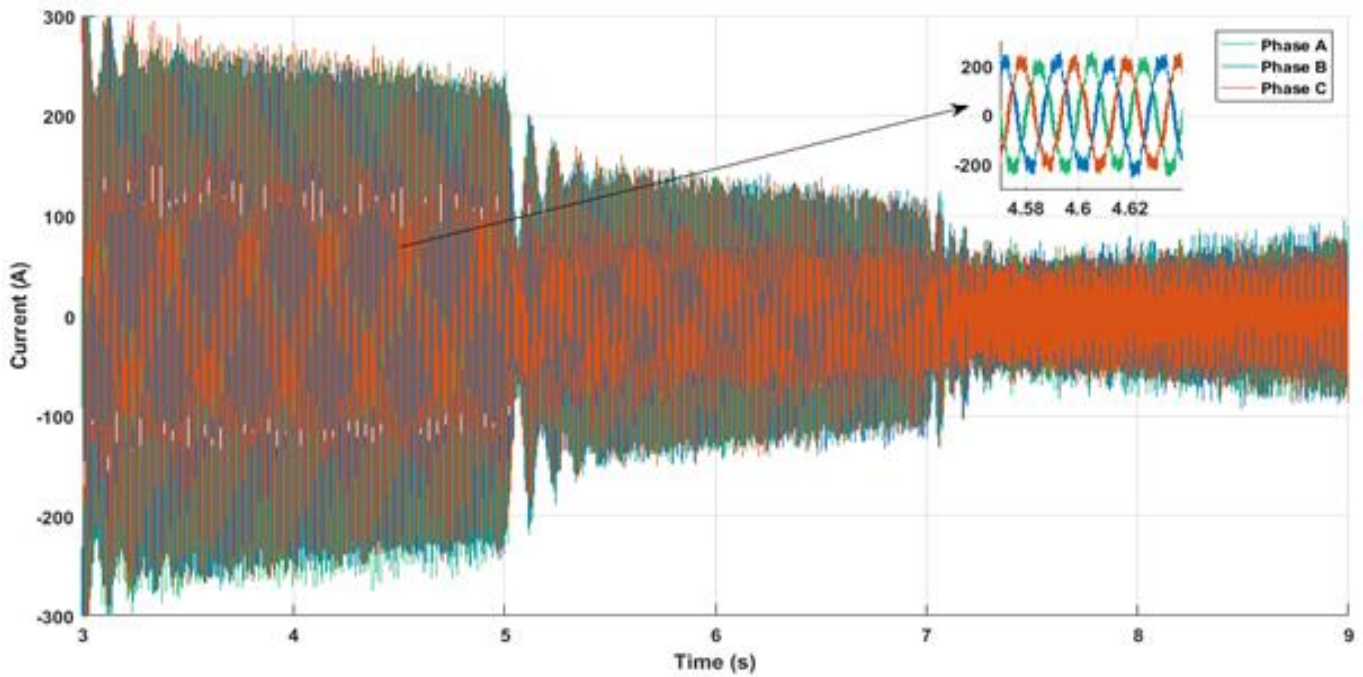


Fig. 5.28 Graph of three-phase grid side converter currents

Figure 5.28 is a graph of the three-phase grid side converter currents. Since the system is grid connected, the converter currents have a constant frequency but their magnitude varies in direct co-relation to wind speed. From the figure it can be deduced that the decrease in wind speed at five second and seven second results in a decreased magnitude of the converter currents.

J. Tracking of DC link voltage

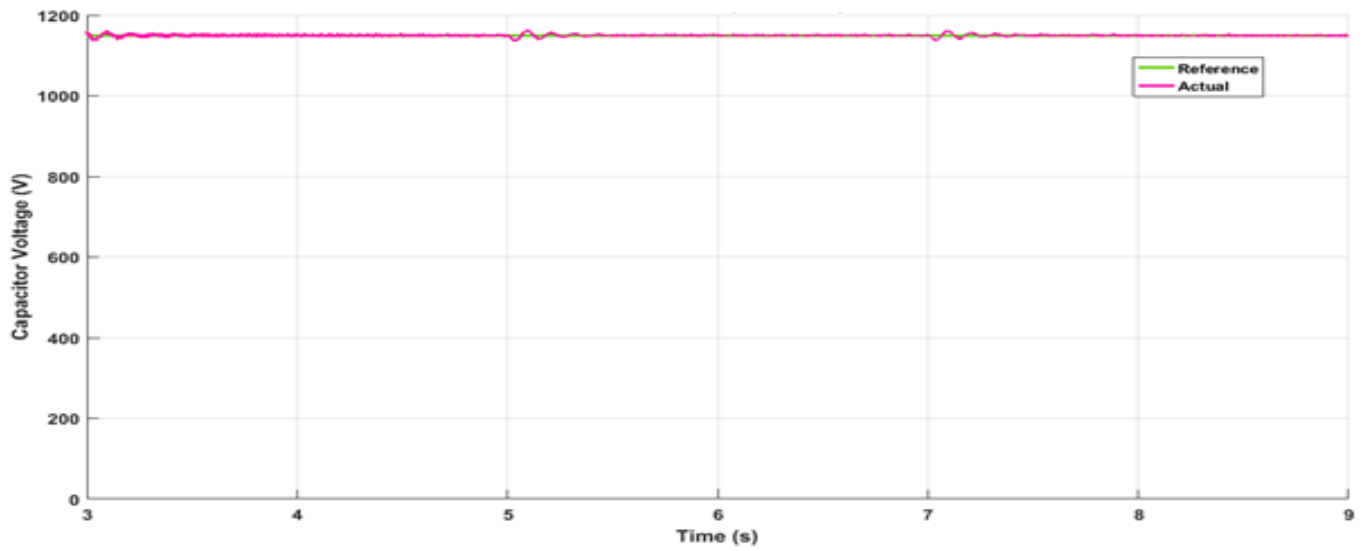


Fig. 5.29 Tracking of dc link voltage

Figure 5.29 illustrates that the dc link voltage has been properly tracked. The voltage fluctuations due to changes in wind speed at five second and seven second are properly smoothed out by the control strategy. Hence, the dc link voltage is maintained at the reference value.

K. Three-phase Stator Voltage/ Grid Voltage

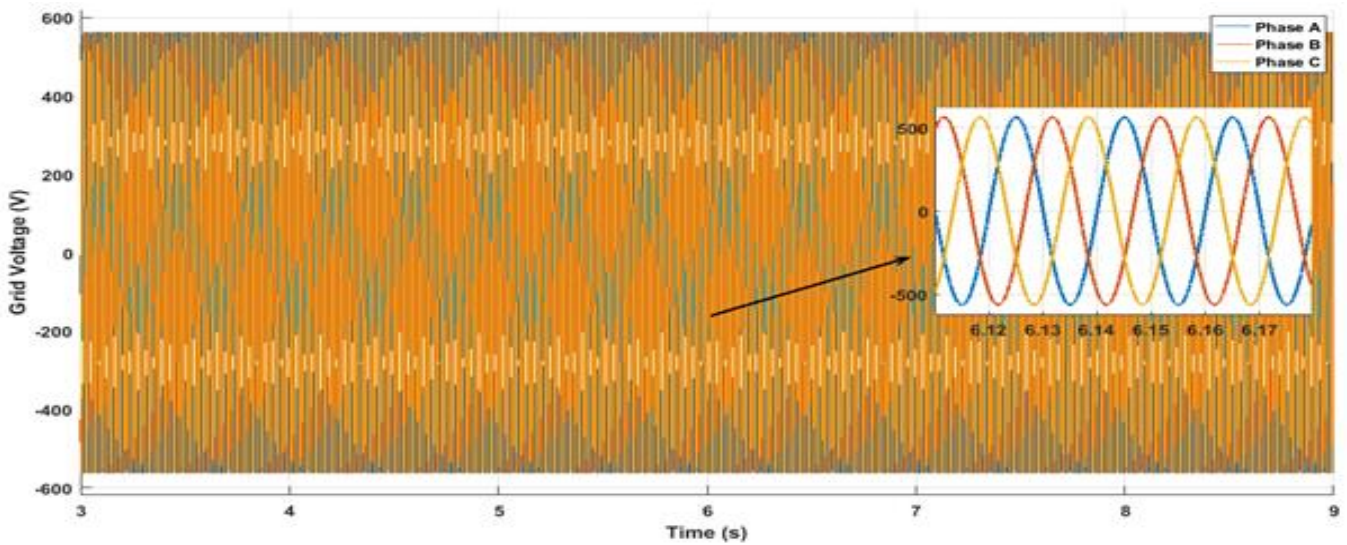


Fig. 5.30 Graph of three-phase stator voltage/ grid voltage

Figure 5.30 is a graph of the three-phase DFIG stator voltage/ grid voltage. The voltage profile remains constant throughout the duration of the simulation.

5.5 CONCLUSION

In this chapter, the optimal values of DFIG rotor current have been obtained using three different rational techniques and corresponding three cases of GA. The first method relates to an algorithm where maximum active power and minimum losses are considered. The second method establishes an algorithm corresponding to minimum losses and minimum reactive power. The third method establishes an algorithm corresponding to maximum active power and minimum reactive power. Equations were formed and simulations carried out using MATLAB 2016a. The data related to optimal current commands, active power, reactive power, efficiency and power factor has been captured. Based on the results obtained in this chapter, the following facts have been conclusively established:

- The scheme that uses reactive power minimization is more close to practical situations. This is owing to the fact that reactive power can be minimized but cannot be altogether nullified.
- The reactive power minimization method proposed in this chapter leads to flexibility of power capture.
- After the comparative analysis of the three cases, it is concluded that best efficiency is obtained in case 1 while the best range of power factor corresponds to case 3. Case 2 is immensely useful since it gives an overall greater efficiency as compared to case 3 and a far better power factor as compared to case 1.
- Depending upon the requirement, one of the three methods can be applied to achieve a specific objective. If the constraint relates to efficiency maximization of a DFIG, without much concern related to the reactive power, then case 1 can be put to use. Case 3 is especially useful if the sole concern is the reactive power minimization. For enhanced efficiency as well as good power factor, case 2 offers the best alternative.
- The rational method for determining the current commands will always give the best possible solution in the least possible time. Hence the logical techniques are far better than exhaustive methods.
- The GA technique used in this work is a novel feature which can be put to use to nullify the need of computation. GA becomes especially useful when the number of unknown variables is more than two, in which case rational methods cannot be applied. Moreover, GA can also be used to compare and validate the results obtained via analytical methods.

CHAPTER 6

ANALYSIS OF TWO-LEAD AND THREE-LEAD CONFIGURATION OF DC EXCITED DFIG

6.1 INTRODUCTION

Distributed generation (DG) using locally existing renewable sources can facilitate the achievement of energy self-reliance for remote locations. In this chapter, two novel topologies of DFIG called the two-lead system and the three-lead system respectively have been proposed. This chapter includes an in-depth analysis and comparison of two-lead and three-lead topologies and comparison of total harmonic distortion of the stator sinusoidal output. A modified Perturb and Observe (MP&O) Algorithm has been applied for maximum power point tracking in DFIG DC systems based on the two topologies proposed in this chapter. The benefits of the proposed DFIG topologies and the benefits of MP&O over the traditional P&O algorithm have been validated. The chapter also contains the analysis of a three-lead based autonomous DFIG DC system whose output voltage is held constant under varying wind speeds and changing loads. Hardware results of two-lead and three-lead DFIG system with rotor excited via DC-DC Converter have also been included. The DC-DC converter input is variable but its output is held constant by applying proper control.

6.2 SYSTEM DESCRIPTION

In this chapter, two simplified DFIG topologies have been proposed. The details have been described in the succeeding sub-sections.

6.2.1 DC Two-Lead DFIG Configuration

In the two lead DFIG connection, the two leads from the DC source are connected to any two phases of the rotor. The third phase is connected via a high resistance to any of the other two rotor phases. The circuit diagram can be observed in figure 6.1.

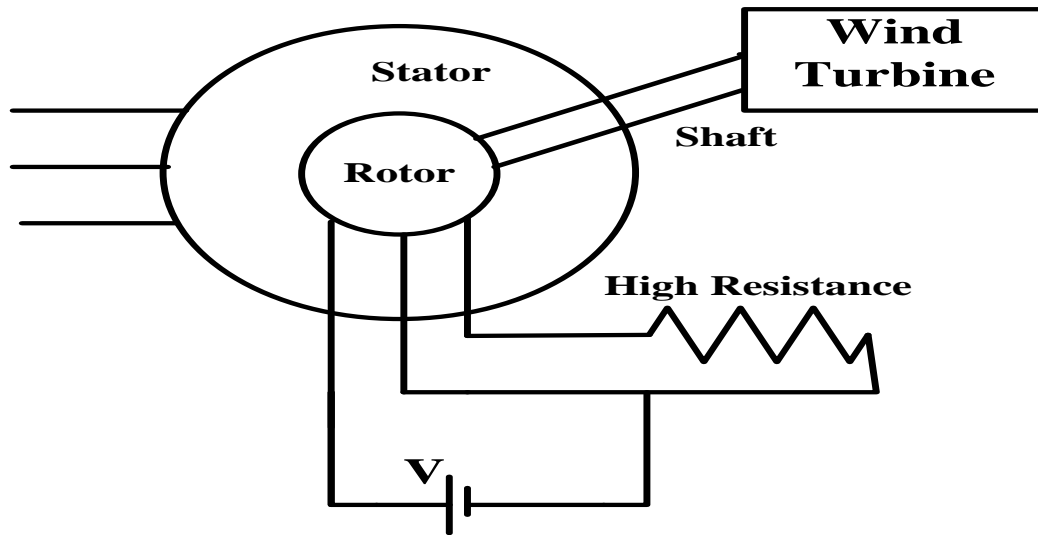


Fig. 6.1 DC two-lead connection of DFIG

6.2.2 DC Three-Lead DFIG Configuration

Three lead connection is made by short circuiting any two phases of the rotor winding and supplying the DC voltage through the two terminals thus formed. The circuit diagram can be observed in figure 6.2.

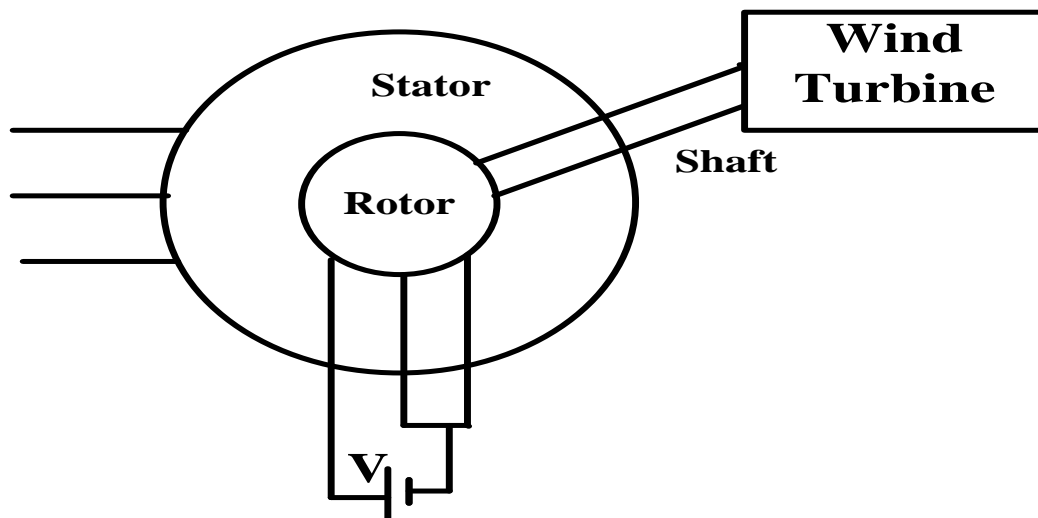


Fig. 6.2 DC three-lead connection of DFIG

6.3 ISOLATED DFIG WITH ROTOR FED BY DC-DC CONVERTER

In this section, two-lead and three-lead connections of DFIG with rotor fed by DC-DC converters have been analysed.

6.3.1 Two-Lead and Three-Lead DFIG Systems fed by Boost Converter

Figure 6.3 shows an isolated DFIG system fed by a Boost Converter. As illustrated in the figure, if $R=0$, it is a DFIG three-lead system. A high value of R will imply a DFIG two-lead system.

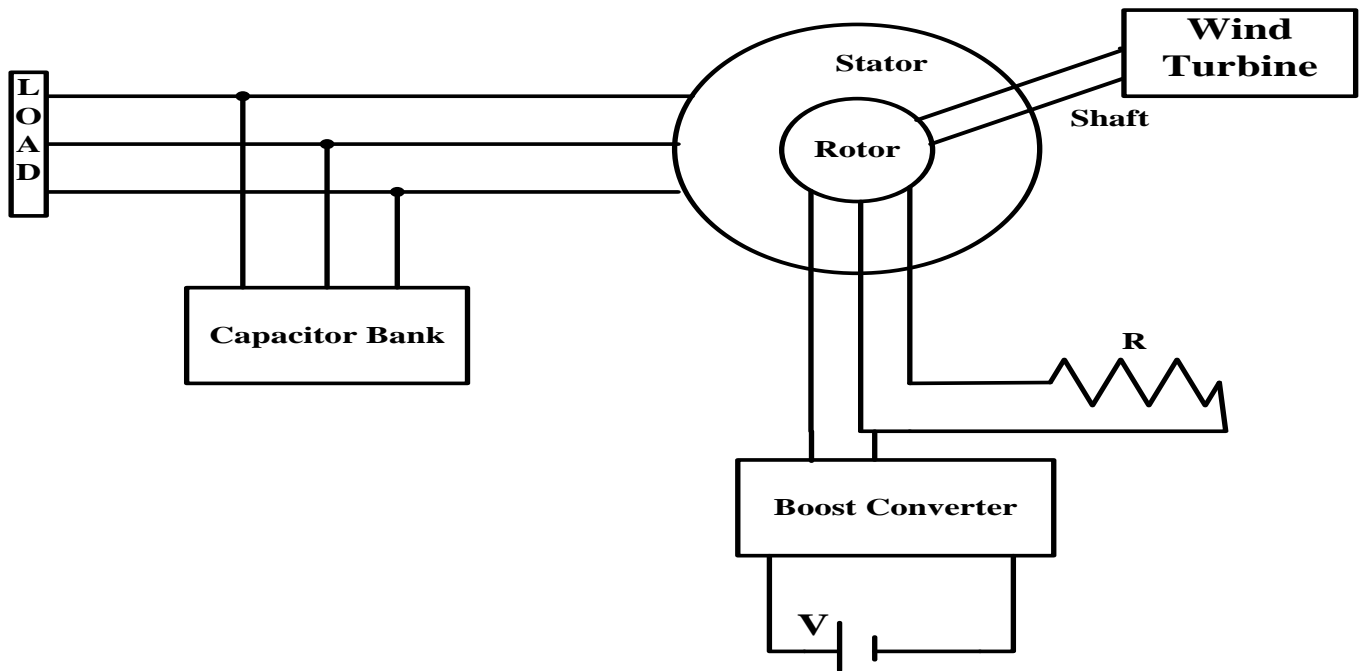


Fig. 6.3 Block diagram of an isolated DFIG system with rotor excited by boost converter

The stator output voltage bears a direct co-relation with the output voltage of the Boost Converter as well as the wind speed. Under no-load condition, the frequency of the stator voltage is solely determined by the speed of the machine shaft.

6.3.2 Control of Three-Lead DFIG System excited by Buck Converter

Closed loop control has been implemented on the three-lead DFIG topology mentioned in this work. A DFIG DC system has been created whose voltage can be controlled using a Buck Converter connected to the rotor of the DFIG. Proper control has been achieved over a wide range of wind speeds and changing loads. Figure 6.4 is an illustration of the closed loop system. Three-lead topology has been used because it has a higher efficiency as compared to the two-lead topology.

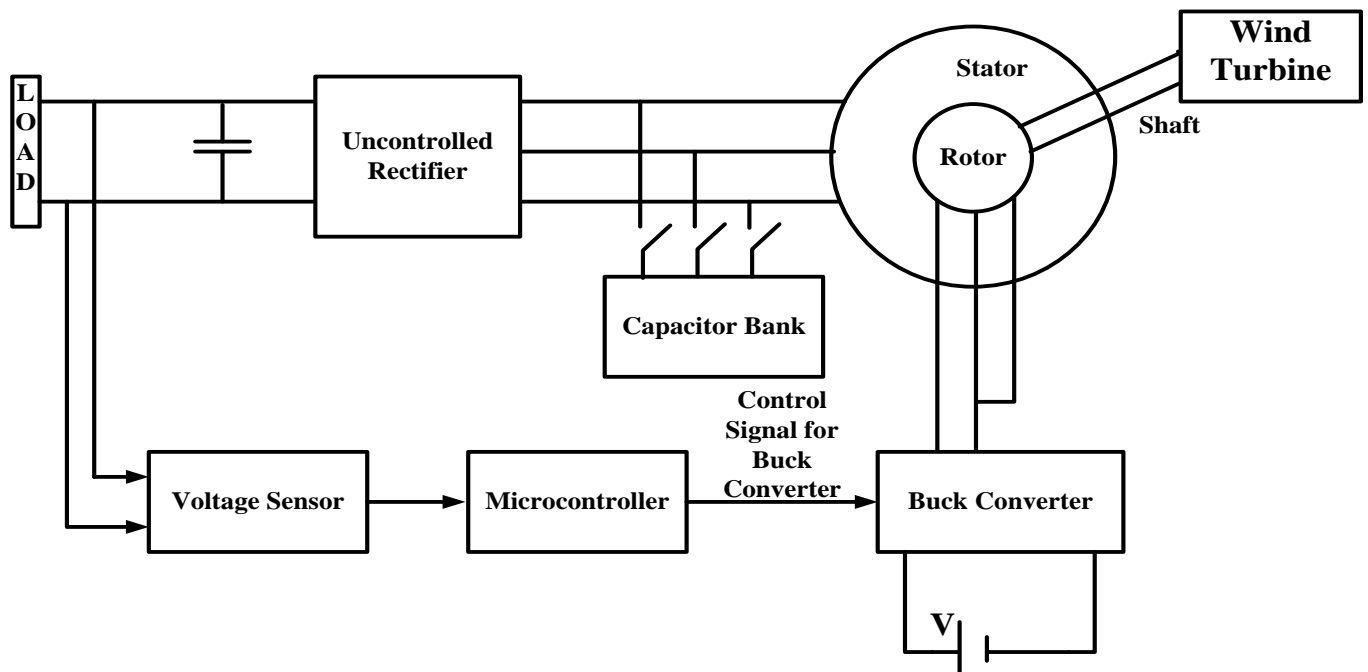


Fig. 6.4 Block diagram of an isolated DFIG system with rotor excited by buck converter

6.4 DFIG DC SYSTEM WITH MPPT

In this section, application of maximum power point tracking (MPPT) on the proposed DFIG topologies have been discussed. Figure 6.5 is the block diagram of the system. The DFIG stator has been connected to an uncontrolled rectifier followed by a Boost converter for implementing MPPT.

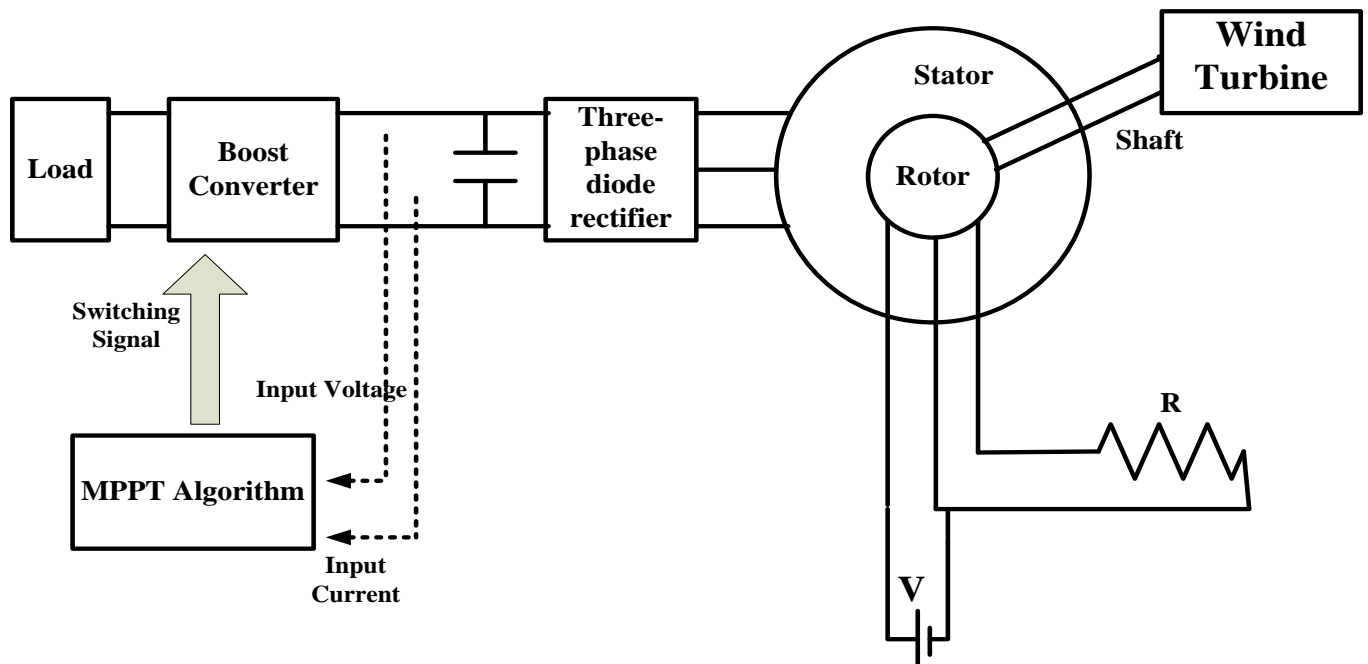


Fig. 6.5 Block diagram of isolated DFIG system for MPPT implementation

As illustrated in figure 6.5, if $R=0$, it is a DFIG three-lead system. A high value of R will imply a DFIG two-lead system.

In this work, the MPPT algorithm used is a modified P & O algorithm. This scheme resolves the problem of oscillation due to the unsettlement of peak point which is inherent to the traditional P & O algorithm. The duty cycle of the Boost converter is controlled by sensing its input voltage and input current. Equations (6.1) to (6.3) are the conditions required to be fulfilled for achieving maximum power point.

$$P = VI \quad (6.1)$$

For maximum power, the slope of power curve at that point should be zero.

$$\text{Hence, } \frac{dP}{dV} = V \frac{dI}{dV} + I = 0 \quad (6.2)$$

Equation (6.2) can be rewritten as follows:

$$\frac{dI}{dV} + \frac{I}{V} = 0 \quad (6.3)$$

The modified P & O control algorithm has been framed by using the condition mentioned in equation (6.3) to remove the oscillations around the peak point of the traditional P & O algorithm. Figure 6.6 is a flowchart depicting the logic of the modified P & O algorithm.

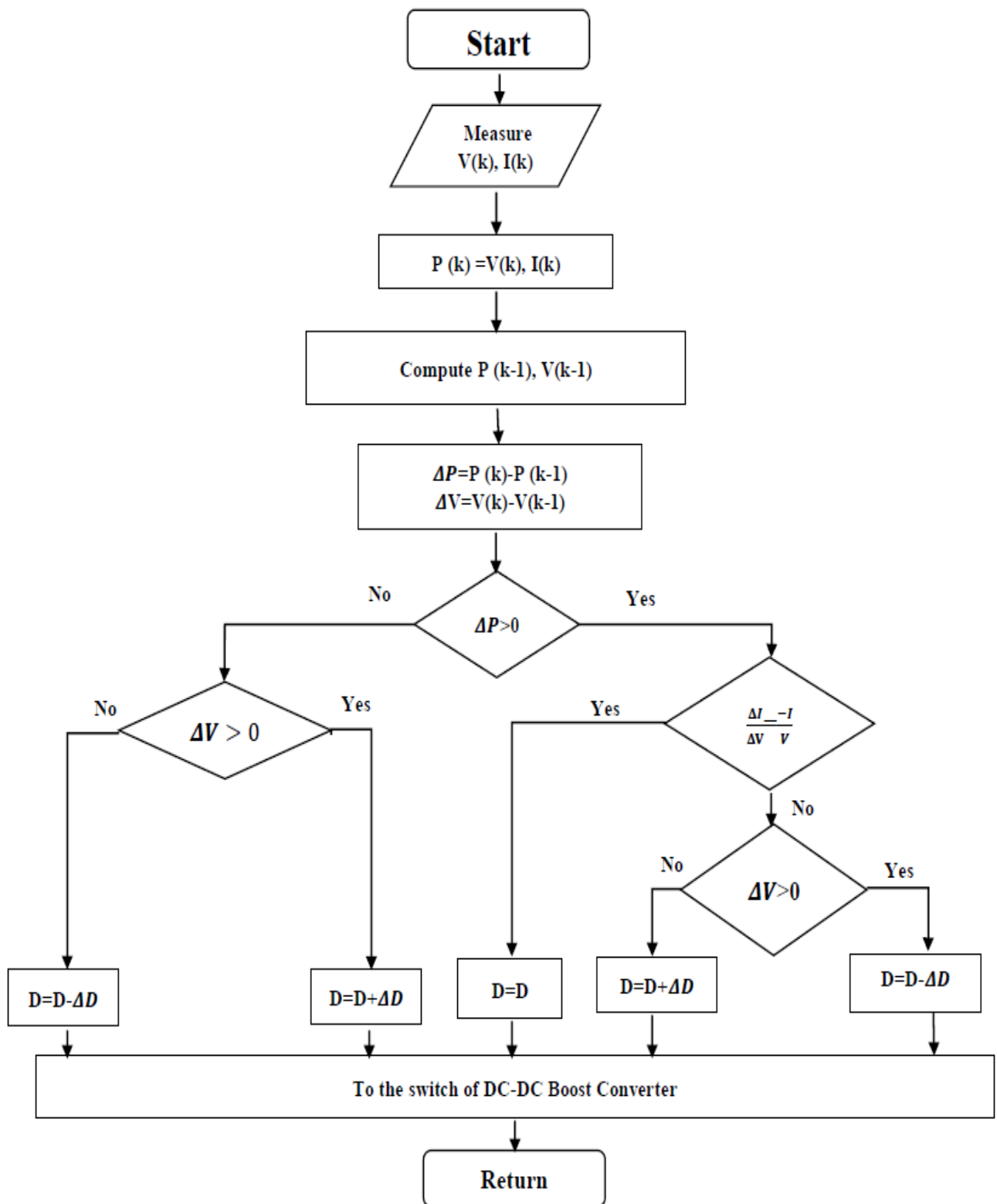
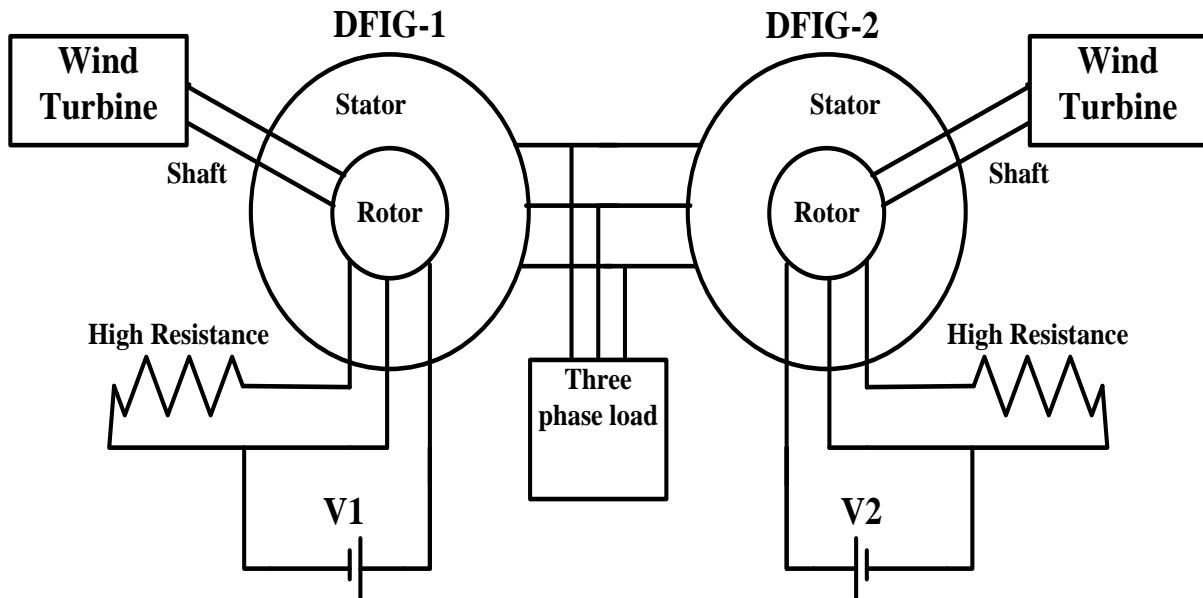
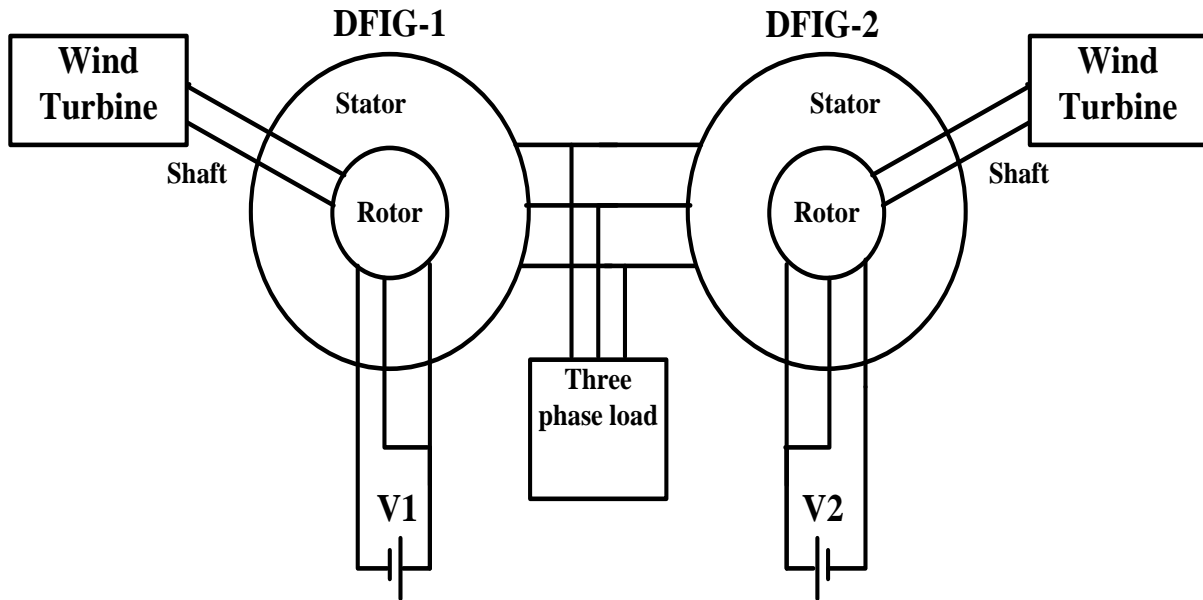
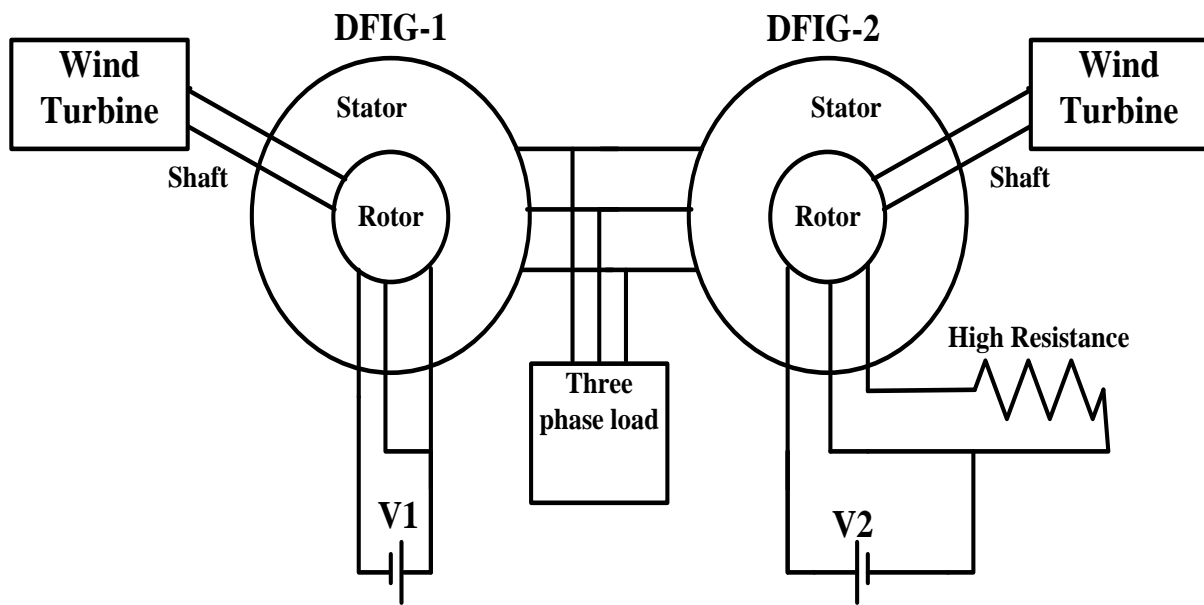


Fig. 6.6 Modified P & O algorithm control flowchart

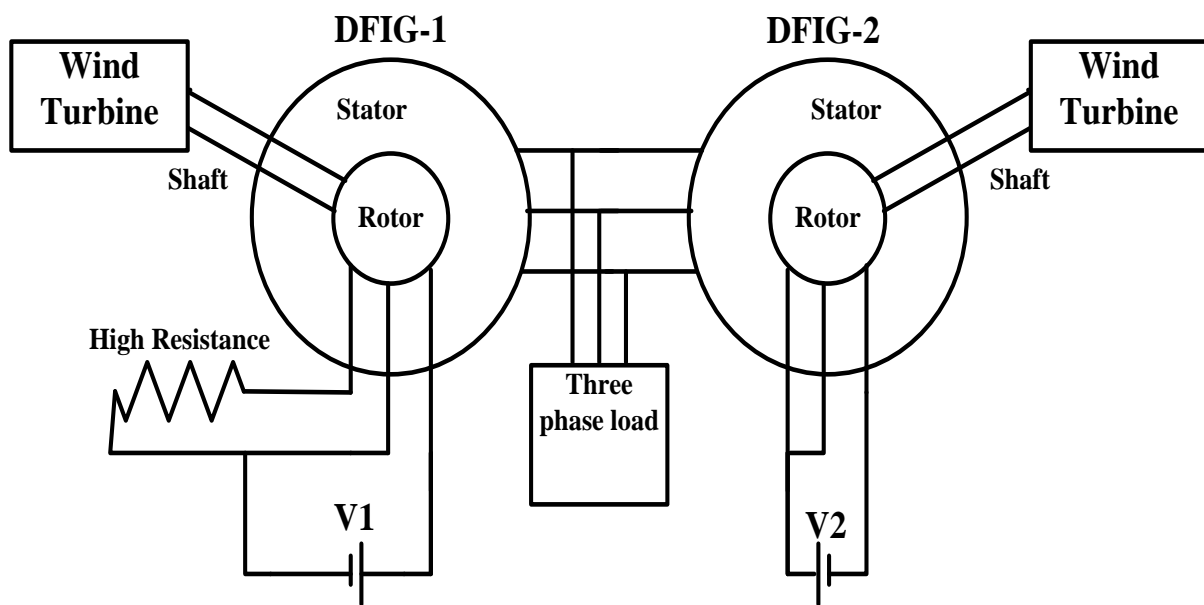
6.5 TWO-LEAD AND THREE-LEAD TOPOLOGIES IN PARALLEL

In this section, the parallel operation of two DFIG's of different ratings has been discussed. The two DFIGs used for analysis are rated at 4 KW (5.4 HP) and 746 W (1 HP) respectively. The 4 KW DFIG has been termed “DFIG-1” while the 746 W DFIG is referred to as “DFIG-2” in this work. The parameters of DFIG-1 and DFIG-2 are given in the Appendix A. The illustration of the systems have been done by figure 6.7.





(c)



(d)

Fig. 6.7 Parallel connection of DFIG-1 and DFIG-2 (a) Both DFIGs connected in three-lead (b) Both DFIGs connected in two-lead (c) DFIG-1 is three-lead while DFIG-2 is two-lead (d) DFIG-1 is two-lead while DFIG-2 is three-lead

The DFIGs have been run at a fixed shaft speed of 1500 rpm. For the four combinations illustrated in figure 6.7, analysis of the output voltage variation due to the following effects has been done:

- Introduction of loads.
- A ten percent dip in the rotor voltage of DFIG-1.
- A ten percent dip in the rotor voltage of DFIG-2.

The main objective of this investigation was to determine the following:

- The dependence of the change in output voltage on the type of interconnection i.e. two-lead versus three-lead.
- The dependence of change in output voltage on the rating of the DFIG.

6.6 RESULTS AND ANALYSIS

For the proposed topologies, investigations have been carried out both in simulation as well as hardware. For hardware experimentation, a DFIG referred to as ‘DFIG-2’ in this work, has been used. The parameters of DFIG-2 have been mentioned in Appendix A.

6.6.1 Comparative of DC Two-Lead System with Three-Lead System

Simulation based experiments have been done to evaluate and compare the transient response and the steady state response of the two topologies illustrated in figure 6.1 and 6.2. For the two-lead topology, a 1000 Ω resistance has been connected between the two rotor terminals. Table 6.1 contains the details of the inputs and output of the topologies corresponding to which figures 6.8 to 6.15 have been obtained.

Table 6.1 Input and output of two-lead topology and three-lead topology

Topology	Rotor Voltage (DC)	Shaft Speed	Stator Voltage (AC)
Two-lead	42 V	1500 rpm	400 V
Three-lead	39 V	1500 rpm	400 V

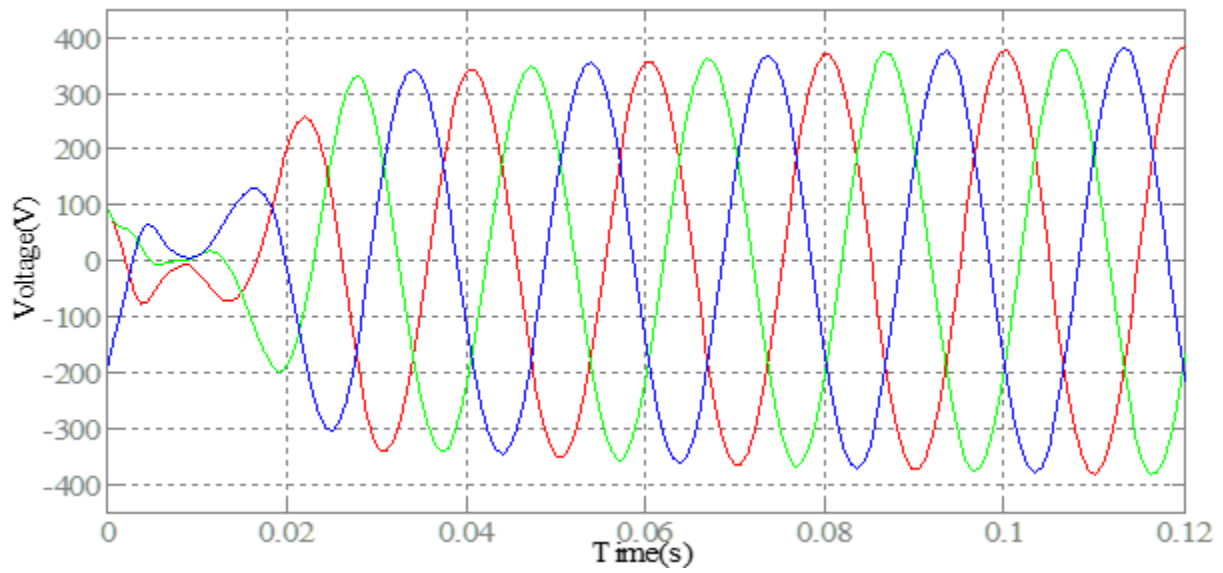


Fig. 6.8 Starting transients of two-lead connection of DFIG-2

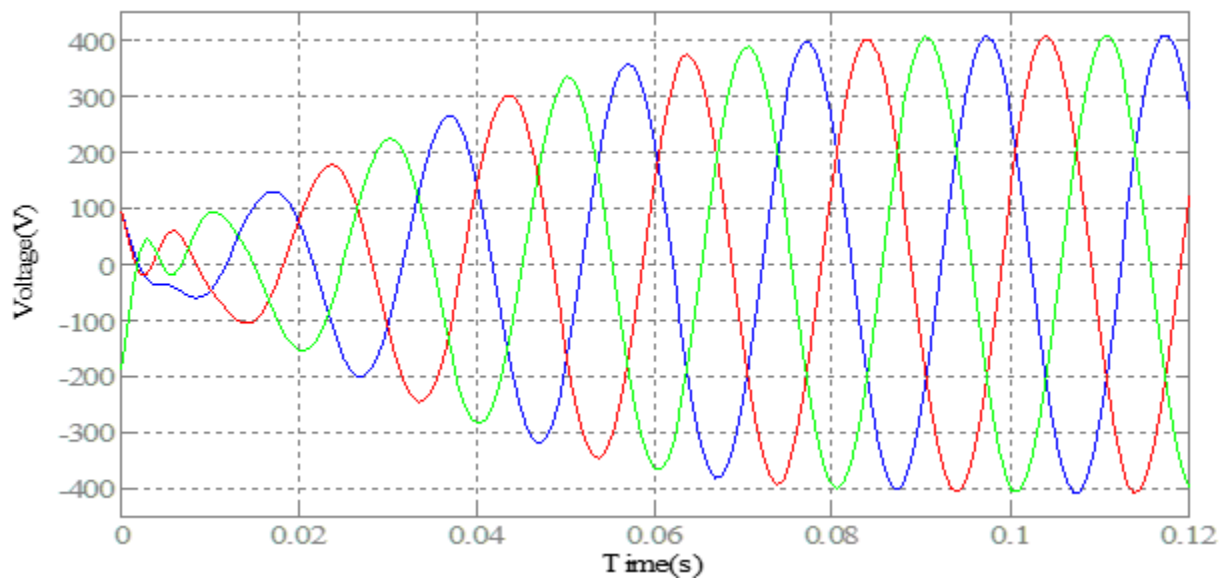


Fig. 6.9 Starting transients of three-lead connection of DFIG-2

From figures 6.8 and 6.9 it can be inferred that it is evident that the two-lead connection gives faster settling transients as compared to the three-lead connection.

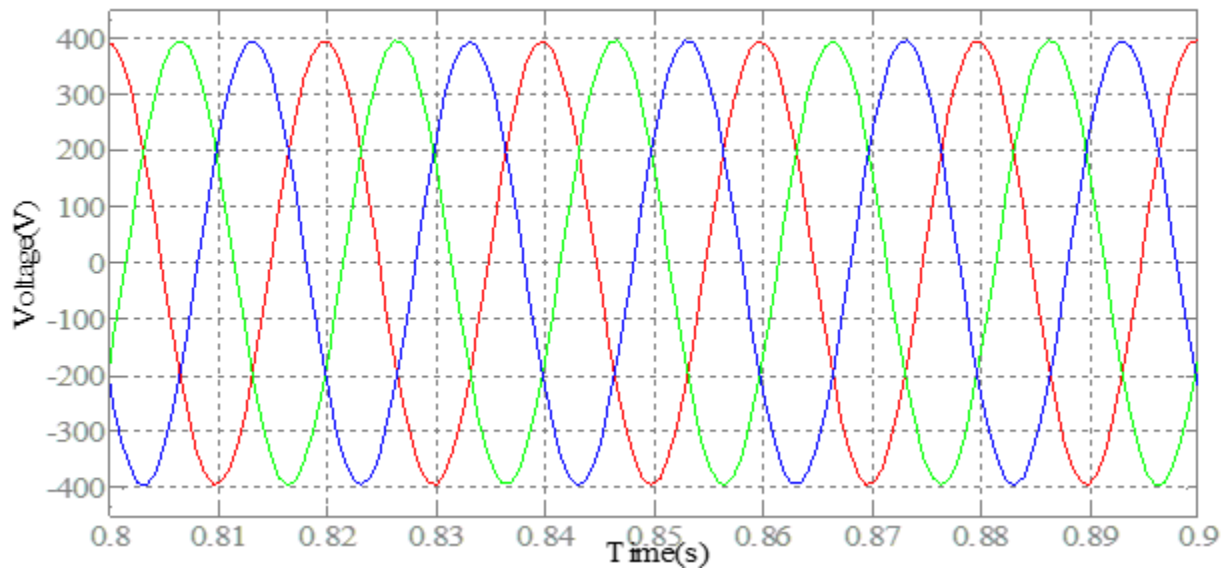


Fig. 6.10 Steady state voltages of two-lead connection of DFIG-2

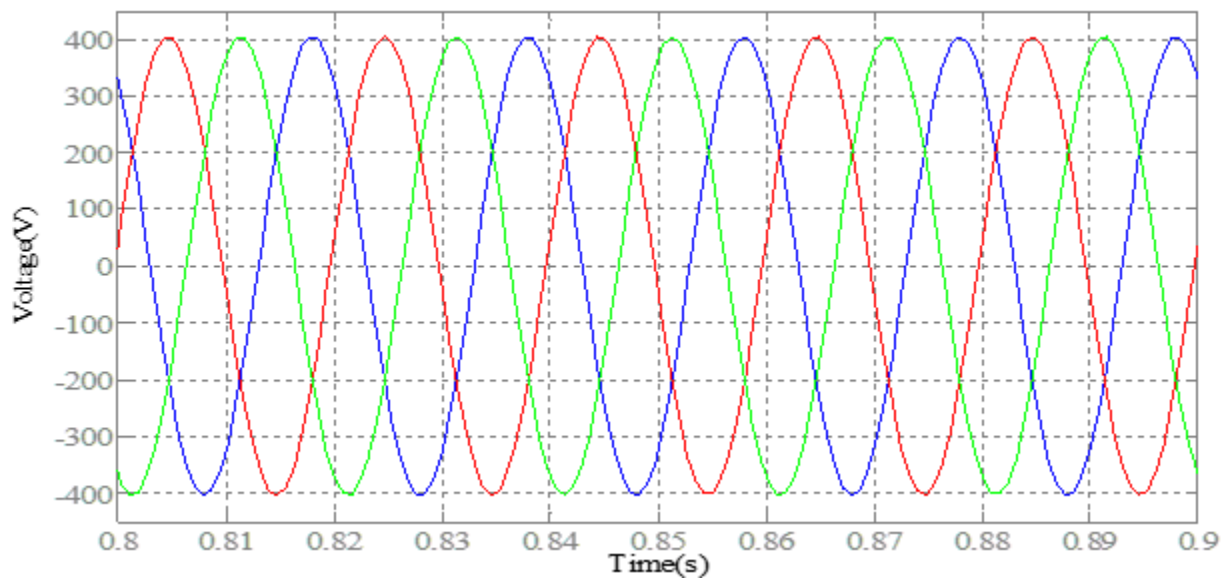


Fig. 6.11 Steady state voltages of three-lead connection of DFIG-2

From figures 6.10 and 6.11 it can be inferred that the three-lead connection yields greater output as compared to the two-lead connection. For obtaining a stator voltage output of 400 V, the two-lead connection requires a dc rotor voltage of 42 V while the three-lead connection is given a dc rotor voltage of 39 V.

Figures 6.12 and 6.13 illustrate the THD analysis of the starting transients of the DFIG stator voltage for the two-lead and three-lead topology. The THD has been computed from 0 second for 10 cycles before steady state is attained.

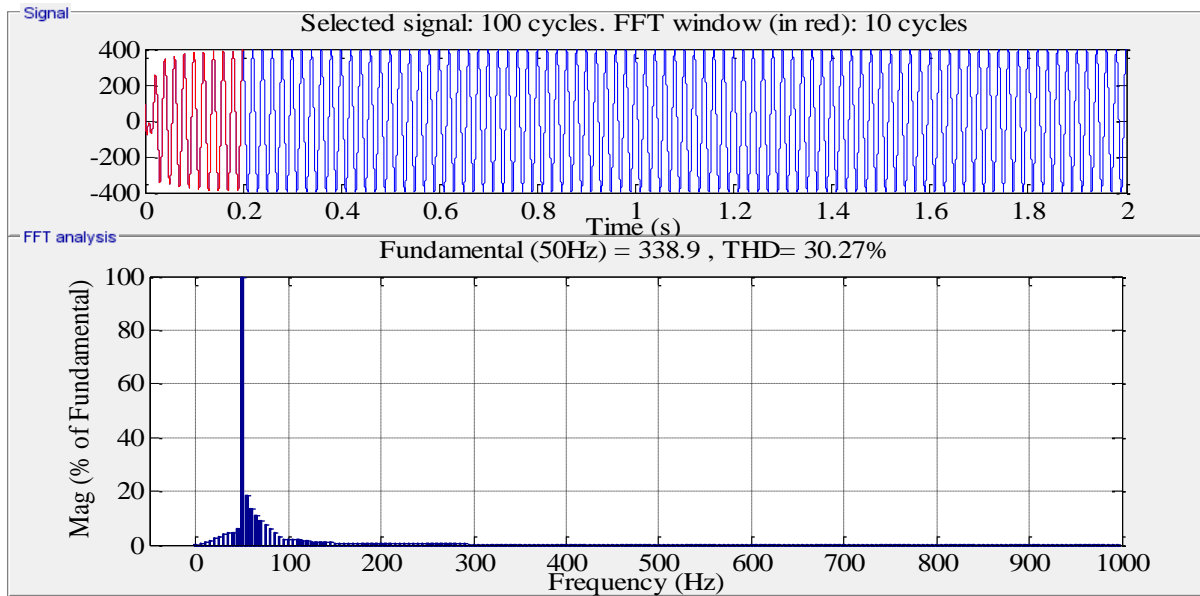


Fig. 6.12 Transient state THD analysis of DFIG-2 two-lead configuration

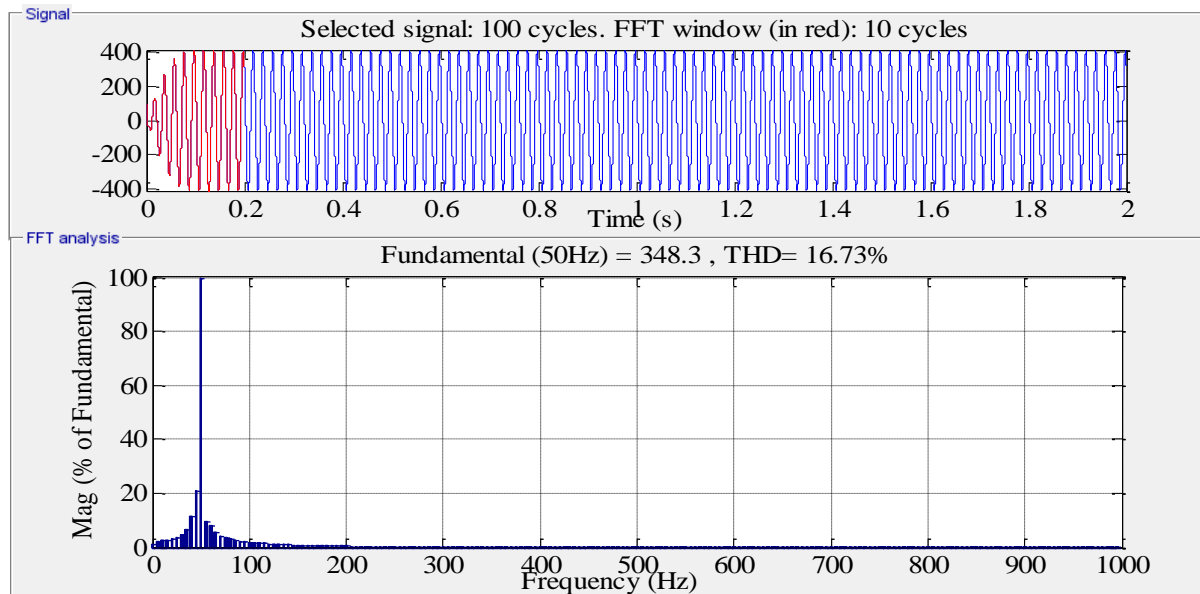


Fig. 6.13 Transient state THD analysis of DFIG-2 three-lead configuration

From figures 6.12 and 6.13 it can be observed that the three-lead connection yields a much lower value of stator voltage THD as compared to the two-lead connection.

Figures 6.14 and 6.15 illustrate the THD analysis at steady state of one stator phase voltage out of the three phases for both the two-lead and the three-lead configurations.

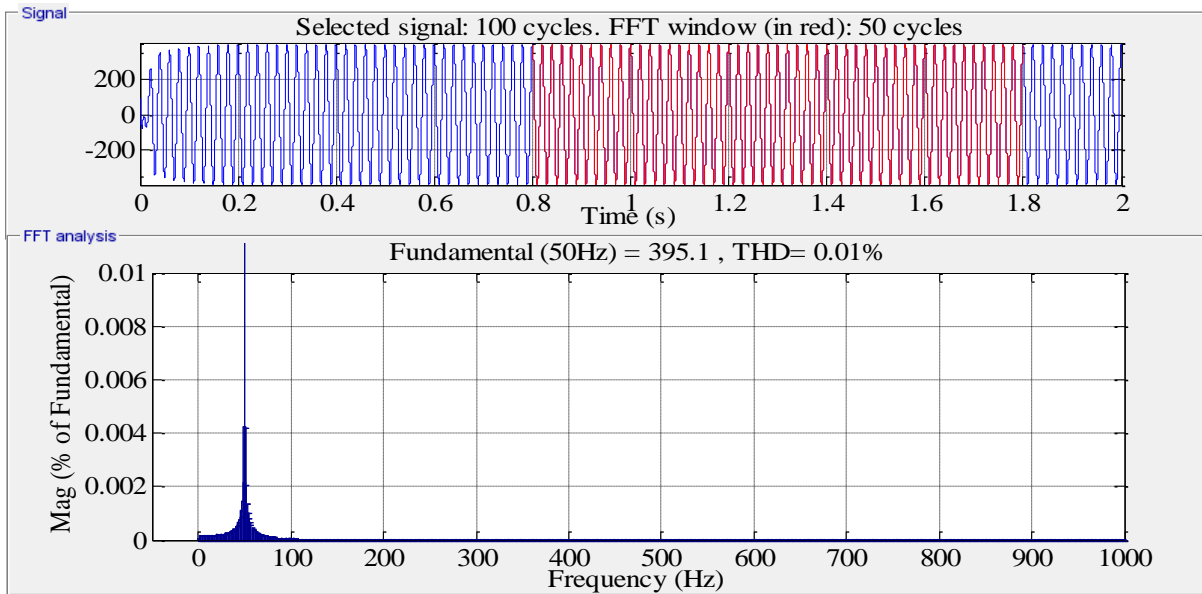


Fig. 6.14 Steady state THD analysis of DFIG-2 two-lead configuration

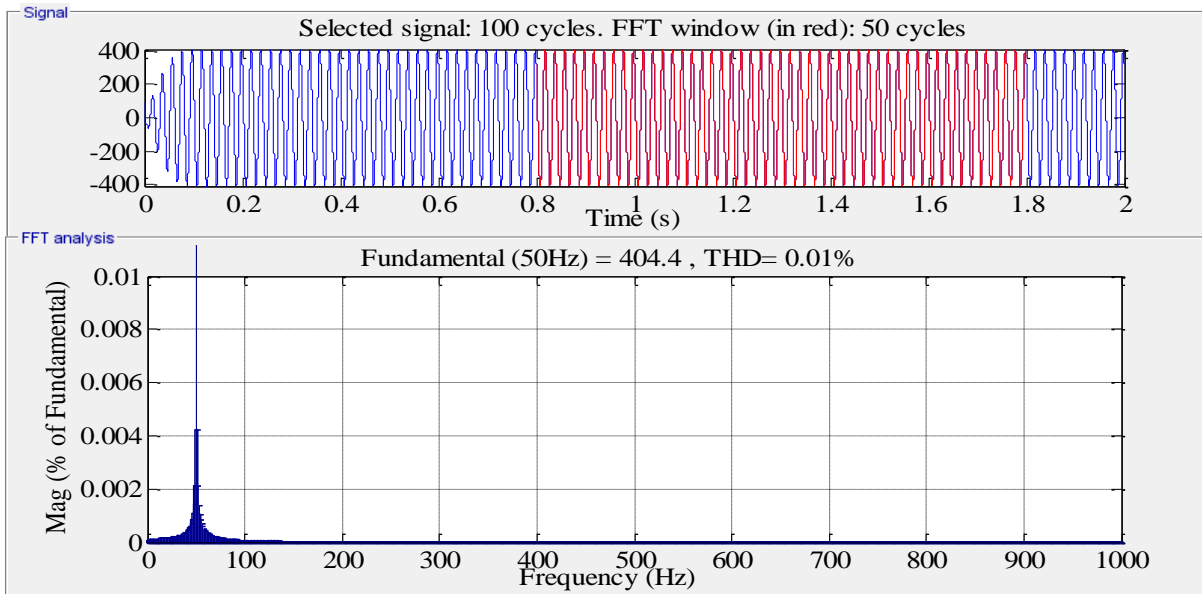


Fig. 6.15 Steady state THD analysis of DFIG-2 three-lead configuration

The analysis of figures 6.14 and 6.15 draws out the conclusion that a near perfect sinusoidal is obtained at steady state for both topologies.

A close scrutiny of results displayed by figures 6.8 to 6.15 yields the following deductions:

- Two-lead DFIG connection gives faster settling transients as compared to its three-lead counterpart.
- Three-lead DFIG connection yields a much lower value of stator voltage THD as compared to the two-lead connection.

6.6.2 Two-Lead and Three-Lead Systems excited by Boost Converter

In this section, simulation results of two-lead and three-lead systems of DFIG-2 when excited by a Boost converter has been presented (figure 6.4). The boost converter has been made to operate at a 50% duty cycle for both two-lead and three-lead connections of the DFIG-2. The switching frequency is 3900 Hz.

For the duration of the simulation i.e. six seconds, the DFIG-2 stator had been loaded as per the following scheme:

- Purely resistive load between one second and two second.
- An R-L load of power factor 0.9 between three second and five second.

Other than the above mentioned durations, the DFIG-2 is made to run on no load. The shaft speed of DFIG-2 has been fixed at 1500 rpm. Figures 6.16 and 6.17 are the illustrations of the stator phase A output voltage and load current respectively of the DFIG for the two-lead connection and three-lead connection.

For the two-lead connection, the output of the stator is a balanced three phase voltage with a frequency of 50 Hz. For a rotor voltage of 31 V, the DFIG no-load phase voltage is 219 V at steady state. The voltage falls to about 173 V when the resistive load is connected. The resistive load draws a current of 1.27 A at steady state. The stator voltage attains a value of 136 V with the application of RL load. The RL load draws a current equal to 1.41 A at steady state.

For the three-lead connection, the output of the stator is a balanced three phase voltage with a frequency of 50 Hz. For a rotor voltage of 26 V, the DFIG no-load phase voltage is 219 V at steady state. The voltage falls to about 168 V when the resistive load is connected. The resistive load draws a current of 1.24 A at steady state. The stator voltage attains a value of 131 V with the application of RL load. The RL load draws a current equal to 1.38 A at steady state.

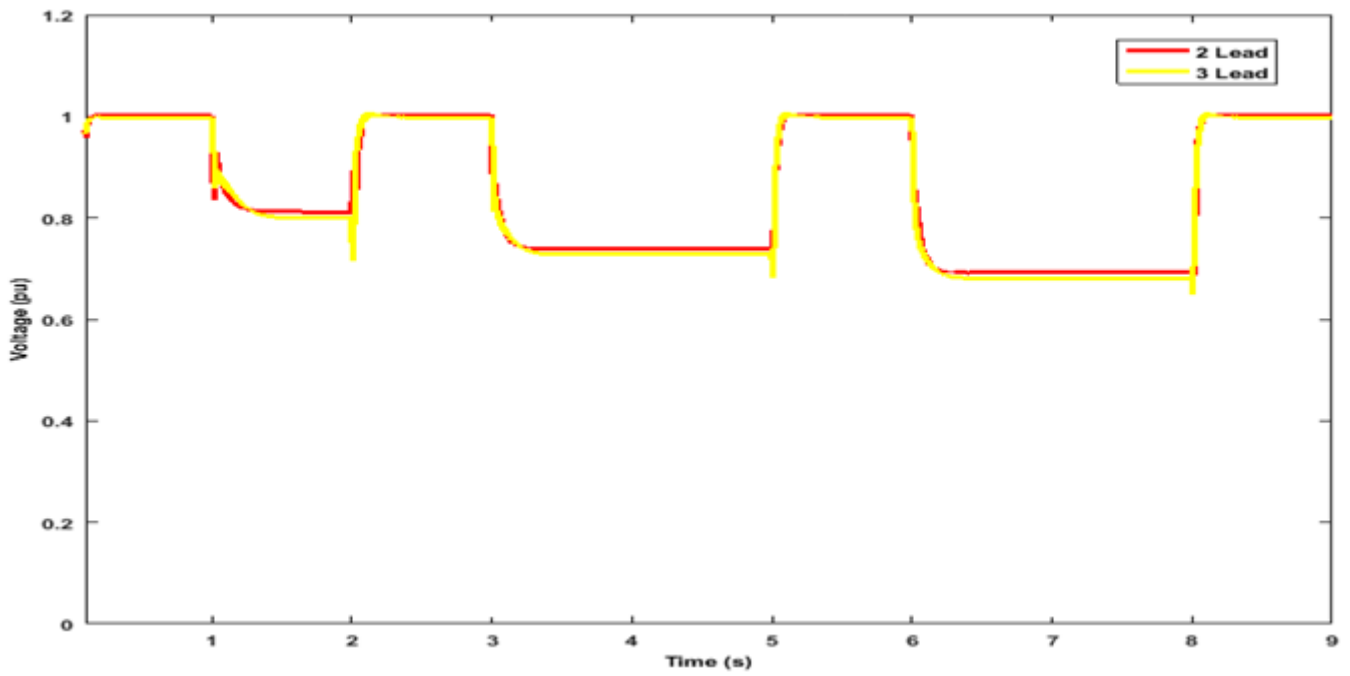


Fig. 6.16 DFIG phase A stator voltage in pu under loading conditions

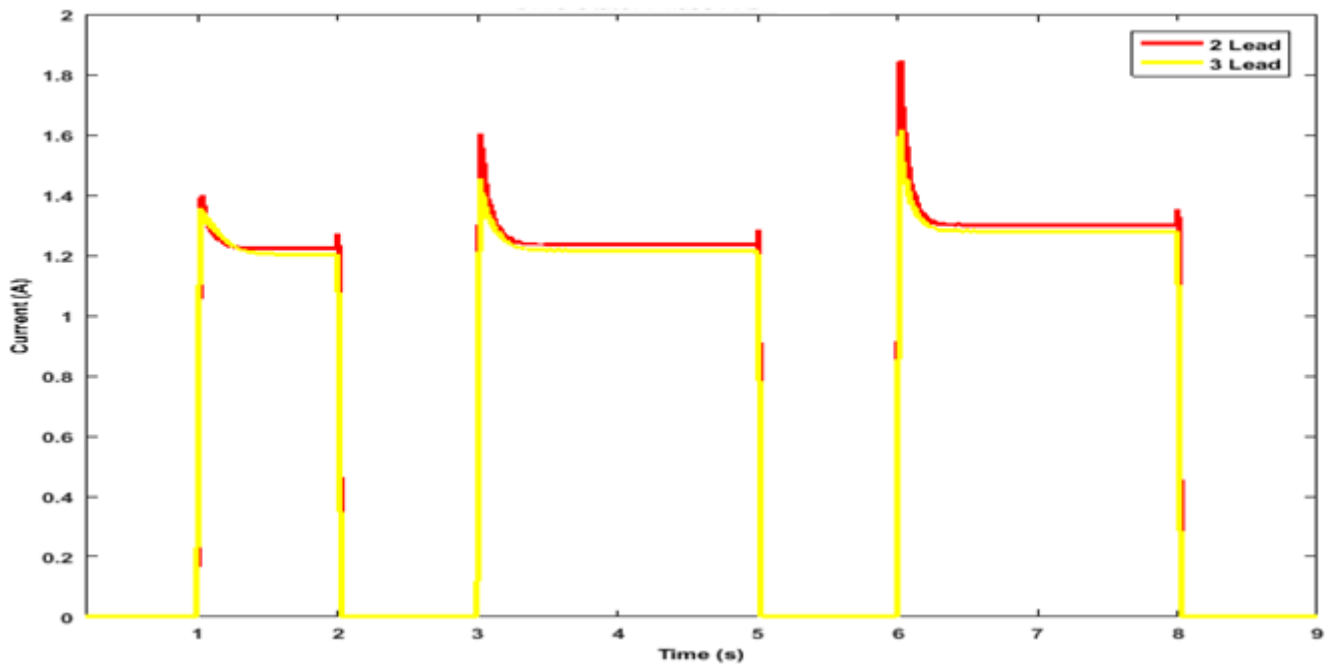


Fig. 6.17 DFIG phase A load current

Table 6.2 is a comparison of the two-lead DFIG-2 and three-lead DFIG-2 configurations when fed by the Boost converter.

Table 6.2 Comparison of the boost fed two-lead and three-lead DFIG-2 configurations

Connection Type	V_{THD}	I_{THD}		Voltage Regulation		Current (A)	
		R Load	RL Load	R Load	RL Load	R Load	RL Load
Two-lead	0.81	0.01	0.01	0.21	0.38	1.27	1.41
Three-lead	0.15	0	0	0.23	0.4	1.25	1.38

A close scrutiny of Table 6.2 yields the following deductions:

- The load current total harmonic distortion (THD) is minimum when the three-lead DFIG connection is incorporated.
- Among the two configurations, two-lead DFIG connection results in the better voltage regulation.

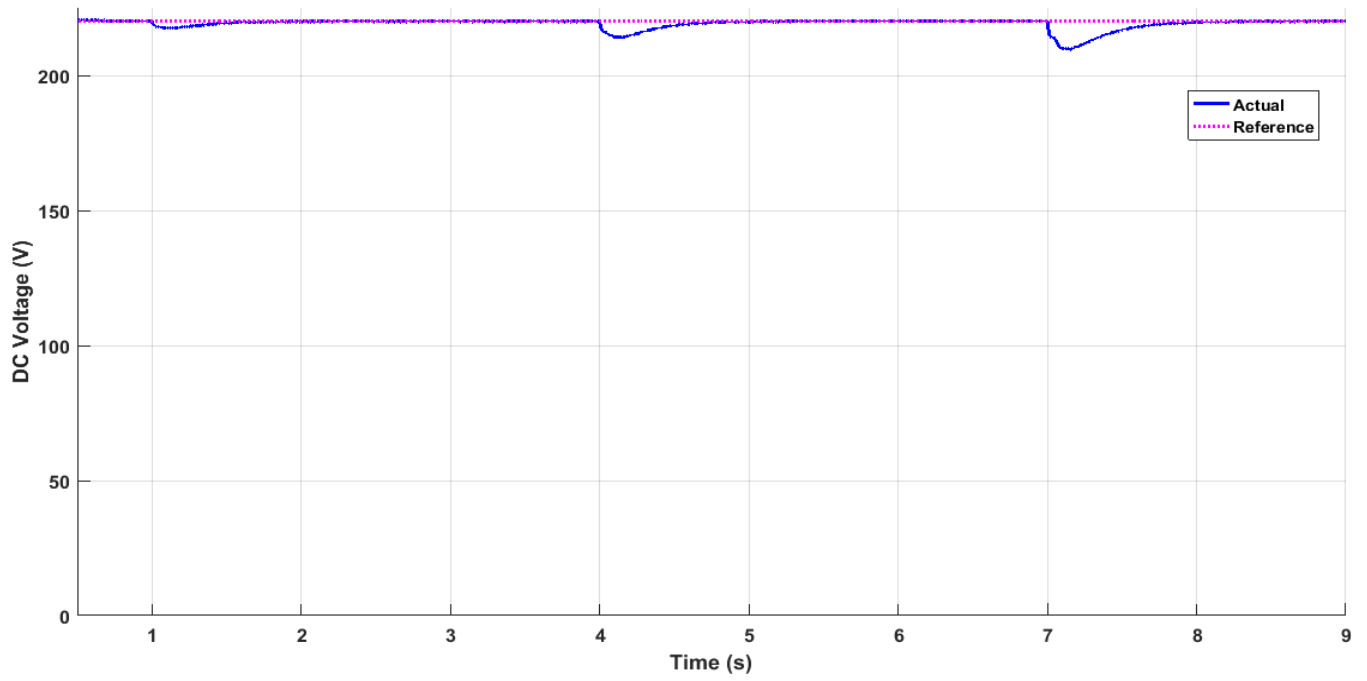
6.6.3 Three-Lead DFIG System excited by Buck Converter

In this section, the results related to a three-lead DFIG system with rotor excited by a Buck converter has been discussed. The block diagram of the system has been illustrated in figure 6.4. A DFIG-DC system has been formed by rectifying and filtering the stator voltage output of DFIG-2. The DC voltage so obtained has been held constant under variation of wind speed. Close loop voltage control has been applied by generating proper switching signals of the Buck converter connected to the rotor of the DFIG-2.

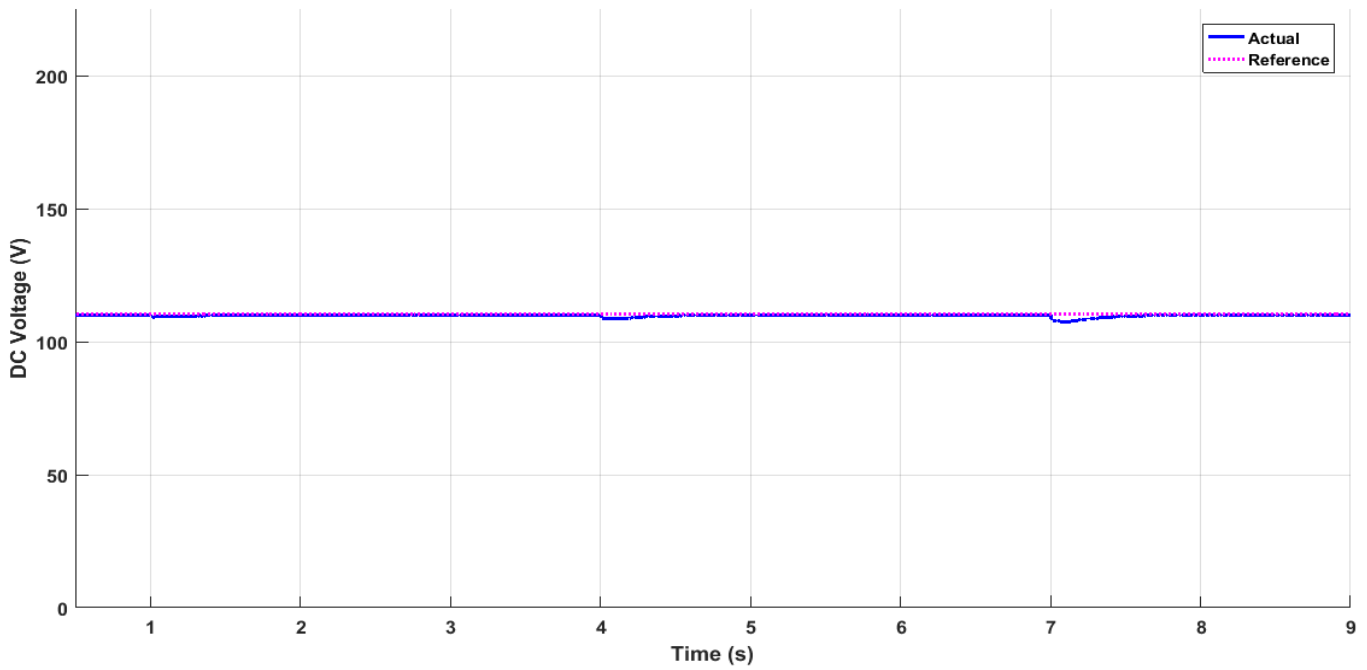
The relevant data related to the simulation are as follows:

- Buck Converter input voltage is 50 V.
- The DFIG-DC system has been successively loaded by resistances of rating 100 W, 200 W and 300 W at one second, four second and seven second respectively. At the end of seven seconds, the load on the system is 600 W.
- The wind speed input at the turbine is 12 m/s from 0 to 3 seconds, 10 m/s from 3 to 6 seconds and 7 m/s thereafter.

The DFIG-DC system with voltage control via Buck converter connected on the DFIG rotor is a very simple method of control. In the proposed system, the set point can be varied over a large range while ensuring proper regulation. The graph of the DFIG-DC voltage against time has been obtained for the input data mentioned above. Figures 6.18 is the graph of the DFIG-DC system output plotted against time with two different voltage references.



(a)



(b)

Fig. 6.18 DFIG-DC system output voltage with reference (a) 220 V (b) 110 V

It can be observed in figure 6.18 that the introduction of loads at one second, four second and seven second results in a change in the DFIG-DC voltage. However, the output is regulated to the set point in less than one

second. The control mechanism also offsets any variation in the output due to changing wind speeds at three second and six second.

In this section it has been conclusively established that a three-lead DFIG DC system with rotor excited by Buck converter is simple in terms of control implementation. Hence, it can be employed for constructing isolated DFIG DC system instead of the existing topologies which use a greater number of power electronic converters with complex control strategies. Two-lead DFIG DC system with rotor excited by Buck converter is not considered since it is less efficient as compared to the three-lead system.

6.6.4 MPPT implementation on DFIG DC System

For the two-lead and three-lead DFIG DC systems illustrated in figure 6.5, MPPT has been implemented using P&O algorithm as well as modified P&O algorithm. DFIG-1 has been used for the MPPT simulations. The operating range of a DFIG is usually $\pm 30\%$ slip. Hence, the shaft speed has been maintained as follows:

- DFIG shaft speed is 1950 rpm from 0 to 3 seconds (slip= -0.3).
- DFIG shaft speed is 1500 rpm from 3 to 5 seconds (slip= 0).
- DFIG shaft speed is 1050 rpm from 5 to 7 seconds (slip= +0.3).

Figures 6.19 to 6.22 illustrate the obtained results.

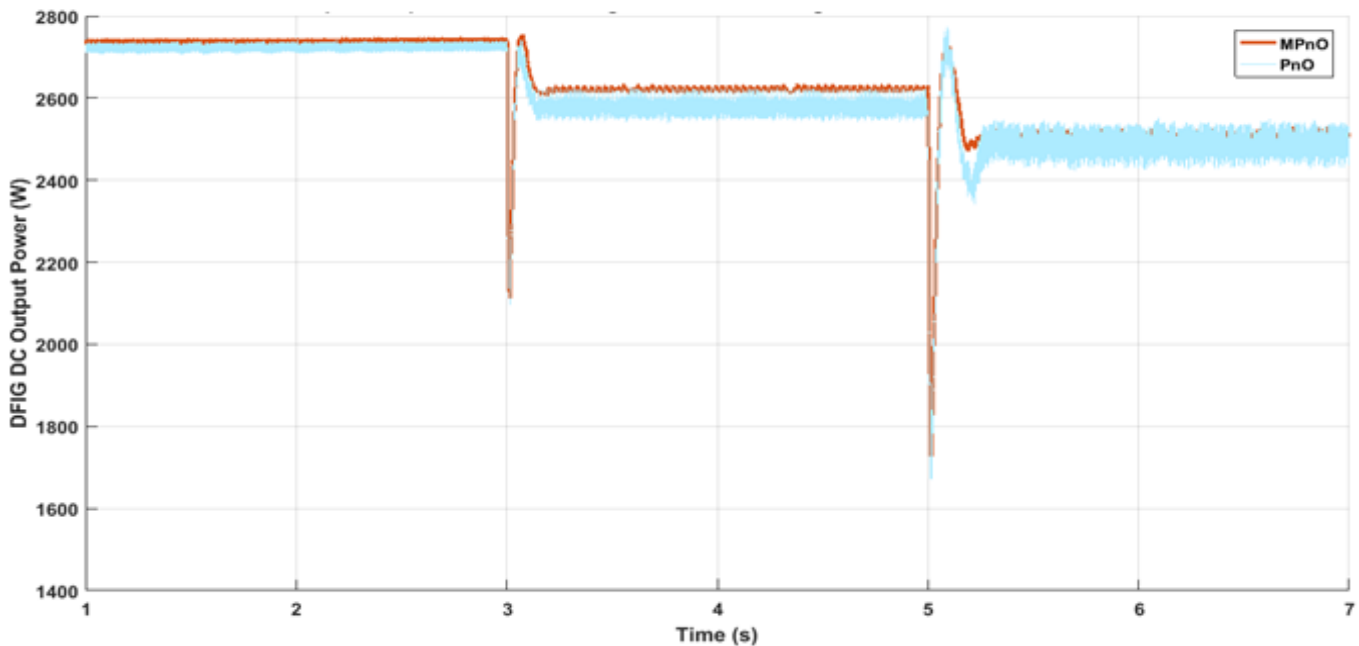


Fig. 6.19 Output power of three-lead DFIG-DC system with MP&O and P&O MPPT

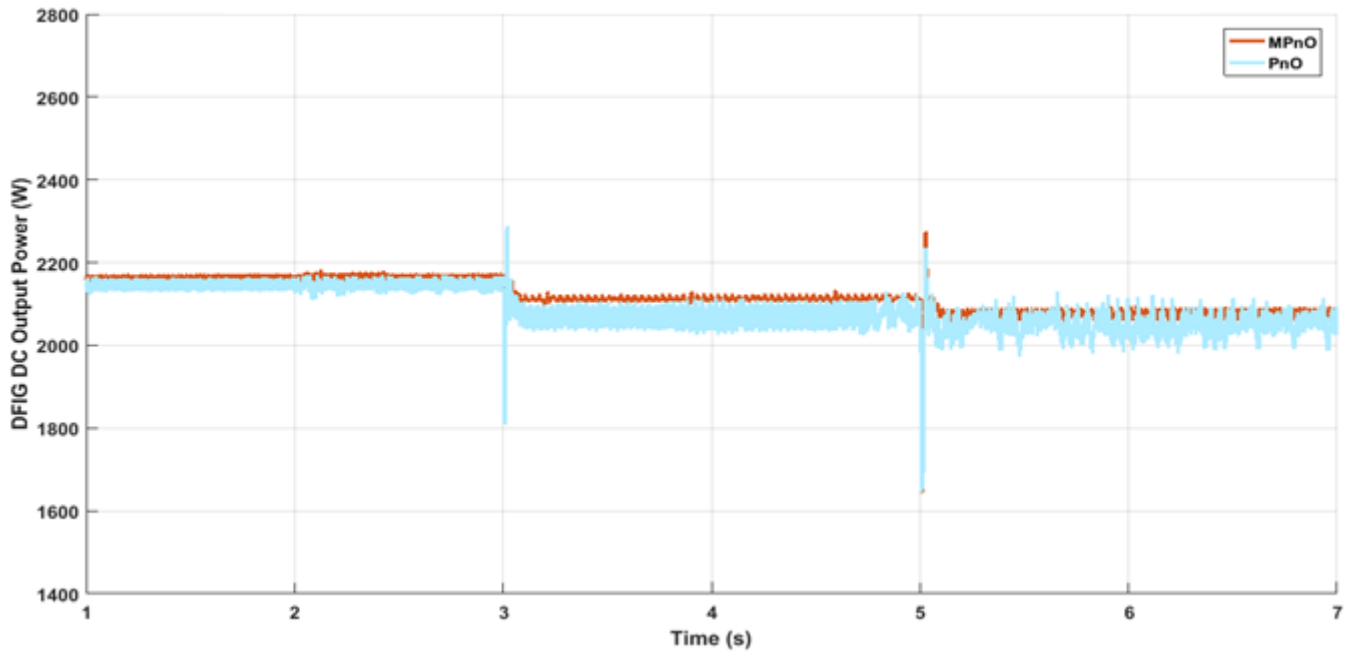


Fig. 6.20 Output power of two-lead DFIG-DC system with MP&O and P&O MPPT

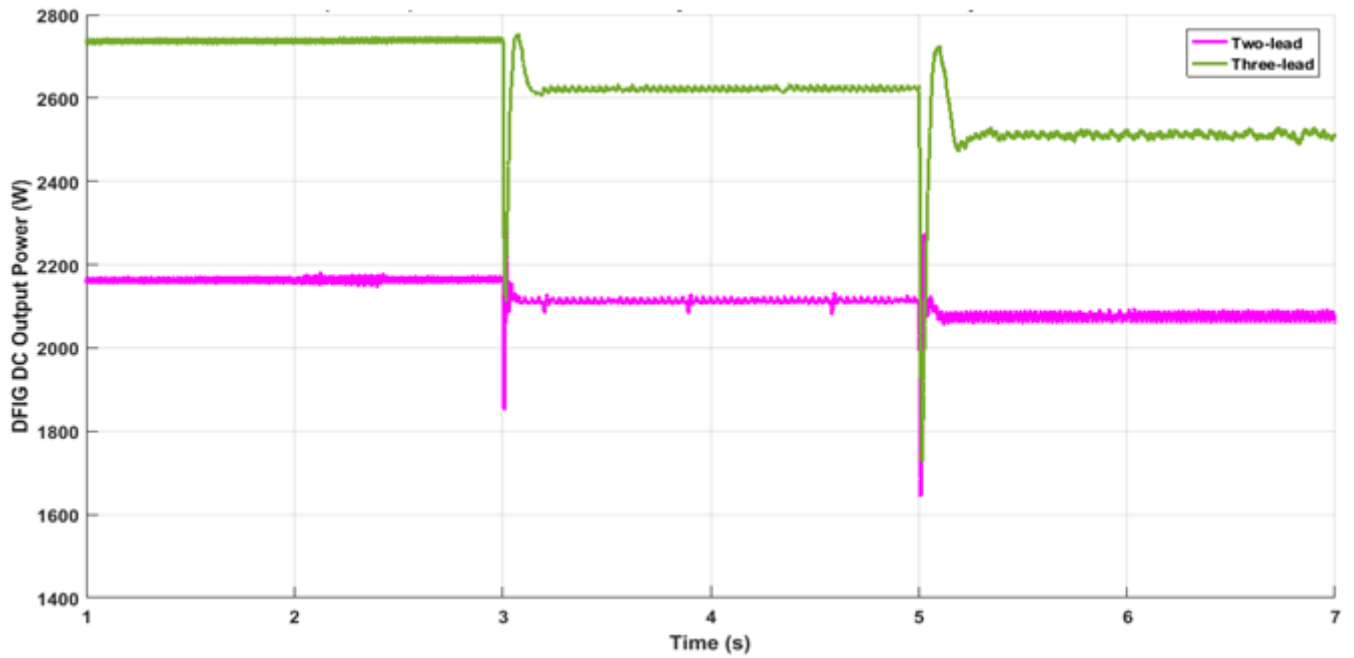


Fig. 6.21 Comparison of two-lead and three-lead power outputs for MP&O Algorithm

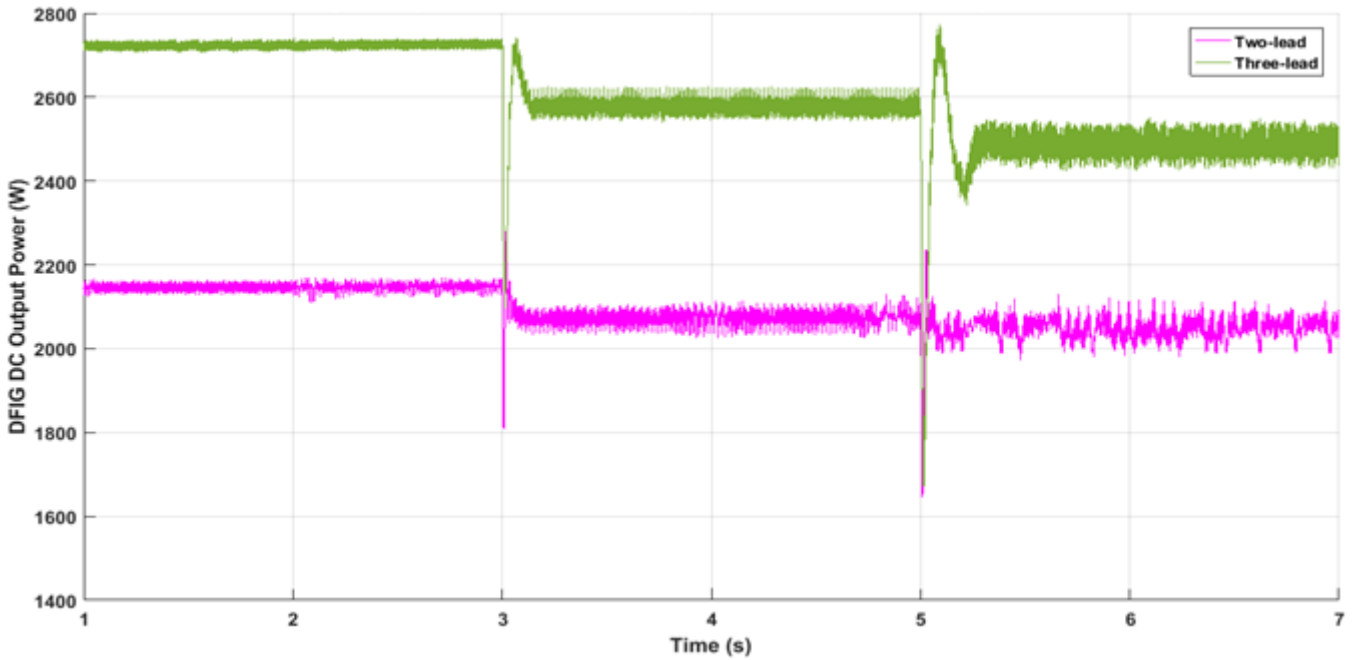


Fig. 6.22 Comparison of two-lead and three-lead power outputs for P&O Algorithm

Scrutiny of figures 6.19 to 6.22 yield the following conclusions:

- The MP&O method of MPPT is superior to the P&O method owing to significantly less fluctuations about the maximum power point.
- Three-lead DFIG configuration is more efficient as compared to the two-lead DFIG configuration. For the same input conditions, the output yield of three-lead DFIG DC is greater than that of its two-lead counterpart.

6.6.5 Parallel connection of DFIG topologies

In this section, the results related to the parallel operation of two DFIG's of different ratings has been discussed. The two DFIGs used for analysis are rated at 4 KW (DFIG-1) and 746 W (DFIG-2) respectively. The parameters of DFIG-1 and DFIG-2 are given in appendix A. The DFIGs have been run at a fixed shaft speed of 1500 rpm. As illustrated in figure 6.7, the four different parallel interconnections investigated in this work are as follows:

- 1) DFIG-1 as well as DFIG-2 are operating in the three-lead topology.
- 2) DFIG-1 as well as DFIG-2 are operating in the two-lead topology.
- 3) DFIG-1 is connected in the three-lead topology while DFIG-2 is connected in the two-lead topology.
- 4) DFIG-1 is connected in the two-lead topology while DFIG-2 is connected in the three-lead topology.

The parallel combination of DFIGs have been loaded with a balanced three-phase resistive load of 50 Ω . An additional balanced three-phase resistive load of 100 Ω has been introduced on the system from 1 second to 2 second. The simulation has been run for 3 seconds.

The effect of change in rotor voltage on the stator output of the parallel combination has been investigated for all the four cases. The rotor voltage corresponding to the rated stator voltage of both machines has been varied as mentioned below:

- The rotor voltage of DFIG-1 has been decreased by 10% while retaining the original rotor voltage of DFIG-2. The effect on the output voltage of the parallel connection has been noted.
- The rotor voltage of DFIG-2 has been decreased by 10% while retaining the original rotor voltage of DFIG-1. The effect on the output voltage of the parallel connection has been noted.

A. DFIG-1 as well as DFIG-2 operating in the three-lead topology

For parallel connection, the DFIG stator voltage of both machines have been initially maintained at a phase voltage of 230 V. For 230 V stator output, DFIG-1 needs a rotor voltage of 14.56 V while DFIG-2 rotor voltage has to be kept at 94.64 V. Table 6.3 summarises the result of the investigations carried out on the parallel combination of the three-lead topology of DFIGs.

Table 6.3 Parallel combination of three-lead topologies of DFIG-1 and DFIG-2

S.No.	Rotor Voltage (V)		Stator Voltage (V)	
	DFIG-1 (3- Lead)	DFIG-2 (3- Lead)	Before Dip	After Dip
1	14.56	94.64	230	NA
2	13.1	94.64	230	218
3	14.56	85.18	230	219

From Table 6.3, it can be clearly observed that the change in output voltage of the parallel combination is the same if the rotor voltage of either machine is dipped by the same percentage.

B. DFIG-1 as well as DFIG-2 operating in the two-lead topology

For parallel connection, the DFIG stator voltage of both machines have been initially maintained at a phase voltage of 230 V. For 230 V stator output, DFIG-1 needs a rotor voltage of 16.81 V while DFIG-2 rotor

voltage has to be kept at 109.3 V. Table 6.4 summarises the result of the investigations carried out on the parallel combination of the two-lead topology of DFIGs.

Table 6.4 Parallel combination of two-lead topologies of DFIG-1 and DFIG-2

S.No.	Rotor Voltage (V)		Stator Voltage (V)	
	DFIG-1 (2-Lead)	DFIG-2 (2-Lead)	Before Dip	After Dip
1	16.81	109.3	230	NA
2	15.13	109.3	230	218.5
3	16.81	98.37	230	219

From Table 6.4, it can be clearly observed that the change in output voltage of the parallel combination is the same if the rotor voltage of either machine is dipped by the same percentage.

C. Three-lead DFIG-1 and two-lead DFIG-2 operating in parallel

For parallel connection, the DFIG stator voltage of both machines have been initially maintained at a phase voltage of 230 V. For 230 V stator output, DFIG-1 needs a rotor voltage of 14.56 V while DFIG-2 rotor voltage has to be kept at 109.3 V. Table 6.5 summarises the result of the investigations carried out on the parallel combination of the three-lead/ two-lead hybrid topology of DFIGs.

Table 6.5 Parallel combination of three-lead DFIG-1 and two-lead DFIG-2 topology

S.No.	Rotor Voltage (V)		Stator Voltage (V)	
	DFIG-1 (3-Lead)	DFIG-2 (2-Lead)	Before Dip	After Dip
1	14.56	109.3	230	NA
2	13.1	109.3	230	207.6
3	14.56	98.37	230	208

From Table 6.5, it can be clearly observed that the change in output voltage of the parallel combination is the same if the rotor voltage of either machine is dipped by the same percentage.

D. Two-lead DFIG-1 and three-lead DFIG-2 operating in parallel

For parallel connection, the DFIG stator voltage of both machines have been initially maintained at a phase voltage of 230 V. For 230 V stator output, DFIG-1 needs a rotor voltage of 16.81 V while DFIG-2 rotor voltage has to be kept at 94.64 V. Table 6.6 summarises the result of the investigations carried out on the parallel combination of the two-lead/ three-lead hybrid topology of DFIGs.

Table 6.6 Parallel combination of two-lead DFIG-1 and three-lead DFIG-2 topology

S.No.	Rotor Voltage (V)		Stator Voltage (V)	
	DFIG-1 (2-Lead)	DFIG-2 (3-Lead)	Before Dip	After Dip
1	16.81	94.64	230	NA
2	15.13	94.64	230	214.6
3	16.81	85.18	230	214.6

From Table 6.6, it can be clearly observed that the change in output voltage of the parallel combination is the same if the rotor voltage of either machine is dipped by the same percentage.

Table 6.7 is a comparison of the four topologies mentioned in figures 6.7 to 6.10 under loading conditions.

Table 6.7 Comparison of the DFIG parallel topologies under loading conditions

S.No.	Topology	Rotor Voltage (V)		Stator Voltage (V)	
		DFIG-1	DFIG-2	Before Loading	After Loading
1	Both three-lead	14.56	94.64	230	199
2	Both two-lead	16.81	109.3	230	199
3	3-lead DFIG-1 and 2-lead DFIG-2	14.56	109.3	230	189.5
4	2-lead DFIG-1 and 3-lead DFIG-2	16.81	94.64	230	196

From Table 6.7, it can be inferred that the largest dip in voltage under loading conditions occurs in the 3-lead DFIG-1 and 2-lead DFIG-2 parallel combination.

A close scrutiny of Tables 6.3 to 6.7 makes it evident that the three-lead/ three-lead combination of DFIGs is best suited for parallel operation.

6.6.5 Hardware Results of Two-lead and Three-lead DFIG topologies

In this section the hardware validation of the two-lead and the three-lead DFIG topologies has been discussed. DFIG-2 has been used for the hardware operation. The parameters of DFIG-2 have been mentioned in Appendix A. The rotor of DFIG-2 has been fed by a buck converter whose constructional details are mentioned in Appendix B. Figure 6.23 is a snapshot of the hardware setup.

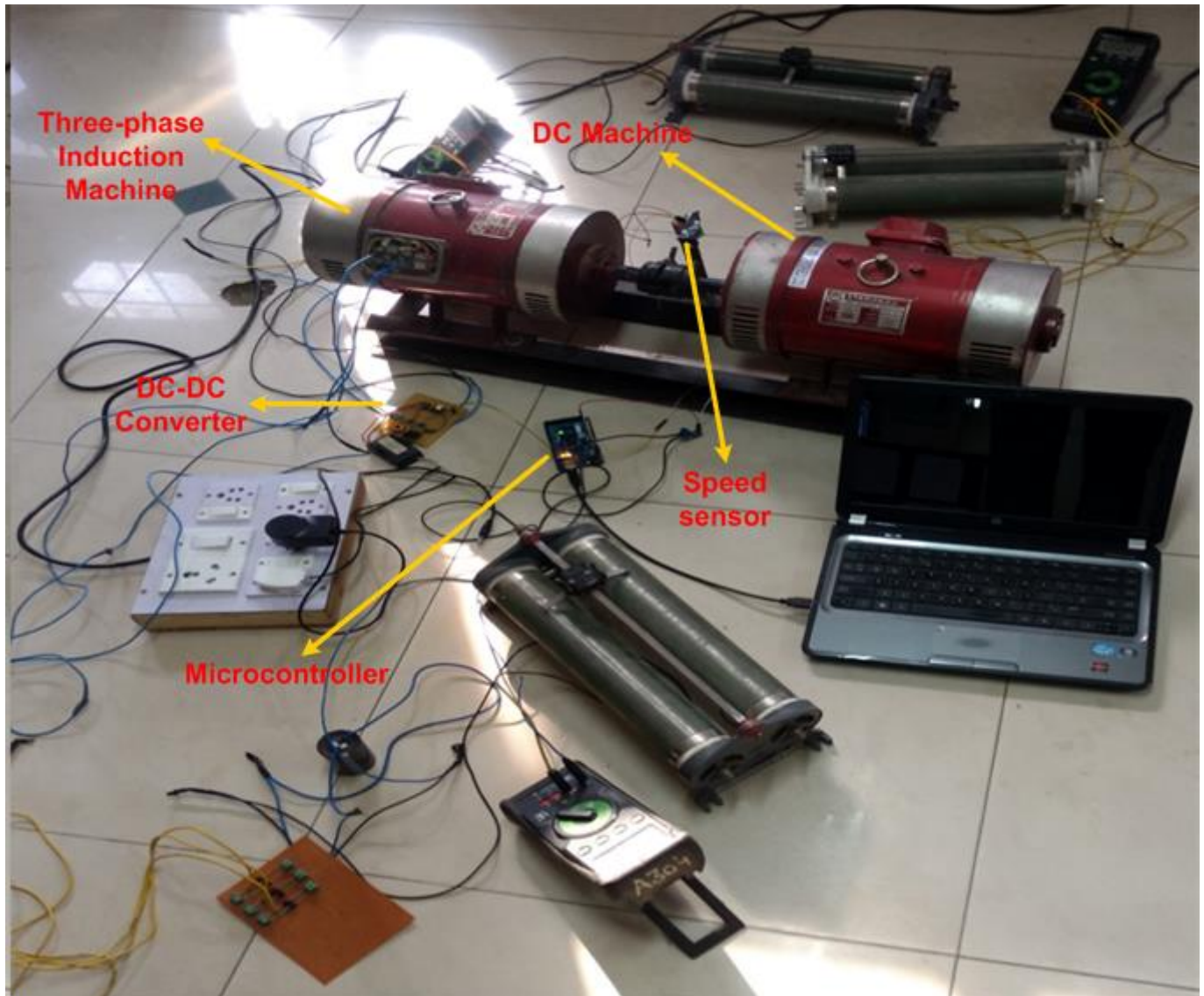


Fig. 6.23 Experimental setup

The input to the buck converter is a variable DC source. The DFIG rotor voltage has been kept constant by implementing closed loop voltage control on the Buck converter by Arduino Mega microcontroller.

The salient features related to the experimental set up are as follows:

- The Buck output is held constant at the desired value, even when the input is varied from 36 V to 60 V.
- Buck switching frequency is 3900 Hz.

The DFIG is run at 600 rpm and 750 rpm under no-load at two distinct rotor voltages for both two-lead as well as three-lead configurations.

Table 6.8 is a summary of the results obtained in hardware.

Table 6.8 Summary of the hardware results

		Two-lead		Three-lead	
Rotor Speed (N_r) in rpm	Buck Output (V_{dc}) in volts	Stator Line Voltage Without Capacitor (V_{ac}) in volts	Stator Line Voltage With Capacitor (V_{ac}) in volts	Stator Line Voltage Without Capacitor (V_{ac}) in volts	Stator Line Voltage With Capacitor (V_{ac}) in volts
600	16.42	80.6	153.8	95.4	171
600	19	89.6	170.2	105.6	184.4
750	16.42	110.2	332	129	346
750	19	122.6	344.8	145.6	352.2

The stator voltages obtained on DSO for two-lead and three-lead DFIG connections with a rotor speed of 600 rpm and a rotor voltage of 16.42 V have been illustrated in figures 6.24 to 6.27 as follows:

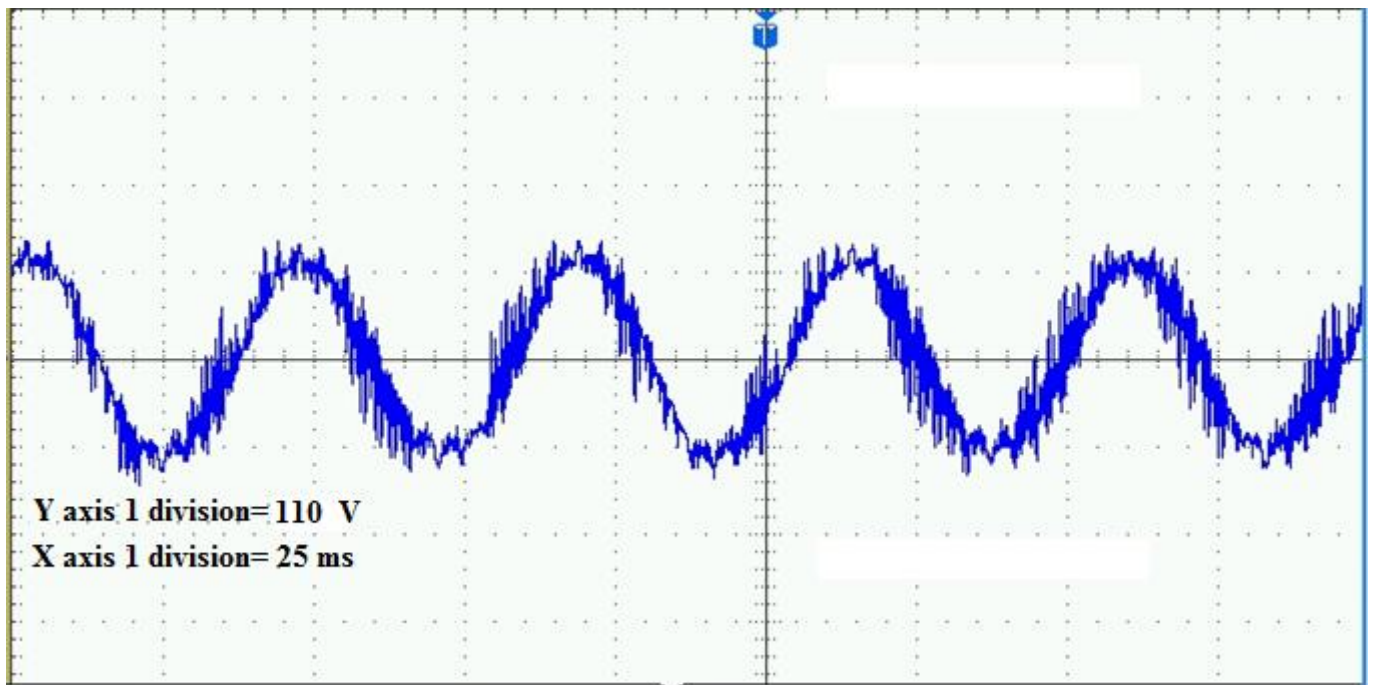


Fig. 6.24 Stator line voltage for two-lead connection without stator capacitor. $V_{ac}=0.2$ pu, $f=0.4$ pu

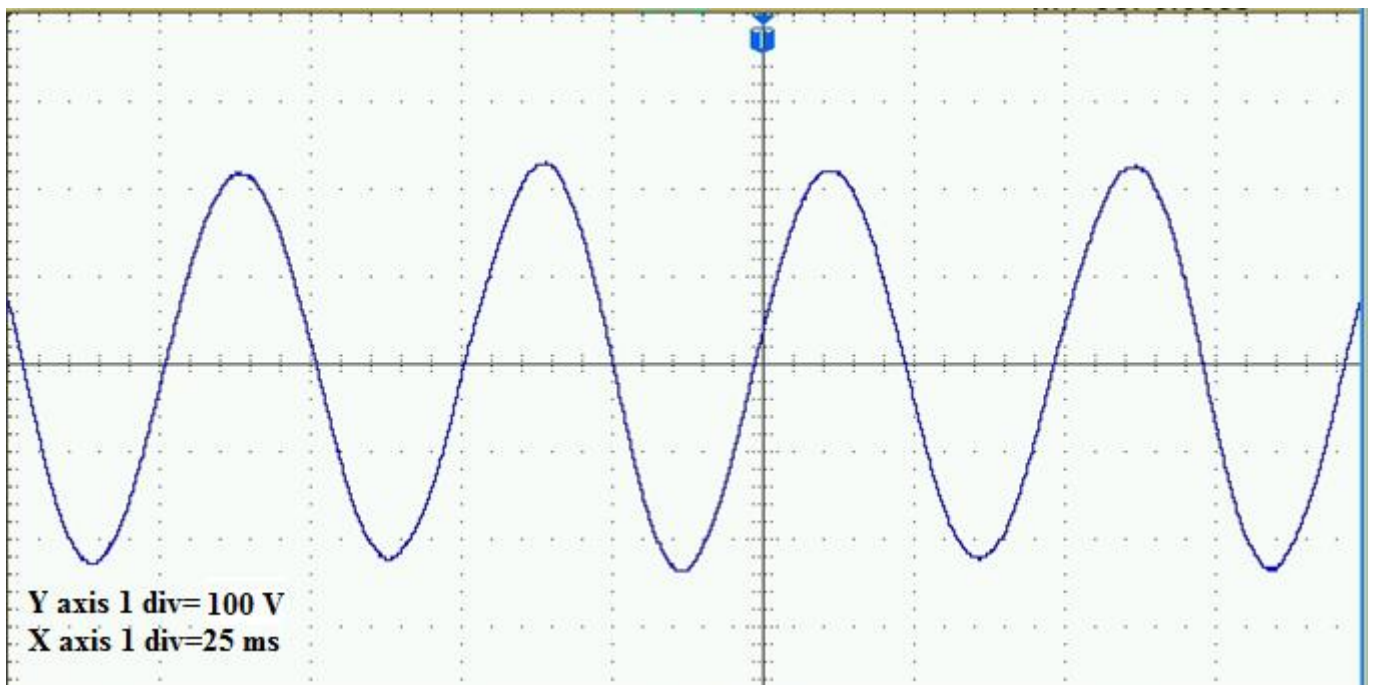


Fig. 6.25 Stator line voltage for two-lead connection with stator capacitor. $V_{ac}=0.38$ pu, $f=0.4$ pu

Comparison of figure 6.25 and figure 6.26 leads to the conclusion that the addition of a capacitor bank on the stator leads to improvement of the DFIG output voltage profile.

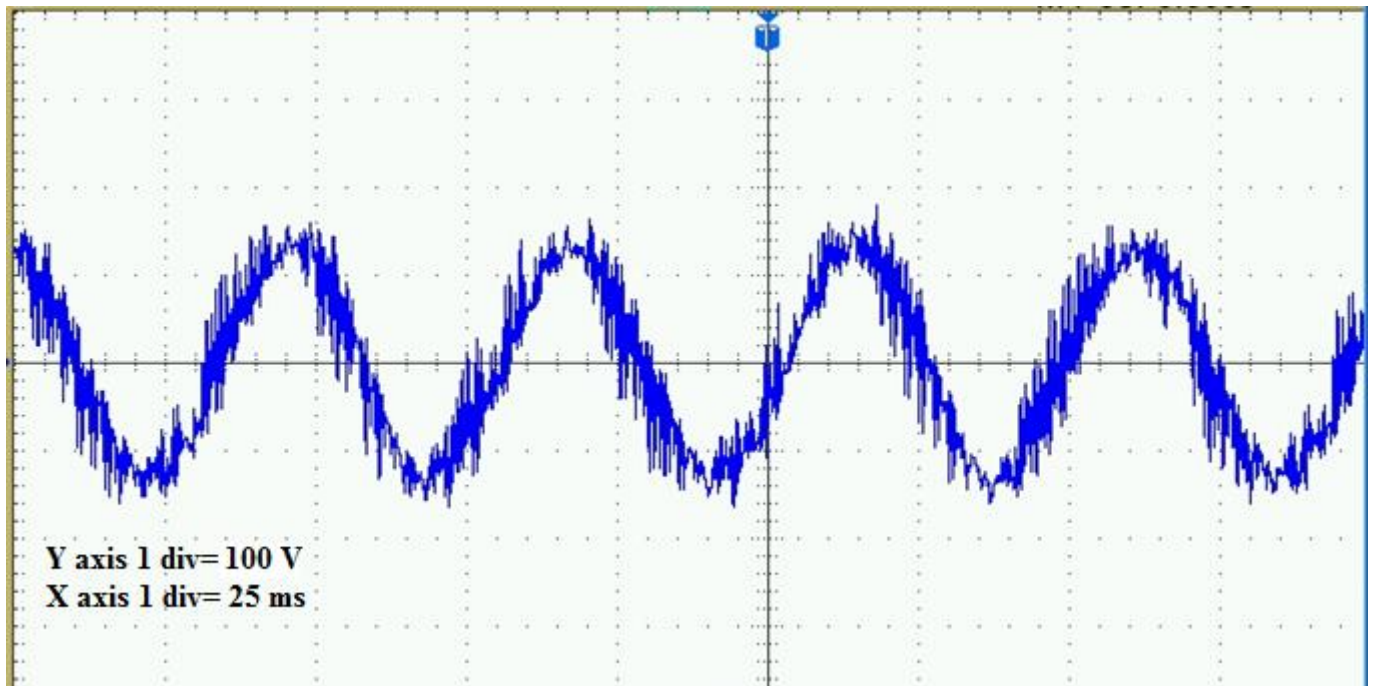


Fig. 6.26 Stator line voltage for three-lead connection without stator capacitor. $V_{ac}=0.24$ pu, $f=0.4$ pu

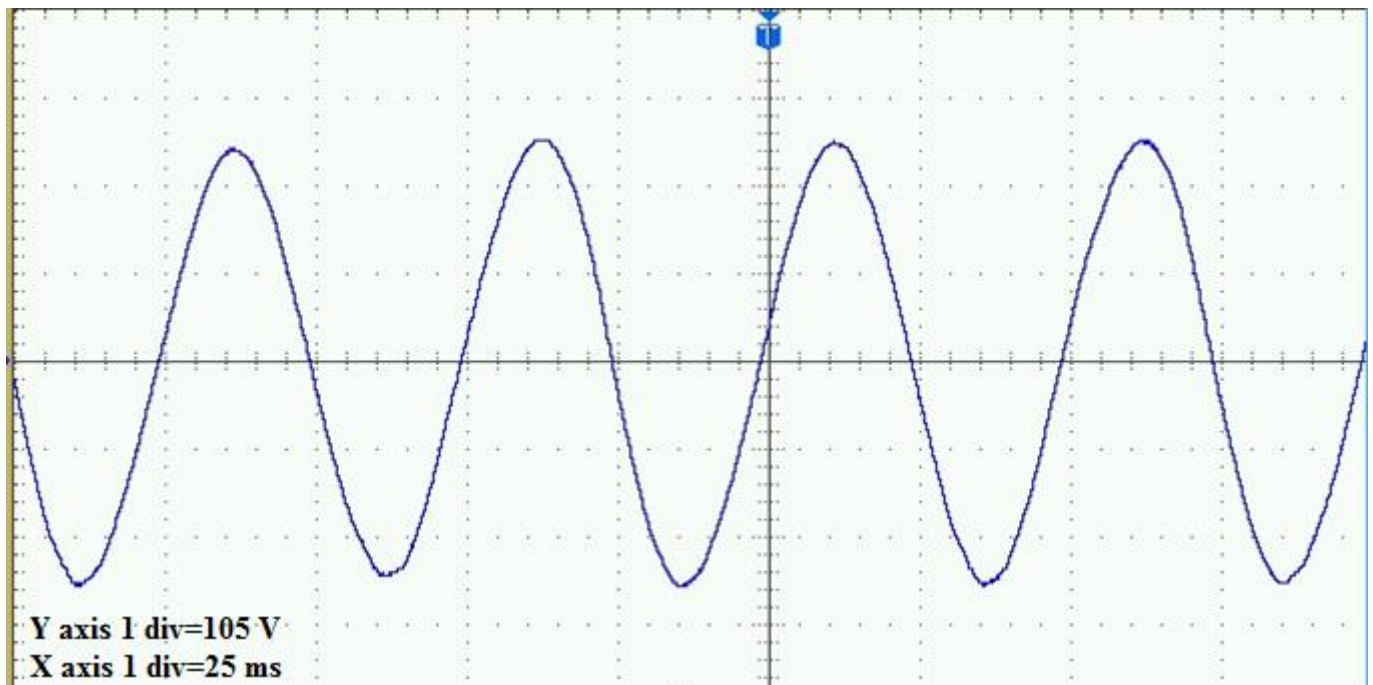


Fig. 6.27 Stator line voltage for three-lead connection with stator capacitor. $V_{ac}=0.43$ pu, $f=0.4$ pu

The stator voltages obtained on DSO for two-lead and three-lead DFIG connections with a rotor speed of 600 rpm and a rotor voltage of 19 V have been illustrated in figures 6.28 to 6.31 as follows:

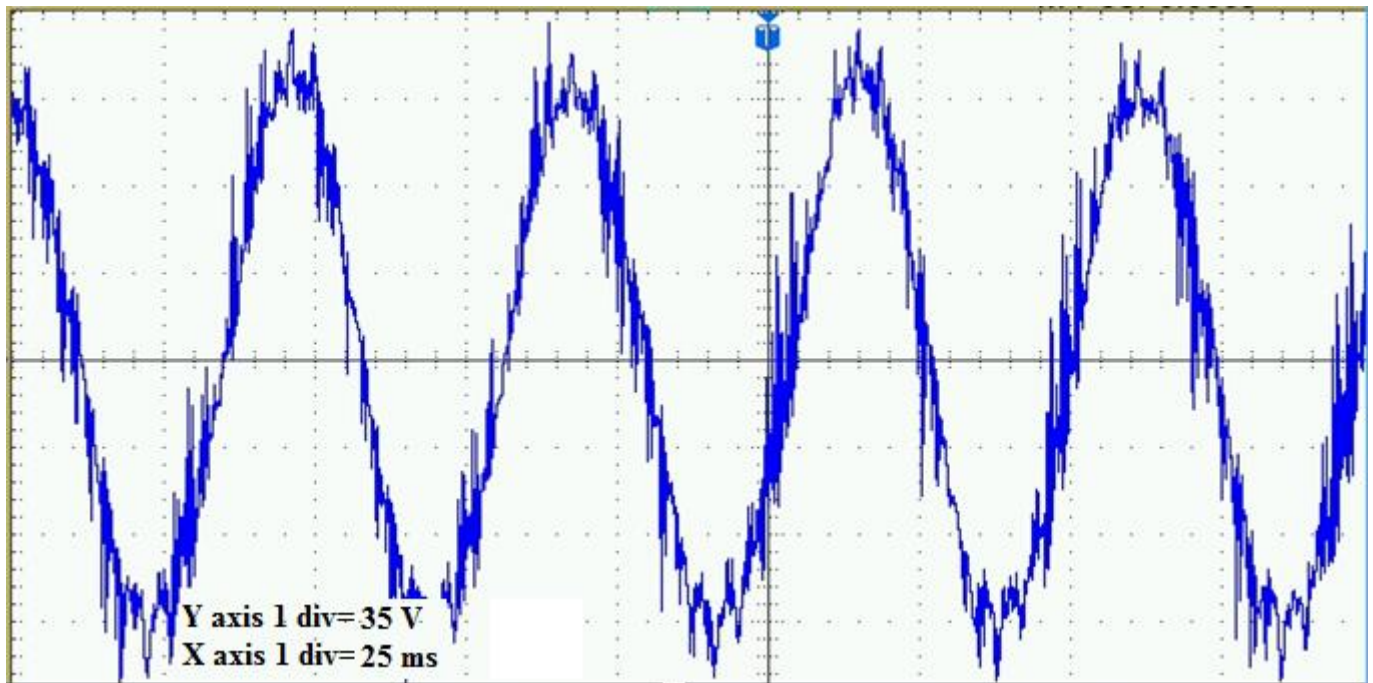


Fig. 6.28 Stator line voltage for two-lead connection without stator capacitor. $V_{ac}=0.22$ pu, $f=0.4$ pu

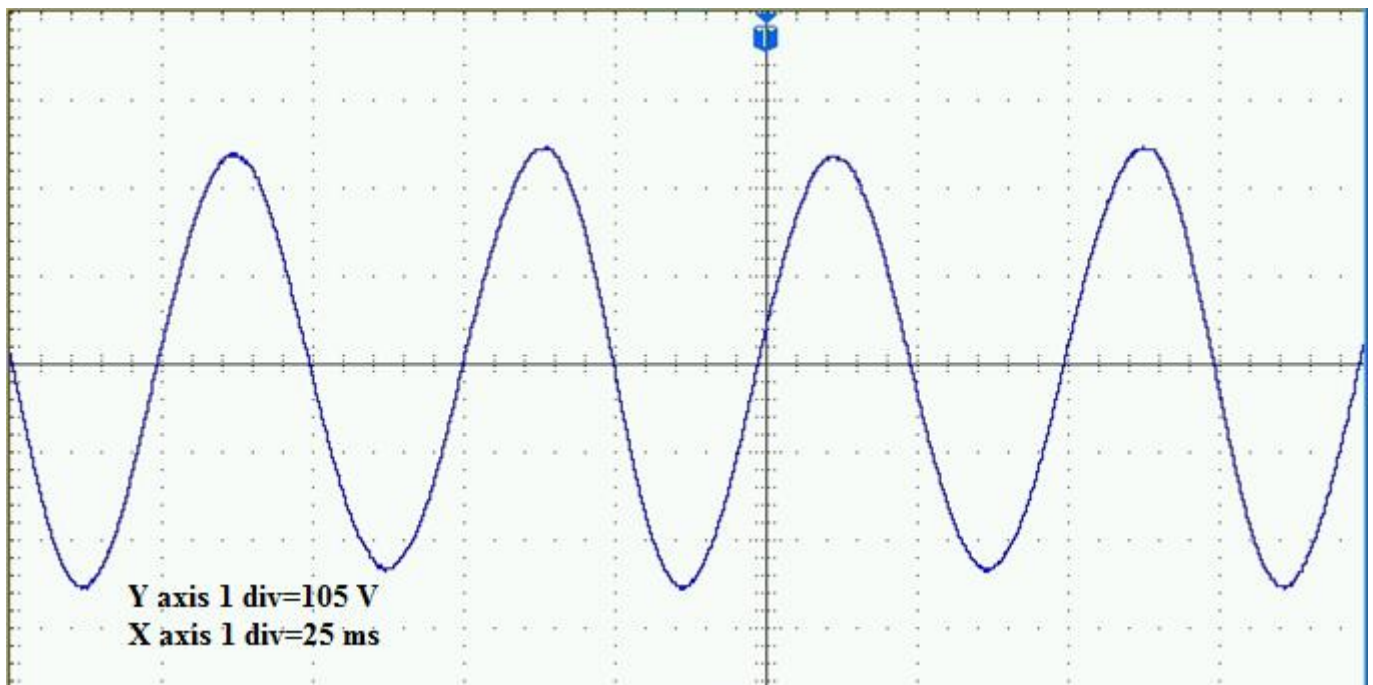


Fig. 6.29 Stator line voltage for two-lead connection with stator capacitor. $V_{ac}=0.43$ pu, $f=0.4$ pu

It can be observed from figure 6.28 and figure 6.29 that the inclusion of a capacitor bank on the DFIG stator results in a better output voltage profile.

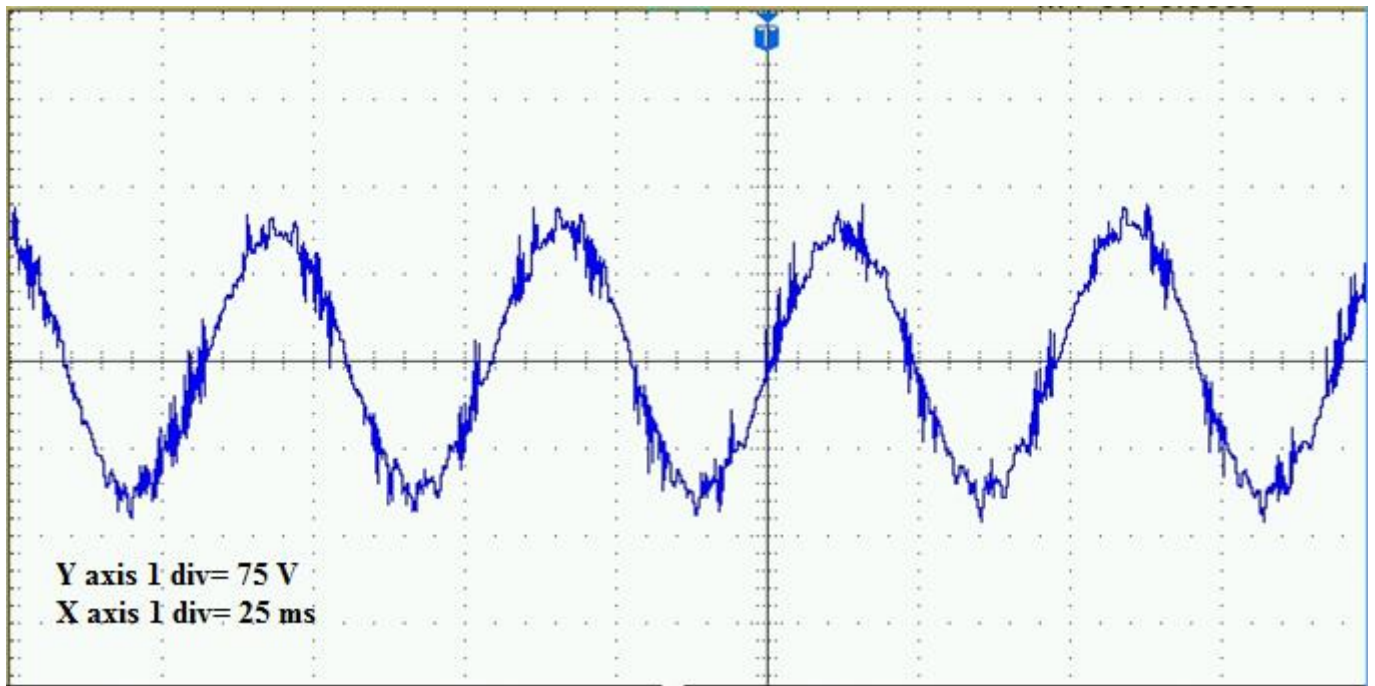


Fig. 6.30 Stator line voltage for three-lead connection without stator capacitor. $V_{ac}=0.26$ pu, $f=0.4$ pu

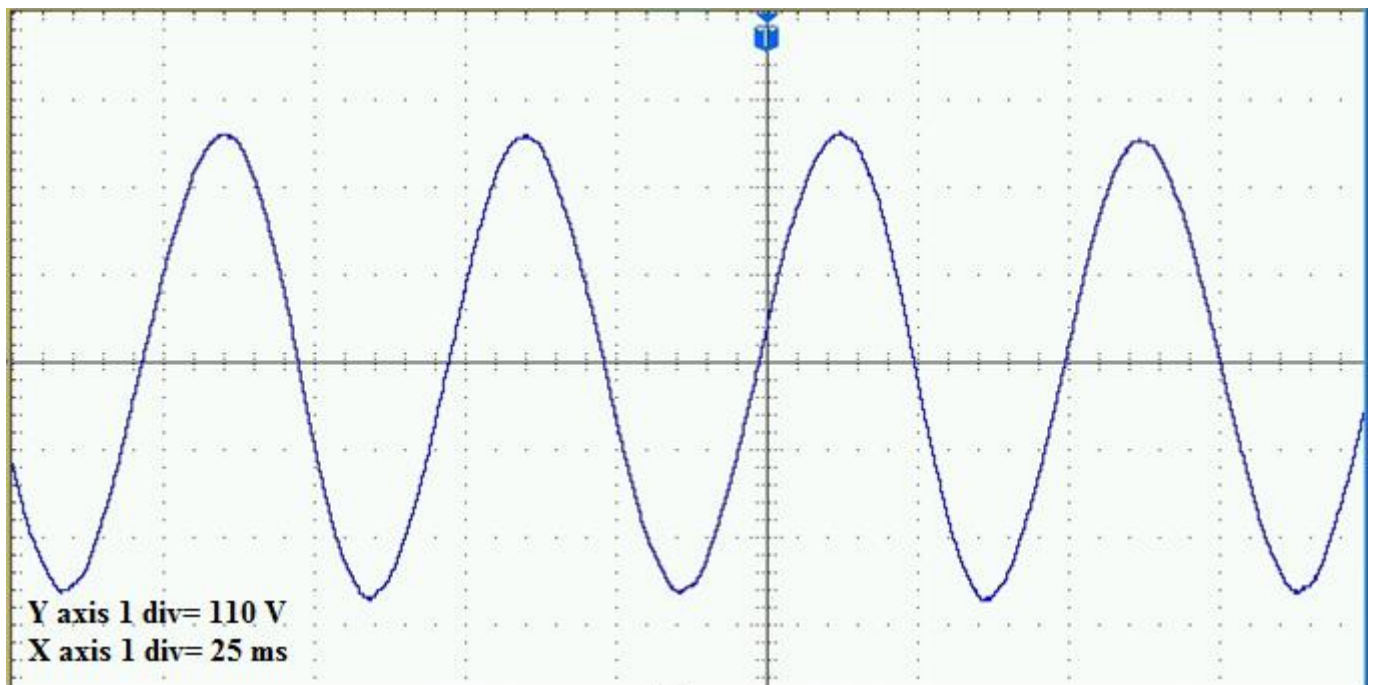


Fig. 6.31 Stator line voltage for three-lead connection with stator capacitor. $V_{ac}=0.46$ pu, $f=0.4$ pu

The stator voltages obtained on DSO for two-lead and three-lead DFIG connections with a rotor speed of 750 rpm and a rotor voltage of 16.42 V have been illustrated in figures 6.32 to 6.35 as follows:

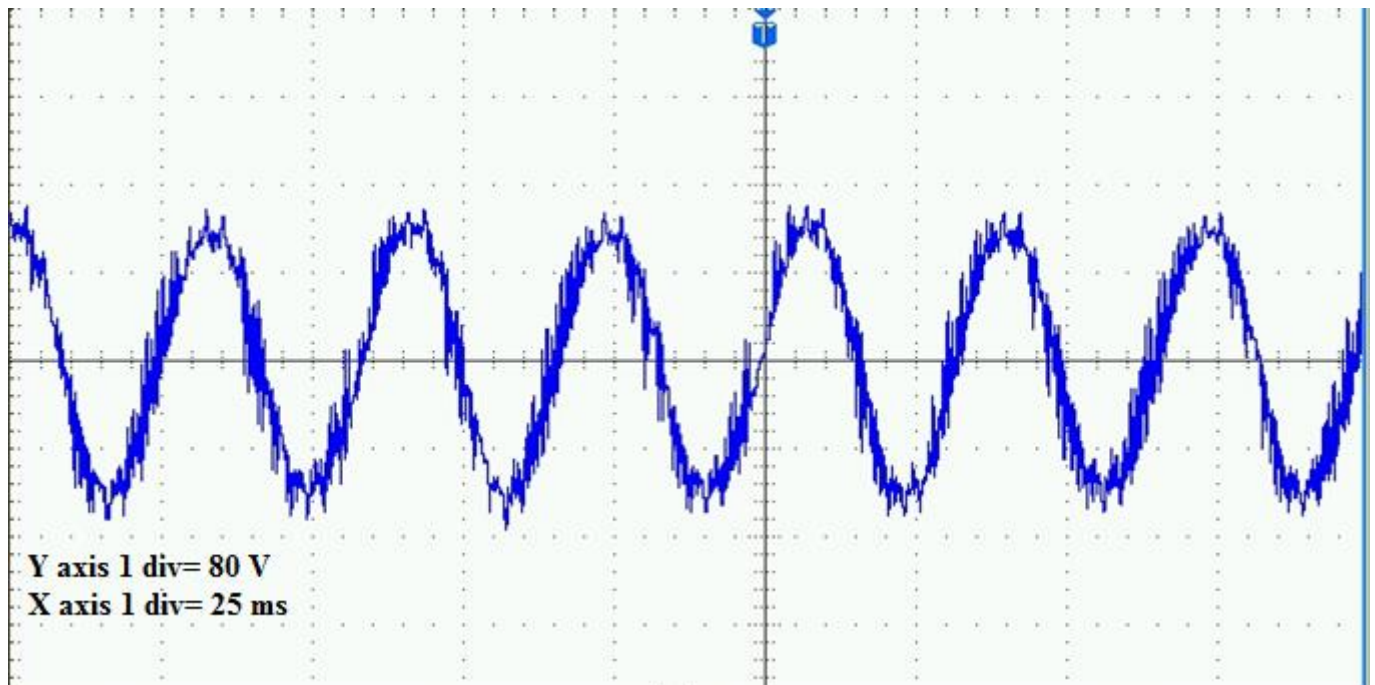


Fig. 6.32 Stator line voltage for two-lead connection without stator capacitor. $V_{ac}=0.28$ pu, $f=0.5$ pu

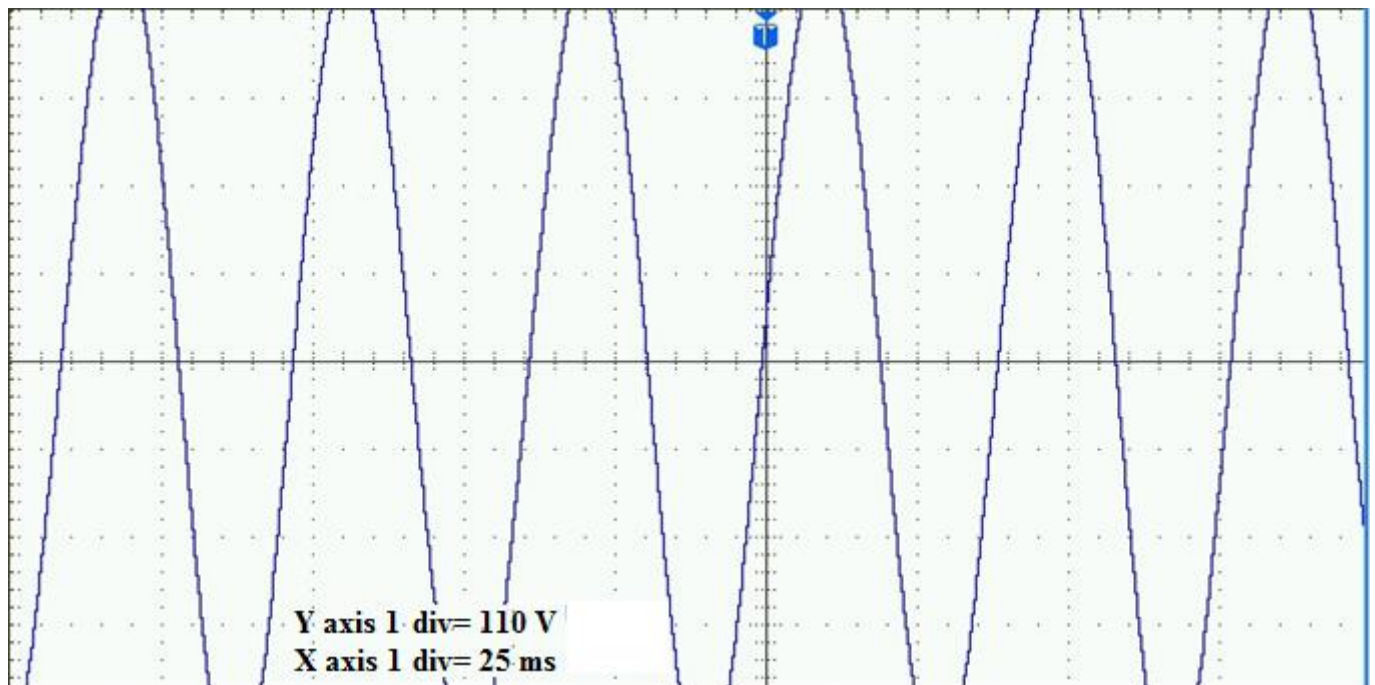


Fig. 6.33 Stator line voltage for two-lead connection with stator capacitor. $V_{ac}=0.83$ pu, $f=0.5$ pu

It can be concluded from figure 6.32 and figure 6.33 that connecting a capacitor bank on the DFIG stator improves the magnitude and shape of the output voltage.

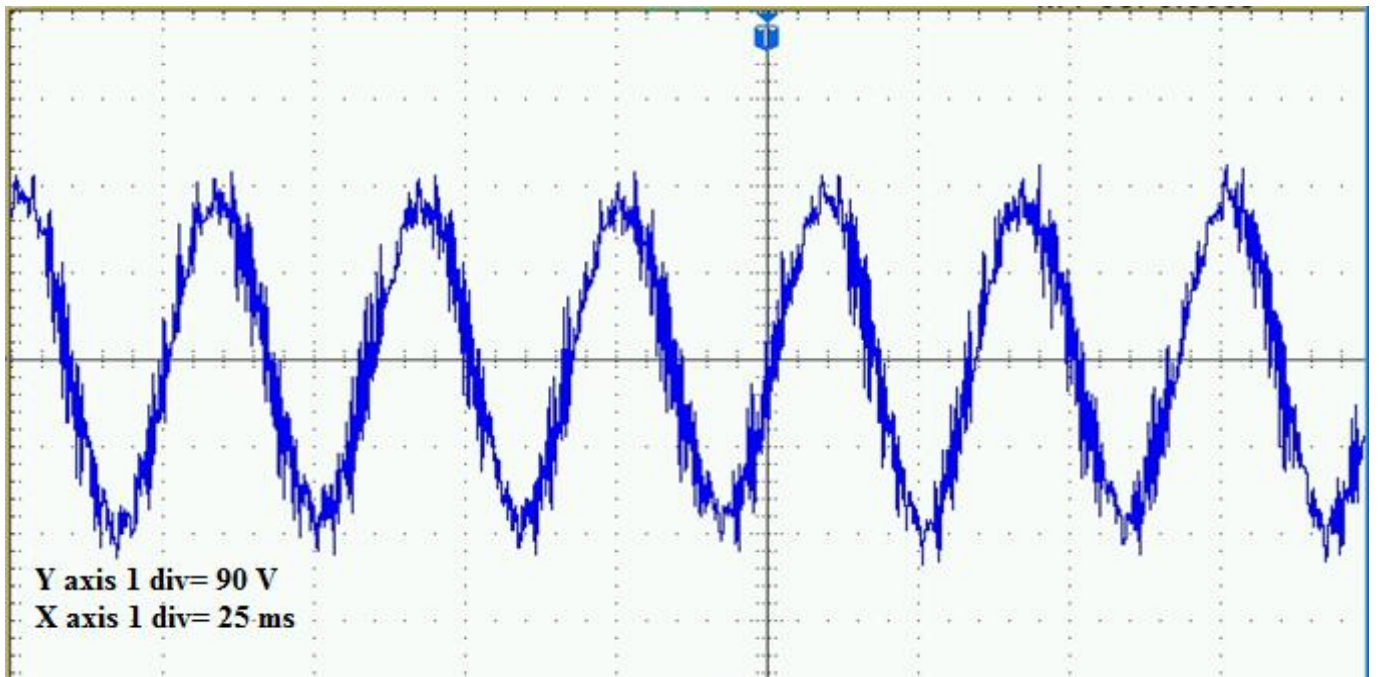


Fig. 6.34 Stator line voltage for three-lead connection without stator capacitor. $V_{ac}=0.32$ pu, $f=0.5$ pu

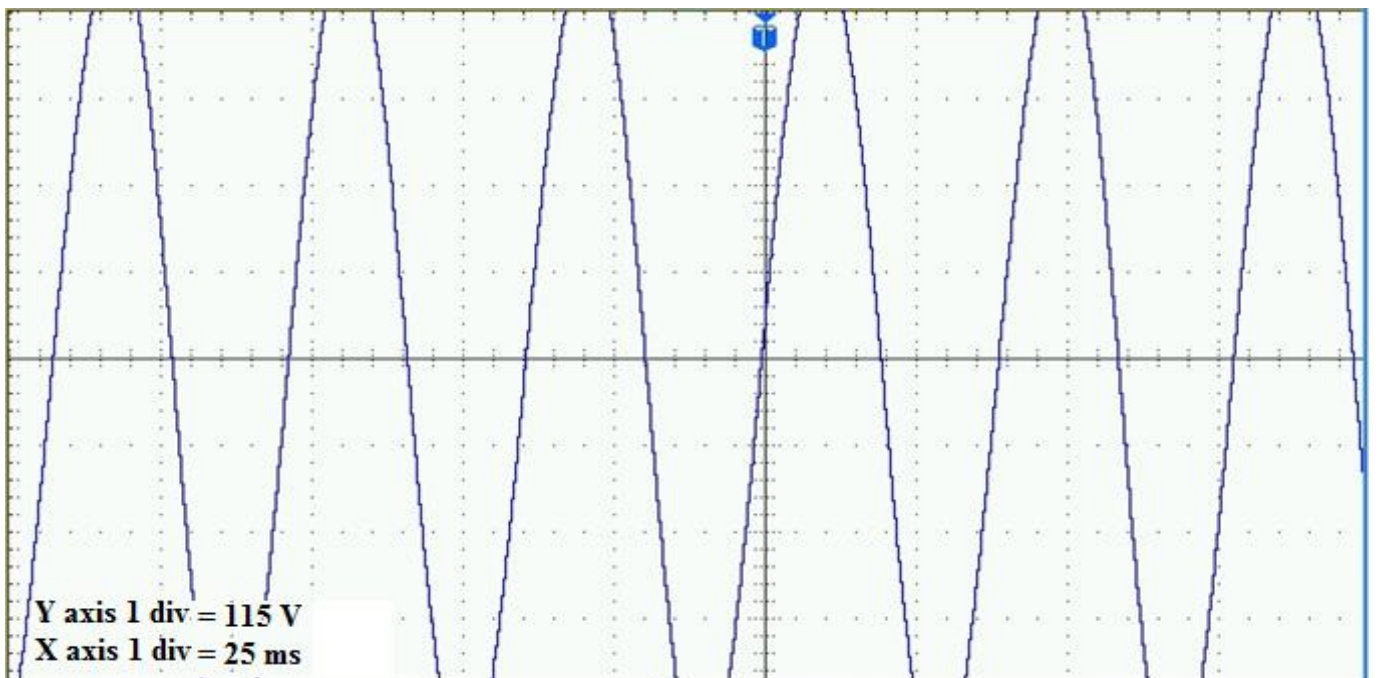


Fig. 6.35 Stator line voltage for three-lead connection with stator capacitor. $V_{ac}=0.86$ pu, $f=0.5$ pu

The stator voltages obtained on DSO for two-lead and three-lead DFIG connections with a rotor speed of 750 rpm and a rotor voltage of 19 V have been illustrated in figures 6.36 to 6.39 as follows:

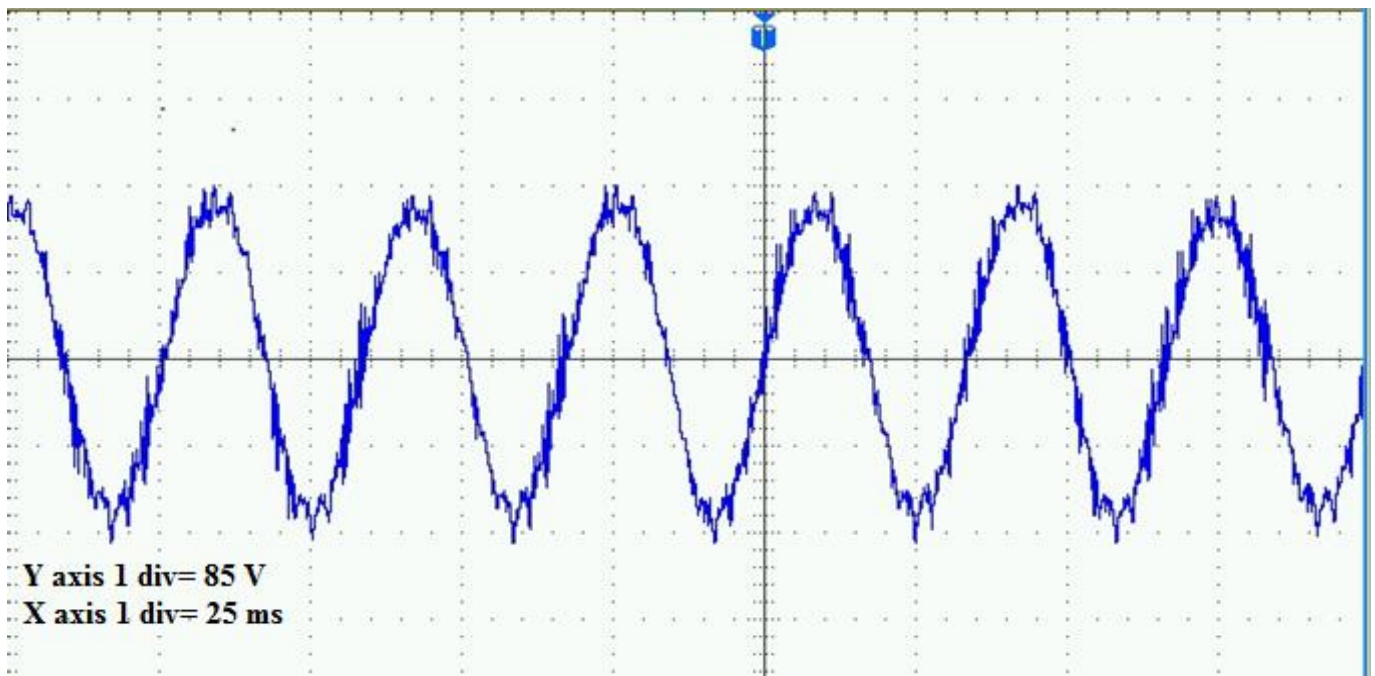


Fig. 6.36 Stator line voltage for two-lead connection without stator capacitor. $V_{ac}=0.31$ pu, $f=0.5$ pu

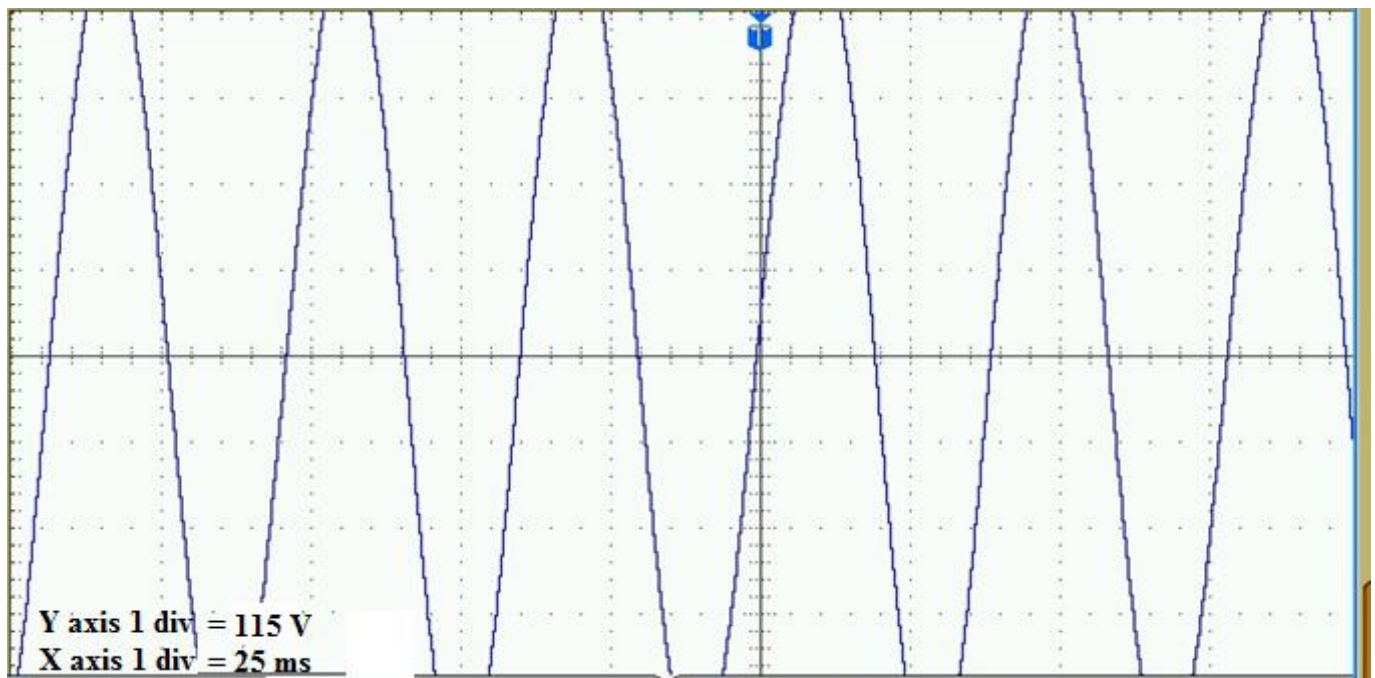


Fig. 6.37 Stator line voltage for two-lead connection with stator capacitor. $V_{ac}=0.86$ pu, $f=0.5$ pu

A comparison of figure 6.36 and figure 6.37 leads to the deduction that connecting a capacitor bank on the DFIG stator significantly improves the output voltage profile.

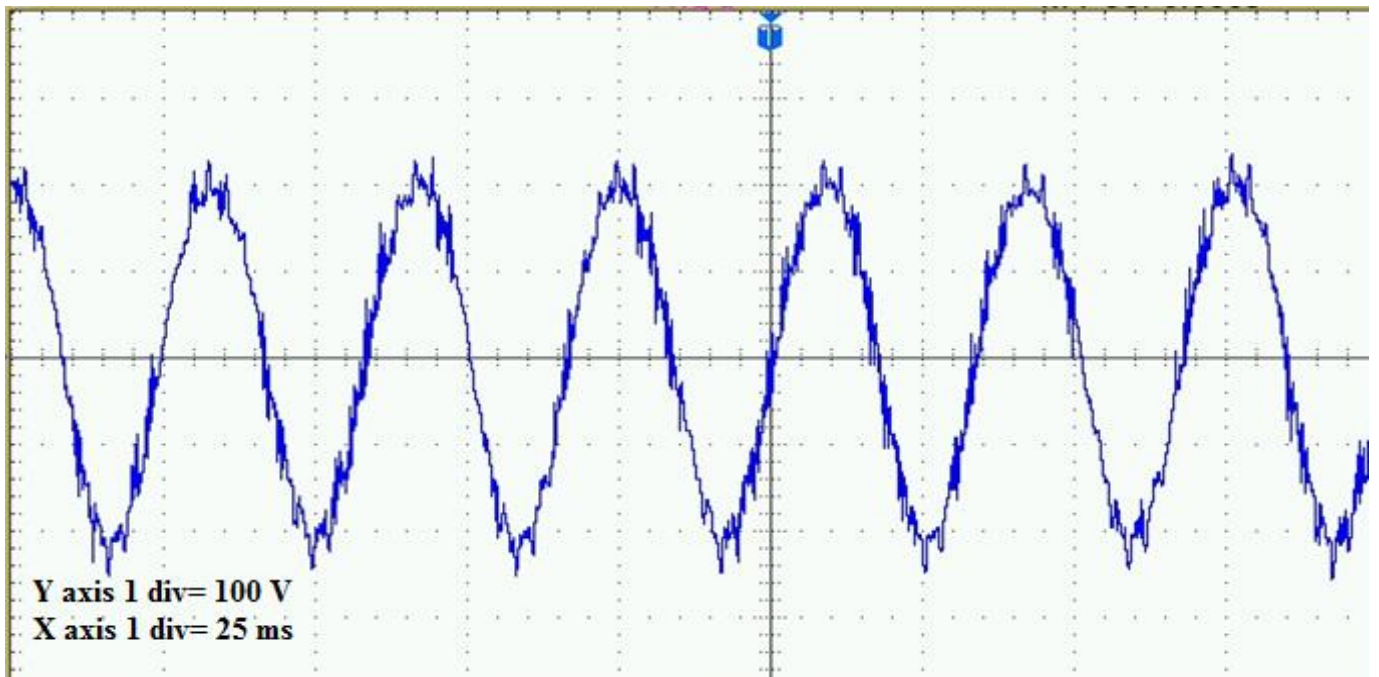


Fig. 6.38 Stator line voltage for three-lead connection without stator capacitor. $V_{ac}=0.36$ pu, $f=0.5$ pu

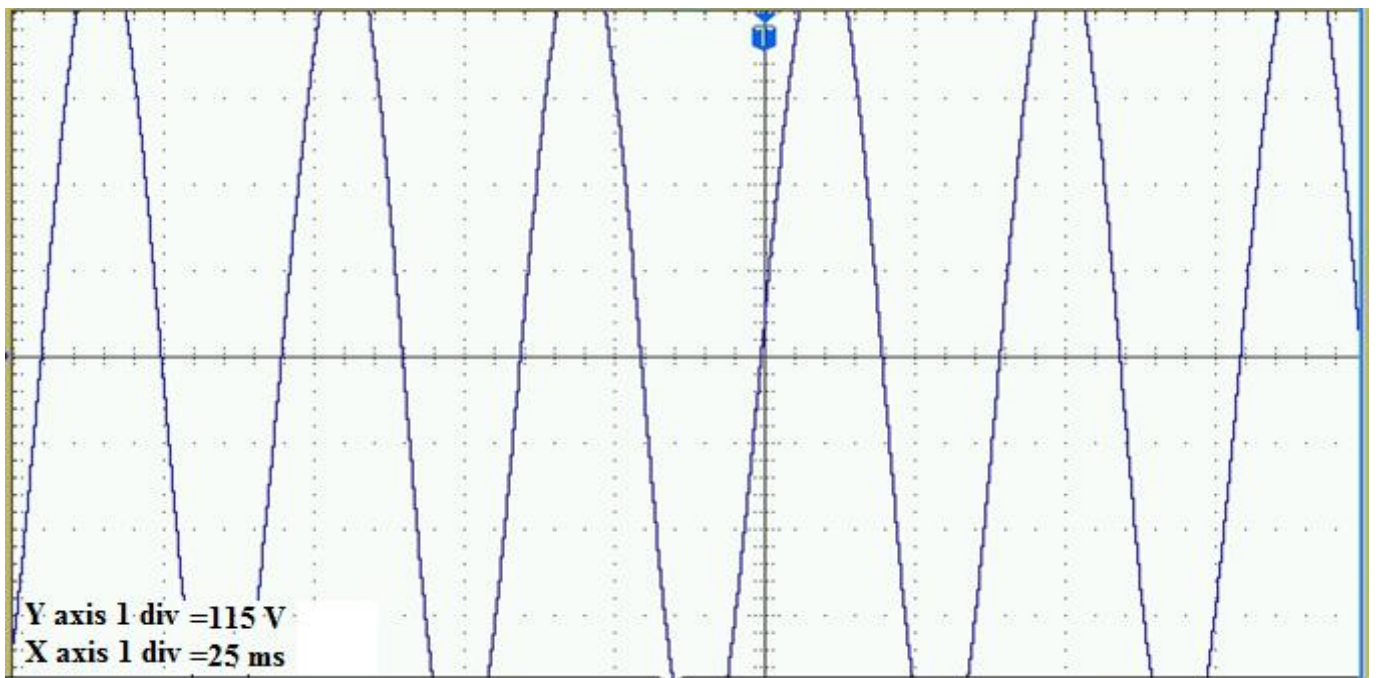


Fig. 6.39 Stator line voltage for three-lead connection with stator capacitor. $V_{ac}=0.88$ pu, $f=0.5$ pu

From table 6.8 and figures 6.24 to 6.39 following important conclusions can be drawn:

- The stator line voltage for the DFIG two-lead connection is lesser than the corresponding situations for three-lead.

- The stator line voltage for the DFIG two-lead connection is more stable than the corresponding situations for three-lead.
- Stator line voltage frequency is independent of Buck converter switching frequency.
- Under no-load condition, stator line voltage frequency and rotor speed for a four pole machine are related by equation (6.4).

$$f_s = \frac{N_m}{30} \quad (6.4)$$

6.7 CONCLUSION

In this chapter, two novel topologies of DFIG, called the two-lead system and the three-lead system respectively, have been proposed and validated. A thorough analysis and comparison of two-lead and three-lead DFIG topologies has been done. The important conclusions derived from the simulation as well as hardware results are as follows:

- Two-lead DFIG connection gives faster settling transients as compared to its three-lead counterpart.
- Three-lead DFIG connection yields a much lower value of stator voltage THD as compared to the two-lead connection.
- The load current total harmonic distortion (THD) is minimum when the three-lead DFIG connection is incorporated.
- Two-lead DFIG connection results in the better voltage regulation under loading conditions.
- Three-lead DFIG configuration is more efficient as compared to the two-lead DFIG configuration. For the same input conditions, the output yield of a three-lead DFIG system is greater than that of its two-lead counterpart.
- A three-lead DFIG DC system with rotor excited by Buck converter is simple in terms of control implementation. Hence, it can be employed for constructing isolated DFIG DC systems instead of the existing topologies which use a greater number of power electronic converters with complex control strategies.
- The MP&O method of MPPT is superior to the P&O method owing to significantly less fluctuations about the maximum power point.
- Three-lead/ three-lead combination of DFIGs is best suited for parallel operation.
- In a parallel combination of two DFIGs connected in any permutation of two-lead/ three-lead topology, same percentage change in rotor voltage on either DFIG results in same change in magnitude of the output voltage of the combination. This phenomenon is irrespective of the ratings of the rotor.

- Other conditions remaining the same, for a particular magnitude of rotor voltage, the stator voltage of the DFIG two-lead connection is lesser than the corresponding magnitude of its three-lead counterpart.
- When excited by a DC-DC converter, the stator voltage of the DFIG two-lead connection is more stable than its three-lead counterpart.

Chapter 7

CONCLUSION AND SCOPE OF FUTURE WORK

7.1 INTRODUCTION

In this chapter a summary of the important conclusions from the previous chapters has been presented. The research work undertaken has been systematically organized in the following chapters:

Chapter 01: Introduction

Chapter 02: Literature Review of DFIG based Energy Conversion System

Chapter 03: Mathematical Modelling of System Components

Chapter 04: Simulation and Hardware Implementation of Power Electronic Converters

Chapter 05: Analysis of Grid-Connected DFIG System using Rational Methods and Genetic Algorithm

Chapter 06: Analysis of Two-lead and Three-lead Configuration of DC Excited DFIG

Chapter 07: Conclusion and Scope of Future Work

Apart from chapter 1 and chapter 2 which includes the introduction to the subject area and formulation of the research problem using literature survey, the major findings as reported in chapters 3, 4, 5 and 6 may be concluded in the chapter 7 as follows:

Chapter 3 describes the development of the dynamic mathematical model of a DFIG. This model can be designed as a compact set of equations that can be simulated by a digital system like a computer-based hardware. This simulated model is capable of mimicking the behaviour of the DFIG under most operating conditions. Such modelling enables the incessant monitoring of all the variables of the machine. The existing Simulink DFIG model can be used for ascertaining the machine outputs corresponding to different inputs. However, the mathematical model of a DFIG makes it very convenient to design controller parameters for efficient control.

Chapter 4 elucidates a simple method for the quick development of PECs. A DFIG standalone system has been presented as a practical application of XSG based converters in the domain of renewables. It has been conclusively demonstrated via hardware that the Simulink-based XSG platform is a diligent tool for the generation of control schemes. Two topologies of single-phase inverters and a three-phase inverter have been realised in simulation as well as hardware. A detailed explanation of the XSG-based technique used for the construction of the triangular and the sinusoidal signal has been presented. The usage of XSG nullifies the need of learning programming techniques, thereby speeding up hardware prototyping of converters. This is a huge advantage in terms of saving time as well as increased flexibility. The absolute correspondence between the simulation results and the hardware results completely justify the ease of usage by invoking XSG.

In chapter 5, the optimal values of DFIG rotor current have been obtained using three different rational techniques and corresponding three cases of GA. The first method relates to an algorithm where maximum active power and minimum losses are considered. The second method establishes an algorithm corresponding to minimum losses and minimum reactive power. The third method establishes an algorithm corresponding to maximum active power and minimum reactive power. To analyze the effectiveness of the control during bulk power generation, vector control has been implemented on a standard multi megawatt DFIG. The DFIG used has a rating of 2 MW and is usually employed with Vestas V-80, Gamesa G-87 or Ecotecnica Eco-80 wind turbine. After the comparative analysis of the three cases, it is concluded that best efficiency is obtained in case 1 while the best range of power factor corresponds to case 3. Case 2 is immensely useful since it gives an overall greater efficiency as compared to case 3 and a far better power factor as compared to case 1.

In chapter 6, two novel topologies of DFIG called the two-lead system and the three-lead system respectively, have been proposed. Analysis and comparison of two-lead and three-lead topologies in terms of total harmonic distortion of the stator sinusoidal output has been investigated. A modified Perturb and Observe (MP&O) Algorithm has been applied for maximum power point tracking in DFIG DC systems. The advantages of the proposed novel DFIG topologies have been validated. Analysis of an autonomous DFIG DC system in the three-lead configuration has been done. The output voltage of the autonomous DFIG DC has been held constant under intermittent conditions. The hardware results of a one hp DFIG experimental setup have also been encompassed in the chapter.

7.2 SCOPE OF FUTURE WORK

Research work reported in this thesis can be extended in the following areas:

- A grid connected three-lead DFIG topology with rotor excited by DC-DC converters can be developed. The control aspects of such a topology can be compared in terms of complexity to the existing back-to-back converter fed DFIG topologies.
- Using DC-DC converter at the DFIG rotor can contribute to the implementation of a novel hybrid wind-solar system.

7.3 CONCLUSION

Based upon the findings as reported in this thesis, the contributions are as follows:

- To compute the optimal values of DFIG rotor current commands, novel analytical techniques as well as genetic algorithm based techniques have been developed. The rotor current commands have been used to enhance the efficiency as well as the power factor of a grid based DFIG.
- Two novel autonomous DFIG topologies have been proposed and validated. It has been demonstrated that the control aspects of the proposed novel DFIG topologies is simpler as compared to the existing topologies.
- An autonomous DFIG DC system with a simple control strategy has been simulated. The DC output voltage has been held constant under varying wind speeds and dynamic loading conditions.
- The parallel operation of two DFIGs of different ratings connected in combination of two-lead and three-lead topology has been presented. The change in output voltage of the parallel combination owing to loading conditions and changing input has been analyzed.

REFERENCES

- [1] <https://powermin.nic.in/en/content/power-sector-glance-all-india>
- [2] <https://library.wwindea.org/global-statistics/>
- [3] S. Bhowmik and R. Spee, "Wind speed estimation based variable speed wind power generation," *Proceedings of the 24th Annual Conference of the IEEE Industrial Electronics Society*, Aachen, Germany, pp. 596-601, 1998.
- [4] A. Miller, E. Muljadi and D. S. Zinger, "A variable speed wind turbine power control," *IEEE Transactions on Energy Conversion*, vol. 12, no. 2, pp. 181-186, 1997.
- [5] F. Blaabjerg, Zhe Chen and S. B. Kjaer, "Power electronics as efficient interface in dispersed power generation systems," *IEEE Transactions on Power Electronics*, vol. 19, no. 5, pp. 1184-1194, 2004.
- [6] M. Tsili and S. Papathanassiou, "A review of grid code technical requirements for wind farms," *IET Renewable Power Generation*, vol. 3, no. 3, pp. 308-332, 2009.
- [7] G. Singh, M. Matuonto and K. Sundaram, "Impact of Imbalanced Wind Turbine Generator Cooling on Reliability," *Proceedings of International Renewable Energy Congress*, Sousse, Tunisia, pp. 1-6, 2019.
- [8] J. Zhang, H. Sun, Z. Sun, W. Dong, Y. Dong and S. Gong, "Reliability Assessment of Wind Power Converter Considering SCADA Multistate Parameters Prediction Using FP-Growth, WPT, K-Means and LSTM Network," *IEEE Access*, vol. 8, pp. 84455-84466, 2020.
- [9] F. Spinato, P. J. Tavner, G. J. W. V. Bussel and E. Koutoulakos, "Reliability of wind turbine subassemblies," *IET Renewable Power Generation*, vol. 3, no. 4, pp. 387-401, 2009.
- [10] H. Arabian-Hoseynabadi, P. J. Tavner, and H. Oraee, "Reliability comparison of direct-drive and geared drive wind turbine concepts," *Wind Energy*, vol. 13, no. 1, pp. 62-73, 2010.
- [11] K. Fischer, K. Pelka, A. Bartschat, B. Tegtmeier, D. Coronado, C. Broer, and J. Wenske, "Reliability of Power Converters in Wind Turbines: Exploratory Analysis of Failure and Operating Data From a Worldwide Turbine Fleet," *IEEE Transactions on Power Electronics*, vol. 34, no. 7, pp. 6332-6344, 2019.
- [12] D. Zhou, Y. Song, Y. Liu and F. Blaabjerg, "Mission Profile Based Reliability Evaluation of Capacitor Banks in Wind Power Converters," *IEEE Transactions on Power Electronics*, vol. 34, no. 5, pp. 4665-4677, 2019.
- [13] H. Polinder, H. Lendenmann, R. Chin and W. M. Arshad, "Fault tolerant generator systems for wind turbines," *Proceedings of International Electric Machines and Drives Conference*, Miami, United States, pp. 675-681, 2009.

- [14] J. F. Manwell, J. G. McGowan, and A. L. Rogers, *Wind Energy Explained: Theory, Design and Application*, 2nd edition Chichester, United Kingdom: Wiley, 2009.
- [15] M. Liserre, R. Cárdenas, M. Molinas and J. Rodriguez, "Overview of Multi-MW Wind Turbines and Wind Parks," *IEEE Transactions on Industrial Electronics*, vol. 58, no. 4, pp. 1081-1095, 2011.
- [16] H. Tian, X. Xu and H. Lin, "Simulation study on direct-drive wind power system," *The Journal of Engineering*, vol. 2019, no. 23, pp. 9183-9189, 2019.
- [17] A. D. Hansen, F. Iov, F. Blaabjerg, and L. H. Hansen, "Review of contemporary wind turbine concepts and their market penetration," *Wind Engineering*, vol. 28, no. 3, pp. 247–263, 2004.
- [18] H. Polinder, S. W. H. de Haan, M. R. Dubois, and J. G. Slootweg, "Basic operation principles and electrical conversion systems of wind turbines," *European Power Electronics and Drives Journal*, vol. 15, no. 4, pp. 43–50, 2005.
- [19] H. Polinder, F. F. A. van der Pijl, G. - de Vilder and P. J. Tavner, "Comparison of direct-drive and geared generator concepts for wind turbines," *IEEE Transactions on Energy Conversion*, vol. 21, no. 3, pp. 725-733, 2006.
- [20] H. Polinder, "Overview of and trends in wind turbine generator systems," *Proceedings of Power and Energy Society General Meeting*, Detroit, United States, 2011, pp. 1-8.
- [21] E. Bogalecka and Z. Krzeminski, "Control systems of doubly-fed induction machine supplied by current controlled voltage source inverter," *Proceedings of International Conference on Electrical Machines and Drives*, Oxford, United Kingdom, pp. 168-172, 1993.
- [22] R. Pena, J. C. Clare and G. M. Asher, "Doubly fed induction generator using back-to-back PWM converters and its application to variable-speed wind-energy generation," *IEE Proceedings - Electric Power Applications*, vol. 143, no. 3, pp. 231-241, 1996.
- [23] Z. Chen and E. Spooner, "Grid interface options for variable-speed, permanent-magnet generators," *IEE Proceedings - Electric Power Applications*, vol. 145, no. 4, pp. 273-283, 1998.
- [24] Z. Chen and E. Spooner, "Wind turbine power converters: a comparative study," *Proceedings of International Conference on Power Electronics and Variable Speed Drives*, London, United Kingdom, pp. 471-476, 1998.
- [25] Z. Chen and E. Spooner, "Current source thyristor inverter and its active compensation system," *IEE Proceedings - Generation, Transmission and Distribution*, vol. 150, no. 4, pp. 447-454, 2003.
- [26] P. W. Wheeler, J. Rodriguez, J. C. Clare, L. Empringham and A. Weinstein, "Matrix converters: a technology review," *IEEE Transactions on Industrial Electronics*, vol. 49, no. 2, pp. 276-288, 2002.

- [27] M. Aten, G. Towers, C. Whitley, P. Wheeler, J. Clare and K. Bradley, "Reliability comparison of matrix and other converter topologies," *IEEE Transactions on Aerospace and Electronic Systems*, vol. 42, no. 3, pp. 867-875, 2006.
- [28] A. Alesina and M. G. B. Venturini, "Analysis and design of optimum-amplitude nine-switch direct AC-AC converters," *IEEE Transactions on Power Electronics*, vol. 4, no. 1, pp. 101-112, 1989.
- [29] D. Casadei, G. Serra, A. Tani and L. Zarri, "Matrix converter modulation strategies: a new general approach based on space-vector representation of the switch state," *IEEE Transactions on Industrial Electronics*, vol. 49, no. 2, pp. 370-381, 2002.
- [30] T. Kume et al., "Integrated Filters and Their Combined Effects in Matrix Converter," *IEEE Transactions on Industry Applications*, vol. 43, no. 2, pp. 571-581, 2007.
- [31] T. F. Podlesak, D. C. Katsis, P. W. Wheeler, J. C. Clare, L. Empringham and M. Bland, "A 150-kVA vector-controlled matrix converter induction motor drive," *IEEE Transactions on Industry Applications*, vol. 41, no. 3, pp. 841-847, 2005.
- [32] P. Wheeler, J. Clare, D. Lampard, S. Pickering, K. Bradley, and L. Empringham, "An integrated 30 kW matrix converter based induction motor drive," *Proceedings of Power Electronics Specialists Conference*, Recife, Brazil, pp. 2390-2395, 2005.
- [33] H. Keyuan and H. Yikang, "Investigation of a matrix converter-excited brushless doubly-fed machine wind-power generation system," *Proceedings of International Conference on Power Electronics and Drive Systems*, Singapore, pp. 743-748, 2003.
- [34] D. Casadei, J. Clare, L. Empringham, G. Serra, A. Tani, A. Trentin, P. Wheeler, and L. Zarri, "Large-signal model for the stability analysis of matrix converters," *IEEE Transactions on Industrial Electronics*, vol. 54, no. 2, pp. 939-950, 2007.
- [35] D. Casadei, G. Serra, A. Tani, A. Trentin and L. Zarri, "Theoretical and experimental investigation on the stability of matrix converters," *IEEE Transactions on Industrial Electronics*, vol. 52, no. 5, pp. 1409-1419, 2005.
- [36] Furong Liu, C. Klumpner and F. Blaabjerg, "Stability analysis and experimental evaluation of a matrix converter drive system," *Proceedings of 29th Annual Conference of the IEEE Industrial Electronics Society*, Roanoke, United States, pp. 2059-2065, 2003.
- [37] D. Casadei, G. Serra, A. Tani and L. Zarri, "Effects of input voltage measurement on stability of matrix converter drive system," *IEE Proceedings - Electric Power Applications*, vol. 151, no. 4, pp. 487-497, 2004.
- [38] H. Mosskull, J. Galic and B. Wahlberg, "Stabilization of Induction Motor Drives With Poorly Damped Input Filters," *IEEE Transactions on Industrial Electronics*, vol. 54, no. 5, pp. 2724-2734, 2007.

- [39] B. Choi, D. Kim, D. Lee, S. Choi and J. Sun, "Analysis of Input Filter Interactions in Switching Power Converters," *IEEE Transactions on Power Electronics*, vol. 22, no. 2, pp. 452-460, 2007.
- [40] S. M. Barakati, M. Kazerani and X. Chen, "A new wind turbine generation system based on matrix converter," *Proceedings of IEEE Power Engineering Society General Meeting*, San Francisco, United States, pp. 2083-2089, 2005.
- [41] R. Melicio, V. M. F. Mendes and J. P. S. Catalao, "Modeling and simulation of a wind energy system: Matrix versus multilevel converters," *Proceedings of Mediterranean Electrotechnical Conference*, Ajaccio, France, pp. 604-609, 2008.
- [42] J. Wang, D. Xu, B. Wu and Z. Luo, "A Low-Cost Rectifier Topology for Variable-Speed High-Power PMSG Wind Turbines," *IEEE Transactions on Power Electronics*, vol. 26, no. 8, pp. 2192-2200, 2011.
- [43] D. S. Oliveira, Jr., M. M. Reis, C. E. A. Silva, L. H. S. Colado Barreto, F. L. M. Antunes and B. L. Soares, "A Three-Phase High-Frequency Semiconrolled Rectifier for PM WECS," *IEEE Transactions on Power Electronics*, vol. 25, no. 3, pp. 677-685, 2010.
- [44] Z. Chen, "Issues of Connecting Wind Farms into Power Systems," *Proceedings of IEEE/PES Transmission & Distribution Conference & Exposition: Asia and Pacific*, Dalian, China, pp. 1-6, 2005.
- [45] Z. Saad-Saoud and N. Jenkins, "The application of advanced static VAr compensators to wind farms," *Proceedings of IEE Colloquium on Power Electronics for Renewable Energy*, London, United Kingdom, pp. 6/1-6/5, 1997.
- [46] J. G. Slootweg, H. Polinder and W. L. Kling, "Initialization of wind turbine models in power system dynamics simulations," *Proceedings of IEEE Porto Power Tech*, Porto, Portugal, pp. 6, 2001.
- [47] T. Gjengedal, "Integration of wind power and the impact on power system operation," *Proceedings of Large Engineering Systems Conference on Power Engineering*, Montreal, Canada, pp. 76-83, 2003.
- [48] V. Akhmativ and H. Knudsen, "Modelling of windmill induction generators in dynamic simulation programs," *Proceedings of Power Tech*, Budapest, Hungary, pp. 108, 1999.
- [49] Z. Chen and Y. Hu, "Dynamics performance improvement of a power electronic interfaced wind power conversion system," *Proceedings of International Power Electronics and Motion Control Conference*, Xi'an, China, 2004, pp. 1641-1646.
- [50] Z. Chen and Y. Hu, "Power system dynamics influenced by a power electronic interface for variable speed wind energy conversion systems," *Proceedings of Universities Power Engineering Conference*, Bristol, United Kingdom, pp. 659-663, 2004.
- [51] Z. Chen, F. Blaabjerg and Y. Hu, "Voltage recovery of dynamic slip control wind turbines with a STATCOM," *Proceedings of International Power Engineering Conference*, Singapore, pp. 1093-1100, 2005.

- [52] S. K. Salman and A. L. J. Teo, "Windmill modeling consideration and factors influencing the stability of a grid-connected wind power-based embedded generator," *IEEE Transactions on Power Systems*, vol. 18, no. 2, pp. 793-802, 2003.
- [53] J. Wiik, J. O. Gjefde and T. Gjengedal, "Impacts from large scale integration of wind energy farms into weak power systems," *Proceedings of International Conference on Power System Technology*, Perth, Australia, pp. 49-54, 2000.
- [54] Zhaoyang Su, Ping Wang and Pengxian Song, "Research on control strategy of DFIG rotor side converter," *Proceedings of International Transportation Electrification Conference Asia-Pacific*, Beijing, China, pp. 1-5, 2014.
- [55] B. Hamane, M. L. Doumbia, M. Bouhamida and M. Benghanem, "Control of wind turbine based on DFIG using Fuzzy-PI and Sliding Mode controllers," *Proceedings of Ecological Vehicles and Renewable Energies*, Monte-Carlo, Monaco, pp. 1-8, 2014.
- [56] S. Pati and S. Samantray, "Decoupled control of active and reactive power in a DFIG based wind energy conversion system with conventional P-I controllers," *Proceedings of International Conference on Circuits, Power and Computing Technologies*, Nagercoil, India, pp. 898-903, 2014.
- [57] Z. Kara and K. Barra, "Wind energy conversion based doubly fed induction generator controlled by direct matrix converter," *Proceedings of International Renewable Energy Congress*, Hammamet, Tunisia, pp. 1-6, 2014.
- [58] N. K. Swami Naidu and B. Singh, "Doubly Fed Induction Generator for Wind Energy Conversion Systems With Integrated Active Filter Capabilities," *IEEE Transactions on Industrial Informatics*, vol. 11, no. 4, pp. 923-933, 2015.
- [59] S. Pati, S. K. Kar, K. B. Mohanty and S. S. Dash, "Voltage profile improvement of a micro grid system using a DFIG based wind energy conversion system," *Proceedings of Power Electronics, Drives and Energy Systems*, Mumbai, India, pp. 1-6, 2014.
- [60] R. G. Wandhare and V. Agarwal, "Novel Integration of a PV-Wind Energy System With Enhanced Efficiency," *IEEE Transactions on Power Electronics*, vol. 30, no. 7, pp. 3638-3649, 2015.
- [61] N. K. S. Naidu and B. Singh, "Experimental implementation of Doubly Fed Induction Generator based Standalone Wind Energy Conversion System," *Proceedings of India International Conference on Power Electronics*, Kurukshetra, India, pp. 1-6, 2014.
- [62] A. Boukhriss, A. Essadki, A. Bouallouch and T. Nasser, "Maximization of generated power from wind energy conversion systems using a doubly fed induction generator with active disturbance rejection control," *Proceedings of World Conference on Complex Systems*, Agadir, Morocco, pp. 330-335, 2014.

- [63] R. A. McMahon, P. C. Roberts, X. Wang and P. J. Tavner, "Performance of BDFM as generator and motor," *IEE Proceedings - Electric Power Applications*, vol. 153, no. 2, pp. 289-299, 2006.
- [64] T. Long, S. Shao, E. Abdi, P. Malliband, M. E. Mathekga, R. A. McMahon and P. J. Tavner, "Symmetrical low voltage ride-through of a 250 kW brushless DFIG," *Proceedings of Power Electronics, Machines and Drives*, Bristol, United Kingdom, pp. 1-6, 2012.
- [65] C. S. Brune, R. Spee and A. K. Wallace, "Experimental evaluation of a variable-speed, doubly-fed wind-power generation system," *IEEE Transactions on Industry Applications*, vol. 30, no. 3, pp. 648-655, 1994.
- [66] E. Abdi, X. Wang, S. Shao, R. A. McMahon and P. Tavner, "Performance Characterisation of Brushless Doubly-Fed Generator," *Proceedings of IEEE Industry Applications Society Annual Meeting*, Edmonton, Canada, pp. 1-6, 2008.
- [67] R. Carlson, H. Voltolini, F. Runcos, P. Kuo-Peng and N. J. Batistela, "Performance Analysis with Power Factor Compensation of a 75 kW Brushless Doubly Fed Induction Generator Prototype," *Proceedings of IEEE International Electric Machines & Drives Conference*, Antalya, Turkey, pp. 1502-1507, 2007.
- [68] P. C. Roberts, R. A. McMahon, P. J. Tavner, J. M. Maciejowski and T. J. Flack, "Equivalent circuit for the brushless doubly fed machine (BDFM) including parameter estimation and experimental verification," *IEE Proceedings - Electric Power Applications*, vol. 152, no. 4, pp. 933-942, 2005.
- [69] S. M. R. Kazmi, H. Goto, H. Guo and O. Ichinokura, "A Novel Algorithm for Fast and Efficient Speed-Sensorless Maximum Power Point Tracking in Wind Energy Conversion Systems," *IEEE Transactions on Industrial Electronics*, vol. 58, no. 1, pp. 29-36, 2011.
- [70] W. Qiao, J. Liang, G. K. Venayagamoorthy and R. Harley, "Computational intelligence for control of wind turbine generators," *Proceedings of IEEE Power and Energy Society General Meeting*, Detroit, United States, pp. 1-6, 2011.
- [71] W. Qiao, "Intelligent mechanical sensorless MPPT control for wind energy systems," *Proceedings of IEEE Power and Energy Society General Meeting*, San Diego, United States, pp. 1-8, 2012.
- [72] C. Wei, Z. Zhang, W. Qiao and L. Qu, "Intelligent maximum power extraction control for wind energy conversion systems based on online Q-learning with function approximation," *Proceedings of IEEE Energy Conversion Congress and Exposition*, Pittsburgh, United States, pp. 4911-4916, 2014.
- [73] P. Cheng, C. Wu, J. Ma and F. Blaabjerg, "Coordinated Derived Current Control of DFIG's RSC and GSC Without PLL Under Unbalanced Grid Voltage Conditions," *IEEE Access*, vol. 8, pp. 64760-64769, 2020.
- [74] G. A. Smith and K. A. Nigim, "Wind-energy recovery by a static Scherbius induction generator," *IEE Proceedings C - Generation, Transmission and Distribution*, vol. 128, no. 6, pp. 317-324, 1981.

- [75] Z. M. Salameh and L. F. Kazda, "Analysis of the Steady State Performance of the Double Output Induction Generator," *IEEE Transactions on Energy Conversion*, vol. EC-1, no. 1, pp. 26-32, 1986.
- [76] M. S. Vicatos and J. A. Tegopoulos, "Steady state analysis of a doubly-fed induction generator under synchronous operation," *IEEE Transactions on Energy Conversion*, vol. 4, no. 3, pp. 495-501, 1989.
- [77] R. Pena, J. C. Clare and G. M. Asher, "A doubly fed induction generator using back-to-back PWM converters supplying an isolated load from a variable speed wind turbine," *IEE Proceedings - Electric Power Applications*, vol. 143, no. 5, pp. 380-387, 1996.
- [78] A. Petersson, T. Thiringer, L. Harnefors and T. Petru, "Modeling and experimental verification of grid interaction of a DFIG wind turbine," *IEEE Transactions on Energy Conversion*, vol. 20, no. 4, pp. 878-886, 2005.
- [79] I. Boldea, L. Tutelea and A. Popa, "Large variable speed generators design and their control: a revisit in 2019," *Proceedings of Aegean Conference on Electrical Machines and Power Electronics*, Istanbul, Turkey, pp. 29-40, 2019.
- [80] H. Banakar, C. Luo and B. T. Ooi, "Steady-state stability analysis of doubly-fed induction generators under decoupled P-Q control," *IEE Proceedings - Electric Power Applications*, vol. 153, no. 2, pp. 300-306, 2006.
- [81] M. Kayikci and J. V. Milanovic, "Reactive Power Control Strategies for DFIG-Based Plants," *IEEE Transactions on Energy Conversion*, vol. 22, no. 2, pp. 389-396, 2007.
- [82] D. Aguglia, P. Viarouge, R. Wamkeue and J. Cros, "Analytical determination of steady-state converter control laws for wind turbines equipped with doubly fed induction generators," *IET Renewable Power Generation*, vol. 2, no. 1, pp. 16-25, 2008.
- [83] J. M. Mauricio, A. E. LeÓN, A. GÓmez-Expósito and J. A. Solsona, "An Adaptive Nonlinear Controller for DFIM-Based Wind Energy Conversion Systems," *IEEE Transactions on Energy Conversion*, vol. 23, no. 4, pp. 1025-1035, 2008.
- [84] G. Tsourakis, B. M. Nomikos and C. D. Vournas, "Contribution of Doubly Fed Wind Generators to Oscillation Damping," *IEEE Transactions on Energy Conversion*, vol. 24, no. 3, pp. 783-791, 2009.

- [85] B. C. Rabelo, W. Hofmann, J. L. da Silva, R. G. de Oliveira and S. R. Silva, "Reactive Power Control Design in Doubly Fed Induction Generators for Wind Turbines," *IEEE Transactions on Industrial Electronics*, vol. 56, no. 10, pp. 4154-4162, 2009.
- [86] S. Engelhardt, I. Erlich, C. Feltes, J. Kretschmann and F. Shewarega, "Reactive Power Capability of Wind Turbines Based on Doubly Fed Induction Generators," *IEEE Transactions on Energy Conversion*, vol. 26, no. 1, pp. 364-372, 2011.
- [87] O. Abdel-Baqi and A. Nasiri, "Series Voltage Compensation for DFIG Wind Turbine Low-Voltage Ride-Through Solution," *IEEE Transactions on Energy Conversion*, vol. 26, no. 1, pp. 272-280, 2011.
- [88] I. Cadirci and M. Ermis, "Double-output induction generator operating at subsynchronous and supersynchronous speeds: steady-state performance optimisation and wind-energy recovery," *IEE Proceedings B - Electric Power Applications*, vol. 139, no. 5, pp. 429-442, 1992.
- [89] A. T. Alexandridis, G. C. Konstantopoulos and Q. Zhong, "Advanced Integrated Modeling and Analysis for Adjustable Speed Drives of Induction Motors Operating With Minimum Losses," *IEEE Transactions on Energy Conversion*, vol. 30, no. 3, pp. 1237-1246, 2015.
- [90] P. Chrin, M. David, P. Maussion, J. Saint-Michel, E. Fournier and L. Bun, "Modeling iron, mechanical and rotor copper losses in induction machine with the design of experiments," *Proceedings of 40th Annual Conference of the IEEE Industrial Electronics Society*, Dallas, United States, pp. 729-735, 2014.
- [91] B. E. Elnaghi and S. A. Selim, "Performance of double fed induction generator based wind turbine using Adaptive Neuro-Fuzzy Inference System," *Proceedings of IEEE Conference of Russian Young Researchers in Electrical and Electronic Engineering*, St. Petersburg, Russia, pp. 808-813, 2017.
- [92] N. Karakasis, N. Jabbour, E. Tsioumas and C. Mademlis, "Efficiency increase in a wind system with Doubly Fed Induction Generator," *Proceedings of 42nd Annual Conference of the IEEE Industrial Electronics Society*, Florence, Italy, pp. 4091-4096, 2016.
- [93] C. Liu and Y. Hsu, "Effect of Rotor Excitation Voltage on Steady-State Stability and Maximum Output Power of a Doubly Fed Induction Generator," *IEEE Transactions on Industrial Electronics*, vol. 58, no. 4, pp. 1096-1109, 2011.
- [94] S. Mondal and D. Kastha, "Maximum Active and Reactive Power Capability of a Matrix Converter-Fed DFIG-Based Wind Energy Conversion System," *IEEE Journal of Emerging and Selected Topics in Power Electronics*, vol. 5, no. 3, pp. 1322-1333, 2017.

- [95] Y. Weng and Y. Hsu, "Sliding mode regulator for maximum power tracking and copper loss minimisation of a doubly fed induction generator," *IET Renewable Power Generation*, vol. 9, no. 4, pp. 297-305, 2015.
- [96] G. D. Marques and M. F. Iacchetti, "Field-Weakening Control for Efficiency Optimization in a DFIG Connected to a DC-Link," *IEEE Transactions on Industrial Electronics*, vol. 63, no. 6, pp. 3409-3419, 2016.
- [97] H. Misra and A. K. Jain, "Analysis of Stand-Alone DFIG-DC System and DC Voltage Regulation With Reduced Sensors," *IEEE Transactions on Industrial Electronics*, vol. 64, no. 6, pp. 4402-4412, 2017.
- [98] B. Chen, T. Lu, Y. Hsu, W. Chen and Z. Lee, "An Analytical Approach to Maximum Power Tracking and Loss Minimization of a Doubly Fed Induction Generator Considering Core Loss," *IEEE Transactions on Energy Conversion*, vol. 27, no. 2, pp. 449-456, 2012.
- [99] Yifan Tang and Longya Xu, "A flexible active and reactive power control strategy for a variable speed constant frequency generating system," *IEEE Transactions on Power Electronics*, vol. 10, no. 4, pp. 472-478, 1995.
- [100] A. Luna, F. K. A. Lima, D. Santos, P. Rodriguez, E. H. Watanabe and S. Arnaltes, "Simplified Modeling of a DFIG for Transient Studies in Wind Power Applications," *IEEE Transactions on Industrial Electronics*, vol. 58, no. 1, pp. 9-20, 2011.
- [101] H. Nian, Y. Song, P. Zhou and Y. He, "Improved Direct Power Control of a Wind Turbine Driven Doubly Fed Induction Generator During Transient Grid Voltage Unbalance," *IEEE Transactions on Energy Conversion*, vol. 26, no. 3, pp. 976-986, 2011.
- [102] J. Hu, H. Nian, H. Xu and Y. He, "Dynamic Modeling and Improved Control of DFIG Under Distorted Grid Voltage Conditions," *IEEE Transactions on Energy Conversion*, vol. 26, no. 1, pp. 163-175, 2011.
- [103] H. Xu, J. Hu and Y. He, "Operation of Wind-Turbine-Driven DFIG Systems Under Distorted Grid Voltage Conditions: Analysis and Experimental Validations," *IEEE Transactions on Power Electronics*, vol. 27, no. 5, pp. 2354-2366, 2012.
- [104] V. Phan and H. Lee, "Control Strategy for Harmonic Elimination in Stand-Alone DFIG Applications With Nonlinear Loads," *IEEE Transactions on Power Electronics*, vol. 26, no. 9, pp. 2662-2675, 2011.
- [105] G. Iwanski and W. Koczara, "Simple autonomous sensorless generation system with wound induction machine," *Proceedings of IEEE International Symposium on Industrial Electronics, Ajaccio, France*, pp. 929-934 vol. 2, 2004.

- [106] S. Bifaretti, L. Tarisciotti, A. Watson, P. Zanchetta, A. Bellini and J. Clare, "Distributed commutations pulse-width modulation technique for high-power AC/DC multi-level converters," *IET Power Electronics*, vol. 5, no. 6, pp. 909-919, 2012.
- [107] B. -. Lin, C. -. Huang and Y. -. Lee, "Asymmetrical pulse-width modulation bidirectional DC-DC converter," *IET Power Electronics*, vol. 1, no. 3, pp. 336-347, 2008.
- [108] R. Barzegarkhoo, Y. P. Siwakoti and F. Blaabjerg, "A New Switched-Capacitor Five-Level Inverter Suitable for Transformerless Grid-Connected Applications," *IEEE Transactions on Power Electronics*, vol. 35, no. 8, pp. 8140-8153, 2020.
- [109] S. Mikkili and A. K. Panda, "Simulation and real-time implementation of shunt active filter id-iq control strategy for mitigation of harmonics with different fuzzy membership functions," *IET Power Electronics*, vol. 5, no. 9, pp. 1856-1872, 2012.
- [110] P. Zumel, C. Fernandez, M. Sanz, A. Lazaro and A. Barrado, "Step-By-Step Design of an FPGA-Based Digital Compensator for DC/DC Converters Oriented to an Introductory Course," *IEEE Transactions on Education*, vol. 54, no. 4, pp. 599-609, 2011.
- [111] M. Naouar, E. Monmasson, A. A. Naassani, I. Slama-Belkhodja and N. Patin, "FPGA-Based Current Controllers for AC Machine Drives—A Review," *IEEE Transactions on Industrial Electronics*, vol. 54, no. 4, pp. 1907-1925, 2007.
- [112] J. J. Rodriguez-Andina, M. J. Moure and M. D. Valdes, "Features, Design Tools, and Application Domains of FPGAs," *IEEE Transactions on Industrial Electronics*, vol. 54, no. 4, pp. 1810-1823, 2007.
- [113] E. Monmasson and M. N. Cirstea, "FPGA Design Methodology for Industrial Control Systems—A Review," *IEEE Transactions on Industrial Electronics*, vol. 54, no. 4, pp. 1824-1842, 2007.
- [114] X. Lin-Shi, F. Morel, A. M. Llor, B. Allard and J. Retif, "Implementation of Hybrid Control for Motor Drives," *IEEE Transactions on Industrial Electronics*, vol. 54, no. 4, pp. 1946-1952, 2007.
- [115] J. Acero, D. Navarro, L. A. Barragan, I. Garde, J. I. Artigas and J. M. Burdio, "FPGA-Based Power Measuring for Induction Heating Appliances Using Sigma-Delta A/D Conversion," *IEEE Transactions on Industrial Electronics*, vol. 54, no. 4, pp. 1843-1852, 2007.

- [116] A. Fratta, G. Griffero and S. Nieddu, "Comparative analysis among DSP and FPGA-based control capabilities in PWM power converters," *Proceedings of 30th Annual Conference of IEEE Industrial Electronics Society*, Busan, South Korea, pp. 257-262, 2004.
- [117] Ying-Yu Tzou and Hau-Jean Hsu, "FPGA realization of space-vector PWM control IC for three-phase PWM inverters," *IEEE Transactions on Power Electronics*, vol. 12, no. 6, pp. 953-963, 1997.
- [118] N. D. Patel and U. K. Madawala, "A Bit-Stream-Based PWM Technique for Sine-Wave Generation," *IEEE Transactions on Industrial Electronics*, vol. 56, no. 7, pp. 2530-2539, 2009.
- [119] A. Myaing, M. O. Faruque, V. Dinavahi and C. Dufour, "Comparison of insulated gate bipolar transistor models for FPGA-based real-timesimulation of electric drives and application guideline," *IET Power Electronics*, vol. 5, no. 3, pp. 293-303, 2012.
- [120] S. Mekhilef and A. Masaoud, "Xilinx FPGA Based Multilevel PWM Single Phase Inverter," *Proceedings of International Conference on Industrial Technology*, Mumbai, India, pp. 259-264, 2006.
- [121] S. Mekhilef and N. A. Rahim, "Xilinx FPGA based three-phase PWM inverter and its application for utility connected PV system," *Proceedings of IEEE Region 10 Conference on Computers, Communications, Control and Power Engineering*, Beijing, China, pp. 2079-2082, 2002.
- [122] A. Monti, E. Santi, R. A. Dougal and M. Riva, "Rapid prototyping of digital controls for power electronics," *IEEE Transactions on Power Electronics*, vol. 18, no. 3, pp. 915-923, 2003.
- [123] B. Lu, X. Wu, H. Figueroa and A. Monti, "A Low-Cost Real-Time Hardware-in-the-Loop Testing Approach of Power Electronics Controls," *IEEE Transactions on Industrial Electronics*, vol. 54, no. 2, pp. 919-931, 2007.
- [124] F. Filho, Y. Cao and L. M. Tolbert, "11-Level cascaded H-bridge grid-tied inverter interface with solar panels," *Proceedings of Twenty-Fifth Annual IEEE Applied Power Electronics Conference and Exposition*, Palm Springs, United States, pp. 968-972, 2010.
- [125] Xilinx Inc. System Generator for DSP User Guide, December 2010.
- [126] Xilinx Inc.: ISE Design Suite: Installation, Licensing, and Release Notes Guide, UG631 (v 12.4) December 14, 2010.
- [127] X. Liu, A. H. Osman and O. P. Malik, "Real-Time Implementation of a Hybrid Protection Scheme for Bipolar HVDC Line Using FPGA," *IEEE Transactions on Power Delivery*, vol. 26, no. 1, pp. 101-108, 2011.

- [128] G. Oriti and A. L. Julian, "Three-Phase VSI with FPGA-Based Multisampled Space Vector Modulation," *IEEE Transactions on Industry Applications*, vol. 47, no. 4, pp. 1813-1820, 2011.
- [129] V. Sabatini, L. Bigarelli, M. Di Benedetto, A. Lidozzi, L. Solero and G. Brown, "FPGA-based Model Predictive Control for High Frequency Variable Speed Generating Units," *Proceedings of Symposium on Power Electronics, Electrical Drives, Automation and Motion*, Amalfi, Italy, pp. 1364-1369, 2018.
- [130] W. Li, G. Joos and J. Belanger, "Real-Time Simulation of a Wind Turbine Generator Coupled With a Battery Supercapacitor Energy Storage System," *IEEE Transactions on Industrial Electronics*, vol. 57, no. 4, pp. 1137-1145, 2010.
- [131] M. Gunasekaran and R. Potluri, "Low-Cost Undergraduate Control Systems Experiments Using Microcontroller-Based Control of a DC Motor," *IEEE Transactions on Education*, vol. 55, no. 4, pp. 508-516, 2012.
- [132] M. Huang, P. Yeh, U. Yeh and M. Huang, "Digital-Controlled Single-Phase Transformer-Based Inverter for Non-Linear Load Applications," *IEEE Transactions on Industrial Informatics*, vol. 9, no. 2, pp. 1084-1093, 2013.
- [133] A. Kirubakaran, S. Jain and R. K. Nema, "DSP-Controlled Power Electronic Interface for Fuel-Cell-Based Distributed Generation," *IEEE Transactions on Power Electronics*, vol. 26, no. 12, pp. 3853-3864, 2011.
- [134] F. Mendoza-Mondragon, A. Espinosa-Calderon, A. m. Martinez-Hernandez and J. Rodriguez-Resendiz, "Implementation of high resolution unipolar PWM inverter using Xilinx System Generator," *Proceedings of Mechatronics, Adaptive and Intelligent Systems*, Hermosillo, Mexico, pp. 1-6, 2016.
- [135] S. J. Pinto, G. Panda and R. Peesapati, "An Implementation of Hybrid Control Strategy for Distributed Generation System Interface Using Xilinx System Generator," *IEEE Transactions on Industrial Informatics*, vol. 13, no. 5, pp. 2735-2745, 2017.
- [136] M. Sedighizadeh and A. Rezazadeh, "Self tuning control of wind turbine using neural network identifier," *Electrical Engineering, Springer*, vol. 90, no. 7, pp. 479-491, 2008.
- [137] E. Cadenas and W. Rivera, "Short term wind speed forecasting in La Venta.Oaxaca, Mexico, using artificial neural networks," *Renewable Energy*, vol. 34, no. 1, pp.274-278, 2009.

- [138] M. Cellura, G. Cirrincione, A. Marvuglia and A. Miraoui, "Wind speed spatial estimation for energy planning in Sicily: A neural kriging application," *Renewable Energy*, vol. 33, no. 6, pp. 1251-1266, 2008.
- [139] K. Ro and Han-ho Choi, "Application of neural network controller for maximum power extraction of a grid-connected wind turbine system," *Electrical Engineering, Springer*, vol. SB, no. 1, pp. 45-53, 2005.
- [140] R. S. Khela, R. K. Bansal, K. S. Sandhu and A. K. Goel, "Application of artificial neural network for analysis of self-excited induction generator," *Journal of Computer Science and Technology*, vol. 6, no. 2, pp. 73-79, 2006.
- [141] R. S. Khela, R. K. Bansal, K. S. Sandhu and A. K. Goel, "Cascaded ANN for evaluation of frequency and air-gap voltage of self-excited induction generator," *International Journal of Electrical, Computer and Systems Engineering*, vol. 1, no. 1, pp. 57-63, 2007.
- [142] F. Giraud and Z. M. Salameh, "Neural network modeling of the gust effects on a grid interactive wind energy conversion system with battery storage," *Electric Power Systems Research*, vol. 50, no. 3, pp. 155-161, 1999.
- [143] N. Mrabet Bellaaj, L. Bouzidi and M. Elleuch, "Development of a neural model for wind power integration into the dispatching process," *Journal of Electrical Systems*, vol. 4, no. 4, pp. 1-12, 2008.
- [144] H. M. Jabr, D. Lu and N. C. Kar, "Design and Implementation of Neuro-Fuzzy Vector Control for Wind-Driven Doubly-Fed Induction Generator," *IEEE Transactions on Sustainable Energy*, vol. 2, no. 4, pp. 404-413, 2011.
- [145] C. Opathella, B. N. Singh, D. Cheng and B. Venkatesh, "Intelligent wind generator models for power flow studies in PSS®E and PSS®SINCAL," *IEEE Transactions on Power Systems*, vol. 28, no. 2, pp. 1149-1159, 2013.
- [146] R. A. de Marchi, P. S. Dainez, F. J. Von Zuben and E. Bim, "A Multilayer Perceptron Controller Applied to the Direct Power Control of a Doubly Fed Induction Generator," *IEEE Transactions on Sustainable Energy*, vol. 5, no. 2, pp. 498-506, 2014.
- [147] C. Wei, L. Qu and W. Qiao, "Evaluation of ANN estimation-based MPPT control for a DFIG wind turbine," *Proceedings of IEEE Symposium on Power Electronics and Machines for Wind and Water Applications*, Milwaukee, United States, pp. 1-6, 2014.

- [148] H. Chaoui and O. Okoye, "Nonlinear power control of doubly fed induction generator wind turbines using neural networks," *Proceedings of IEEE 25th International Symposium on Industrial Electronics (ISIE)*, Santa Clara, United States, pp. 562-567, 2016.
- [149] L. Djilali, E. N. Sanchez and M. Belkheiri, "Real-time neural sliding mode field oriented control for a DFIG-based wind turbine under balanced and unbalanced grid conditions," *IET Renewable Power Generation*, vol. 13, no. 4, pp. 618-632, 2019.
- [150] L. Krichen, B. Francois and A. Ouali, "A fuzzy logic supervisor for active and reactive power control of a fixed speed wind energy conversion system," *Electric Power Systems Research*, vol. 78, no. 3, pp. 418-424, 2008.
- [151] G. Capizzi and G. Tina, "Long-term operation optimization of integrated generation systems by fuzzy logic-based management," *Energy*, vol. 32, no. 7, pp. 1047-1054, 2007.
- [152] H. M. Mashaly, A. M. Sharaf, A. A. El-Sattar and M. M. Mansour, "Implementation of a fuzzy logic controller for wind energy induction generator DC link scheme," *Proceedings of IEEE 3rd International Fuzzy Systems Conference*, Orlando, United States, pp. 978-982, 1994.
- [153] S. Velusami and S. Singaravelu, "Steady state modeling and fuzzy logic based analysis of wind driven single phase induction generators," *Renewable Energy*, vol. 32, no. 14, pp. 2386-2406, 2007.
- [154] M. G. Simoes, B. K. Bose and R. J. Spiegel, "Fuzzy logic based intelligent control of a variable speed cage machine wind generation system," *IEEE Transactions on Power Electronics*, vol. 12, no. 1, pp. 87-95, 1997.
- [155] A. Dida and D. Benattous, "Fuzzy logic based sensorless MPPT algorithm for wind turbine system driven DFIG," *Proceedings of Control, Engineering & Information Technology*, Tlemcen, Algeria, pp. 1-6, 2015.
- [156] S. Krishnama Raju and G. N. Pillai, "Design and Implementation of Type-2 Fuzzy Logic Controller for DFIG-Based Wind Energy Systems in Distribution Networks," *IEEE Transactions on Sustainable Energy*, vol. 7, no. 1, pp. 345-353, 2016.
- [157] S. Ullah, I. M. Qureshi and M. M. Zohaib, "Design of an Artificial-Intelligence based controller for doubly fed induction generator based wind energy conversion system," *Proceedings of International Conference on Intelligent Systems Engineering*, Islamabad, Pakistan, pp. 318-325, 2016.

- [158] T. K. Mahmoud, Z. Y. Dong and J. Ma, "A Developed Integrated Scheme Based Approach for Wind Turbine Intelligent Control," *IEEE Transactions on Sustainable Energy*, vol. 8, no. 3, pp. 927-937, 2017.
- [159] A. Ashouri-Zadeh, M. Toulabi, S. Bahrami and A. M. Ranjbar, "Modification of DFIG's Active Power Control Loop for Speed Control Enhancement and Inertial Frequency Response," *IEEE Transactions on Sustainable Energy*, vol. 8, no. 4, pp. 1772-1782, 2017.
- [160] D. Sun, L. Sun, F. Wu, L. Zhang, W. Geng, J. Peng, and F. Liu, "Research on frequency inertia response control strategy of SCESS-DFIG system considering variable wind speed," *The Journal of Engineering*, vol. 2019, no. 16, pp. 2995-3001, 2019.
- [161] S. Puchalapalli and B. Singh, "A Single Input Variable FLC for DFIG-Based WPGS in Standalone Mode," *IEEE Transactions on Sustainable Energy*, vol. 11, no. 2, pp. 595-607, 2020.
- [162] Sandeep Banerjee, Dheeraj Joshi, and Madhusudan Singh, "Genetic algorithm approach for efficiency maximization and power factor enhancement of a grid connected doubly fed induction generator," *Journal of Information and Optimization Sciences*, vol. 40, no. 2, pp. 535-545, 2019.
- [163] K. Deb, A. Anand and D. Joshi, "A Computationally Efficient Evolutionary Algorithm for Real-Parameter Optimization," *Evolutionary Computation*, vol. 10, no. 4, pp. 371-395, 2002.
- [164] R. Jayashri and R. P. Kumudini Devi, "Effect of tuned unified power flow controller to mitigate the rotor speed instability of fixed-speed wind turbines," *Renewable Energy*, vol. 34, no. 3, pp. 591-596, 2009.
- [165] N. Kumaresan, M. P. Selvan and M. Subbiah, "Design optimisation and speed extension of wind-driven self-excited induction generators-A new approach," *Electric Power Components and Systems*, vol. 32, no. 2, pp. 215-228, 2004.
- [166] Y. N. Anagreh and I. S. Al-Kofahi, "Genetic algorithm-based performance analysis of self excited induction generator," *International Journal of Modelling and Simulation*, vol. 26, no.2, pp. 175-279, 2006.
- [167] J. P. A. Vieira, M. V. A. Nunes, U. H. Bezerra and A. C. D. Nascimento, "Designing optimal controllers for doubly fed induction generators using a genetic algorithm," *IET Generation, Transmission & Distribution*, vol. 3, no. 5, pp. 472-484, 2009.
- [168] T. D. Vrionis, X. I. Koutiva and N. A. Vovos, "A Genetic Algorithm-Based Low Voltage Ride-Through Control Strategy for Grid Connected Doubly Fed Induction Wind Generators," *IEEE Transactions on Power Systems*, vol. 29, no. 3, pp. 1325-1334, 2014.

- [169] A. Ashouri-Zadeh, M. Toulabi and A. M. Ranjbar, "Coordinated design of fuzzy-based speed controller and auxiliary controllers in a variable speed wind turbine to enhance frequency control," *IET Renewable Power Generation*, vol. 10, no. 9, pp. 1298-1308, 10 2016.
- [170] W. Ning, X. Wu, Y. J. Guan and F. Chen, "Method to suppress sub-synchronous oscillation of DFIG-based wind farms based on virtual impedance," *The Journal of Engineering*, vol. 2017, no. 13, pp. 2173-2177.
- [171] C. Tian, X. Luo, J. Dong, B. Chen and J. Yuan, "Voltage and reactive power optimisation of offshore wind farms based on terminal voltage control mode of DFIG," *The Journal of Engineering*, vol. 2017, no. 13, pp. 874-879, 2017.
- [172] A. Chen, D. Xie, D. Zhang, C. Gu and K. Wang, "PI Parameter Tuning of Converters for Sub-Synchronous Interactions Existing in Grid-Connected DFIG Wind Turbines," *IEEE Transactions on Power Electronics*, vol. 34, no. 7, pp. 6345-6355, 2019.
- [173] I. Erazo-Damián, J. M. Apsley, R. Perini, M. F. Iacchetti and G. D. Marques, "Stand-Alone DFIG FOC Sensitivity and Stability Under Mismatched Inductances," *IEEE Transactions on Energy Conversion*, vol. 34, no. 2, pp. 860-869, 2019.
- [174] G. Poddar and V. T. Ranganathan, "Sensorless field-oriented control for double-inverter-fed wound-rotor induction motor drive," *IEEE Transactions on Industrial Electronics*, vol. 51, no. 5, pp. 1089-1096, 2004.
- [175] N. Holtsmark, H. J. Bahirat, M. Molinas, B. A. Mork and H. K. Hoidalen, "An All-DC Offshore Wind Farm With Series-Connected Turbines: An Alternative to the Classical Parallel AC Model?," *IEEE Transactions on Industrial Electronics*, vol. 60, no. 6, pp. 2420-2428, 2013.
- [176] P. Karlsson and J. Svensson, "DC bus voltage control for a distributed power system," *IEEE Transactions on Power Electronics*, vol. 18, no. 6, pp. 1405-1412, 2003.
- [177] T. Dragičević, X. Lu, J. C. Vasquez and J. M. Guerrero, "DC Microgrids—Part I: A Review of Control Strategies and Stabilization Techniques," *IEEE Transactions on Power Electronics*, vol. 31, no. 7, pp. 4876-4891, 2016.
- [178] M. G. Jahromi, G. Mirzaeva, S. D. Mitchell and D. Gay, "Powering Mobile Mining Machines: DC Versus AC Power," *IEEE Industry Applications Magazine*, vol. 22, no. 5, pp. 63-72, 2016.

- [179] B. Zahedi and L. E. Norum, "Modeling and Simulation of All-Electric Ships With Low-Voltage DC Hybrid Power Systems," *IEEE Transactions on Power Electronics*, vol. 28, no. 10, pp. 4525-4537, 2013.
- [180] M. F. Iacchetti, G. D. Marques and R. Perini, "A Scheme for the Power Control in a DFIG Connected to a DC Bus via a Diode Rectifier," *IEEE Transactions on Power Electronics*, vol. 30, no. 3, pp. 1286-1296, 2015.
- [181] S. Yan, A. Zhang, H. Zhang and J. Wang, "A novel converter system for DFIG based on DC transmission," *Proceedings of 40th Annual Conference of the IEEE Industrial Electronics Society*, Dallas, United States, pp. 4133-4139, 2014.
- [182] M. V. Gururaj and N. P. Padhy, "A Cost-Effective Single Architecture to Operate DC Microgrid Interfaced DFIG Wind System During Grid-Connected, Fault, and Isolated Conditions," *IEEE Transactions on Industrial Informatics*, vol. 16, no. 2, pp. 922-934, 2020.
- [183] L. M. Castro and E. Acha, "On the Dynamic Modeling of Marine VSC-HVDC Power Grids Including Offshore Wind Farms," *IEEE Transactions on Sustainable Energy*, 2020.
- [184] R. Zhu, Z. Chen and X. Wu, "Diode rectifier bridge-based structure for DFIG-based wind turbine," *Proceedings of Applied Power Electronics Conference and Exposition*, Charlotte, United States, pp. 1290-1295, 2015.
- [185] G. D. Marques and M. F. Iacchetti, "Field-Weakening Control for Efficiency Optimization in a DFIG Connected to a DC-Link," *IEEE Transactions on Industrial Electronics*, vol. 63, no. 6, pp. 3409-3419, 2016.
- [186] M. F. Iacchetti, G. D. Marques and R. Perini, "Operation and design issues of a doubly fed induction generator stator connected to a dc net by a diode rectifier," *IET Electric Power Applications*, vol. 8, no. 8, pp. 310-319, 2014.
- [187] S. Bayhan, H. Abu-Rub and O. Ellabban, "Sensorless model predictive control scheme of wind-driven doubly fed induction generator in dc microgrid," *IET Renewable Power Generation*, vol. 10, no. 4, pp. 514-521, 2016.
- [188] A. Gundavarapu, H. Misra and A. K. Jain, "DC voltage regulation with field oriented control of WRIG-DC system feeding an isolated DC load," *Proceedings of International Conference on Power Systems*, New Delhi, India, pp. 1-6, 2016.

- [189] H. Misra, A. Gundavarapu and A. K. Jain, "Control Scheme for DC Voltage Regulation of Stand-Alone DFIG-DC System," *IEEE Transactions on Industrial Electronics*, vol. 64, no. 4, pp. 2700-2708, 2017.
- [190] H. Misra and A. K. Jain, "Analysis of Stand-Alone DFIG-DC System and DC Voltage Regulation With Reduced Sensors," *IEEE Transactions on Industrial Electronics*, vol. 64, no. 6, pp. 4402-4412, 2017.
- [191] G. D. Marques and M. F. Iacchetti, "Inner Control Method and Frequency Regulation of a DFIG Connected to a DC Link," *IEEE Transactions on Energy Conversion*, vol. 29, no. 2, pp. 435-444, 2014.
- [192] G. D. Marques and M. F. Iacchetti, "Stator Frequency Regulation in a Field-Oriented Controlled DFIG Connected to a DC Link," *IEEE Transactions on Industrial Electronics*, vol. 61, no. 11, pp. 5930-5939, 2014.
- [193] G. D. Marques and M. F. Iacchetti, "Sensorless Frequency and Voltage Control in the Stand-Alone DFIG-DC System," *IEEE Transactions on Industrial Electronics*, vol. 64, no. 3, pp. 1949-1957, 2017.
- [194] J. Li and K. Corzine, "A sensorless flux oriented control scheme for a DFIG connected to a DC link," *Proceedings of Power Systems Conference*, Clemson, United States, pp. 1-5, 2015.
- [195] G. D. Marques, D. M. Sousa and M. F. Iacchetti, "Air-Gap Power-Based Sensorless Control in a DFIG Connected to a DC Link," *IEEE Transactions on Energy Conversion*, vol. 30, no. 1, pp. 367-375, 2015.
- [196] G. D. Marques and M. F. Iacchetti, "A Self-Sensing Stator-Current-Based Control System of a DFIG Connected to a DC-Link," *IEEE Transactions on Industrial Electronics*, vol. 62, no. 10, pp. 6140-6150, 2015.
- [197] P. Maciejewski and G. Iwanski, "Modeling of six-phase Double Fed Induction Machine for autonomous DC voltage generation," *Proceedings of Ecological Vehicles and Renewable Energies*, Monte Carlo, Monaco, pp. 1-6, 2015.
- [198] M. F. Iacchetti, G. D. Marques and R. Perini, "Torque Ripple Reduction in a DFIG-DC System by Resonant Current Controllers," *IEEE Transactions on Power Electronics*, vol. 30, no. 8, pp. 4244-4254, 2015.
- [199] H. Nian, C. Wu and P. Cheng, "Direct Resonant Control Strategy for Torque Ripple Mitigation of DFIG Connected to DC Link through Diode Rectifier on Stator," *IEEE Transactions on Power Electronics*, vol. 32, no. 9, pp. 6936-6945, 2017.
- [200] A. Gundavarapu, H. Misra and A. K. Jain, "Direct Torque Control Scheme for DC Voltage Regulation of the Standalone DFIG-DC System," *IEEE Transactions on Industrial Electronics*, vol. 64, no. 5, pp. 3502-3512, 2017.

- [201] P. Maciejewski and G. Iwanski, "Direct Torque Control for Autonomous Doubly Fed Induction Machine based DC Generator," *Proceedings of Ecological Vehicles and Renewable Energies*, Monte Carlo, Monaco, pp. 1-6, 2017.
- [202] C. Wu and H. Nian, "Sinusoidal Current Operation of a DFIG-DC System Without Stator Voltage Sensors," *IEEE Transactions on Industrial Electronics*, vol. 65, no. 8, pp. 6250-6258, 2018.
- [203] G. D. Marques and M. F. Iacchetti, "Minimization of Torque Ripple in the DFIG-DC System Via Predictive Delay Compensation," *IEEE Transactions on Industrial Electronics*, vol. 65, no. 1, pp. 103-113, 2018.
- [204] C. Wu and H. Nian, "An Improved Repetitive Control of DFIG-DC System for Torque Ripple Suppression," *IEEE Transactions on Power Electronics*, vol. 33, no. 9, pp. 7634-7644, 2018.
- [205] S. M. A. Cruz, G. D. Marques, P. F. C. Gonçalves and M. F. Iacchetti, "Predictive Torque and Rotor Flux Control of a DFIG-DC System for Torque Ripple Compensation and Loss Minimization," *IEEE Transactions on Industrial Electronics*, vol. 65, no. 12, pp. 9301-9310, 2018.
- [206] H. Nian and X. Yi, "Coordinated control strategy for doubly-fed induction generator with DC connection topology," *IET Renewable Power Generation*, vol. 9, no. 7, pp. 747-756, 2015.
- [207] S. Yan, A. Zhang, H. Zhang, J. Wang and B. Cai, "An Optimum Design for a DC-Based DFIG System by Regulating Gearbox Ratio," *IEEE Transactions on Energy Conversion*, vol. 33, no. 1, pp. 223-231, 2018.
- [208] Y. Kawabata, E. Ejiogu and T. Kawabata, "Vector-controlled double-inverter-fed wound-rotor induction motor suitable for high-power drives," *IEEE Transactions on Industry Applications*, vol. 35, no. 5, pp. 1058-1066, 1999.
- [209] F. BonnetFrancois, P. Vidal and M. Pietrzak-David, "Dual Direct Torque Control of Doubly Fed Induction Machine," *IEEE Transactions on Industrial Electronics*, vol. 54, no. 5, pp. 2482-2490, 2007.
- [210] G. Poddar and V. T. Ranganathan, "Direct torque and frequency control of double-inverter-fed slip-ring induction motor drive," *IEEE Transactions on Industrial Electronics*, vol. 51, no. 6, pp. 1329-1337, 2004.
- [211] G. Poddar and V. T. Ranganathan, "Sensorless double-inverter-fed wound-rotor induction-Machine drive," *IEEE Transactions on Industrial Electronics*, vol. 53, no. 1, pp. 86-95, 2006.

- [212] S. Yan, A. Zhang, H. Zhang, J. Wang and B. Cai, "Optimized and coordinated model predictive control scheme for DFIGs with DC-based converter system," *Journal of Modern Power Systems and Clean Energy*, vol. 5, no. 4, pp. 620-630, 2017.
- [213] S. Yan, A. Zhang, H. Zhang and J. Wang, "Control scheme for DFIG converter system based on DC-transmission," *IET Electric Power Applications*, vol. 11, no. 8, pp. 1441-1448, 2017.
- [214] S. Yan, A. Zhang, H. Zhang, J. Wang and B. Cai, "Transient stability enhancement of DC-connected DFIG and its converter system using fault protective device," *Journal of Modern Power Systems and Clean Energy*, vol. 5, no. 6, pp. 887-896, 2017.
- [215] <https://www.alldatasheet.com/datasheet-pdf/pdf/611087/FAIRCHILD/FGA15N120AND.html>
- [216] <https://www.alldatasheet.com/datasheet-pdf/pdf/131336/TOSHIBA/TLP250.html>
- [217] <https://www.alldatasheet.com/datasheet-pdf/pdf/1183426/SS/7812.html>
- [218] <https://www.alldatasheet.com/datasheet-pdf/pdf/1192013/SS/7912.html>

APPENDIX A

Stator and rotor of all the DFIGs of table A.1 are connected in star and the rotor quantities have been referred to the stator.

Table A.1 Parameters of machines 1, 2, 3 and 4

Machine Parameters	DFIG-1	DFIG-2	DFIG-3	DFIG-4
Rated power (kW)	4	0.746	2.2	2000
Stator/ Rotor line voltage (V)	400	380	380	690
Frequency (Hz)	50	50	60	50
Stator resistance (Ω)	1.405	9.5	1.14	0.0026
Stator leakage inductance (H)	0.0058	0.02814	0.00586	0.000087
Rotor resistance (Ω)	1.395	8.04	2.818	0.0029
Rotor leakage inductance (H)	0.0058	0.02814	0.00586	0.000087
Mutual inductance (H)	0.1722	0.165	0.0714	0.0025
Pole pairs	2	2	3	2
Rated torque (N m)	25.465	4.75	17.51	12732
Rated stator current (A)	6.79	1.33	3.93	1760
Moment of inertia (kg m^2)	0.0131	0.0027	0.0099	127

APPENDIX B

The component details of the Buck Converter have been mentioned in Table B.1.

Table B.1 Design parameters of buck converter

Symbol	Quantity	Values (in respective Units)
L	Inductor	10 mH
C_o	Output Filter Capacitor	47 μ F
V_p	Breakdown Voltage of FR diode used in Buck converter	600 Volts

APPENDIX C

The electrical characteristics of IGBT switch FGA15N120AND [215] has been mentioned in Table C.1.

Table C.1 Electrical characteristics of IGBT switch FGA15N120AND

Electrical Characteristics of the IGBT						
T _C = 25°C unless otherwise noted						
Symbol	Parameter	Test Conditions	Min.	Typ.	Max.	Units
Off Characteristics						
BV _{CE3}	Collector-Emitter Breakdown Voltage	V _{GE} = 0V, I _C = 3mA	1200	–	–	V
ΔB _{VCE3} /ΔT _J	Temperature Coefficient of Breakdown Voltage	V _{GE} = 0V, I _C = 3mA	–	0.6	–	V/°C
I _{CE3}	Collector Cut-Off Current	V _{CE} = V _{CE3} , V _{GE} = 0V	–	–	3	mA
I _{GE3}	G-E Leakage Current	V _{GE} = V _{GE3} , V _{CE} = 0V	–	–	± 100	nA
On Characteristics						
V _{GE(th)}	G-E Threshold Voltage	I _C = 15mA, V _{CE} = V _{GE}	3.5	5.5	7.5	V
V _{CE(sat)}	Collector to Emitter Saturation Voltage	I _C = 15A, V _{GE} = 15V	–	2.4	3.2	V
		I _C = 15A, V _{GE} = 15V, T _C = 125°C	–	2.9	–	V
		I _C = 24A, V _{GE} = 15V	–	3.0	–	V
Dynamic Characteristics						
C _{ies}	Input Capacitance	V _{CE} = 30V, V _{GE} = 0V, f = 1MHz	–	1150	–	pF
C _{oes}	Output Capacitance		–	120	–	pF
C _{res}	Reverse Transfer Capacitance		–	56	–	pF
Switching Characteristics						
t _{d(on)}	Turn-On Delay Time	V _{CC} = 600 V, I _C = 15A, R _G = 20Ω, V _{GE} = 15V, Inductive Load, T _C = 25°C	–	90	–	ns
t _r	Rise Time		–	70	–	ns
t _{d(off)}	Turn-Off Delay Time		–	310	–	ns
t _f	Fall Time		–	60	120	ns
E _{on}	Turn-On Switching Loss		–	3.27	4.9	mJ
E _{off}	Turn-Off Switching Loss		–	0.6	0.9	mJ
E _{ts}	Total Switching Loss		–	3.68	5.8	mJ
t _{d(on)}	Turn-On Delay Time	V _{CC} = 600 V, I _C = 15A, R _G = 20Ω, V _{GE} = 15V, Inductive Load, T _C = 125°C	–	80	–	ns
t _r	Rise Time		–	60	–	ns
t _{d(off)}	Turn-Off Delay Time		–	310	–	ns
t _f	Fall Time		–	50	–	ns
E _{on}	Turn-On Switching Loss		–	3.41	–	mJ
E _{off}	Turn-Off Switching Loss		–	0.84	–	mJ
E _{ts}	Total Switching Loss		–	4.25	–	mJ
Q _g	Total Gate Charge	V _{CE} = 600 V, I _C = 15A, V _{GE} = 15V	–	120	180	nC
Q _{ge}	Gate-Emitter Charge		–	9	14	nC
Q _{gc}	Gate-Collector Charge		–	63	95	nC
L _e	Internal Emitter Inductance	Measured 5mm from PKG	–	14	–	nH

APPENDIX D

The electrical characteristics of IGBT driver IC TLP 250 [216] has been mentioned in Table D.1.

Table D.1 Electrical characteristics of IGBT driver IC TLP 250

Electrical Characteristics (Ta = -20~70°C, unless otherwise specified)

Characteristic		Symbol	Test Circuit	Test Condition		Min.	Typ.*	Max.	Unit
Input forward voltage		V _F	—	I _F = 10 mA, Ta = 25°C			1.6	1.8	V
Temperature coefficient of forward voltage		ΔV _F / ΔTa	—	I _F = 10 mA		—	-2.0	—	mV / °C
Input reverse current		I _R	—	V _R = 5V, Ta = 25°C			—	10	μA
Input capacitance		C _T	—	V = 0, f = 1MHz, Ta = 25°C		—	45	250	pF
Output current	"H" level	I _{OPH}	3	V _{CC} = 30V (*1)	I _F = 10 mA V _{B-6} = 4V	-0.5	-1.5	—	A
	"L" level	I _{OPL}	2		I _F = 0 V _{B-5} = 2.5V	0.5	2	—	
Output voltage	"H" level	V _{OH}	4	V _{CC1} = +15V, V _{EE1} = -15V R _L = 200Ω, I _F = 5mA		11	12.8	—	V
	"L" level	V _{OL}	5	V _{CC1} = +15V, V _{EE1} = -15V R _L = 200Ω, V _F = 0.8V		—	-14.2	-12.5	
Supply current	"H" level	I _{CCH}	—	V _{CC} = 30V, I _F = 10mA Ta = 25°C		—	7	—	mA
				V _{CC} = 30V, I _F = 10mA		—	—	11	
	"L" level	I _{CCL}	—	V _{CC} = 30V, I _F = 0mA Ta = 25°C		—	7.5	—	
				V _{CC} = 30V, I _F = 0mA		—	—	11	
Threshold input current	"Output L→H"	I _{FLH}	—	V _{CC1} = +15V, V _{EE1} = -15V R _L = 200Ω, V _O > 0V		—	1.2	5	mA
Threshold input voltage	"Output H→L"	I _{FHL}	—	V _{CC1} = +15V, V _{EE1} = -15V R _L = 200Ω, V _O < 0V		0.8	—	—	V
Supply voltage		V _{CC}	—			10	—	35	V
Capacitance (input-output)		C _S	—	V _S = 0, f = 1MHz Ta = 25°C		—	1.0	2.0	pF
Resistance(input-output)		R _S	—	V _S = 500V, Ta = 25°C R.H. ≤ 60%		1×10 ¹²	10 ¹⁴	—	Ω

* All typical values are at Ta = 25°C (*1): Duration of I_Q time ≤ 50μs

APPENDIX E

The electrical characteristics of voltage regulator IC 7812 [217] has been mentioned in Table E.1.

Table E.1 Electrical characteristics of voltage regulator IC 7812

DC Electrical Characteristics, $V_I = 18V$, $I_{OUT} = 500mA$, $C_I = 0.33\mu F$, $C_O = 0.1\mu f$, $T_{MIN} \leq T_J \leq T_{MAX}$ (unless noted otherwise)

PARAMETER	SYMBOL	TEST CONDITIONS	MIN	TYP	MAX	UNITS
Output Voltage	V_{OUT}	$T_J = 25^\circ C$	11.5	12	12.5	V
		$5mA \leq I_{OUT} \leq 1A$, $14.5V \leq V_{IN} \leq 27V$, $P_D \leq 15$ Watts	11.4	12	12.6	
Line Regulation	ΔV_{OUT}	$14.5V \leq V_{IN} \leq 30V$, $T_J = 25^\circ C$	-	3.8	24	mV
		$16V \leq V_{IN} \leq 22V$, $T_J = 25^\circ C$	-	0.3	24	
		$14.8V \leq V_{IN} \leq 27V$, $I_{OUT} = 1A$, $T_J = 25^\circ C$	-	-	48	
Load Regulation	ΔV_{OUT}	$5mA \leq I_{OUT} \leq 1.5A$, $T_J = 25^\circ C$	-	8.1	60	
Input Bias Current	I_B		-	3.4	6.5	mA
Input Bias Current Change	ΔI_B	$14.5V \leq V_{IN} \leq 30V$, $I_{OUT} = 1A$, $T_J = 25^\circ C$	-	-	0.7	mA
		$15V \leq V_{IN} \leq 30V$	-	-	0.8	
		$5mA \leq I_{OUT} \leq 1A$	-	-	0.5	
Output Noise Voltage	V_n	$10Hz \leq f \leq 100KHz$, $T_J = 25^\circ C$	-	10	-	$\mu V/V_{OUT}$
Ripple Rejection	RR	$15V \leq V_{IN} \leq 25V$, $f = 120Hz$	55	60	-	dB
Dropout Voltage	$V_{IN} - V_{OUT}$	$I_{OUT} = 1A$, $T_J = 25^\circ C$	-	2	-	V
Output Resistance	r_{OUT}	$f = 1 kHz$	-	1.1	-	m Ω
Short-Circuit Current Limit	I_{SC}	$V_{IN} = 35V$, $T_A = 25^\circ C$	-	0.2	-	A
Peak Output Current	I_{MAX}	$T_J = 25^\circ C$	-	2.2	-	A
Avg. Output Voltage Temp. Coefficient	TCV_{OUT}		-	-0.8	-	mV/ $^\circ C$

APPENDIX F

The electrical characteristics of voltage regulator IC 7912 [218] has been mentioned in Table F.1.

Table F.1 Electrical characteristics of voltage regulator IC 7912

DC Electrical Characteristics, $V_I = -10V$, $I_{OUT} = 500mA$, $C_I = 0.33\mu F$, $C_O = 0.1\mu f$, $T_{MIN} \leq T_J \leq T_{MAX}$ (unless noted otherwise)

PARAMETER	SYMBOL	TEST CONDITIONS	MIN	TYP	MAX	UNITS
Output Voltage	V_{OUT}	$T_J = 25^\circ C$	-11.50	-12	-12.50	V
		$5mA \leq I_{OUT} \leq 1A$, $-14.5V \geq V_{IN} \geq -27V$, $P_D \leq 15$ Watts	-11.40	-	-12.60	
Line Regulation	ΔV_{OUT}	$-14.5V \geq V_{IN} \geq -30V$, $I_{OUT} = 0.1A$, $T_J = 25^\circ C$	-	13	120	mV
		$-16V \geq V_{IN} \geq -22V$, $I_{OUT} = 0.1A$, $T_J = 25^\circ C$	-	6	60	
		$-14.5V \geq V_{IN} \geq -30V$, $I_{OUT} = 0.5A$, $T_J = 25^\circ C$	-	55	240	
		$-16V \geq V_{IN} \geq -22V$, $I_{OUT} = 0.5A$, $T_J = 25^\circ C$	-	24	120	
Load Regulation	ΔV_{OUT}	$5mA \leq I_{OUT} \leq 1.5A$, $T_J = 25^\circ C$	-	46	240	
		$250mA \leq I_{OUT} \leq 750mA$, $T_J = 25^\circ C$	-	17	120	
Input Bias Current	I_B	$T_J = 25^\circ C$	-	4.3	7.8	mA
Input Bias Current Change	ΔI_B	$-14.5V \geq V_{IN} \geq -27V$	-	-	1.0	mA
		$5mA \leq I_{OUT} \leq 1.5A$	-	-	0.5	
Output Noise Voltage	V_n	$10Hz \leq f \leq 100KHz$, $T_J = 25^\circ C$	-	75	-	$\mu V/V_{OUT}$
Ripple Rejection	RR	$I_{OUT} = 20mA$, $f = 120Hz$,	-	61	-	dB
Dropout Voltage	$V_{IN} - V_{OUT}$	$I_{OUT} = 1A$, $T_J = 25^\circ C$	-	2	-	V
Peak Output Current	I_{MAX}	$T_J = 25^\circ C$	-	2.1	-	A
Avg. Output Voltage Temp. Coefficient	TCV_{OUT}	$I_{OUT} = 5mA$, $0^\circ C \leq T_J \leq +125^\circ C$	-	-1.0	-	mV/ $^\circ C$

LIST OF PUBLICATIONS

PUBLICATIONS IN INTERNATIONAL JOURNALS

- 1) Sandeep Banerjee, Dheeraj Joshi, and Madhusudan Singh, "Genetic algorithm approach for efficiency maximization and power factor enhancement of a grid connected doubly fed induction generator," *Journal of Information and Optimization Sciences*, vol. 40, no. 2, pp. 535-545, 2019.
- 2) Sandeep Banerjee, Dheeraj Joshi, and Madhusudan Singh, "Mathematical modelling of doubly-fed induction generator," *Journal of Interdisciplinary Mathematics*, vol. 23, no. 5, pp. 927-934, 2020.
- 3) Sandeep Banerjee, Dheeraj Joshi, and Madhusudan Singh, "Investigations on Two-lead and Three-lead Rotor Connections of Doubly Fed Induction Generator," *Asian Journal of Water, Environment and Pollution*, vol. 17, no. 2, pp. 37-42, 2020.

PUBLICATIONS IN INTERNATIONAL CONFERENCES

- 1) S. Banerjee, D. Joshi, M. Singh and R. Sharma, "Analytical and comparative evaluation of advanced digital PWM control techniques," *Proceedings of Power India International Conference*, Delhi, India, pp. 1-6, 2014.
- 2) S. Banerjee, D. Joshi, M. Singh and R. Sharma, "Performance assessment of different control strategies for five level DCMLIs supplying static loads and dynamic loads," *Proceedings of India International Conference on Power Electronics*, Kurukshetra, India, pp. 1-6, 2014.
- 3) S. Banerjee, D. Joshi, M. Singh and R. Sharma, "Evaluation of modulation strategies for PV fed DCMLIs and its application to dynamic load," *Proceedings of International Conference on Power, Control and Embedded Systems*, Allahabad, India, pp. 1-6, 2014.
- 4) Sandeep Banerjee, Dheeraj Joshi, Madhusudan Singh "Comparison of Basic Control Strategies for Three Phase VSI," *Proceedings of International Conference On Advance Trends In Engineering, Technology And Research*, Kota, India, pp. 6-10, 2015.
- 5) S. Banerjee, D. Joshi and M. Singh, "A rational technique to maximize active power & diminish losses and reactive power of a DFIG," *Proceedings of International Conference on Power Systems*, New Delhi, India, pp. 1-6, 2016.